THESE DE DOCTORAT

NNT : 2023UPASP087

Study of additional radiation in the initial-state-radiation processes $e^+e^- \to \mu^+\mu^-\gamma$ and $e^+e^- \to \pi^+\pi^-\gamma$ in the *BABAR* experiment

Etude du rayonnement additionnel dans les processus de rayonnement à l'état initial $e^+e^- \to \mu^+\mu^-\gamma$ et $e^+e^- \to \pi^+\pi^-\gamma$ dans l'expérience BABAR

Thèse de doctorat de l'université Paris-Saclay et de Shanghai Jiao Tong University

School of Physics and Astronomy, Shanghai Jiao Tong University

École doctorale n° 576 : particules, hadrons, énergie et noyau : instrumentation, imagerie, cosmos et simulation (PHENIICS)
Spécialité de doctorat: Physique des particules
Graduate School : Physique. Référent : Faculté des sciences d'Orsay

Thèse préparée dans les unités de recherche **IJCLab** (Université Paris-Saclay) et **School of Physics and Astronomy** (Shanghai Jiao Tong University), sous la direction de **Zhiqing ZHANG**, Directeur de recherche, et la co-direction de **Liang LI**, Professeur

Thèse soutenue à Shanghai, le 22 septembre 2023, par

Dongyun BAI

Composition du jury

Membres du jury avec voix délibérative

Denis BERNARD Directeur de recherche, LLR, Ecole Polytechnique	Président
José OCARIZ Professeur, LPNHE, Sorbonne Université	Rapporteur & Examinateur
Changzheng YUAN Professeur, IHEP, Chinese Academy of Sciences	Rapporteur & Examinateur
Emi KOU Directrice de recherche, IJCLab, Université Paris-Saclay	Examinatrice
Haijun YANG Professeur, Shanghai Jiao Tong University	Examinateur

上海交通大學

SHANGHAI JIAO TONG UNIVERSITY

上海交通大学博士学位论文

论文题目：Study of additional radiation in the initial-state-radiation processes $e^+e^- \to \mu^+\mu^-\gamma$ and $e^+e^- \to \pi^+\pi^-\gamma$ in the *BABAR* experiment

姓　名：白栋允

学　号：019072210004

导　师：李 亮

学　院：物理与天文学院

université PARIS-SACLAY

ÉCOLE DOCTORALE
Particules, hadrons, énergie et noyau : instrumentation, imagerie, cosmos et simulation (PHENIICS)

上海交通大學 SHANGHAI JIAO TONG UNIVERSITY

Titre: Etude du rayonnement additionnel dans les processus de rayonnement à l'état initial $e^+e^- \to \mu^+\mu^-\gamma$ et $e^+e^- \to \pi^+\pi^-\gamma$ dans l'expérience *BABAR*

Mots clés: rayonnement additionnel, rayonnement dans l'état initial, ordre suivant le premier (NLO), ordre supérieur (NNLO), expérience *BABAR*

Résumé: Cette thèse présente une étude dédiée du rayonnement supplémentaire dans les événements $e^+e^- \to \mu^+\mu^-\gamma$ et $e^+e^- \to \pi^+\pi^-\gamma$ avec un rayonnement dans l'état initial (ISR). L'étude est basée sur les données recueillies par le détecteur *BABAR*, correspondant à une luminosité intégrée de 424,2 fb^{-1} et 43,9 fb^{-1} à la résonance $\Upsilon(4S)$ et en dessous de la résonance, respectivement. Les événements ISR à deux corps sont sélectionnés en exigeant que l'énergie du photon ISR dans le système du centre de masse $E^*_{\gamma_{\rm ISR}}$ soit supérieure à 4 GeV et que l'angle polaire dans le laboratoire soit compris entre 0,35 et 2,4 rad, et qu'il y ait exactement deux traces avec les charges opposées, chacune avec une impulsion transverse $p_{\rm T} > 0,1$ GeV et dans la plage angulaire entre 0,4 et 2,45 rad. Dans les événements avec deux candidats photons ISR, le photon ISR est choisi comme étant celui avec l'énergie $E^*_{\gamma_{\rm ISR}}$ la plus élevée. Des ajustements cinématiques d'ordre suivant (NLO) et d'ordre supérieur (NNLO) sont effectués pour étudier le rayonnement d'un ou deux photons respectivement dans les états initiaux et finals en plus du photon ISR. Plusieurs arbres de décision boostés (BDTs) basés sur la technique multivariée sont réalisés pour (1) déterminer les facteurs de normalisation des bruits de fonds multihadrons simulés à partir des processus $q\bar{q}$ et 3π, (2) séparer les signaux dimuon et dipion des bruits de fond dans un plan bidimensionnel en χ^2 d'ajustements cinématiques avec un photon supplémentaire à petit ou grand angle, et (3) supprimer les contributions des bruits de fond dans des échantillons de dipions avec deux photons supplémentaires. Suivant les méthodes de l'analyse précédente de *BABAR*, de nouveaux résultats sont présentés sur les processus NLO et comparés aux prédictions, en comparaison avec les prédictions des générateurs Monte Carlo (MC) PHOKHARA et AFKQED. La comparaison révèle des écarts dans les taux et également dans les distributions angulaires du photon supplémentaire entre les données et le générateur PHOKHARA. Le désaccord observé a un effet négligeable sur la mesure *BABAR* de la section efficace du dipion, mais il pourrait affecter de manière plus significative d'autres mesures basées sur la méthode ISR. Pour approfondir les résultats de l'analyse NLO, une analyse 0C basée sur la reconstruction cinématique à zéro contrainte de l'échantillon complet de muons est effectuée et valide le désaccord observé. Les contributions substantielles de NNLO sont étudiées et quantifiées dans les processus dimuon et dipion. Les implications de ces résultats pour d'autres expériences sont brièvement discutées et comparées.

université PARIS-SACLAY

ÉCOLE DOCTORALE
Particules, hadrons, énergie et noyau : instrumentation, imagerie, cosmos et simulation (PHENIICS)

上海交通大學 SHANGHAI JIAO TONG UNIVERSITY

Title: Study of additional radiation in the initial-state-radiation processes $e^+e^- \to \mu^+\mu^-\gamma$ and $e^+e^- \to \pi^+\pi^-\gamma$ in the *BABAR* experiment

Keywords: additional radiation, initial state radiation, next-to-leading order, next-to-next-to-leading order, *BABAR* experiment

Abstract: This thesis presents a dedicated study of additional radiation in $e^+e^- \to \mu^+\mu^-\gamma$ and $e^+e^- \to \pi^+\pi^-\gamma$ initial-state-radiation (ISR) events. This study is based on the data collected by the *BABAR* detector, corresponding to an integrated luminosity of 424.2 fb^{-1} and 43.9 fb^{-1} at and below the $\Upsilon(4\mathrm{S})$ resonance, respectively. Two-body ISR events are selected by requiring the ISR photon energy in the center-of-mass frame $E^*_{\gamma_{\mathrm{ISR}}}$ be greater than 4 GeV and the laboratory polar angle in the range 0.35−2.4 rad, and exactly two opposite charged tracks, each with transverse momentum $p_{\mathrm{T}} > 0.1$ GeV and within the angular range 0.40−2.45 rad. In the events with two ISR photon candidates, the ISR photon is chosen to be that with the higher $E^*_{\gamma_{\mathrm{ISR}}}$. Kinematic fits of next-to-leading order (NLO) and next-to-next-to-leading order (NNLO) are performed to probe the radiation of one or two photons respectively in the initial and final states in addition to the ISR photon. Several boosted decision trees (BDTs) based on the multivariate technique are performed to (1) determine the normalization factors for simulated multihadron backgrounds from $q\bar{q}$ and 3π processes, (2) separate dimuon and dipion signals from backgrounds in a two-dimensional χ^2 plane of kinematic fits with a small- or large-angle additional photon, and (3) suppress background contributions in dipion samples with two additional photons. New results are presented for processes at NLO following the previous *BABAR* analysis, comparing with predictions from PHOKHARA and AFKQED Monte Carlo (MC) generators. The comparison reveals discrepancies in the one-photon rates and angular distributions between the data and the PHOKHARA generator. The observed disagreement has a negligible effect on the *BABAR* measurement of the dipion cross section, but it could affect other ISR-based measurements more significantly. To further investigate the results from the NLO analysis, a 0C analysis which stands for zero constraint kinematic reconstruction of the full muon sample is performed and validates the observed disagreement. Substantial NNLO contributions are studied and quantified in both dimuon and dipion processes. Implications of these results for other experiments are briefly discussed and compared.

Contents

List of Figures

List of Tables

Chapter 1

Introduction

1.1 The Standard Model

The ultimate goal of particle physics is to understand the fundamental law of matter which is made up of elementary particles and the interactions between them. Developed during the twentieth century, the physics model describing the world in the subatomic level is called the *Standard Model* (SM). The SM is a quantum field theory and it describes three of the four known fundamental forces: electromagnetic, weak and strong interactions, excluding the gravitational interaction. The SM includes two classes of elementary particle, namely fermions and bosons. Fermions are spin $\frac{1}{2}$ particles which make up the concrete matter. Fermions consist of three generations of quarks, leptons and neutrinos, and together with their anti-particle partners. Bosons are defined as force carriers that mediate the electromagnetic, weak and strong fundamental interactions, by photon, weak gauge bosons (Z, W^+, W^-) and gluons respectively. The newly discovered Higgs boson associated with Higgs field accounts for the mass generation of particles. The summary of the elementary particles in the SM can be found in Fig. 1.1.

The SM is a very successful and self-consistent model for the fundamental constitutes and three fundamental interactions between them, which can already explain most of the experimental results so far. Some remarkable and significant confirmations of the SM include the discovery of the $W^{\pm}$ bosons [1, 2] and the Z^0 boson at CERN [3], the top quark from Fermilab [4] and the Higgs boson by Large Hadron Collider (LHC) [5, 6]. However, the SM leaves some physical phenomena unexplained and so falls short for a final complete theory model. For example, the SM does not incorporate the full theory of gravitation described by the relativity theory, nor can account for the dark matter and the large matter-antimatter asymmetry. And the SM assumes neutrinos are massless, which goes against neutrino oscillation experiments. The recent measurement of the W boson mass from the Collider Detector at Fermilab (CDF) collaboration [7] shows a roughly 7σ discrepancy from the SM prediction, which disagrees with measurements from ATLAS and some other experiments. All of these mentioned indicate some *new physics* beyond the *Standard Model* (BSM). Concerning the experiments, one method to search for the BSM at this moment is to improve the precision of the measurements to observe some real difference from the SM.

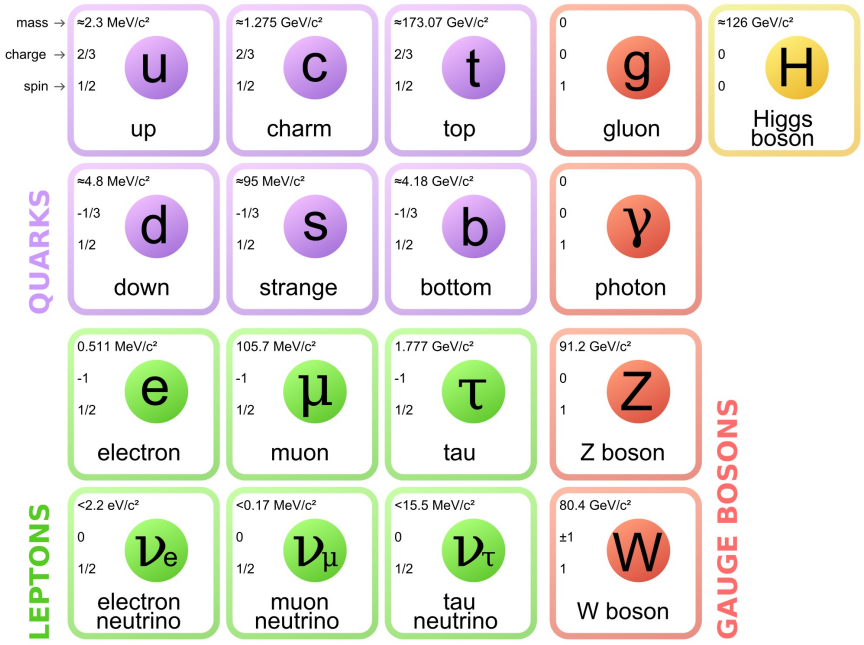

Figure 1.1: The elementary particles in the SM. Picture is from Particle Data Group website.

1.2 Motivation

1.2.1 The anomalous magnetic moment of the muon

The magnetic moment $\vec{\mu}$ for an elementary particle with intrinsic angular momentum (spin $\vec{S}$) and charge q is given by

$$\vec{\mu} = g\frac{q}{2m}\vec{S} \tag{1.1}$$

where g is the gyromagnetic ratio and m is the mass of the particle. The Dirac equation predicts $g = 2$ for fermions with $|\vec{S}| = \frac{1}{2}$. At tree-level, this prediction remains true. However, from the relativistic quantum theories, radiative corrections contribute to this g quantity, where the interaction of the elementary particle with a photon is influenced by additional interactions with virtual particles. These corrections modify g, and thus cause a deviation from $g = 2$. In 1948, the first order corrections from quantum electrodynamics (QED) was found to be a deviation from g of exactly α/π [8], where α is the fine-structure constant. Experimental confirmation by Kusch and Foley followed in the same year [9]. For the charged muons, the magnetic anomaly a_μ is defined as $a_\mu = (g-2)_\mu/2$, which is the fractional deviation from $g = 2$. a_μ plays an important role in the history of the SM and continues to serve as a test of the SM to date. The long-standing discrepancy between the experimental measurements a_μ^{exp} and the SM theoretical prediction a_μ^{SM} has caused significant interest since it could be a hint of yet undiscovered *New Physics*.

The updated measurement results from Run 1 dataset (2018) by the E989 Muon $g-2$ Collaboration at Fermilab (FNAL) were published in 2021 with a 0.46 ppm precision with $a_\mu(\text{FNAL}) = 116\ 592\ 040\ (54) \times 10^{-11}\ (0.46\ \text{ppm})$ [10]. Combining with the previous Brookhaven National Laboratory (BNL) measurement [11], the experimental average is

$a_\mu(\text{exp}) = 116\ 592\ 061\ (41) \times 10^{-11}$ (0.35 ppm). From the theoretical side, the Muon $g-2$ Theory Initiative recommended value for the SM is $a_\mu(\text{SM}) = 116\ 591\ 810\ (43) \times 10^{-11}$ (0.37 ppm). The discrepancy amounts to 4.2σ between a_μ^{exp} and a_μ^{SM}, as shown in Fig. 1.2 . The latest measurement results published from FNAL in August 2023 extends this discrepancy to 5.0σ [12]. Tension is also observed with the lattice QCD evaluation [13–16]. It should be mentioned here the discrepancy is reduced to 2.1σ by the recent theoretical results predicted by lattice QCD method from the BMW collaboration [14].

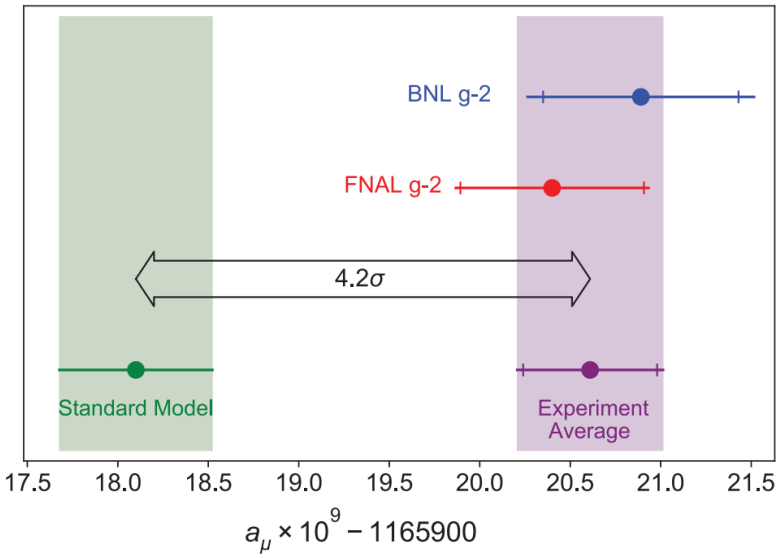

Figure 1.2: Comparison between the latest experimental value and the recommended prediction value from the Muon $g-2$ Theory Initiative [10].

1.2.2 Hadronic vacuum polarization

Vacuum polarization (VP) originates from creation and annihilation of virtual particle-antiparticle states [17]. The simplest case is that an e^+e^- pair is emitted and re-absorbed by a virtual photon in the propagation. At the quantum level, the e^+e^- pairs reduce the strength of the electromagnetic force carried by the exchanged photon, and therefore it is crucial to consider VP when evaluating the effective interaction caused by the photon exchange. The vacuum can be polarized by any pair of charged particle, and also by fluctuations involving strongly interacting particles which is called hadronic vacuum polarization (HVP). HVP in the propagation of a photon (shown in Fig. 1.3) plays an important role in the precision tests of the SM.

Among the various applications of the HVP calculations, two important cases are emphasised: one case is for the evaluation of the running of the fine-structure constant α to the Z boson mass scale, another case is for the contribution to anomalous magnetic moment of the muon.

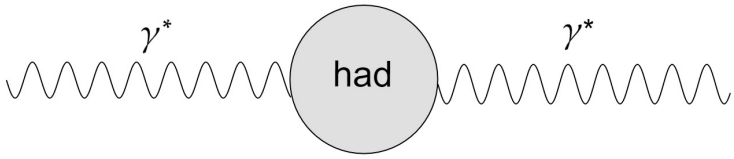

Figure 1.3: Feynman diagram of the hadronic vacuum polarization.

The evaluation of the electromagnetic coupling of the Z mass scale can be written as

$$\alpha(\mathrm{M_Z^2}) = \frac{\alpha}{1 - \delta\alpha(\mathrm{M_Z^2})} \tag{1.2}$$

where $\alpha = \frac{e^2}{4\pi}$ is the fine-structure constant of the QED process and the correction $\delta\alpha(\mathrm{M_Z^2})$ at the Z mass scale originates from the VP in the photon propagator and the hadronic contribution $\delta\alpha_{\mathrm{had}}(\mathrm{M_Z^2})$ is at the order of $275{\times}10^{-4}$. The current precision of $\delta\alpha_{\mathrm{had}}(\mathrm{M_Z^2})$ is sufficient to obtain the accuracy for the Standard Theory fit to the electroweak (EW) data.

The theoretical SM prediction for the anomalous magnetic moment of the muon can be generally divided into electromagnetic, electroweak, and hadronic contributions (see Fig. 1.4),

$$a_\mu^{\mathrm{SM}} = a_\mu^{\mathrm{QED}} + a_\mu^{\mathrm{EW}} + a_\mu^{\mathrm{had}} \tag{1.3}$$

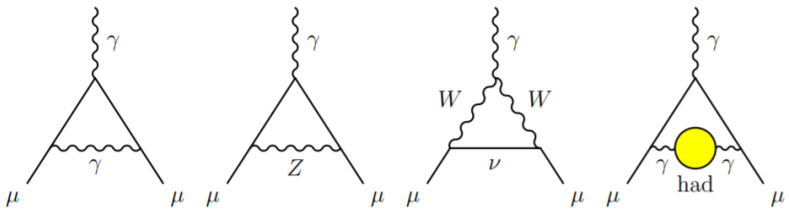

Figure 1.4: Representative Feynman diagrams contributing to a_μ^{SM}. From left to right: first order QED (Schwinger term), lowest-order weak from Z and W bosons, lowest-order hadronic.

The theoretical QED contributions a_μ^{QED} including all photonic and leptonic (e, μ, τ) loops are computed [18, 19] and are known up to five-loop accuracy, which give:

$$a_\mu^{\mathrm{QED}} = (116\,584\,718.931 \pm 0.104) \times 10^{-11}. \tag{1.4}$$

where the uncertainty is owing to the lepton mass, the high-order QED estimation and the fine-structure constant α (see [20]).

The contribution a_μ^{EW} from the EW includes Z, $W^{\pm}$ and Higgs boson loop, and is known to two-loop accuracy since the three-loop level correction is negligible. The updated estimate with the known Higgs mass gives

$$a_\mu^{\mathrm{EW}} = (153.6 \pm 1.0) \times 10^{-11}. \tag{1.5}$$

The estimates for $a_\mu^{\rm QED}$ and $a_\mu^{\rm EW}$ are very well under control and their corresponding uncertainty is negligible compared to that from $a_\mu^{\rm had}$.

The dominant uncertainty of $a_\mu^{\rm SM}$ comes from the hadronic contributions $a_\mu^{\rm had}$, which can be divided into two terms (see Fig. 1.5):

$$a_\mu^{\rm had} = a_\mu^{\rm had,VP} + a_\mu^{\rm had,LBLS}, \tag{1.6}$$

where $a_\mu^{\rm had,VP}$ is the hadronic vacuum polarization contribution and $a_\mu^{\rm had,LBLS}$ is the hadronic light-by-light scattering (HLBLS) contribution. $a_\mu^{\rm had,VP}$ can be further divided into the leading-order (LO) and higher-order (mainly next-to-leading order (NLO) and next-to-next-leading order (NNLO)) contributions.

Although $a_\mu^{\rm QED}$ and $a_\mu^{\rm EW}$ can be calculated properly using perturbation theory, the running of the strong coupling constant $\alpha_s(q^2)$ is large at low energies, which implies that the perturbative expansion of $\alpha_s(q^2)$ is not valid at low energies [21]. Therefore, the perturbative QCD is not reliable at these low-energy domains. The HVP contributions are dominated by the exchange of the virtual photons with low q^2, requiring an alternative method to calculate the loop integrals. The problem of the perturbative QCD at low scales has been overcome by a dispersion integral technique involving experimental data measuring the cross section $e^+e^- \to$ hadrons.

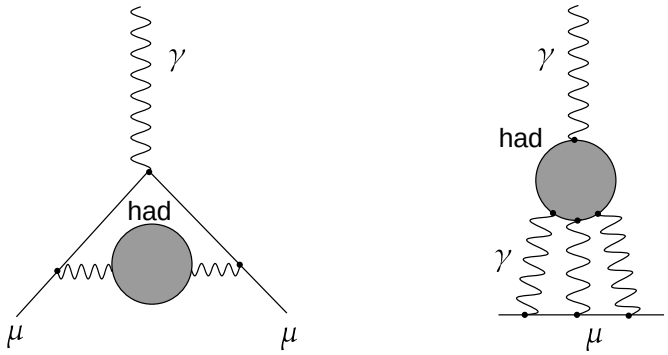

Figure 1.5: Representative Feynman diagrams for the hadronic vacuum polarization of the LO contribution (left) and the hadronic light-by-light scattering contribution (right) to the $a_\mu^{\rm SM}$.

Using unitarity and analyticity, the HVP contribution from the dominant LO can be calculated by the dispersion integral:

$$a_\mu^{\rm had,LO} = \frac{\alpha^2(0)}{3\pi^2}\int_{4m_\pi^2}^{\infty}\frac{K(s)}{s}R(s)ds\,, \tag{1.7}$$

where $K(s)$ is the kernel function

$$K(s) = x^2(1-\frac{x^2}{2}) + \frac{(1+x^2)(1+x)^2}{x^2}\left(\ln(1+x) - x + \frac{x^2}{2}\right) + x^2\frac{1+x}{1-x}\ln x, \tag{1.8}$$

where $x = \frac{1-\beta_\mu}{1+\beta_\mu}$, $\beta_\mu = \sqrt{1-4m_\mu^2/s}$. $R(s)$ from Eq. (1.7) is called hadronic R-ratio defined by

$$R(s) = \frac{\sigma^0\left(e^+e^- \to \text{hadrons}(+\gamma)\right)}{\sigma_{\rm pt}} = \frac{\sigma^0\left(e^+e^- \to \text{hadrons}(+\gamma)\right)}{4\pi\alpha^2/(3s)}, \tag{1.9}$$

where $\sigma_{\rm pt} = 4\pi\alpha^2/(3s)$ is the cross section for point-like charged fermions. With the integration kernel $K(s)/s \sim 1/s^2$ at low energies, contributions in Eq. (1.7) are weighted more strongly by the lower s regime. Measured hadronic cross section data from different experiments are used as the input for $\sigma^0\left(e^+e^- \to \text{hadrons}(+\gamma)\right)$. σ^0 here denotes the *bare* cross section which includes the final-state radiation (FSR) of additional photons but excludes the leptonic and hadronic vacuum polarization effects. At low energies, the total hadronic contributions must be obtained by summing all possible different final states. At center-of-mass (CM) energies $\sqrt{s} < 1.8$ GeV, over 90% of the total contribution to $a_\mu^{\rm had,LO}$ is accumulated, and the most important channel is the two-pion final state which contributes more than 70% of $a_\mu^{\rm had,LO}$ and this final state stems mainly from decays of the ρ (770) meson with an ω admixture. $a_\mu^{\rm had,LO}$ is responsible for greater than 90% of the total uncertainty of the $a_\mu^{\rm SM}$.

The higher-order contributions including NLO [22] and NNLO [23] have been derived using similar dispersion integrals and they are given explicitly as

$$a_\mu^{\rm had,NLO} = (-98.3 \pm 0.7) \times 10^{-11} \tag{1.10}$$

$$a_\mu^{\rm had,NNLO} = (12.4 \pm 0.1) \times 10^{-11} \tag{1.11}$$

where the NLO contributions are at the same order of the HLBLS but with negative sign, and the NNLO contributions are somewhat larger than expected and should be evaluated as a nonnegligible component.

Hadronic light-by-light scattering contribution, which is more complicated than HVP, is one of the largest uncertainties of the $a_\mu^{\rm SM}$. The latest estimation summing up the weighted average between the phenomenology value and the lattice-QCD value, together with the HLBLS NLO contribution is obtained as:

$$a_\mu^{\rm had,HLBLS} = (92 \pm 18) \times 10^{-11}. \tag{1.12}$$

1.2.3 The current status of $a_\mu^{\rm had,LO}$

On the SM prediction side, $a_\mu^{\rm had,LO}$ is estimated by using $e^+e^- \to$ hadrons data from Eq. (1.7), with full evaluations from DHMZ19 [24], KNT19 [22], BDJ19 [25] and FJ17 [26] listed in Table 1.1.

	DHMZ19	KNT19	BDJ19	FJ17
$a_\mu^{\rm had,LO}$	$694.0(4.0) \times 10^{-10}$	$692.8(2.4) \times 10^{-10}$	$687.1(3.0) \times 10^{-10}$	$688.1(4.1) \times 10^{-10}$

Table 1.1: Full evaluations of $a_\mu^{\rm had,LO}$ from DHMZ19, KNT19, BDJ19 and FJ17.

With conservative merging of model-dependent results, the value of $a_\mu^{\rm had,LO}$ should be quoted as [20]:

$$a_\mu^{\rm had,LO} = (693.1 \pm 4.0) \times 10^{-10}. \tag{1.13}$$

The most important $\pi^+\pi^-$ channel accounts for over 70% of the full hadronic contribution to the muon $g-2$ and dominates its total uncertainty, which is expected to have the highest precision. In the last twenty years, many experimental measurements with improving

statistics and small systematic uncertainties have been achieved. However, the current situation is not ideal as the two most precise measurements, performed by *BABAR* and KLOE, do not show good agreement within their quoted uncertainties. The situation is not tempered after the three KLOE measurements based on different initial-state radiation (ISR) methods are combined [27], as the reduced uncertainty does not reconcile the disagreement between *BABAR* and KLOE. The data points between *BABAR* and KLOE show a significant discrepancy to one, which may imply several systematic effects are not properly covered by the estimated systematic uncertainties. The evaluations of $a_\mu^{\text{had, LO}}$ from $\pi^+\pi^-$ channel contributions between 0.6 and 0.88 GeV for different experimental data sets are shown in Fig. 1.6, where CLEO/SND/BESIII/CMD-2 results are all consistent with either *BABAR* or KLOE. New tensions in the dominant $\pi^+\pi^-$ channel between CMD-3 experiment operating in scan mode [28] and KLOE and also with *BABAR* are observed which require further detailed studies of the various approach to clarify.

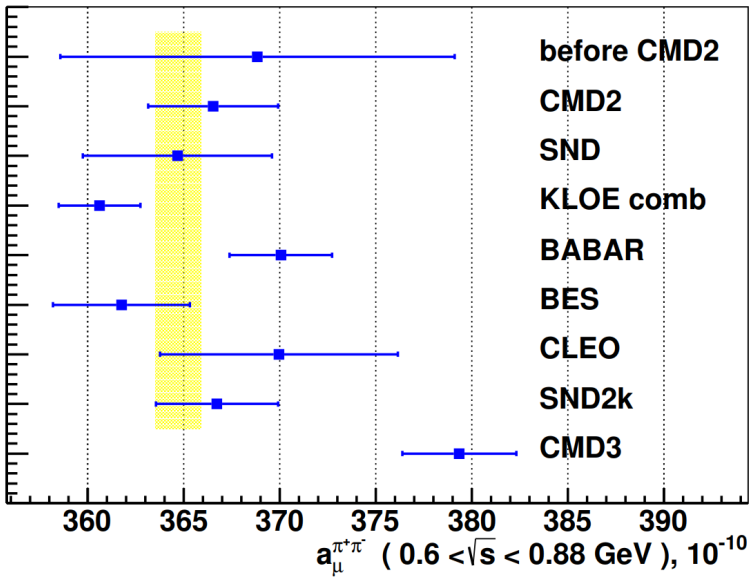

Figure 1.6: Comparison of results from various experiments for $a_\mu^{\text{had, LO}}$ from $\pi\pi$ channel between 0.6 and 0.88 GeV [28].

1.3 The ISR approach

The traditional method to measure the e^+e^- annihilation is using point-by-point energy-scan techniques that data are collected for different collision energies. The exclusive e^+e^- cross section measurements were performed in Novosibirsk and Orsay. In the following years, different colliders with high energy such as PEP, VEPP-4 and BEPC measured the total inclusive cross section ratio R. In case of the $e^+e^- \to \pi^+\pi^-$ channel, the CMD experiment performed detailed scans of the ρ energy region with small 2% systematic uncertainty and later the CMD-2 experiment achieved measurements with systematic precision to 0.6% [29, 30].

However, energy-scan techniques have several limitations: The combinations of data from different experiments can cause problems due to the different conditions of the data-taking; The changes in the beam energy will lead to 'point-to-point systematics'; The presence of beam backgrounds and the details of the hadronic model will contribute largely to the overall systematics.

The ISR method [31–34] has been proposed as an effective way to study e^+e^- annihilation processes instead of the standard energy-scan method. The main advantage of the ISR approach is that the final-state mass spectrum can be obtained in a single configuration of the e^+e^- storage rings and of the detection apparatus, thus allowing a cross section measurement over a wide range from the threshold. Consequently, a better control of the systematic uncertainty can be obtained compared with the direct energy-scan method. The main disadvantage of ISR approach is the reduction of the measured cross section which is offset by the availability of high-luminosity e^+e^- storage rings, designed as K and B factories.

In the ISR approach, the cross section for $e^+e^- \to X$ at the reduced energy $\sqrt{s'} = m_X$, where X can represent any final state, is inferred from a measurement of the radiative process $e^+e^- \to X\gamma$ where the photon is emitted by the initial e^+ or e^- particle. The reduced energy is calculated as $s' = s(1 - 2E^*_\gamma/\sqrt{s})$, where E^*_γ is the energy of the ISR photon in the e^+e^- CM frame and s is the square of the e^+e^- CM energy [1]. In this analysis, $s \sim (10.58\,\mathrm{GeV})^2$ and $\sqrt{s'}$ ranges from threshold to 3 GeV. Two-body ISR processes with $X = \mu^+\mu^-(\gamma)$ and $X = \pi^+\pi^-(\gamma)$ are also measured, where the ISR photon is detected at large angle to the beams, and the charged particle pair can be associated with a final-state radiation (FSR) photon.

Feynman diagrams relevant to this study are shown in Fig. 1.7. Several issues need to be considered. First, the lowest-order (LO) radiated photon can be either from ISR or FSR. For the case of the muon channel, ISR is the dominant in the measurement range, but the LO FSR contribution needs to be subtracted out using QED [35]. For the case of the pion channel, FSR is model-dependent, but LO FSR is strongly suppressed by the large s value [36]. A dedicated study performed by *BABAR* [36] using a π^+/π^- asymmetry showed that the LO amplitude for pions was consistent with radiation from quarks and recombination into a pion pair and that the contribution of the $|\mathrm{FSR}|^2$ term is well below 7×10^{-4} level between threshold and 1 GeV, and increasing to 1.2% at 1.3 GeV. In both channels, interference between ISR and FSR amplitudes vanishes for a charge-symmetric detector. Second, in order to control the overall efficiency to high precision, it was found necessary to include higher-order radiation in the sample. In practice, the NLO correction in α is sufficient to reach accuracy of order 10^{-3}, while the NNLO correction is expected to be at least one order of magnitude smaller than NLO. Consequently, the selection keeps $\pi\pi\gamma\gamma(\mu\mu\gamma\gamma)$ as well as $\pi\pi\gamma(\mu\mu\gamma)$ final states, where the additional photon can be either from ISR or FSR.

1.4 The current and forthcoming analysis

The main goal of current thesis is to study the additional radiation in the ISR process $e^+e^- \to \mu\mu\gamma$ and $e^+e^- \to \pi\pi\gamma$ in the *BABAR* experiment. The selected events correspond to a final

[1] Quantities related to kinematics with an upper * index are measured in the e^+e^- CM system.

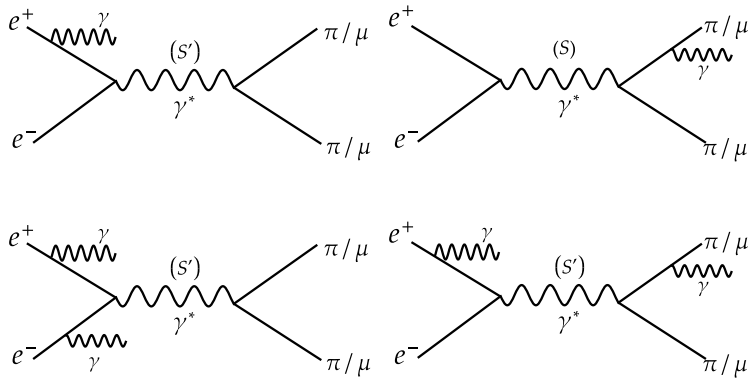

Figure 1.7: The Feynman diagrams for the processes relevant to this analysis. Top: lowest-order (LO) ISR for $\mu\mu$ or $\pi\pi$, LO FSR for $\mu\mu$ or $\pi\pi$ (corresponding process for $\pi\pi$ very tiny). Bottom: next-to-leading order (NLO) ISR with additional ISR for $\mu\mu$ or $\pi\pi$, NLO with additional FSR. The NLO process with two FSR also contributes for $\mu\mu$ at a small level in the mass range considered in this analysis.

state with two tracks and the ISR candidate, all in the detector acceptance. Kinematic fits provide discrimination of the channels under study from other processes. For the multihadrons from the $q\bar{q}$ background and multihadronic ISR background, the boosted decision tree (BDT) based on multivariate technique is performed in detail to separate the corresponding signal and background samples in different mass regions. The data over MC ratios are thus obtained after applying the optimal BDT selection for different cases, respectively. In addition to the NLO fits, which are part of the standard *BABAR* method, a specific analysis is extended to search for NNLO radiation with two additional photons in the final state. The optimized 2D-χ^2 selection is applied to the NLO study while it is not the case for the NNLO study since NNLO events are expected to yield larger χ^2 values. For the pion processes near the ρ peak region of NNLO samples, due to the large non-$\pi\pi$ background, the BDT method is applied for different kinematic fits to reduce the background. The data and MC samples are compared by the fractions over the corresponding total number of events to avoid potential bias. To further investigate the results from the NLO analysis part, a 0C calculation where 0C stands for zero constraint kinematic reconstruction of the full muon event sample is performed, where the energy and momentum conservation relations are used to calculate four unknowns: the energy and angles of the additional photon as well as the energy of the main ISR photon. The final results of different fit categories [2] are obtained by correcting the feed-through effects by iterations [3], the full selection efficiency and the fake photon contributions.

A *blind analysis* is an approach to measurement or experimentation that aims to minimize the experimenter's bias by performing the analysis without knowledge of the expected or desired outcome. For precision analysis involving multiple corrections of systematic effects it

[2]The LO and NLO fit categories are discussed in Section 4.1, and the NNLO fit categories are discussed in Section 7.1.

[3]The feed-through effects, or the mis-classification between the fitted and true categories, are studied in detail in Section 8.1.

is essential and mandatory to proceed in a blind way to avoid being influenced by external factors such as results from other experiments or any theoretical biases. This is particularly true here since the results obtained from the $e^+e^- \to \pi^+\pi^-\gamma(\gamma)$ cross section analysis are utilized in computing the hadronic vacuum polarization. These results play a direct role in the calculation of contributions to various phenomena, such as to the running of $\alpha_{\rm QED}(s)$ and to the anomalous muon magnetic moment a_μ. In the case of the latter application, some ambiguity arising from e^+e^- data from different experiments. Some confusion is observed between on one hand of Novosibirsk (CMD-2, SND and the latest CMD-3 [28]) and of KLOE. The confirmation of a discrepancy between the direct measurement at BNL and the SM prediction thus relies on the clarification of this situation.

The radiation study in this thesis which is crucial to the ongoing cross section analysis is conducted in a manner that prevents inadvertent biases with the previously published results, including that from *BABAR* . This is accomplished through a blind way, where key individual data/MC corrections, like trigger and tracking efficiencies, are hidden by applying offsets that are known only to one individual for each task. Only after successfully completing all the studies with internal consistency checks, the offsets will then be disclosed and absolute cross sections can be calculated.

For the forthcoming final cross section analysis, the main goal is to measure the amount of the signal events with high precision, where the absolute overall efficiencies are crucial and dominate the systematic uncertainties. The $\pi\pi(\gamma)\gamma_{\rm ISR}$ and $\mu\mu(\gamma)\gamma_{\rm ISR}$ processes are measured independently with full internal checks before unblinding and the ratio which yields the measured absolute $\pi\pi$ cross section. One of the most demanding tests is the so-called QED test, which is the absolute comparison of the $\mu\mu(\gamma)\gamma_{\rm ISR}$ cross section (the *BABAR* luminosity L_{ee} is used) to the NLO QED prediction. In the previous 2012 analysis [35], the separation between the different two-prong final states (including $\mu^+\mu^-(\gamma)\gamma_{\rm ISR}$ process) relies exclusively on the identification of the charged particles. In the forthcoming new analysis to be completed, the separation between the different two-prong final states relies on the fit of the $\cos\theta^*_\pi$ distributions in each $m_{\pi\pi}$ interval. Background reduction and control of the remaining background contributions are another challenge in this analysis, particularly, the pion channel away from the ρ peak resonance.

Although the final state of two-body ISR processes is rather simple, the main difficulty of the forthcoming analysis resides in the full control of all involved efficiencies. Relying on the MC only could not grant the required precision. Therefore all efficiencies are measured relying on data. As is known to all, the generation and simulation of MC samples are not perfect, there are always differences between MC and data. At first step, the MC simulation is used in order to incorporate in a consistent way with all effects entering the final event acceptance. Through dedicated studies performed on data and simulation, corrections for data-to-MC differences are obtained for each efficiency. The main contributions for these corrections originate from trigger, tracking, momentum calibration, and the χ^2 selection of the kinematic fits. Corrections will be applied in two steps: (1) relative data-to-MC corrections as a function of $\cos\theta^*_\pi$ are made to the MC reference distributions before performing the fits, and (2) absolute data-to-MC corrections are applied to the $\pi\pi$ and $\mu\mu$ mass spectra (for unblinding). The correction terms are reviewed in turn. These corrections are applied as mass-dependent corrections to MC efficiency. They add up to at most a few percent and are known

to a few permil level or better. Efficiency measurements are designed to avoid correlations between different correction terms.

The final unblinding is foreseen to be done in two stages, first with the $e^+e^- \to \mu^+\mu^-\gamma(\gamma)$ cross section which can be compared to QED as a final check [35], then with the measurement of the $e^+e^- \to \pi^+\pi^-\gamma(\gamma)$ cross section as the final goal of the forthcoming analysis.

1.5 Expected behavior of additional radiation

1.5.1 Studies of $e^+e^- \to \mu^+\mu^-\gamma(\gamma)$ with PHOKHARA

The latest version of the PHOKHARA event generator [37] is supposed to provide an accurate picture of the ISR process $e^+e^- \to \mu^+\mu^-\gamma(\gamma)$ since it incorporates all contributions from NLO QED [4]. More specifically, it includes the LO ISR and FSR processes and NLO contributions from real photon emission by the e^+ or e^- beams and the outgoing muons, as well as the soft emission and loop virtual contributions, as shown in Fig. 1.7.

Samples of ISR events are generated with PHOKHARA in the *BABAR* conditions for this analysis: ISR photon at large angle (range between 20° and 160°) in the e^+e^- CM system, two-charged particle mass from threshold to $1.4\,\mathrm{GeV}$, and an initial CM energy $\sqrt{s} = 10.58\,\mathrm{GeV}$. The sum of soft and hard emission is chosen to be 5 MeV so that both contributions can be handled under control. From an experimental point of view both LO and soft+virtual NLO lead to event configurations which can be reconstructed with 'LO' kinematics (only one ISR photon with two charged particles in the final state), whereas sufficiently hard NLO necessitates a different kinematic treatment. Here the transition energy is more related to the detector performance and background conditions. The rate of hard radiation turns out to be relatively large, NLO ISR being enhanced by a large $\ln(s/m_e^2)$ factor, and is strongly dependent on the photon energy threshold. For muons, starting with a value of 59.5% for E^*_γ above 5 MeV, the fraction then decreases to 38.1% above 50 MeV, and still 25.0% above 200 MeV. In the 2009 and 2012 *BABAR* measurement [35, 38], a large fraction was indeed observed above 200 MeV. In this *BABAR* analysis a value of 50 MeV is chosen as it is actually the energy threshold for a kinematically-fitted photon, as will be discussed later.

The generated samples allow to study the features of different topologies, taking advantage of the options to run the generator. The effect of soft and virtual contributions can be explored using samples generated at LO with either LO ISR only or the full LO with ISR+FSR+interference, and NLO samples with either NLO ISR or the full configuration with NLO ISR and FSR. In particular, it has been checked that final states at LO (one-photon radiation) are indistinguishable from NLO when additional radiation E^*_γ larger than 100 MeV is excluded, as their muon angular distributions are consistent within $\pm 1\%$ in the large detector acceptance. This property has an important consequence: from an experimental point

[4] To dispel some possible confusion, note that LO is defined with respect to the process under study. While the Born cross section is given by LO QED and one-photon radiation corresponds to NLO, in this thesis the ISR process is considered to be LO order, despite being NLO with respect to the Born cross section.

of view, final states are identical for LO and NLO soft+virtual contributions and they are measured together indistinguishably [5].

It is of interest to separate the contributions from ISR and FSR additional photons, as the ISR contribution is expected to dominate. However it is not possible in PHOKHARA generator to tell the origin of the photon for each individual event as the two-photon final state results from an NLO matrix element with interfering amplitudes. A feasible way out was used for data [35, 38], and applied here for Monte Carlo, taking the advantage of the event topology to separate FSR from ISR on a statistical basis, which is achieved by considering the distribution of the angle $\theta^*_{\rm min}$ between the softer photon (ie., the energetic main ISR photon is excluded) and the closet muon track. In this way the FSR contribution stands out as a peak at small angle above a wide distribution from large-angle ISR which is shown in Fig. 1.8. The fractions of the full NLO samples are then calculated with PHOKHARA in different topologies taking 50 MeV as the hard photon threshold in the CM system: 61.9% for 'LO' (true LO + NLO soft + virtual), 27.2% for NLO ISR hard not in acceptance (forward and backward blind cones of 20° in CM), 7.5% for NLO ISR hard in acceptance, and 3.3% for NLO FSR hard in acceptance. All these NLO topologies are selected in the *BABAR* analysis, with the full event reconstructed, even in the case where the additional photon is not detected, but inferred from a constrained kinematic fit.

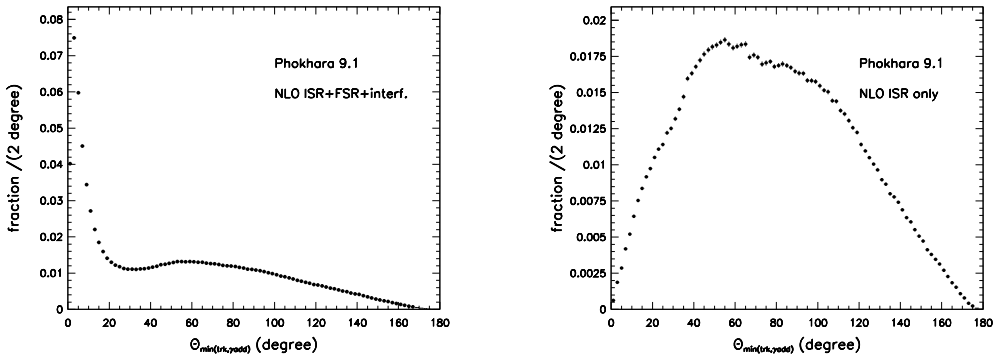

Figure 1.8: The distribution of the angle $\theta_{\rm min(trk,\gamma_{add})}$ in the CM frame between the additional photon and the closest outgoing muon track shows a peak below 25° from FSR superimposed on a wide distribution from large-angle ISR, not correlated with the muons. These two plots are obtained at the generated 4-vector level in *BABAR* kinematical conditions for photons in the detector range for two options of the PHOKHARA generator. Left: full LO+NLO ISR+FSR PHOKHARA sample. Right: sample with FSR turned off.

It is interesting to compare the results of the cross section which are provided by PHOKHARA at LO and NLO levels. For the *BABAR* conditions quoted above, the full NLO ISR cross section for $e^+e^- \to \mu^+\mu^-\gamma(\gamma)$ is 17.159 pb which is compared with 17.452 pb with only LO amplitudes kept. The sum of all NLO contributions corresponds to a relatively

[5] Actually the loop contributions introduce a tiny forward-backward asymmetry, but this disappears in the measured cross section in a charge-symmetric detector.

small reduction by $-1.68 \pm 0.01\%$ of the LO value. As we have obtained that the NLO ISR hard part above 100 MeV corresponds to a large increase of $38.2 \times 17.159/17.452 = 37.5\%$, it follows that it is almost compensated by a reduction of 39.1% due to the soft/virtual contribution.

The near cancellation between hard and soft/virtual effects is known since long in QED [39], but sometimes it could lead to an incorrect appreciation of the effect of higher-order corrections when systematic uncertainties are quoted. Thus this issue requires a careful evaluation of the part of the cross section which is actually measured and of the radiative correction arising from the missing part due to higher-order effects. This important issue is addressed in the following section.

1.5.2 $e^+e^- \to \pi^+\pi^-\gamma(\gamma)$ with PHOKHARA

The situation for the $e^+e^- \to \pi^+\pi^-\gamma(\gamma)$ ISR process is very similar to the muon case. In fact the NLO ISR involes the same initial state, but it differs slightly due to the different cross section shape. As for NLO FSR, pions are more complicated than muons since pions are composite objects and an appropriate model is required to describe the corresponding radiative behavior. In PHOKHARA the model used is scalar QED assuming point-like pions [37]. It is therefore of interest to measure this NLO FSR contribution directly in data in order to test the validity of the model used and then apply a correction if necessary in case the evaluation depends on the Monte Carlo simulations.

1.5.3 The AFKQED generator and NNLO contributions

Another second ISR event generator, named AFKQED, has been used in the analyses presented in this thesis. It is based on the formalism from Refs. [33, 40]. The LO ISR (or LO FSR) photon is generated at large angle, in the detector acceptance range. Additional ISR photons are generated with the structure function method [41], assumed to be collinear to the e^+ or e^- beams. In this way leading logarithms of order $\alpha \ln(s/m_e^2)$ are resummed to all orders. Thus, not as PHOKHARA, AFKQED includes higher-order contributions (more than one additional photons) beyond NLO. Because of the collinear approximation, bunches of 0, 1, or more photons, each with the proper QED probability to be radiated from one of the beams leads to an equivalent single photon resumming their individual energies. As a consequence the only explicit NNLO ISR topology that can be accessed is when multiple photon emission occurs on both beams. For additional FSR photons only NLO is implemented using PHOTOS [42]. Another explicit NNLO topology occurring in AFKQED corresponds to one additional ISR photon and one additional FSR photon. In addition the only visible N^{3}LO contribution with three additional photons is generated with one equivalent photon along each beam and one FSR photon.

So far there exists no complete NNLO calculation of the ISR cross section $e^+e^- \to \mu^+\mu^-\gamma(\gamma)(\gamma)$ and consequently no event generator to be used by the experiments, beyond the collinear approximation of AFKQED. Experience with the Born cross section and the ISR process leads us to expect a similar behavior, namely an overall small effect on the cross section, possibly at the level of a few per mil, but significantly larger contributions from hard

radiation which are accessible to experimental investigation and are the subject of this thesis. A very rough guess one could expect contributions for photon energies above 200 MeV is of $(0.25)^2$, thus of order a few percent, within the reach of a high-statistics experiment with a large selection efficiency such as *BABAR*.

Chapter 2

BABAR experiment

The main goal of the *BABAR* experiment (simply as *BABAR*) is to study the disparity between the matter and antimatter of the universe via measuring the Charge Parity (**CP**) violation. *BABAR* locates at the Stanford Linear Accelerator Center (SLAC) National Accelerator Laboratory in California, and the *BABAR* detector is focused on the study of the millions of B mesons produced by the PEP-II storage ring. Due to its high luminosity of B mesons production, the PEP-II collider is also called B factory. In this chapter, a brief introduction to the PEP-II collider and *BABAR* detector will be presented, while more detailed descriptions can be found in Ref. [43]. The schematic plots in Section 2.2 are from Refs. [44, 45].

2.1 The PEP-II asymmetric e^+e^- collider

The PEP-II collider system is designed to produce B mesons that enable the **CP** violation measurement by the *BABAR* detector. As shown in Fig. 2.1, the PEP-II system consists of four major subsystems: Injector, high-energy ring (HER), low-energy ring (LER) and interaction region (IR).

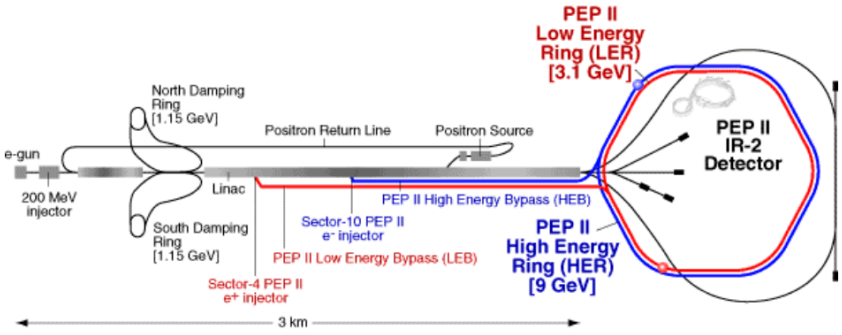

Figure 2.1: The schematic of the PEP-II accelerator system layout.

The powerful injector includes the electron and positron beams extraction, transport lines and match lines from the SLAC three-kilometer LINAC. The HER is for the 9 GeV electron

beam which is originated from PEP but with updated design of vacuum, radio-frequency (RF), diagnostics and feedback systems. The LER mounted on top of the HER is responsible for the 3.1 GeV positron beam. The IR is the most complicate part of the PEP-II and is designed to bring two beams into head-on collision and separate them cleanly. The *BABAR* detector is located in the IR. The collision of the two asymmetric electron and positron beams results in the collider operating at the CM energy $\sqrt{s} = 10.58\,\mathrm{GeV}$, the mass value of $\Upsilon(4S)$ resonance. The asymmetry in collision means the CM of the electron-positron annihilation system moves fast in the direction of the higher-energy beam. The Lorentz boost $\beta\gamma$ is 0.56 from the collision system to the final states with respect to the *BABAR* detector, which is designed to make the delicate **CP** violation in the *B*-meson system measurable since the neutral *B* mesons live long enough for the particles to propagate a considerable distance before decaying. The relative decay length and the time dependence of the decay rates of the *B* mesons can also be determined from this boost.

2.2 The *BABAR* detector

The *BABAR* detector system has been designed to have a large and uniform acceptance in the CM system to achieve the physics goals required. Its reconstruction efficiency is required to be as good as down to the momentum of 40 MeV/c. Photons are required to be reconstructed down to the momentum of 20 MeV/c efficiently. Good energy and angular resolutions for the photons from π^0 and η^0 decay as well as from radiative decays from 20 MeV to 4 GeV. Additional requirements like excellent vertex resolution, efficient reconstruction of secondary vertices, great electron and muon identification, accurate and efficient discrimination between hadrons and B flavor-tagging, are also required. Figure 2.2 shows a schematic view of the longitudinal section with the principal dimensions and Fig. 2.3 demonstrates a view of a transverse section with the principal dimensions of the *BABAR* detector. To get the maximum geometric acceptance for the boosted $\Upsilon(4S)$ decays, the whole detector is offset 0.37 m along with the electron beam from the interaction point. The *BABAR* right-handed coordinate system is defined as the positive z axis pointing to the traveling direction of the electron beam (also called *forward* direction) with a 20 mrad offset with respect to the electron beam in the horizontal plane, the positive x axis pointing horizontally away from the center of the PEP-II accelerator and the positive y axis pointing vertically upward. The polar angle θ is measured with respect to the z axis, with a coverage from 350 mrad in the forward direction and 400 mrad in the backward direction (the running direction of positron), and the azimuth angle ϕ is measured from the x axis in the $x - y$ plane.

From the inside out, as shown in Fig. 2.2, the detector is composed of six main subsystems: Silicon Vertex Tracker (SVT), Drift Chamber (DCH), Detector of Internally Reflected Cherenkov radiation (DIRC), Caesium Iodide (CsI) Electromagnetic Calorimeter (EMC), superconducting Solenoid with 1.5 T magnetic field, and Instrumented Flux Return (IFR). More details of the detector design can be found in Refs. [44–46] and a brief summary is presented in the following part.

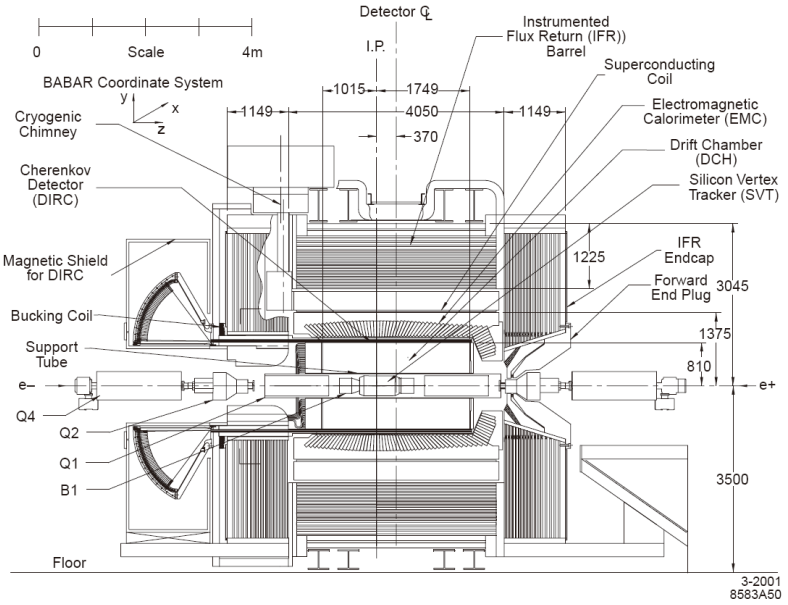

Figure 2.2: The longitudinal section of the *BABAR* detector. The length unit is mm.

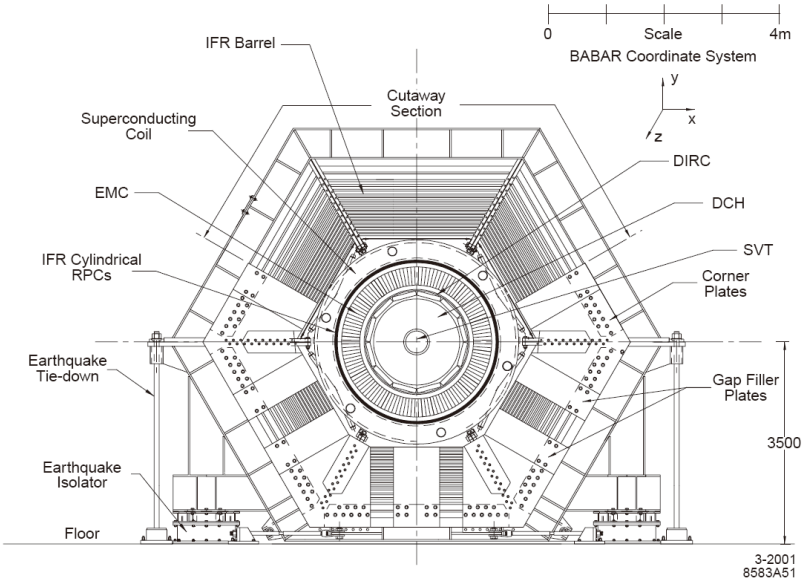

Figure 2.3: The transverse section of the *BABAR* detector. The length unit is mm.

2.2.1 Silicon Vertex Tracker

The SVT is the innermost subdetector in the *BABAR* detector, and as well the only tracking device inside the supporting tube. The primary goal of the SVT is to measure the charged tracks position close to the IR with high precision and to reconstruct the trajectories and decay vertices of the charged particles. The SVT is also designed to detect the low-momentum charged particles that do not reach the DCH. Figure 2.4 shows a schematic view of the longitudinal section of the SVT.

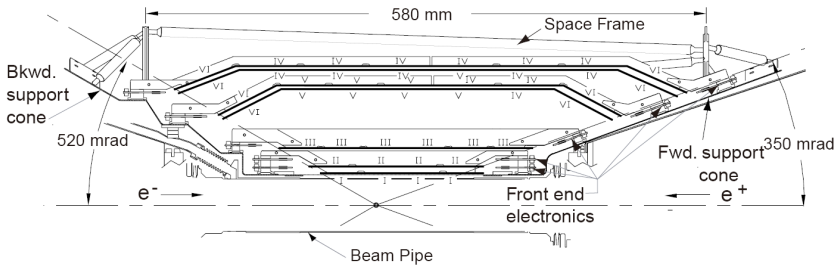

Figure 2.4: The longitudinal section of the SVT.

The SVT consists of five concentric cylindrical, 300 μm thick, double-sided silicon microstrip detectors, with 6, 6, 6, 16 and 18 modules respectively, covering 90% of the solid angle in the CM system. The inner three layers are planar-shaped barrel-style structures used to measure the information of the charged tracks, while the outer two layers are primarily used to match SVT and DCH tracks with arch shapes which enable the detectors to be connected across an angle.

The silicon strips used by the silicon vertex detector are built on high resistivity n-type substrates with n^+ and p^+ fabricated on two sides. The strips normally operate at a bias voltage of 10 V above their typical depletion voltages range from 25 V to 35 V. The ionization of the material forms a current which can be measured by the detector when charged particles pass through the strips. The front-end design includes ICs and the CMOS technology.

The performance of the SVT has been evaluated that the hit reconstruction efficiency is above 95% ($\sim$ 97%), the spatial resolution of the inner three layers is from 10 μm to 15 μm and 40 μm of the outer layers, and the truncated mean dE/dx resolution is $\sim$ 14% for MIPs (*minimum ionizing particle*).

2.2.2 Drift chamber

The multi-wire DCH is the main tracking device of the *BABAR* detector and it is designed to measure momenta and angles with high precision. It also supplies dE/dx measurement for charged tracks. As it is further away from the IR than the SVT, the DCH can therefore measure the curvature and thus the momenta of charged tracks, like the K^0_S decays.

The DCH has relatively small radius, with an inner radius of 236 mm, an outer radius of 809 mm and a length about 2.8 m (shown in Fig. 2.5). It is built with 40 layers of small hexagonal cells which provide up to 40 spatial and ionization loss measurements. Each hexagonal cell has one gold-coated and 20 μm-diameter sense wire, applied with a high positive

voltage, and surrounded by six field wires which are at ground potential. The DCH is filled with a 80:20 gas mixture of helium:isobutane and typically operates at +1960 V to achieve an avalanche gain of approximately 5×10^4.

At the design of +1960 V, the DCH tracking efficiency reaches (98±1)% per track. The resolution of dE/dx achieved is typically 7.5% with the expected value to be 7% and the resolution of $\sigma_{p_T} \approx 0.3\% \times p_T$ for momentum above 1 GeV/c. The DCH has been performing the particle identification (PID) close to the design expectations with stability over time by measuring the ionization loss, dE/dx with all cells fully operational.

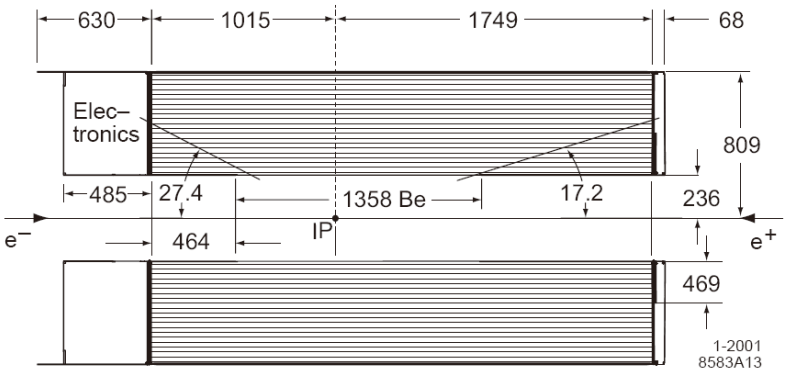

Figure 2.5: The side view of longitudinal section of the DCH with principal dimensions.

2.2.3 Detector of internally reflected Cherenkov radiation

To better separate pions and kaons from the rare two-body decays $B^0 \to \pi^+\pi^-$ and $B^0 \to K^+\pi^-$, a new kind of ring-imaging PID system called the DIRC is used in *BABAR* . The DIRC provides a π/K separation of higher than 3.5σ and it can work for all tracks from B-meson decays over the entire momentum range from the pion Cherenkov threshold up to 4.2 GeV/c. PID in low-momentum range (below 700 MeV/c) primarily relies on the dE/dx measurements in the SVT and the DCH.

As shown in Fig. 2.6, the DIRC system is composed of 4.9 m long, 17 mm by 35 mm rectangular bars of synthetic, fused silica. The 144 DIRC bars are long but thin and light and arranged in a 12-side polygonal barrel, with 12 bars each side. These bars serve both as radiators and as light pipes. The radiator bars cover about 83% of the polar angle and 94% of the azimuthal angle of the CM system. The photon detector in the DIRC is placed at the backward end and the mirrors are placed at the forward end of the bars to reflect incident photons. The produced photons from the radiator bars transport to the backward end of the bars, enter the standoff box and are finally detected by the PMTs (photon multiplier tubes).

The expected Cherenkov light is measured by a tightly packed array of PMTs, which are located about 1.2 m away from the bar end and arranged into 12 sectors of 896 PMTs each. The position and the arriving time of the photons can be obtained from the PMTs. From the measured Cherenkov angle, the mass of the particles can be identified. The DIRC has an excellent separation between pions and muons, about 4.2σ at 3 GeV/c and still about 2.5σ at 4.1 GeV/c.

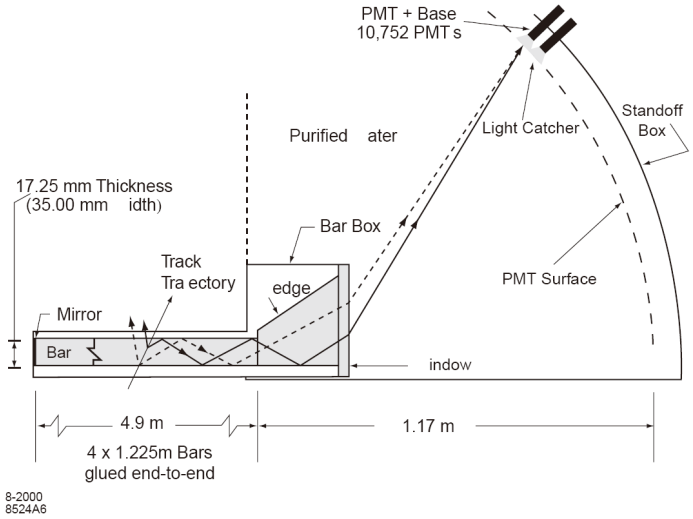

(a) Schematic layout of the DIRC.

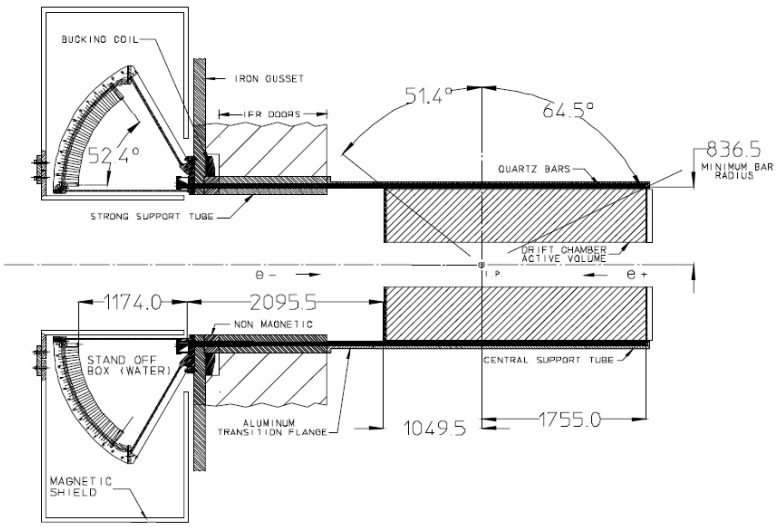

(b) Elevation view of the DIRC geometry.

Figure 2.6: The DIRC geometry view.

2.2.4 Electromagnetic calorimeter

The EMC designed in *BABAR* is a total-absorption calorimeter which has an excellent energy and angular resolution over the energy range between 20 MeV and 9 GeV. This capability allows the high photon detection efficiency from the π^0 and η decays, as well from radiative processes and electromagnetic processes. The EMC consists of 6580 thallium-doped CsI crystals in total, with a cylindrical barrel of 48 rings arranged with 120 identical crystals each ring and a conical forward endcap of 8 rings with a total of 820 crystals. In general, the EMC has a full coverage from 15.8° to 141.8° in polar angle, which translates to a solid-angle coverage of 90% in the CM system (see Fig. 2.7).

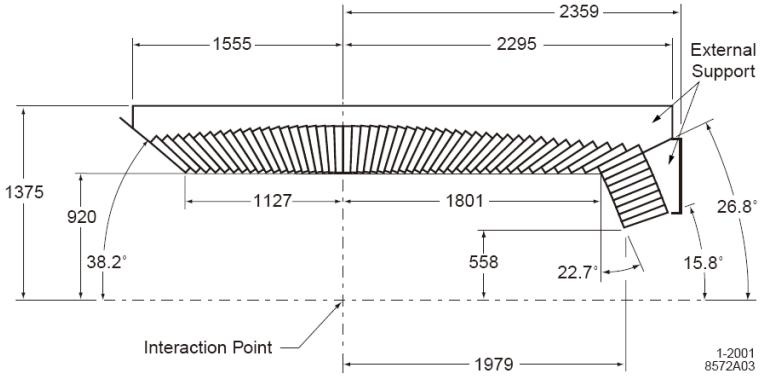

Figure 2.7: The longitudinal cross section of the top-half EMC along the beam direction.

Each crystal of EMC has a tapered trapezoidal-like cross section, with the typical front-face area $4.7 \times 4.7\ \mathrm{cm}^2$ and back-face area $6.1 \times 6.0\ \mathrm{cm}^2$. The crystals perform not only as a total-absorption medium, but also as light guides to collect light at the photodiodes.

The photon detector includes two $2 \times 1\ \mathrm{cm}^2$ silicon PIN diodes at the center of the rear face of the each crystal, where the light from the electromagnetic showers are measured. Electromagnetic showers spread over many adjacent crystals and thus form a cluster of energy deposits. The clusters can then be reconstructed by the reconstruction algorithms. The achieved energy resolution of the EMC is $\sigma_E/E = 5.0 \pm 0.8\%$ at 6.13 MeV and $\sigma_E/E = 1.9 \pm 0.07\%$ at 7.5 GeV. A fit to the energy dependence gives the expression as

$$\frac{\sigma_E}{E} = \frac{(2.32 \pm 0.30)\%}{\sqrt[4]{E(\,\mathrm{GeV})}} \oplus (1.85 \pm 0.12)\%. \tag{2.1}$$

The achieved angular resolution is determined from the π^0 ans η decays to two photons of almost same energy. The resolution varies from 12 mrad at low energies to 3 mrad at high energies. A similar fit result to a parameterization of the energy dependence can be expressed as

$$\sigma_\theta = \sigma_\phi = (\frac{3.87 \pm 0.07}{\sqrt{E(\,\mathrm{GeV})}} \pm 0.00 \pm 0.04)\ \mathrm{mrad}. \tag{2.2}$$

2.2.5 Instrumented flux return

The IFR is the outermost detector of *BABAR* and it was designed to detect muons with large solid angle and high efficiency, and long-lived neutral hadrons (primarily K_L^0 and neutrons) over a wide range of momenta and with good angular resolution. The IFR has double duty, one is as the flux return for the magnetic solenoid, and the other is as a muon and neutral hadron detector. The IFR uses the flux return with layers made of iron and steel as a muon filter and hadron absorber, while single gap resistive plate chambers (RPCs) with two-coordinate readout are used as detectors.

The steel segmentation has been chosen based on the MC simulation of muon penetration and neutral hadron interactions. The steel is sectioned into layers, with thickness from 2 cm for the inner plates to 10 cm for the outermost plates. The nominal gap between the steel plates is 3.5 cm in the inner layers of the barrel and 3.2 cm in other parts. The system consists of a central barrel part and two plugs called end caps to cover a wide angle range. The RPCs are installed in the gaps of the segmented steel of the barrel and the end caps of the flux return. There are 19 PRC layers in the barrel part and 18 layers in the end caps part. Two additional layers of the cylindrical RPCs are installed outside the EMC to detect the particles exiting the EMC.

A planar RPC has two 2 mm-thick bakelite (phenolic polymer) sheets which are separated by a 2 mm gap and have a large resistivity of $10^{11} \sim 10^{12}\ \Omega$. The gap is enclosed at the edge by a 7 mm wide frame and is filled with a non-flammable gas mixture of 56.7% Argon, 38.8% Freon 134a, and 4.5% isobutane. The internal surfaces of the bakelite are linseed-oil coated to prevent large dark currents and discharges in the gas. The external surfaces of the bakelite are coated with graphite to obtain a surface resistivity of $\sim 100\ \mathrm{k}\Omega/\mathrm{square}$, applied $\sim 8\ \mathrm{kV}$ high voltage and ground, and protected by an insulating mylar film.

Muons are generally able to penetrate more layers of steel or iron compared to pions, and this serves as the main discrimination between muons and pions. The muon detection efficiency in the IFR has been achieved close to 90% in the momentum range between 1.5 GeV/c and 3.0 GeV/c, with a fake pion rate about $6 \sim 8\%$. The K_L^0 efficiency increases from 20% to 40% in the momentum range $1 < p < 4\ \mathrm{GeV}/c$ (IFR and EMC combined).

The IFR was forced to be upgraded due to the rapid aging and efficiency loss of the original RPCs. In 2002, the forward end cap was replaced with new improved RPCs and in 2004 two of the barrel PRCs were replaced with limited streamer tubes (LSTs) and brass absorber, mainly to avoid losing muon ID capability. In 2006, the remaining 4 PRC sextants in the barrel were replaced by LSTs.

2.3 The Trigger System

The trigger system in *BABAR* is designed to select events of interest with a stable, high and well-understood efficiency while rejecting other background events at a high rate and keep the total event rate below 120 Hz. The trigger system is implemented as a two-level hierarchy, the Level 1 (L1) in hardware followed by the Level 3 (L3) in software. During normal operation, the L1 is used to have an output rate of 1 kHz, while the L3 receives the output from L1 and then performs a second stage rate reduction related to the main physics source. Typically, the

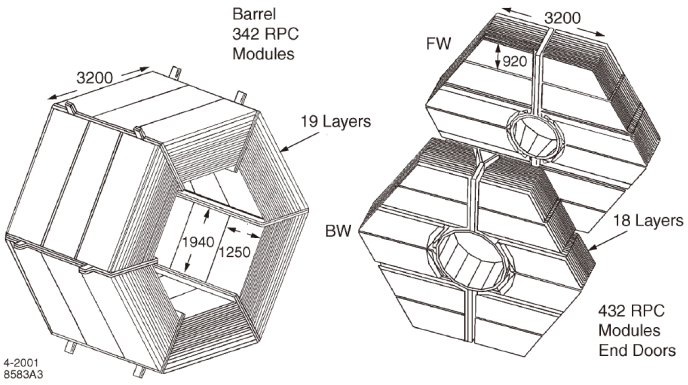

Figure 2.8: Schematic of the IFR system: Barrel sectors, forward (FW) and backward (BW) end doors.

L1 trigger has an efficiency greater than 99.5% for $B\bar{B}$ processes and the L3 trigger maintains the $B\bar{B}$ selection efficiency at more than 90% with data rate reduced to 200 Hz.

2.4 Data Luminosity

The *BABAR* experiment has taken data between 1999 and 2008. The designed instantaneous luminosity for PEP-II has been improved over time by a factor of four, 12×10^{33} $\mathrm{cm}^{-2}\mathrm{sec}^{-1}$, with a peak-luminosity record in August 2006. An integrated luminosity of 553.48 fb^{-1} was collected mostly at the $\Upsilon(4S)$ in 2008 [1]. Figure 2.9 shows the integrated luminosity over time.

[1] This integrated luminosity includes $\Upsilon(4S)$ from Run1 to Run6, and $\Upsilon(3S)$ and $\Upsilon(2S)$ from Run7, where $\Upsilon(4S)$ takes up most of the fraction.

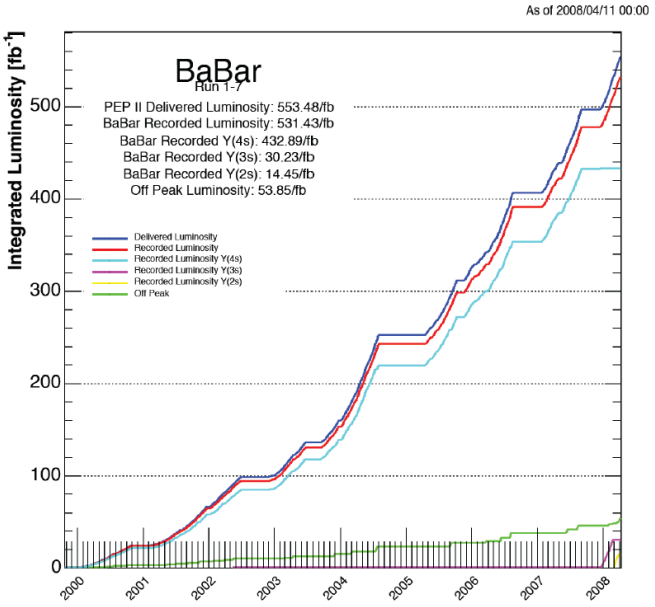

Figure 2.9: The integrated luminosity delivered by PEP-II over time from 1999 to 2008.

Chapter 3

Analysis outline

3.1 Data samples

This analysis is based on the data collected with the *BABAR* detector operated at the $\Upsilon(4S)$ resonance, in run 1 through run 6. The data used corresponds to a total integrated luminosity as

$$\mathcal{L} = 424.2\ \text{fb}^{-1} \tag{3.1}$$

with $43.9\ \text{fb}^{-1}$ of data were collected just below the resonance in addition [47]. The relative uncertainty on the luminosity of the on-resonance (off-resonance) samples is both 0.43%.

3.2 Monte Carlo generators and simulations

Events simulated are produced by using MC methods, which can help better understand the signal, estimate the background distributions, the event selection criteria and the selection efficiencies. In this analysis, the signal ISR processes $e^+e^- \to X\gamma_{\text{ISR}}$ with $X = \mu\mu$, $\pi\pi$ or KK are simulated with the full NLO PHOKHARA event generator [37], which is different from the previous analysis [35] where the signal ISR processes were simulated with AFKQED event generator [40]. The main ISR photon, γ_{ISR} is generated with a wide angular range, $20^\circ - 160^\circ$ in the CM system bracketing the photon detection range with a margin to account for the finite resolution. At production and preselection level, a minimum ISR photon energy of 4 GeV in the CM system is required, thus limiting the mass of the produced final state to $5\,\text{GeV}/c^2$ (the final state beyond $5\ \text{GeV}/c^2$ is treated as pathological), far beyond the $0 - 1.4\,\text{GeV}/c^2$ mass range considered in this study. Samples corresponding to 10 times the number of data events are generated for the signal channels.

In addition, relatively small samples of signal ISR processes are simulated with the AFKQED generator described before. A minimum mass $m_{X_{\text{ISR}}} > 8\,\text{GeV}/c^2$ is imposed at the generation stage, which places an upper bound of 2.3 GeV on the additional ISR photon energy. Additional ISR photons are emitted along the e^+ or e^- beam particle direction produced by AFKQED generator. Within the intrinsic limitations of the generator, AFKQED produces samples of events simulated up to NNLO.

Background ISR processes $e^+e^- \to X\gamma_{\rm ISR}$ (X = $K^+K^-\pi^0, \pi^+\pi^-\pi^0, \pi^+\pi^-2\pi^0$, $2\pi^+2\pi^-$, ..., including resonant states) are simulated with the AFKQED MC event generator. Background processes $e^+e^- \to q\bar{q}$ ($q = u, d, s, c$) are generated with JETSET [48], and $e^+e^- \to \tau^+\tau^-$ with KORALB [49]. The response of the *BABAR* detector is simulated with GEANT4 [50], taking into account the beam variations and the detector conditions over time.

3.3 Event selection

Two-body ISR events are associated with two-charged tracks and one hard photon in the final states of $e^+e^- \to \mu\mu\gamma(\gamma)$ and $e^+e^- \to \pi\pi\gamma(\gamma)$. The basic selection criteria are listed below:

- L1 and L3 trigger satisfied and BGFilter [1] passed
- At least 2 good tracks
- 2 exactly good tracks of opposite charges, each with transverse momentum $p_{\rm T} > 0.1\,{\rm GeV}/c$ and θ polar angle in the range 0.40−2.45 rad, identified as muons or pions, and in the DIRC and IFR active areas
- A photon with the energy larger than 4 GeV in the CM system and laboratory polar angle range 0.35−2.4 rad
- a radiative Bhabha [2] veto based on large ECM deposit ($E_{\rm cal}$) deposits on both tracks
- the transverse distance between the 2-track vertex (calculated using the track helices without refitting) and the beam spot smaller than 0.5 cm to remove conversions

Here the defined good tracks must satisfy the requirements below:

- polar angle θ in the range 0.4−2.45 rad
- number of DCH hits $N_{\rm DCH} \geq 15$
- distance of minimum approach to the beam axis in $x - y$ plane $docaxy < 0.5$ cm
- distance from the beam spot along the beam axis direction within 6 cm ($|dz| < 6$ cm)
- electron veto reducing electron contamination based on a combination of dE/dx and $E_{\rm cal}$, $((E_{\rm cal}/p - 1)/0.15)^2 + ((dE/dx_{\rm DCH} - 690)/150)^2 < 1$, $E_{\rm cal}$ is the deposited energy in the EMC that is associated to the track

A relaxed preselection combination for standard tracks, $docaxy < 2.5$ cm with no cut on the $N_{\rm DCH}$ and $p_{\rm T} > 0.1$ GeV, makes relevant analyses more efficient. All types of ISR events are pre-selected requiring an OR of the following four conditions:

[1] The BGFilter performs a part of the offline reconstruction and then combines the information with the DCH hits and EMC cluster responses for the full event reconstruction selection.

[2] $e^+e^- \to e^+e^-\gamma$ samples

- even number of standard tracks with zero total charge, and the angle between the missing momentum vector (including photons, but excluding the ISR photon, which is the highest-energy photon in the CM system) and the ISR photon smaller than 0.3 rad;
- the same angular cut, but here includes all extra detected photons in the calculation of the missing momentum;
- any odd number of standard tracks (for efficiency study);
- number of K_s^0 candidates (2 tracks with secondary vertex and mass in a window near K_s^0 mass) larger than 1.

There may exist two ISR photon candidates in the detector with $E^*_{\gamma_{\rm ISR}} > 4$ GeV in about 2.5×10^{-3} of the events. In that case, the ISR photon is chosen to be the one with the higher $E^*_{\gamma_{\rm ISR}}$. Note that this choice is conventional since in data as well as in PHOKHARA MC, it is not possible to distinguish which photon is main ISR and which is additional.

3.4 Specificity of the additional radiation study

The focus of our attention is on the radiation study for the $\mu^+\mu^-\gamma(\gamma)$ and $\pi^+\pi^-\gamma(\gamma)$ channels. The present study of additional radiation is performed by distinguishing the muon and pion channels on an event-by-event basis, utilizing PID for the charged tracks. This is justified by the convenience of handling separate samples of radiative events in order to study their specific behavior. In the published $\pi^+\pi^-$ cross section analysis [35], where the pion to muon and kaon separation relied on PID, strong cuts were imposed on the track momentum ($p > 1$ GeV/c) to ensure good identification. In this analysis, no such strong cuts are applied to maintain sensitivity over the full angular distribution of the two-body CM system, with tracks being reconstructed down to 0.1 GeV/c. One thus expects limited PID performance for the low momentum track. However, this challenge is tempered by the fact that the study of additional radiation does not demand the same level of precision as that needed for determining the cross section.

The tag-and-probe method has been used to determine the PID efficiencies. Events are required to pass the selections described in Section 3.3. In addition, the background contribution is reduced by applying the 2D-χ^2 selection describe in Section 4.3.1, particularly for the $\pi\pi$ sample with huge background. Since pairs of particles of the same mass are produced in the selected events, very tight identification of the tag track is required and the identification efficiency is measured using the other probe track. This study employs the standard *BABAR* PID selectors, which are described in details in [46]. A muon track is tagged with the tight BDT muon selector for high-momenta track (larger than 0.7 GeV/c) and the tight BDT low-momentum muon selector for lower-momenta track. A pion track is tagged with very tight piKM pion ECOC selector and vetoed against muon, kaon and electron with loose selectors, which effectively reject these particles while still maintain a high efficiency for pions. The other track is tagged with the same selectors. The efficiencies are calculated separately for the data and PHOKHARA MC samples in a 2D matrix of (p_T, θ) bins. For data, the background contributions are subtracted relying on the simulated background MC samples. For each MC

event, the product of the data/MC ratios of PID efficiencies for the two charged tracks is applied as a correction, each data/MC ratio is obtained by scanning a correction table created in momentum and polar-angle bins.

Chapter 4

Kinematic fitting and background

4.1 Kinematic fitting: NLO description

In *BABAR* analyses, χ^2 cuts have been used after kinematically fitting the events to the relevant X_γ hypothesis. Mostly due to the additional radiation, and partly due to resolution effects, the χ^2 distributions have long tails.

Therefore for both $\mu\mu\gamma$ and $\pi\pi\gamma$ processes, the event definition is enlarged to include the radiation of one photon in addition to the already-required ISR photon. Two types of fits are considered, according to the following situations:

- The additional large-angle (LA) photon is detected in the EMC, in which case its energy and angles can be readily used in the 4-constraint (4C) fit: here we call this the $\gamma_{\rm ISR}\gamma_{\rm LA}$ fit, in which the extra photon can be either from FSR or from ISR at large angle to the beams. The threshold for the additional photon to be considered in the $\gamma_{\rm ISR}\gamma_{\rm LA}$ fit is kept down to 50 MeV. This can introduce some background, but with little effect as the fit in that case will not be different from a standard fit to the $\mu\mu(\gamma)\gamma$ or $\pi\pi(\gamma)\gamma$ hypothesis in practice.

- The additional photon is assumed to be from ISR at a small angle (SA) to the beams. Since no more further information is available, it is postulated that the extra photon is perfectly aligned with either the e^+ or the e^- beam. The corresponding fit is called 3-constraint (3C) fit or $\gamma_{\rm ISR}\gamma_{\rm SA}$ fit, which ignores the additional photons measured in the EMC and returns the fitted collinear ISR photon energy.

In both cases the constrained fit procedures use the ISR photon direction and energy, the measured momenta and angles of the two tracks with their covariance matrix in order to satisfy the four energy-momentum conservation equations. Since the energy response of the EM calorimeter is asymmetric with a long tail when the measured energy is smaller than the true energy, the photon energy variable is thus transformed into a Gaussian-distributed symmetric variable using the Novosibirsk function [51]. For each photon entering the fits, the three parameters of the corresponding Novosibirsk variable Z and its error are initialized using the measured energy of the photon. Calibration of the Z parameters has been performed beforehand on a clean $\mu\mu\gamma$ 'LO' sample with a 3C fit using the two muons and the angles of the ISR photon, by comparing the measured energy and the fitted energy. The χ^2 of the

NLO fits is minimized with the four-momentum conservation constraints in terms of the Z variable(s). The fitted energy of the photon(s) is calculated from the Z values returned by the fit.

Each event is characterized by two χ^2 values, $\chi^2_{\gamma_{\rm ISR}\gamma_{\rm SA}}$ and $\chi^2_{\gamma_{\rm ISR}\gamma_{\rm LA}}$ from the corresponding $\gamma_{\rm ISR}\gamma_{\rm SA}$ and $\gamma_{\rm ISR}\gamma_{\rm LA}$ fits, which can be examined on a two-dimensional (2D) plot. The quantities $\ln(\chi^2+1)$ are used so that the long tails can be properly visualized in practice. Events without any extra measured photons have only the $\chi^2_{\gamma_{\rm ISR}\gamma_{\rm SA}}$ value and they are plotted separately. In the case where several extra photons are detected, $\gamma_{\rm ISR}\gamma_{\rm LA}$ fits are performed using each photon in turn and the fit with the best $\chi^2_{\gamma_{\rm ISR}\gamma_{\rm LA}}$ is retained. If the $\gamma_{\rm ISR}\gamma_{\rm LA}$ fits fail, then the corresponding events have only $\chi^2_{\gamma_{\rm ISR}\gamma_{\rm SA}}$ values and they are plotted as overflow at around 11.5. To be consistent with the final cross section analysis without using PID, the pion mass is assumed for the two charged particles, and in the following studies and the distributions the $\pi\pi$ mass is obtained from the fitted parameters of the two charged particles from the $\gamma_{\rm ISR}\gamma_{\rm SA}$ fit if $\chi^2_{\gamma_{\rm ISR}\gamma_{\rm SA}} < \chi^2_{\gamma_{\rm ISR}\gamma_{\rm LA}}$ and from the $\gamma_{\rm ISR}\gamma_{\rm LA}$ fit in the reverse case.

As depicted in Fig. 4.1 (top-left) for $\pi\pi\gamma$ data without background subtraction, it is easy to visualize the different interesting regions in the 2D-χ^2 plane. Most of the events are LO events (see figures in Appendix. A) and are peaked at small values of both χ^2, but the tails along the axes clearly indicate events with additional radiation: small-angle ISR along the $\chi^2_{\rm LA}$ axis (with large ISR energies at large values of $\chi^2_{\rm LA}$), or FSR or large-angle ISR along the $\chi^2_{\rm SA}$ axis (with large additional radiation energies at large values of $\chi^2_{\rm SA}$). Events along the diagonal do not satisfy either hypothesis and result from resolution effects for the pion tracks (also secondary interactions) or the primary ISR, or possibly more than one additional radiated photon. These effects are investigated further in this analysis. At large χ^2 values, multibody backgrounds populate the background region which is defined in the 2D-χ^2 plane and dominate the $\pi\pi\gamma$ data. As they are mostly events with genuine pions, PID requirements are not efficient and thus specific BDT techniques are developed to select the signal, as explained later in Section 4.2. The 2D-χ^2 distributions from the PHOKHARA MC simulation (middle) and from $\mu\mu\gamma$ samples (right) are also shown in Fig. 4.1 for comparison. In the bottom panels, the $\chi^2_{\gamma_{\rm ISR}\gamma_{\rm SA}}$ distribution of the events which do not have an additional measured photon are compared between data and MC. The zone delimited with red solid lines in the 2D-χ^2 distributions (top and middle), and the vertical dashed line in the 1D distributions (bottom) indicate the optimized selection discussed in Section 4.3.1.

4.2 Background studies

4.2.1 Multihadrons from the $q\bar{q}$ process

Hadronic process, named as usd process in the following, introduces a background in the signal samples that is considerably reduced by the χ^2 selection of the kinematic fits. uds is the dominant background for mass range larger than 0.9 GeV/c^2 and subdominant between 0.6 and 0.9 GeV/c^2. This contribution is estimated using simulated samples for the $e^+e^- \to q\bar{q}$ process. However, the JETSET prediction for $q\bar{q}$ fragmentation into low-multiplicity final states is not necessarily reliable, so the MC rate is normalized using data.

In backgrounds from the $q\bar{q}$ process, the ISR photon candidate is actually produced from

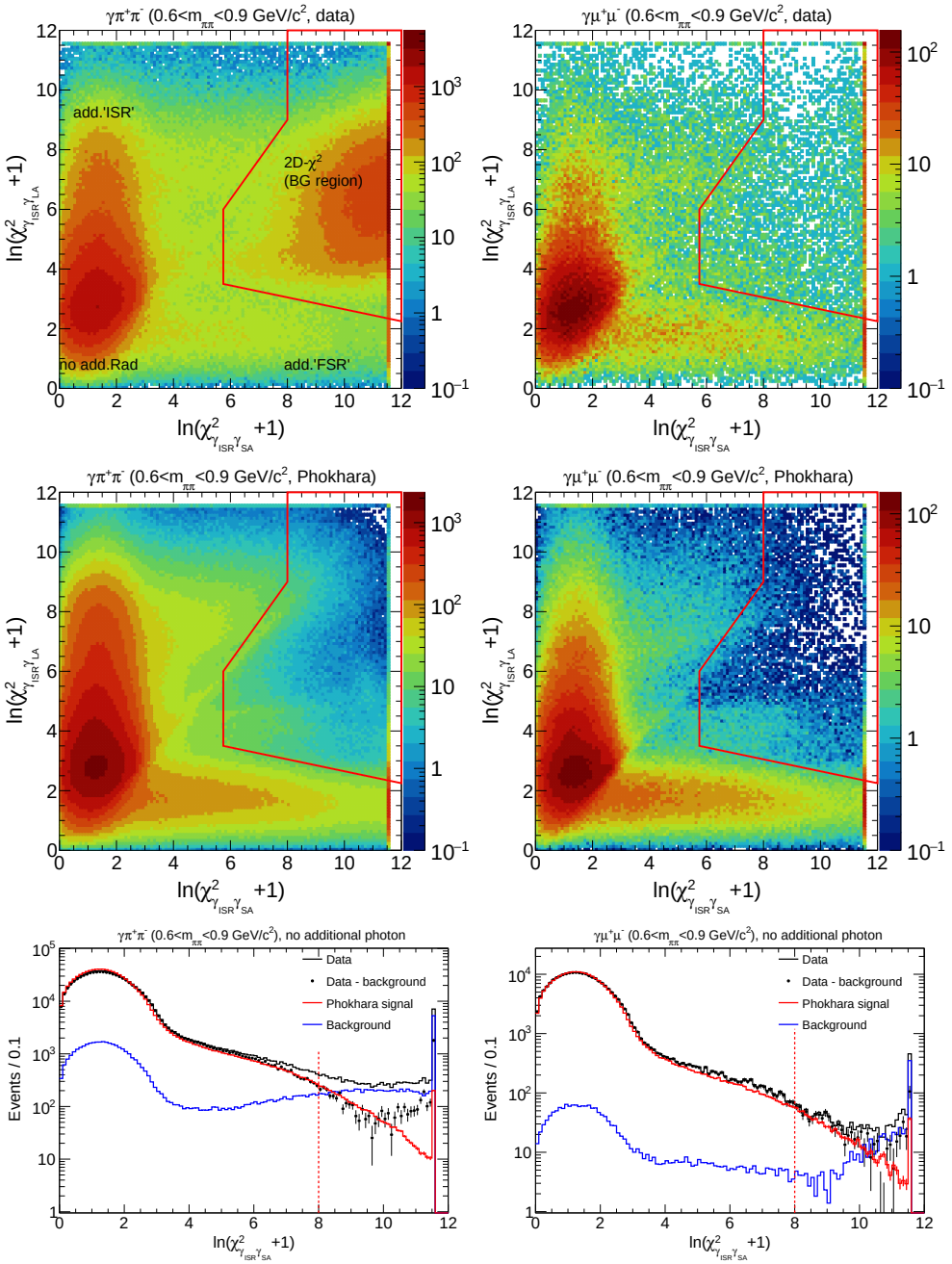

Figure 4.1: The 2D-χ^2 distribution for $\pi\pi\gamma_{\rm ISR}(\gamma_{\rm SA}/\gamma_{\rm LA})$ (left) and $\mu\mu\gamma_{\rm ISR}(\gamma_{\rm SA}/\gamma_{\rm LA})$ (right) in data without background subtraction (top), PHOKHARA MC (middle) and a comparison of $\chi^2_{\gamma_{\rm ISR}\gamma_{\rm SA}}$ between data and MC for those events which do not have any additional measured photon (bottom) in the mass region $0.6 < {\rm m}_{\pi\pi} < 0.9$ GeV/c^2. This mass region for pion is dominated by the ρ resonance. The zone delimited with red lines in the 2D plot and the dashed vertical line in the 1D comparison plot indicate the optimized selection.

the decay of an energetic π^0. The search for such a signature is carried out in both data and MC samples by pairing the ISR photon candidate with all detected additional photons having energy larger than 50 MeV. The pair with $\gamma\gamma$ mass closet to the nominal π^0 mass is retained (notated as $m_{\gamma\gamma}$ in the following). For energetic π^0's the two photons showers are likely to be merged into a single calorimeter cluster, elongated in the transverse distribution. Such a topology can be searched for by using the energy deposits in the EMC crystals (Zernike20 variable). In this case, the $m_{\gamma\gamma}$ calculation requires the inclusion of a second photon, which can originate from either a uds extra π^0 or from beam background. Thus the uds process has two main populations corresponding to resolved and unresolved π^0, which can be clearly seen in Fig. 4.2. Besides the clear resolved π^0 signal it is seen that the continuum in the $m_{\gamma\gamma}$ distribution is also generated by unresolved π^0's, thus providing a way to perform the data/MC comparison for both topologies. The MC normalization is obtained from the observed π^0 rates on one hand and the unresolved π^0 rates on the other hand.

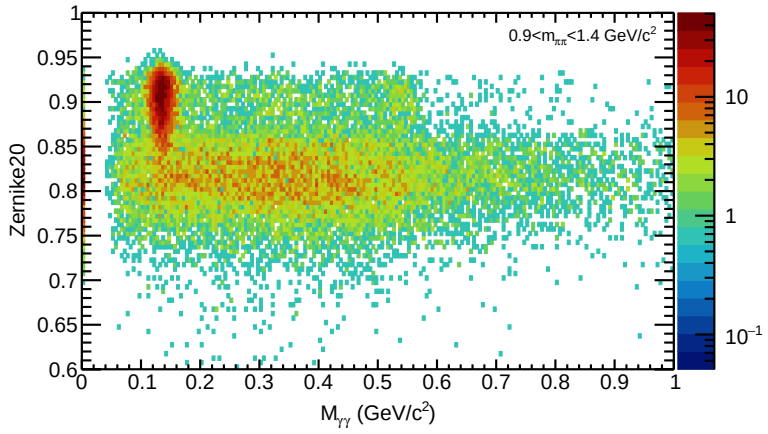

Figure 4.2: The $\gamma\gamma$ mass distribution versus shape variable Zernike20 of the ISR photon candidate from the uds MC sample showing both the resolved π^0 and unresolved π^0. The resolved π^0 population accounts for 20% of the total populations, while the unresolved π^0 population with other measured photon and the unresolved π^0 population without extra photon account for 77% and 3% respectively.

The BDT optimization based on multivariate technique [52] is used to select the hadronic processes in the accepted χ^2 region in three separate $\pi\pi$ mass windows: the low mass window between the threshold and 0.6 GeV/c^2, the intermediate mass window between 0.6 and 0.9 GeV/c^2 near the ρ mass peak, and the high mass window between 0.9 and 1.4 GeV/c^2. For each $\pi\pi$ mass window, two separate BDTs are carried out for $m_{\gamma\gamma} < 0.3$ GeV/c^2 and $m_{\gamma\gamma} > 0.3$ GeV/c^2, respectively. For BDT training, seventeen discriminating variables are chosen excluding the strongly correlated but less discriminating one. The resulting separation between the uds and non-uds processes (all other background processes except for $\tau\tau(\gamma)$ which is not included in the BDT training and subtracted from the mass distribution directly) is presented in Fig. 4.3 for different cases.

The selected BDT input variables are listed in Table 4.1.[1] The shapes of these variables

[1]Unless stated otherwise, the detailed BDT method discussion is concentrated on the high mass

between the uds and non-uds MC samples are compared in Fig. 4.4. The corresponding comparison between the data sample and the MC simulation for these variables is shown in Fig. 4.5. The distributions in dashed lines show the initial MC samples. A non-negligible discrepancy in the resolution of the ISR photon energy in the CM system (E^*_γ) is observed between data and simulation. The distributions in solid line correspond to the corrected distributions by reweighting the E^*_γ distribution in the simulation to that in data. As expected , the reweighting correction also improves other variables related to energy while has little impact on the other variables.

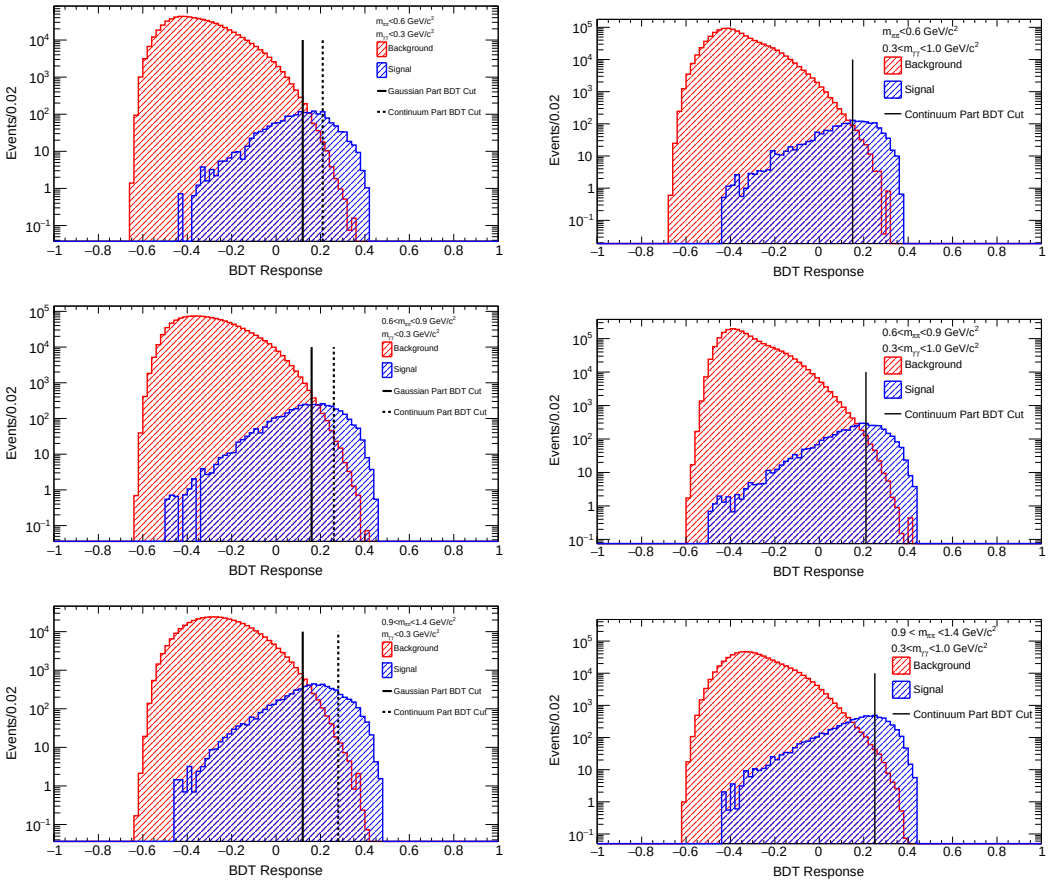

Figure 4.3: BDT response for low mass (top), intermediate (middle) and high (bottom) $m_{\pi\pi}$ mass windows for low (left) and high (right) $m_{\gamma\gamma}$ mass ranges. The red and blue histograms correspond to the absolute non-uds and uds event yields, respectively. The solid (dashed) vertical line in the left panels corresponds to the BDT selection used for obtaining the normalization factor for the π^0 peak (unresolved continuum) for $m_{\gamma\gamma} < 0.3$ GeV/c^2. The solid vertical line in the right panels corresponds to the BDT selection used for obtaining the normalization factor for the unresolved continuum contribution for $m_{\gamma\gamma} > 0.3$ GeV/c^2

The correlation between the BDT input variables for the uds and background (non-uds) MC samples is shown in Fig. 4.6 for the high mass window. Highly correlated variables with less discriminant power have been removed.

window where the multihadronic background processes dominate.

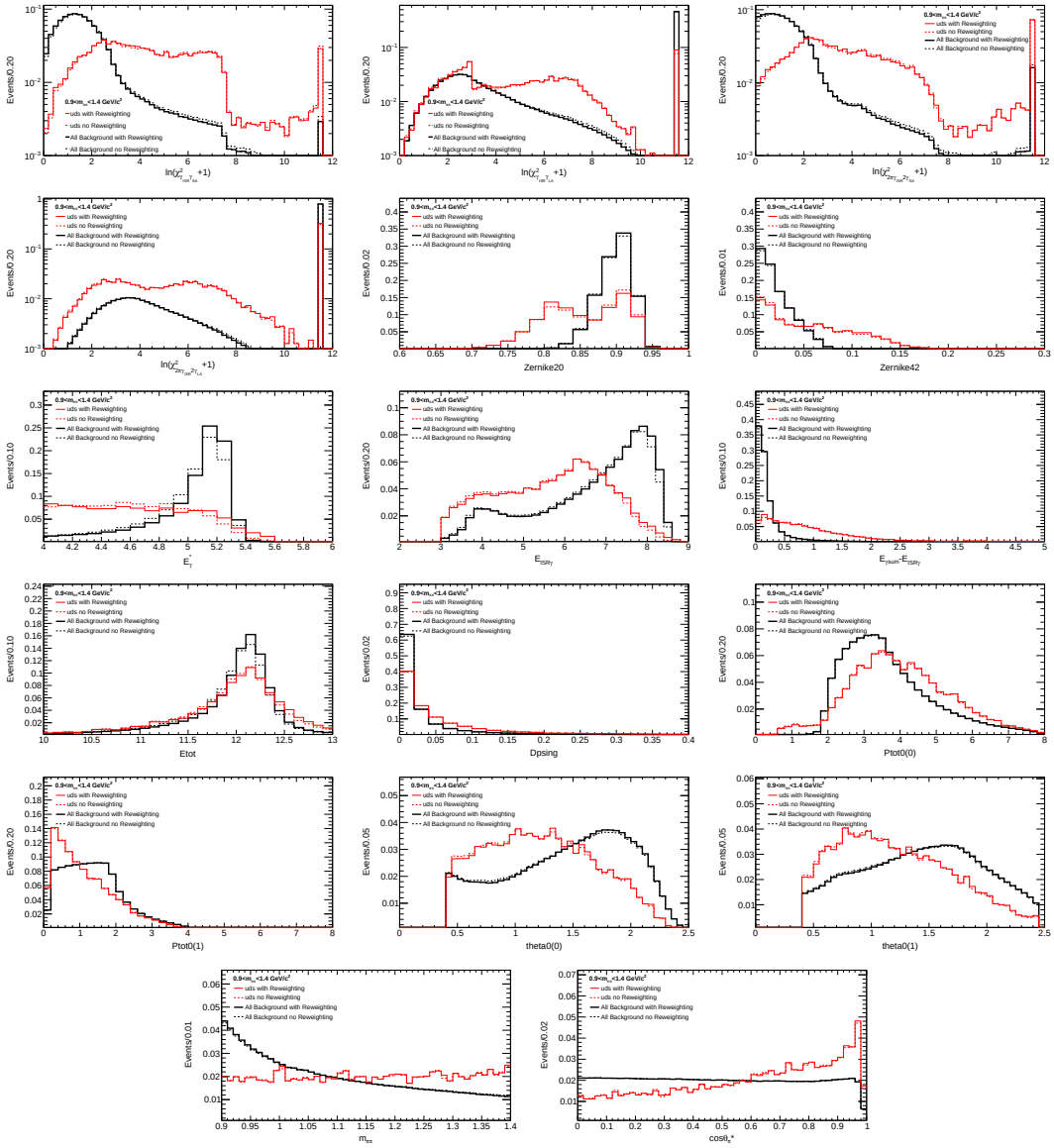

Figure 4.4: Comparison of the shapes between the uds (red) and non-uds (black) MC samples for the selected BDT discriminant variables. The dashed lines show the initial distributions while the solid one the reweighted one after correcting for a difference between data and MC simulation in the energy resolution of the ISR photon in the CM system.

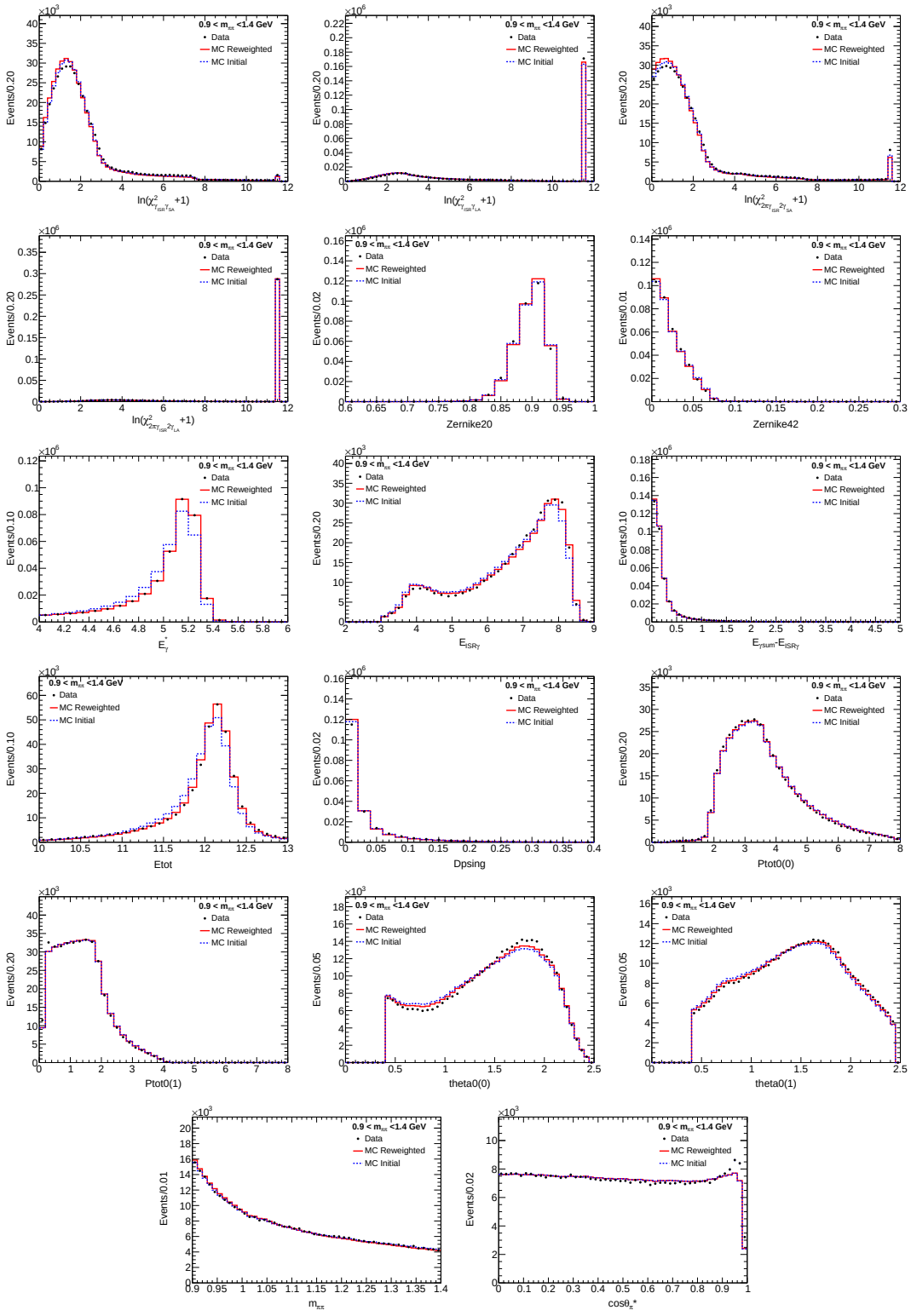

Figure 4.5: Distributions of data compared to normalized MC distributions for the selected BDT input variables. The data are shown with the full black points, the dashed histogram represents the initial MC samples and the full line the reweighted MC samples. The discrepancy in the last two bins in the bottom right plot of $\cos\theta^*_\pi$ variable could be due to the missing $ee\gamma$ contribution in the MC samples.

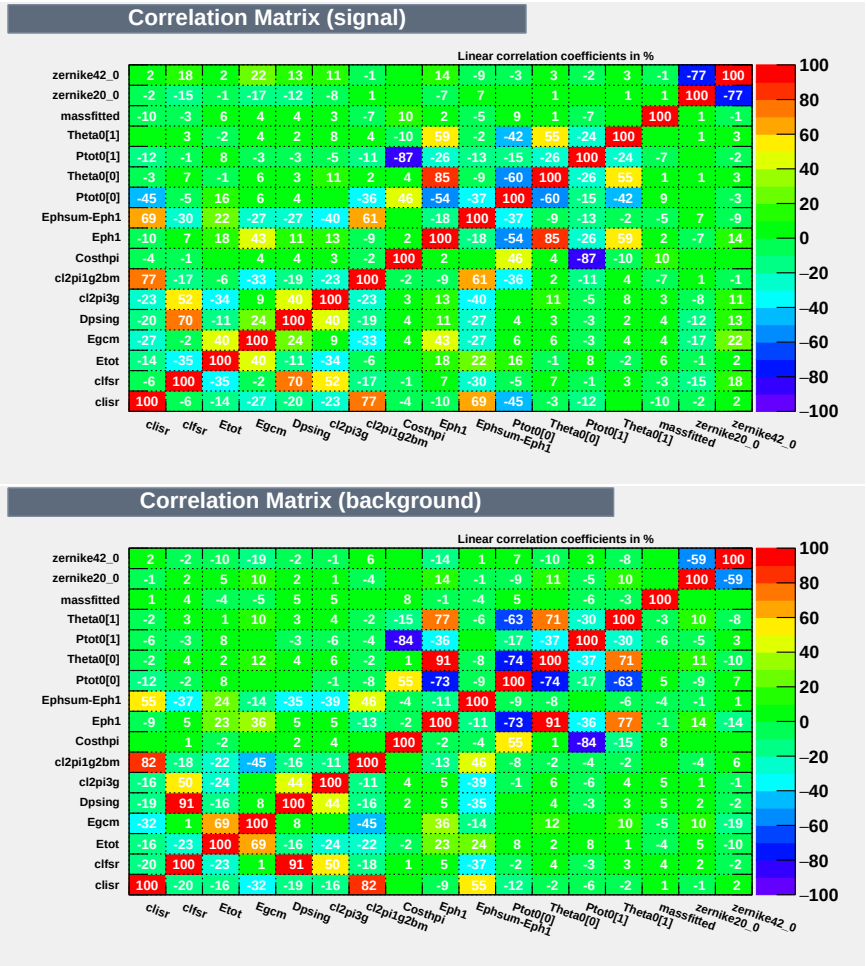

Figure 4.6: Correlation between the BDT input variables for uds (top) and non-uds (bottom) MC samples.

Variable	Description
$\ln(\chi^2_{\gamma_{\rm ISR}\gamma_{\rm SA}}+1)$	χ^2 value of $e^+e^- \to \pi^+\pi^-\gamma_{\rm ISR}\gamma_{\rm SA}$
EphSum − EPH1	Energy sum of all measured photons except for ISR photon
CHI2_2pi1g2bm	χ^2 value of $e^+e^- \to \pi^+\pi^-\gamma_{\rm ISR}2\gamma_{\rm SA}$
ZERNIKE20	Zernike shape variable of ISR photon
EGCM	ISR photon energy in CM
ZERNIKE42	Zernike shape variable of ISR photon
CHI2_2pi3g	χ^2 value of $e^+e^- \to \pi^+\pi^-3\gamma$ fit
$\ln(\chi^2_{\gamma_{\rm ISR}\gamma_{\rm LA}}+1)$	χ^2 value of $e^+e^- \to \pi^+\pi^-\gamma_{\rm ISR}\gamma_{\rm LA}$ fit
DPSING	Angle between ISR photon and missing momentum in laboratory
EPH1	Energy of ISR photon
THETA0$_0$	Polar angle of 1st good track
PTOT0$_0$	Momentum of 1st good track
TETHA0$_1$	Polar angle of 2nd good track
M2PI_2pi2g or M2PI_2pi1g1bm	Fitted $\pi^+\pi^-$ mass depending on the fit χ^2 value
ETOT	Total energy in laboratory
COSTHPI	$\cos\theta^*$ with the π hypothesis
PTOT0$_1$	Momentum of 2nd good track

Table 4.1: Selected discriminating variables used in the BDT selection of the uds process. They are sorted in accordance with their relative importance for the $\pi\pi$ mass window between 0.9 and 1.4 GeV/c^2.

As an example of the BDT selected candidates in data without no-uds contribution subtraction is shown in Fig. 4.7 in the accepted χ^2 region. The BDT selection corresponds to the solid vertical line in the bottom left panel shown in Fig. 4.3. For comparison, the uds MC events are also shown in Fig. 4.7 with or without the BDT selection [2]. Similar distributions between data and MC in the accepted χ^2 region are observed. Furthermore, the BDT selection selects more than half of the uds MC sample.

Fits to $\gamma\gamma$ mass distributions are performed in both data and MC assuming a Gaussian shape for the resolved π^0 peak and taking into account the unresolved part of the uds and non-uds contributions from other processes. For the fit of the π^0 peak, a looser BDT selection corresponding to the solid vertical line in the left panels of Fig. 4.3 is used to gain more statistics. For the fits of the unresolved contribution, a more strict BDT selection corresponding to the dashed vertical line in the left panels of Fig. 4.3 is chosen to minimize the non-uds contributions for which its $\gamma\gamma$ mass distribution from simulation may not be truly reliable. Taking the high mass window as an example, the obtained fits are shown in Fig. 4.8. The unresolved part is fitted with an error function named ERF in the uds MC distributions and then the fitted shape is used in the fit to data. The three parameters (area, mass and width) of the Gaussian peak are fitted in all uds MC distributions but in data only with the loose BDT selection where the Gaussian peak is pronounced. For the strict BDT selection, the mass and width parameters in the fit to data are taken from the corresponding fit with the loose BDT selection.

The results of the fitted normalization factors in the three different mass windows for $m_{\gamma\gamma} < 0.3$ GeV/c^2 are shown in Fig. 4.9. The variation of the normalization factors with

[2] It should be mentioned that this uds background study was performed using the 2D-χ^2 selection from the previous analysis before re-optimizing the 2D-χ^2 selection.

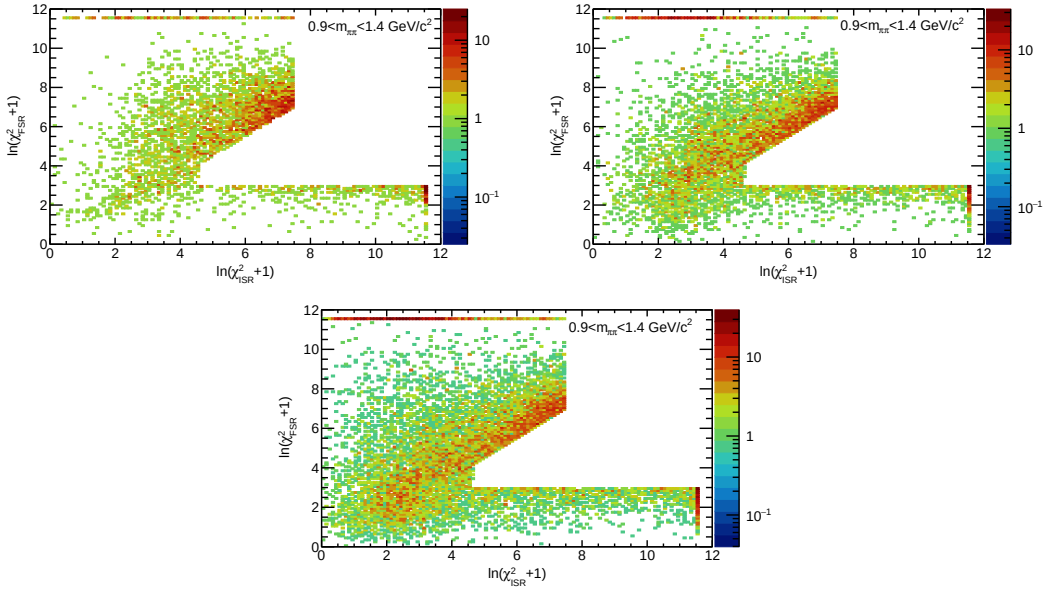

Figure 4.7: Candidate events in data (top left) selected with the BDT selection corresponding to the solid vertical line in the bottom-left panel in Fig. 4.3. Also shown are the uds MC events with (top right) and without (bottom) the BDT selection.

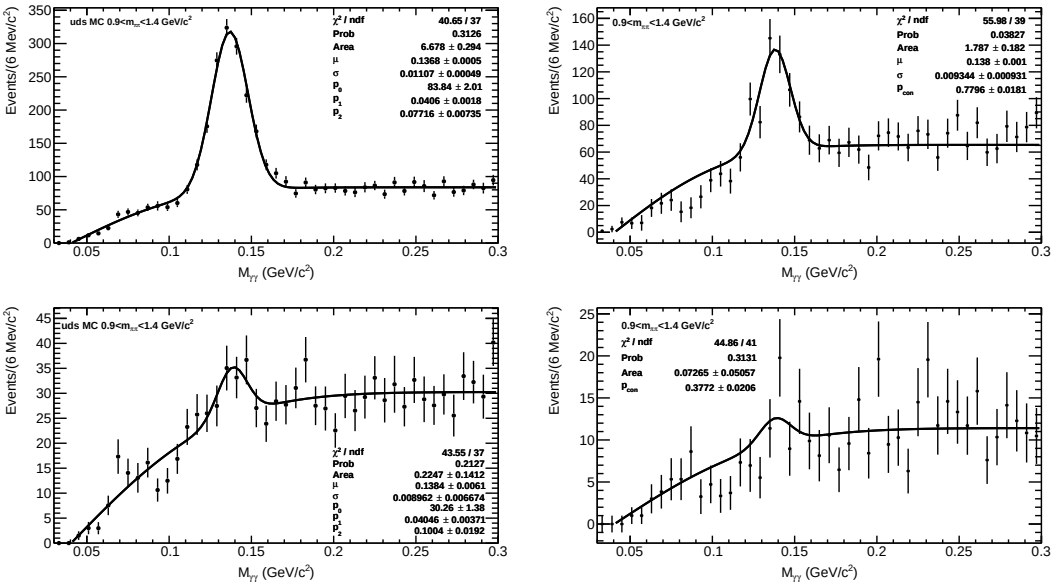

Figure 4.8: Distributions of the $\gamma\gamma$ mass of the uds MC (left) and data after subtracting non-uds contribution (right, the data without background subtraction distribution are shown in Appendix B). The upper plots correspond to fits used to determine the normalization factor of the Gaussian peak (resolved π^0 contribution) while the lower one the normalization factor of the unresolved contribution for $m_{\gamma\gamma} < 0.3$ GeV/c^2. The fits are performed with log likelihood option.

the $\pi\pi$ mass windows is small and remains within the statistical uncertainties. The BDT selections are varied in order to check the impact of the non-uds subtraction and the dependence of the determined normalization factors on the BDT selection is shown in Fig. 4.10. The normalization factors for the resolved π^0 peak sample are fairly independent of the BDT selection, while the other two cases indeed show a weak dependence in particular for looser BDT selections for which the non-uds contributions are still important. The nominal BDT selection is shown in red full dot. The nominal choice is made on the goodness of the fits as well as to gain statistics for the resolved π^0 sample and to minimize non-uds contributions for the unresolved sample. No significant variation is observed in the normalization factors around the nominal BDT selection, suggesting that the systematic uncertainty related to non-uds subtraction can be neglected in comparison to the statistical precision. However, there is clear evidence indicating that the normalization factors for the resolved π^0 contribution are systematically smaller than those of the unresolved contribution.

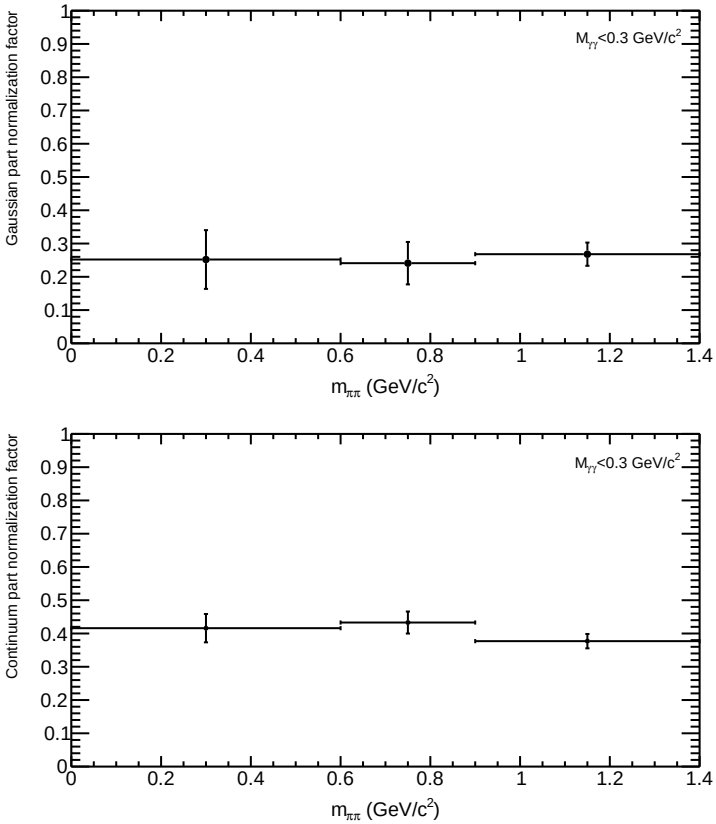

Figure 4.9: Normalization factors of the π^0 (top) and unresolved (bottom) uds versus $\pi\pi$ mass for $m_{\gamma\gamma} < 0.3$ GeV/c^2.

Similar BDTs are utilized to select uds events in each of the three $\pi\pi$ mass windows for $m_{\gamma\gamma} > 0.3$ GeV/c^2. The ratio of the selected uds MC events over those in data with subtracting non-uds contributions using the BDT selection corresponding to the vertical line in the right panels of Fig. 4.3 is presented as a function of $m_{\gamma\gamma}$ in Fig. 4.11 in the three mass windows. In the low and intermediate mass windows where the selected uds event samples

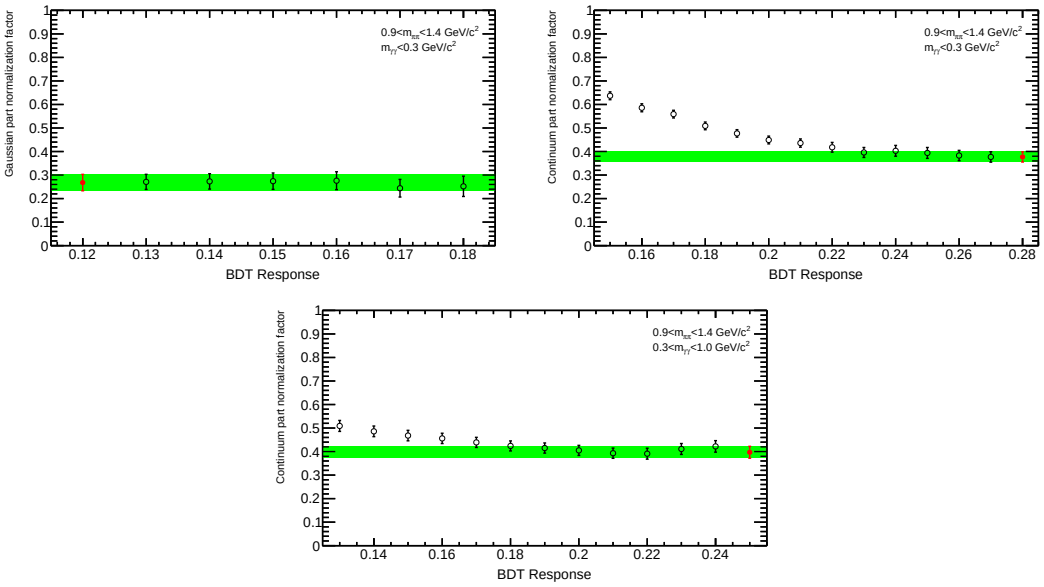

Figure 4.10: Dependence of the determined normalization factors on the BDT selection for resolved π^0 sample (top left), unresolved one at low (top right) and high (bottom) $\gamma\gamma$ mass ranges. The nominal BDT selection corresponds to the red full point. The green error band represents the uncertainty of the normalization factor using the nominal BDT selection.

are relatively small, no significant dependence on $m_{\gamma\gamma}$ is observed while in the high mass window, a clear mass dependence is observed. To investigate whether the mass dependence is due to the non-uds subtraction, we have checked the level of the subtracted non-uds contributions and made the relevant $m_{\gamma\gamma}$ dependence, as shown in Fig. 4.12. The level of non-uds contributions decrease with the $\pi\pi$ mass. The non-uds contributions also show different dependence on the $m_{\gamma\gamma}$. Regarding the high $\pi\pi$ mass window, the non-uds contribution, which accounts for only 10% and is $m_{\gamma\gamma}$-independent, does not explain the observed mass dependence of the normalization factor. In all the cases, the normalization factors are consistent with those of the unresolved contribution at $m_{\gamma\gamma} < 0.3$ GeV/c^2. In terms of the low $m_{\gamma\gamma}$ range, variations in the BDT selection were explored, but no significant systematic effect is observed.

The final numerical results of the normalization factors are summarized in Table 4.2. They are applied for the uds background in the analysis on top of the luminosity scale factor of 0.5919. [3]

4.2.2 Multihadronic ISR processes

The background is estimated by using simulated proecesses $e^+e^- \to X_{\gamma_{\rm ISR}}$ where X represents the final states: $\pi^+\pi^-\pi^0$, $2\pi^+2\pi^-$, $\pi^+\pi^-2\pi^0$, $\eta\pi^+\pi^-$ and K_SK_L, etc. The mass

[3] From Figure 4.2, a small fraction of events at $m_{\gamma\gamma} = 0$ is observed. This fraction corresponds to 1.2%, 1.8% and 3.7% of the uds MC sample in the low, intermediate and high $\pi\pi$ mass windows, respectively. It is assumed that the normalization factor of the unresolved sample at $m_{\gamma\gamma} < 0.3$ GeV/c^2 can be applied to these events.

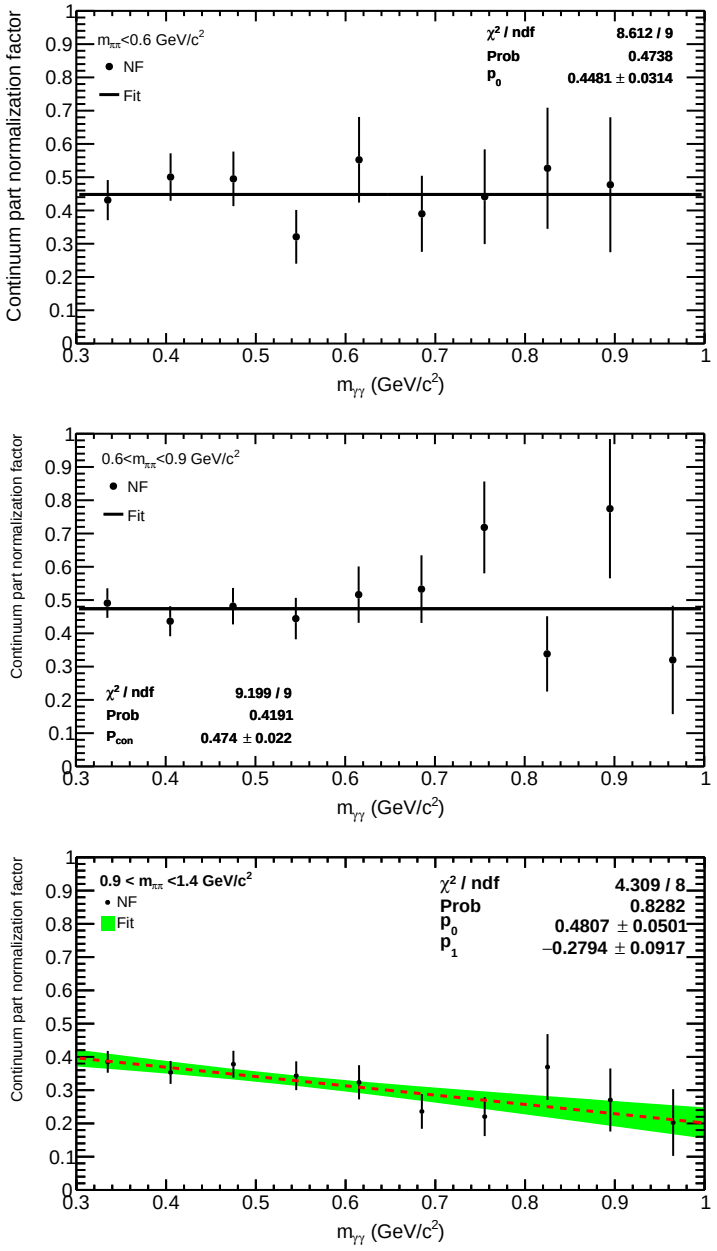

Figure 4.11: Fitted normalization factors of the unresolved uds component as a function of $m_{\gamma\gamma} > 0.3$ GeV/c^2, in the low (upper), intermediate (middle) and high (lower) $\pi\pi$ mass windows. The fits are performed with χ^2 option.

$m_{\pi\pi}$	π^0 $(0.105 < m_{\gamma\gamma} < 0.170$ GeV/$c^2)$ Zernike20 > 0.85	Unresolved	
		$m_{\gamma\gamma} < 0.3$ GeV/c^2	$m_{\gamma\gamma} > 0.3$ GeV/c^2
< 0.6 GeV/c^2	0.252 ± 0.088	0.412 ± 0.043	0.448 ± 0.031
$0.6 - 0.9$ GeV/c^2	0.241 ± 0.064	0.433 ± 0.033	0.474 ± 0.022
$0.9 - 1.4$ GeV/c^2	0.271 ± 0.032	0.377 ± 0.022	$0.481(50) - 0.279(92) \times m_{\gamma\gamma}$ $\rho = -0.952$

Table 4.2: Normalization factors for the uds background in the three $\pi\pi$ mass windows (1st column) for the resolved π^0 contribution (2nd column, the indicated $\gamma\gamma$ mass range corresponds to about ± 3 sigma around the fitted π^0 mass value), the unresolved one at low (3rd column) and high (4th column) $m_{\gamma\gamma}$ ranges. These normalization factors are combined with the luminosity scale factor of 0.5919 for the uds MC sample.

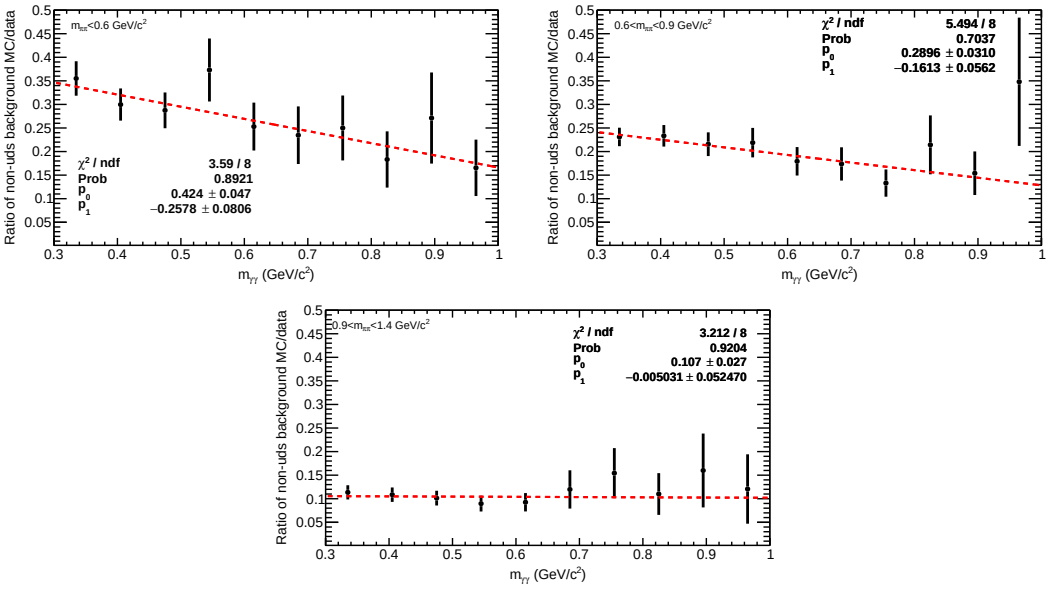

Figure 4.12: Ratio of non-uds contributions over the uds candidates in data selected with the BDT selection corresponding to the vertical line in the right panels in Figure 4.3 as a function of $m_{\gamma\gamma}$ in the low (top left), intermediate (top right) and high (bottom) $\pi\pi$ mass windows.

spectra of these processes have been scaled to the measured cross section based on the combination method implemented in HVPTools [53]. They sum to about 10% at the lower edge of the ρ peak but are strongly suppressed by the 2D χ^2 selection. The dominant contribution for $m_{\pi\pi}$ up to 0.9 GeV/c^2 is from the first process (referred to as 3π for simplicity in the following).

A similar BDT approach, like the one used in the uds background study, is employed to determine the normalization factors of the 3π MC samples in two $m_{\pi\pi}$ regions: low mass (below 0.6 GeV/c^2) and intermediate mass (between 0.6 and 0.9 GeV/c^2). 3π MC process is dominated by the production of ω and ϕ resonances.

Each of the two $m_{\pi\pi}$ mass windows mentioned above is further divided into two cases, one with at least two reconstructed non-ISR photons ($n_\gamma > 2$) and the other with only one reconstructed non-ISR photon ($n_\gamma = 2$). [4] They make up about 72% and 25% of the 3π samples, respectively. The remaining 3% has no photon from the π^0 reconstructed with an energy above 50 MeV within the detector acceptance.

For the case of $n_\gamma > 2$, twelve input variables are used in BDT to separate the 3π background from other processes. More details on the twelve variables and their importance and correlation are described in Appendix C. Three variables, concerning the fit to two charged pions and one ISR photon and two additional large-angle photons, and the invariant mass and energy sum of the two non-ISR photons, are not used for the case $n_\gamma = 2$. This explains the different separation power between the two cases presented in Fig. 4.13.

For a given BDT selection, the distribution of the 3π mass $m_{3\pi}$ [5] is utilized to determine the normalization factor of the 3π process within the mass region of $0.7-1.1$ GeV/c^2 covering the ω and ϕ resonances. The distributions for BDT larger than 0.3 are demonstrated in Fig. 4.14. The corresponding normalization factor is obtained with the total event yields of data with background subtraction over the event yields of the 3π MC samples in the above mass region. The shape comparison between data and MC is quantified with the χ^2 value integrated over 40 bins taking into account the statistical uncertainties of both data and MC samples. The nominal BDT choice is determined as the selection with the best χ^2 value over a scan of the BDT selection around the nominal value. The nominal normalization factor is also compared to the BDT selection with the second best χ^2 value next to the nominal one and any inconsistency between the two normalization factors after taking into account the correlation between the selected samples is treated as a systematic uncertainty. The resulting normalization factor with its uncertainty is presented in Fig. 4.15 and Table 4.3. All the normalization factors are consistent within the quoted uncertainties. For the most important case of $m_{\pi\pi} < 0.6$ GeV/c^2 and $n_\gamma > 2$, we have achieved a precision of 1.5%. The results for $n_\gamma = 2$ are applied to the tiny fraction of events with $n_\gamma = 1$ and the results for $0.6 < m_{\pi\pi} < 0.9$ GeV/c^2 are applied to the 3π MC at higher mass, the contribution of which also becomes small.

[4] n_γ includes the ISR photon.

[5] For $n_\gamma = 2$, either the π^0 is unresolved or the second photon from the decay is not reconstructed. In both cases, the 3π mass is computed assuming the non-ISR photon to have the π^0 mass.

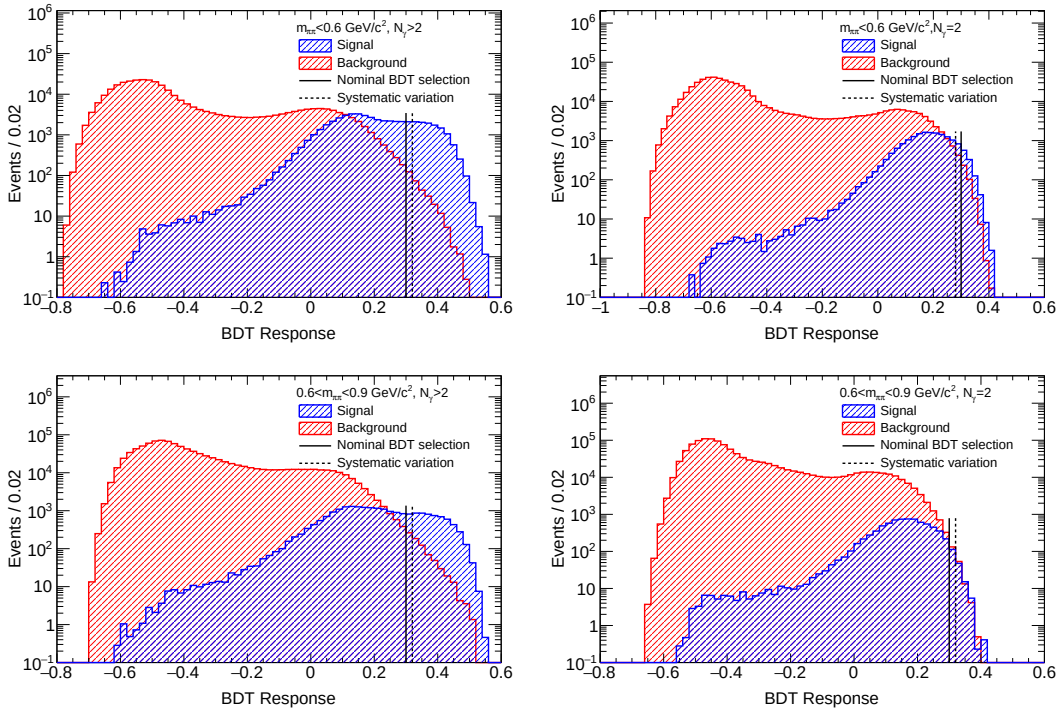

Figure 4.13: BDT response for $m_{\pi\pi} < 0.6$ GeV/c^2 (top) and $0.6 < m_{\pi\pi} < 0.9$ GeV/c^2 (bottom), and $n_\gamma > 2$ (left) and $n_\gamma = 2$ (right). The red and blue histograms correspond to absolute 3π and non-3π event yields, respectively. The solid vertical line represents the nominal BDT selection used to determine the normalization factor, while the dashed line for the systematic variation.

	$m_{\pi\pi} < 0.6$ GeV/c^2	$0.6 < m_{\pi\pi} < 0.9$ GeV/c^2
$n_\gamma = 2$	1.009 ± 0.037	1.097 ± 0.118
$n_\gamma > 2$	$1.003 \pm 0.010 \pm 0.011$	$1.013 \pm 0.021 \pm 0.014$

Table 4.3: Normalization factors for the 3π MC processes in the two $\pi\pi$ mass windows (second and third columns) and for $n_\gamma > 2$ (third row) and $n_\gamma = 2$ (second row). The first uncertainty is statistical and the second (if shown) is systematic.

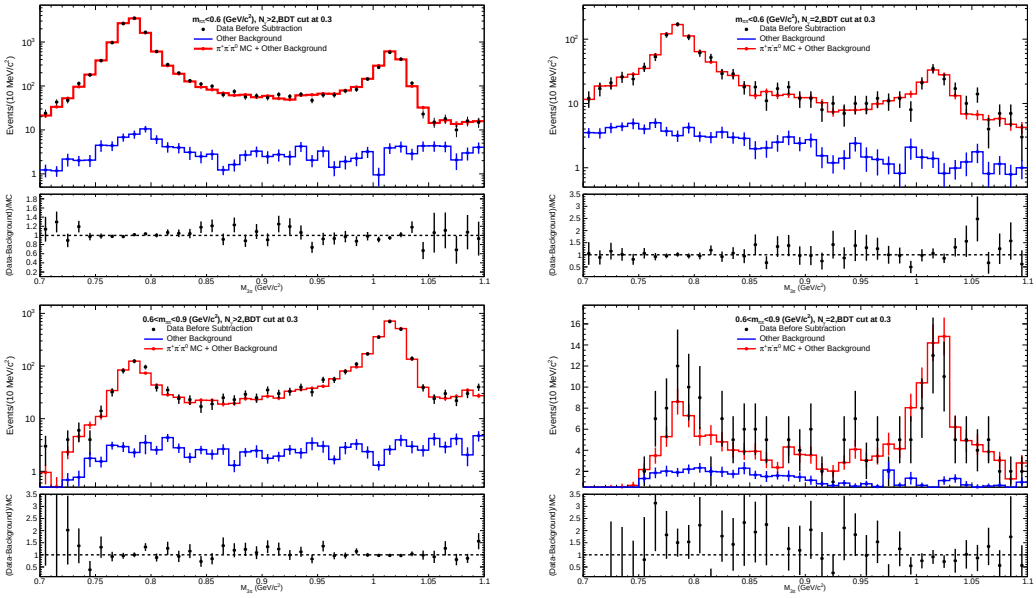

Figure 4.14: Distributions of 3π mass presented in the upper panel for data (black dots), non-3π background contribution (blue histogram) and the sum of 3π MC and non-3π processes (red histogram) for $m_{\pi\pi} < 0.6$ GeV/c^2 and $n_\gamma > 2$ (top left), $m_{\pi\pi} < 0.6$ GeV/c^2 and $n_\gamma = 2$ (top right), $0.6 < m_{\pi\pi} < 0.9$ GeV/c^2 and $n_\gamma > 2$ (bottom left), $0.6 < m_{\pi\pi} < 0.9$ GeV/c^2 and $n_\gamma = 2$ (bottom right), with the ratio of data after subtracting the non-3π background over the 3π MC sample in the corresponding lower panels.

4.2.3 Background from $\tau\tau$ process

The $\tau\tau$ background process is found to be small in the accepted 2D-χ^2 region [6]. However, it dominates in the rejected 2D-χ^2 region by far. In the corner region of the 2D-χ^2 plane where both χ^2 values are in overflow, approximately 28% of the rejected $\tau\tau\gamma$ sample is selected within the mass range between threshold and 1.4 GeV/c^2 after applying strict muon identification to the two good tracks. This specific corner region is used to verify the normalization factor of the $\tau\tau\gamma$ sample. According to the prediction based on the considered processes, the only additional process that contributes to the above selected region is the $\mu\mu\gamma$ process, primarily at the high-energy tail of the measured total energy (Etot) distribution, shown in Fig. 4.16. To obtain a highly pure $\tau\tau\gamma$ event sample, an Etot < 9.0 GeV requirement is imposed due to the unmeasured missing energy in these events. The integrated data and MC event yields give a ratio of data/MC as 1.12 ± 0.04. Given that the $\tau\tau\gamma$ MC process is well modeled, it is proposed to keep the normalization of the process unchanged but to quote a systematic uncertainty of 12% for the $\tau\tau\gamma$ background subtraction.

[6] The 2D-χ^2 selection from the previous analysis as for the uds background.

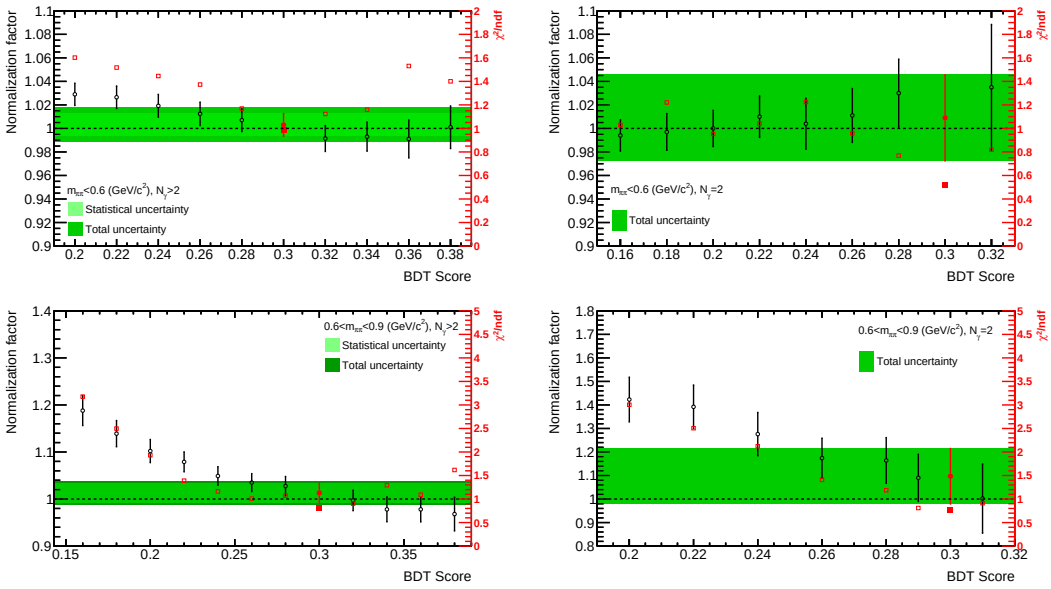

Figure 4.15: Normalization factors are shown with the left y-axis scale as a function of BDT selection values for $m_{\pi\pi} < 0.6$ GeV/c^2 and $n_\gamma > 2$ (top left), $m_{\pi\pi} < 0.6$ GeV/c^2 and $n_\gamma = 2$ (top right), $0.6 < m_{\pi\pi} < 0.9$ GeV/c^2 and $n_\gamma > 2$ (bottom left), and $0.6 < m_{\pi\pi} < 0.9$ GeV/c^2 and $n_\gamma = 2$ (bottom right). For the right y-axis scales, the χ^2 over the number of degrees of freedom (ndf) are shown. The outer horizontal error band shows the total uncertainty of the nominal normalization factor and the inner one (if any) represents the statistical component of the uncertainty.

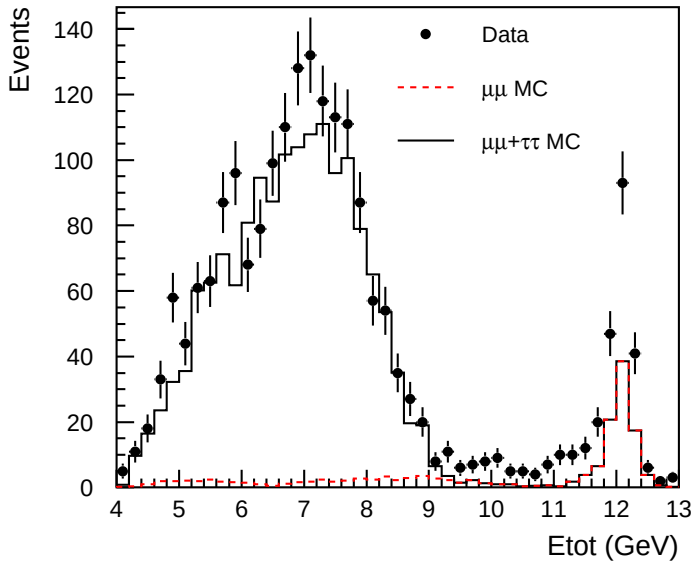

Figure 4.16: Distributions of the total measured energy in the 2D-χ^2 corner region where both χ^2 values are in overflow, which means that both the ISR and FSR fits have failed.

4.3 χ^2 cut efficiency study

4.3.1 Optimization of 2D-χ^2 selection

Multibody background populates the region where both χ^2 values are large and consequently a background region is defined in the 2D-χ^2 plane, which assures the efficiency of the signal and rejection of the background. The BDT method is performed in three separate mass windows, low ($< 0.6\,\mathrm{GeV}/c^2$), intermediate (0.6 - 0.9 GeV/c^2) and high (0.9 - 1.4 GeV/c^2), using the two variables χ^2_{SA} (also notated as χ^2_{ISR}) and χ^2_{LA} (also notated as χ^2_{FSR}), treating the $\pi\pi(\gamma)$, $\mu\mu(\gamma)$ and $KK(\gamma)$ processes as signal and all the other processes as background. The shape comparison of these two variables in different mass windows is shown in Fig. 4.17 using the PHOKHARA MC samples for signal, and background MC samples using AFKQED for ISR processes, KORALB for $\tau\tau\gamma$ and JETSET for $q\bar{q}$ (u, d, s).

The signal significance over background (SOB) ratio is defined as $S/\sqrt{S+B}$, with S and B being the integrated signal and background event yields to the right of a given SOB selection in the BDT response distribution. The results of the optimization are shown in Fig. 4.18 for the three mass windows, where the dashed vertical line corresponds to the best choice that maximizes the SOB value respectively.

The 2D contours of the signal MC samples selected with the best SOB selection in the three mass windows are depicted in Fig. 4.19 (a slightly different version of 2D-χ^2 selection, which is used to study uds and 3π background, is presented in Appendix D for comparison). In practice simple cut-based selections (corresponding to red lines) chosen to be close to the contours of the best SOB value of the BDT selection are used. The signal selection efficiency (Eff), background contamination (Con) and the SOB values between the BDT optimization and the cut-based selection are compared in Table 4.4. In all cases, the cut-based values closely match the optimized values from the BDT selection, with the high efficiency value larger than 98.5% and small background contamination below 2.0%.

	$m_{\pi\pi} < 0.6$ GeV/c^2	$0.6 < m_{\pi\pi} < 0.9$ GeV/c^2	$0.9 < m_{\pi\pi} < 1.4$ GeV/c^2
Eff (cut)	97.7%	98.8%	98.7%
Eff (BDT)	97.5%	98.8%	98.7%
Con (cut)	2.1%	1.3%	1.8%
Con (BDT)	2.0%	1.3%	1.8%
SOB (cut)	1436.0	1973.8	1123.5
SOB (BDT)	1436.0	1973.8	1123.4

Table 4.4: Comparison for signal ($\mu\mu\gamma$ + $\pi\pi\gamma$ + $KK\gamma$) selection efficiency, background contamination and best SOB values between the cut-based selection and the BDT optimization.

The optimized 2D-χ^2 selection is applied to the $\pi\pi\gamma_{\mathrm{ISR}}$ and $\mu\mu\gamma_{\mathrm{ISR}}$ samples after PID selection. Known backgrounds are subtracted from data, 3.9% of the $\pi\pi\gamma(\gamma)$ and 0.25% of the $\mu\mu\gamma(\gamma)$ selected samples respectively, dominated by the $\mu \to \pi$ and $\pi \to \mu$ misidentification. The 2D-χ^2 efficiency of the candidates that satisfy the NLO $\gamma_{\mathrm{ISR}}\gamma_{\mathrm{SA}}$ or the $\gamma_{\mathrm{ISR}}\gamma_{\mathrm{LA}}$ selection is shown in Table 4.5 for PHOKHARA and AFKQED MC events. The table also includes the 2D-χ^2 efficiency for the LO events when the energy of the additional photon

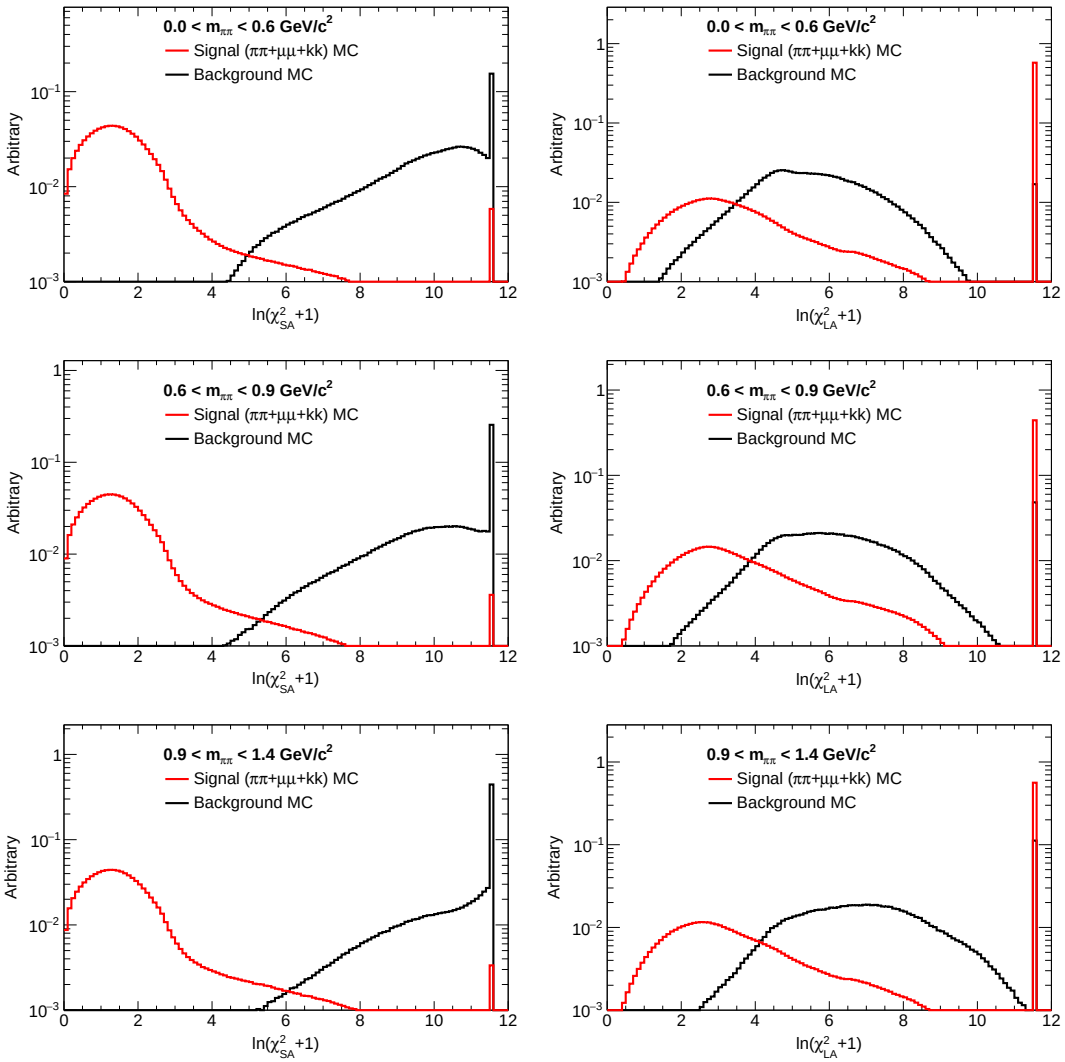

Figure 4.17: Shape comparison of χ^2_{SA} (left) and χ^2_{LA} (right) for low mass window (top), intermediate mass window (middle) and high mass window (bottom).

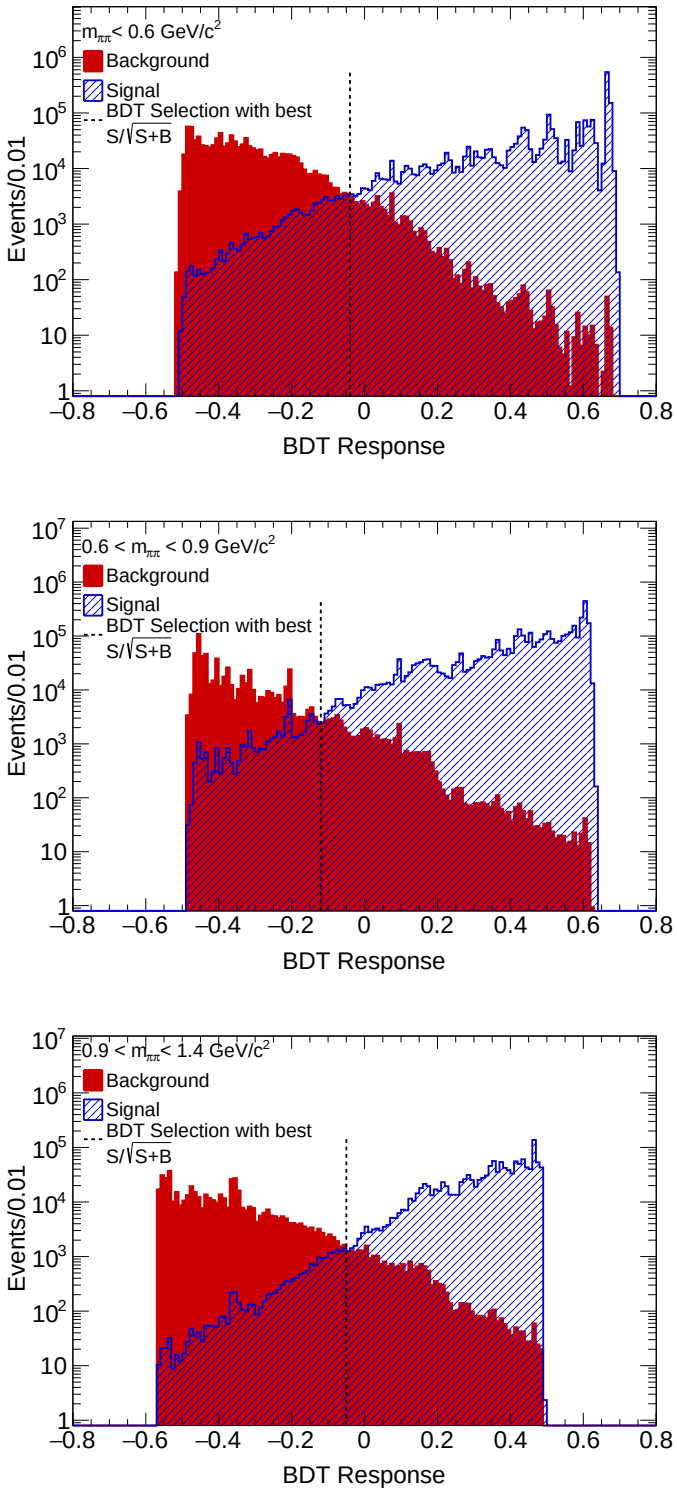

Figure 4.18: The BDT responses for the low (top), intermediate (middle) and high (bottom) mass windows. The dashed vertical line corresponds to the choice that maximizes the SOB value.

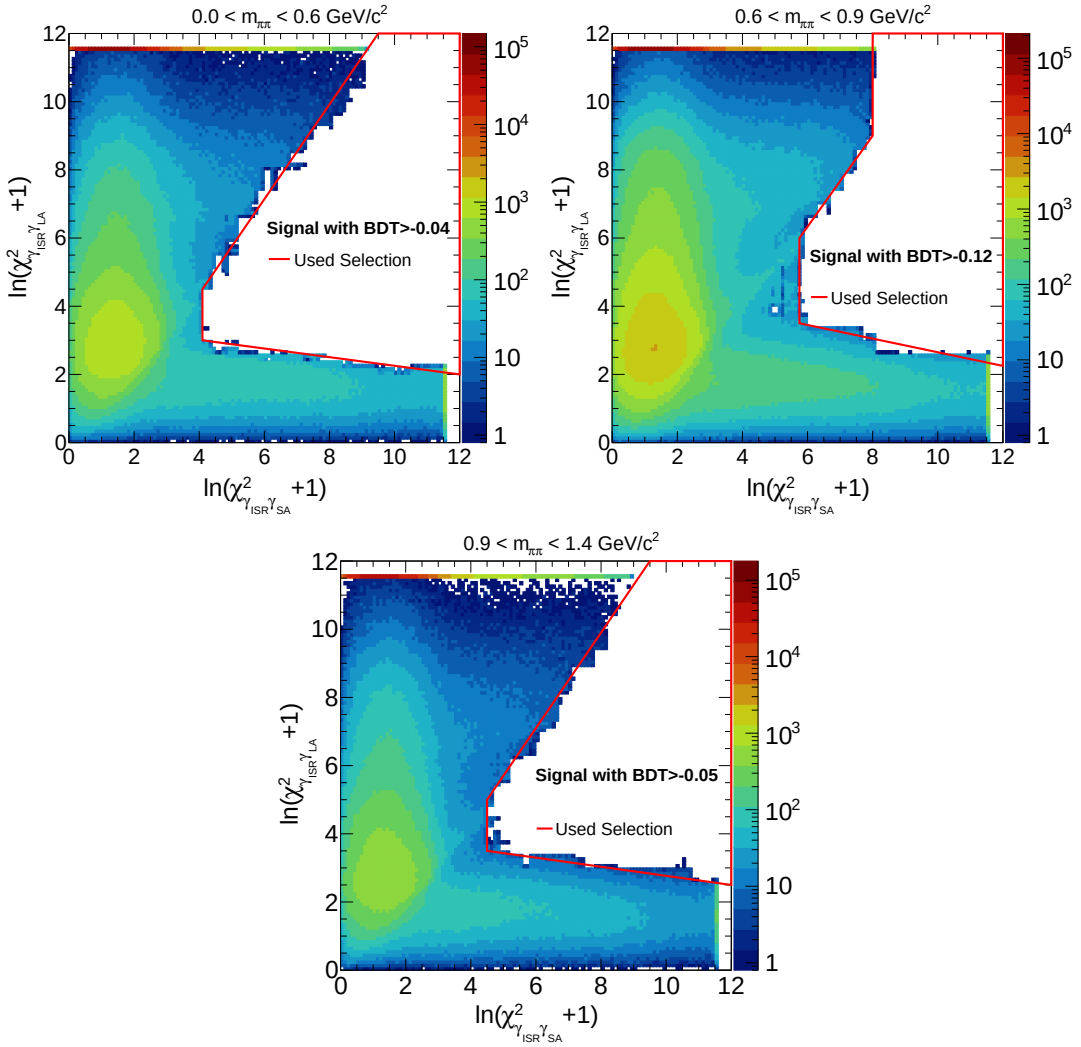

Figure 4.19: The contour of selected signal MC events for the low (top-left), intermediate (top-right) and high (bottom) mass windows corresponding to the best SOB BDT selection in comparison with the final cut-based 2D-χ^2 selection (red solid lines).

is below the threshold. In general, the efficiency of the 2D-χ^2 is high, around or over 99%. The largest impact is on the $\gamma_{\text{ISR}}\gamma_{\text{LA}}$ sample. For the $\gamma_{\text{ISR}}\gamma_{\text{LA}}$ fit, the efficiency difference between the two MC samples AFKQED and PHOKHARA may be due to the fact that the LA ISR photon component is missing in the AFKQED sample. For the $\gamma_{\text{ISR}}\gamma_{\text{SA}}$ fit, the difference is due to the assumption of the collinear emission of the SA ISR photon in the fit and as well in the AFKQED generation. The 2D-χ^2 selection efficiency is measured in data with background subtraction for each fitted category and is also shown in Table 4.5, owing to the low background remaining in the $\mu\mu$ sample after PID requirement. Data to MC differences are observed in the $\mu\mu$ process, particularly for the $\gamma_{\text{ISR}}\gamma_{\text{LA}}$ category, and are taken into account in this thesis. For the $\pi\pi$ process, the efficiency in data cannot be reliably determined due to the huge background in the 2D-χ^2 rejected region, and the data/MC corrections are assumed to be the same as those from the $\mu\mu$ process.

%	LO	$\gamma_{\text{ISR}}\gamma_{\text{SA}}$	$\gamma_{\text{ISR}}\gamma_{\text{LA}}$	LO	$\gamma_{\text{ISR}}\gamma_{\text{SA}}$	$\gamma_{\text{ISR}}\gamma_{\text{LA}}$
	$\mu\mu$ ($m_{\pi\pi} < 1.4\,\text{GeV/c}^2$)			$\pi\pi$ ($0.6 < m_{\pi\pi} < 0.9\,\text{GeV/c}^2$)		
LO	99.978(3) 99.9545(7)			99.986(1) 99.9839(3)		
$\gamma_{\text{ISR}}\gamma_{\text{SA}}$		99.969(8) 98.948(8)			99.971(4) 98.748(5)	
$\gamma_{\text{ISR}}\gamma_{\text{LA}}$			85.9(6) 89.09(4)			85.0(4) 90.44(3)
Overall	99.941(5) 99.905(1) 99.778(7)	99.47(3) 98.731(8) 97.50(4)	72.8(7) 83.85(5) 63.1(2)	99.975(2) 99.9485(5)	99.76(1) 98.368(6)	82.1(4) 84.89(3)

Table 4.5: The impact of the 2D-χ^2 selection in terms of efficiencies (shown in %) calculated using MC samples AFKQED and PHOKHARA (first and second lines in each block, respectively) on true categories (row) versus fitted categories (column), for the $\mu\mu$ (left) and $\pi\pi$ (right) part of the table. The numbers in brackets are statistical uncertainties. The last block 'Overall' corresponds to the global impact for a specific fit category. In the last block, the third row corresponds to the efficiency values of data, shown only for the $\mu\mu$ channel.

4.3.2 Strategy to determine the χ^2 efficiency in data

The background contributions to the $\mu\mu\gamma(\gamma)$ sample are significant only in the background (BG) region of the 2D-χ^2 plane, and they can be handled easily. Thus the determination of the 2D-χ^2 selection efficiency is relatively straightforward in the muon channel. The situation concerning the pion channel presents a significant contrast, as it is not possible to directly measure the efficiency of the 2D-χ^2 selection in data due to the overwhelming background in the rejected region.

The rejected signal events with large χ^2 have several sources: (1) bad input to the kinematic fits, from the ISR photon and the charged tracks; (2) tails of the χ^2 distributions of

events with additional ISR or FSR; (3) more than one additional photon (mainly from ISR); (4) secondary interactions. The first three types are common to pions and muons, and the last type is specific to pions and another difference in their intrinsic $\cos\theta^*$ distributions resulting in different fractions of low momentum tracks and thus different χ^2 selection efficiencies. A minor difference is also expected for the tail of the FSR fit χ^2, as the FSR level is slightly different for pions and muons. Nevertheless, the level of additional FSR is measured in both data and MC and the loss due to FSR can be effectively controlled.

The strategy is to rely on the χ^2 selection studies performed on muon data to address the common loss and then further study the losses specific to pions. Therefore, the χ^2 selection efficiency for pions in data is derived in the following expression:

$$\varepsilon_{\chi^2}^{\pi\pi\gamma(\gamma),\mathrm{data}} = \varepsilon_{\chi^2}^{\mu\mu\gamma(\gamma),\mathrm{data}} + \delta\varepsilon_{\chi^2}^{\pi/\mu}, \tag{4.1}$$

where the π/μ correction term $\delta\varepsilon_{\chi^2}^{\pi/\mu}$ accounts for three effects: (1) the difference in additional FSR level between pions and muons; (2) pion secondary interactions; (3) different $\cos\theta_\pi^*$ distributions. The contributions from the first two components are separated, measured in the simulation, and corrected for data/MC discrepancies. The difference originating from the $\cos\theta_\pi^*$ distributions is derived from appropriately reweighting the MC events.

4.3.3 μ-ID bias induced in the χ^2 efficiency

The efficiency of the 2D-χ^2 selection is measured by the rate of $\mu\mu\gamma$ events in the rejected region. This is achieved by selecting events that have two identified muons by PID.

In the selected regions, the total background contribution is small and amounts to 6×10^{-4}, 7×10^{-3} and 1×10^{-3} in the three mass ranges (as previously defined), respectively. The $\pi\pi\gamma$ background dominates the background process. The situation is very different in the rejected region, where the fraction of the background contribution significantly increases to 8.3%, 21.0% and 27.0%, respectively. In this case, the dominant background is from the $\tau\tau\gamma$ process.

It is important and necessary to check if the requirement of muon identification induces some bias in the determination of the χ^2 efficiency. To evaluate the impact, the $\mu\mu\gamma$ MC samples are employed, with the result shown in Fig. 4.20. In general, it gives a bias of 0.24% with little dependence on mass spectrum except low mass range and larger dependence on $\cos\theta^*$ in particular for values near one. Detailed studies have been performed to explore the sources of the bias and to check the agreement between MC simulation and data. Two primary sources of the bias have been identified: One in the diagonal region in the 2D-χ^2 plane (taking low mass window as an example in Fig. 4.21) with the higher momentum track 1 failing μ-ID due to the overlap with the other track in the EMC; the other is attributed to the lower momentum track 2 failing due to its poorer μ-ID capability. This is shown in Fig. 4.22 in the low mass window. The defined variable $\mathrm{cly} = (\ln(\chi^2_{\mathrm{FSR}}+1) - \ln(\chi^2_{\mathrm{ISR}}+1))/\sqrt{2}$ is used to visualize the diagonal region easily.

For the first case, due to the overlap, the energy associated to track 1 is no longer MIP-like ($0.01 < E_{\mathrm{cal}} < 0.3$ GeV) but larger. A diagonal region is thus defined by requiring $\ln(\chi^2_{\mathrm{ISR}}+1) > 3.5$, 4.0 or 4.5, respectively for the three mass windows, with $\left|\ln(\chi^2_{\mathrm{ISR}}+1) - \ln(\chi^2_{\mathrm{FSR}}+1)\right| < 0.5$. In the defined diagonal region, a sample is further

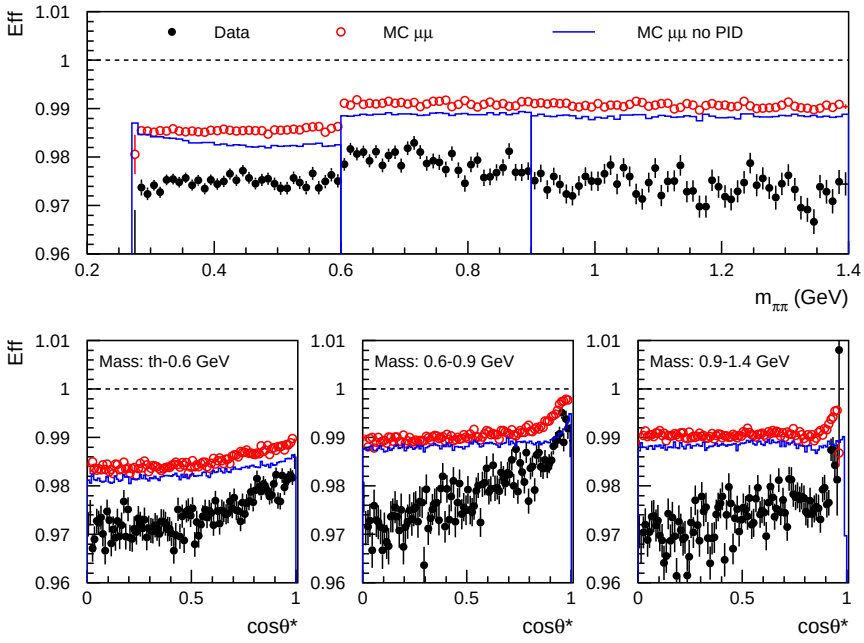

Figure 4.20: The χ^2 efficiency for $\mu\mu\gamma(\gamma)$ data with background subtraction, $\mu\mu\gamma(\gamma)$ MC samples with and without muon ID as functions of $\mathrm{m}_{\pi\pi}$ (top) and $|\cos\theta^*_\pi|$ (bottom) in three mass regions.

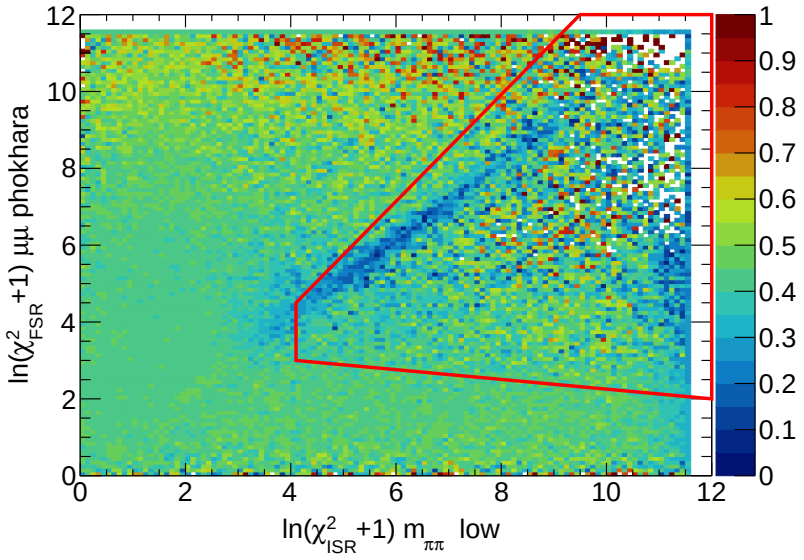

Figure 4.21: The μ-ID efficiency in the 2D-χ^2 plane with $\mathrm{m}_{\pi\pi} < 0.6$ GeV/c^2.

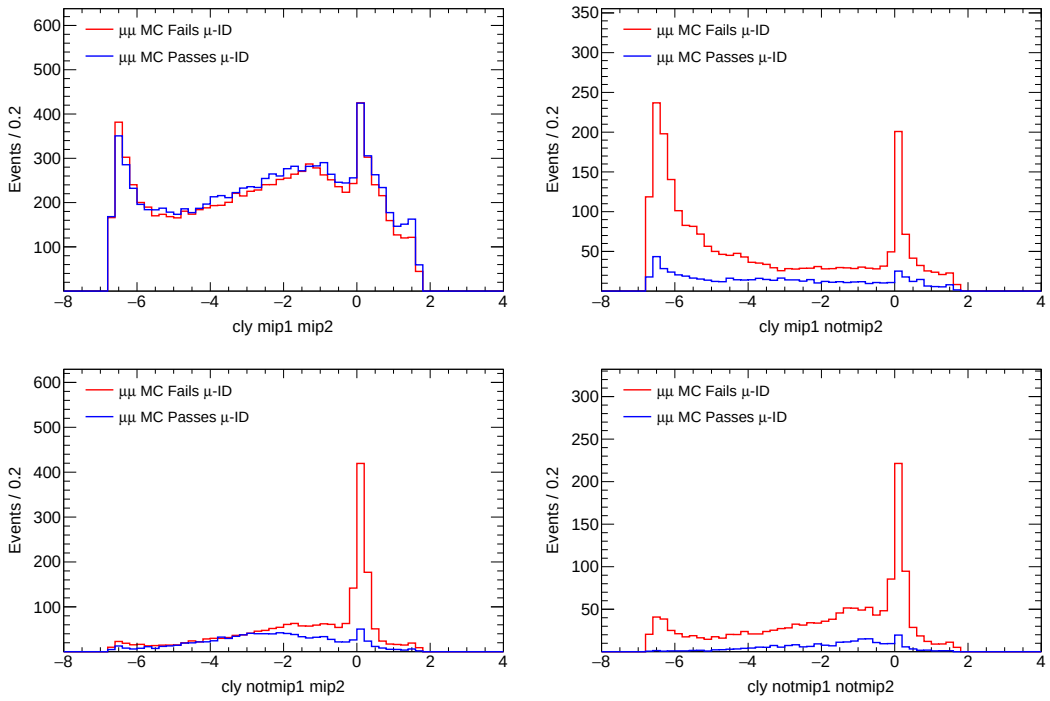

Figure 4.22: Distributions of cly $= (\ln(\chi^2_{\mathrm{FSR}}+1) - \ln(\chi^2_{\mathrm{ISR}}+1))/\sqrt{2}$ in the 2D-χ^2 rejected region for the low mass range. Four cases are taken into account: both tracks are MIP-like (top left); One track is MIP-like while the other is not (top right and bottom left); both tracks are not MIP-like (bottom right). The distributions are normalized to ensure the same number of events in the full 2D-χ^2 plane for both tracks passing the μ-ID and at least one track failing the μ-ID.

selected by requiring that, for each given event, track 2 must satisfy the very tight μ-ID, and track 1 should have an associated $E_{\rm cal}$ energy deposit which is not MIP-like (in the range between 0.3 GeV and 1.0 GeV) and the number of IFR layer hits more than six, failing the tight μ-ID. The IFR requirement is employed to suppress the $\pi\pi$ background. Figure 4.23 shows the IFR layers distribution for the low mass range. The corresponding $E_{\rm cal}$ distribution with the IFR selection and the background subtraction is presented in Fig. 4.24. The data with background subtraction and MC event yields are 249.7 ± 16.5 and 222.6 ± 5.5, respectively. The resulting data/MC ratio is 1.12 ± 0.08. The quoted uncertainties are statistical. For the intermediate mass region, the IFR selection requirement is increased from six hits to seven hits, resulting data/MC ratio of 1.15 ± 0.10. For high mass region, the IFR selection is increased to eight hits, resulting data/MC ratio of 1.05 ± 0.10.

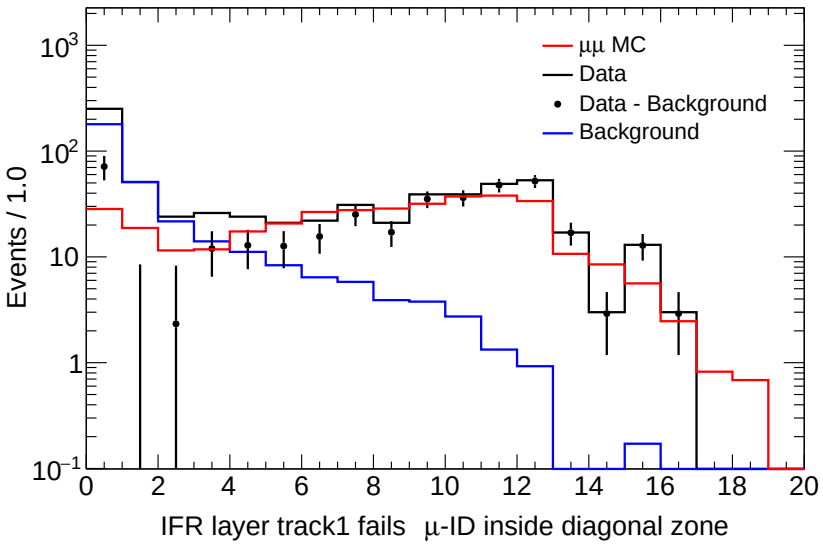

Figure 4.23: Distributions of the number of IFR layer hits for sample selected in the diagonal region in the low mass region, with track 2 satisfying the very tight μ-ID, and track 1 failing the tight μ-ID with $E_{\rm cal}$ energies in the range from 0.3 to 1.0 GeV.

For the second case, track 2 fails the tight μ-ID requirement because its momentum is so low that the track cannot reach the calorimeter and the associated $E_{\rm cal}$ energy is null. The sample is selected in the 2D-χ^2 rejected region with track 1 satisfying the tight μ-ID and the track 2 associated $E_{\rm cal}$ energy being 0. These selected events have very large ISR fit χ^2 value and rather small FSR fit χ^2 value but close to the 2D-χ^2 boundary. The cly distribution for the low mass region is presented in Fig. 4.25. In the negative tail of the distribution, where the estimated background contribution is not large, the data after background subtraction behaves as the expected distribution of the $\mu\mu\gamma$ MC sample. The integrated event yield in the last five bins are 365.2 ± 20.5 for data signal and 461.6 ± 9.0 for MC sample, which results in a data/MC ratio of 0.79 ± 0.05. The quoted uncertainties here are only statistical. Similar procedures are performed for the other two mass regions and the corresponding ratios are 0.83 ± 0.10 for the intermediate mass region and 1.13 ± 0.23 for the high mass region.

In summary, a total bias of 0.24% is observed on the 2D-χ^2 efficiency due to the μ-ID

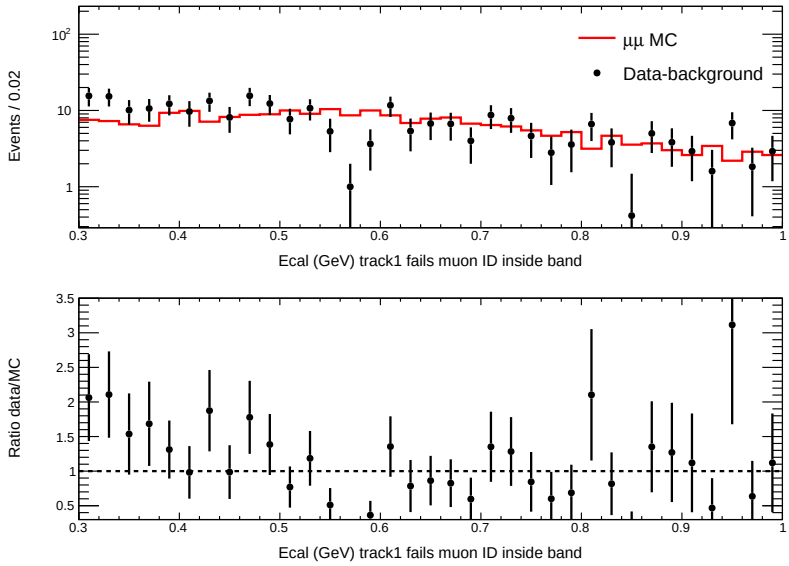

Figure 4.24: Distributions of Ecal energies in the range from 0.3 to 1.0 GeV for events selected in the diagonal region in the low mass region, with track 2 satisfying the very tight μ-ID, and track 1 with the IFR selection and background subtraction while failing the tight μ-ID.

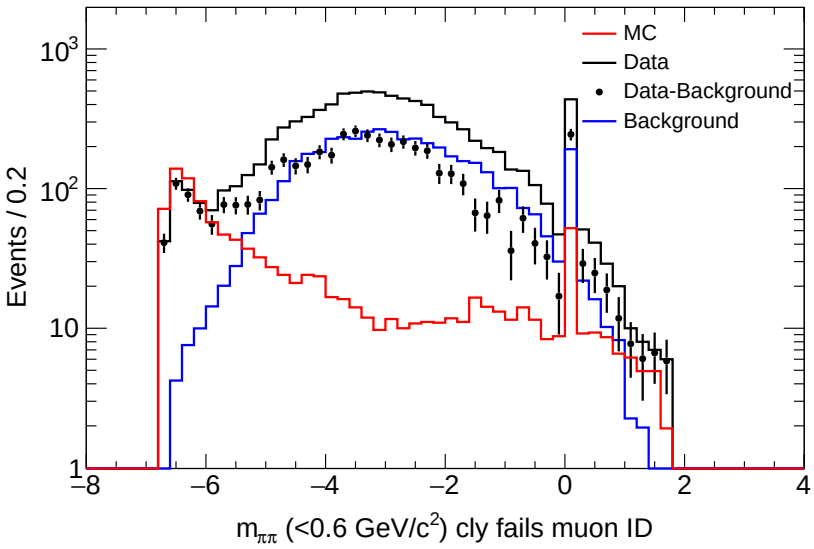

Figure 4.25: Distributions of cly $= (\ln(\chi^2_{\rm FSR}+1) - \ln(\chi^2_{\rm ISR}+1))/\sqrt{2}$ in the 2D-χ^2 rejected region for the low mass range failing μ-ID, where track 1 satisfying the tight μ-ID and the associated $E_{\rm cal}$ energy to track 2 is null.

requirement based on the MC sample, and data/MC consistency has been investigated in three mass regions. Based on the studies above, no correction to the MC-predicted bias is applied but a systematic uncertainty of 25% is quoted conservatively, covering the comparison with data for the two sources of bias. The systematic uncertainty associated with the muon χ^2 selection efficiency is determined to be 0.06%.

Some additional study of χ^2 selection efficiency related to the correction term $\delta\varepsilon_{\chi^2}^{\pi/\mu}$ in Eq. (4.1) is presented in Appendix F, which is important and essential to the ongoing final cross section measurement analysis.

Chapter 5

NLO radiation analysis

5.1 Testing the hypothesis of collinear additional ISR photons

The two NLO fits have already been described in Section 4.1. The ISR NLO $\gamma_{\rm ISR}\gamma_{\rm SA}$ fit assumes the additional photon to be collinear with the e^+ or e^- beam. However, in reality, the ISR radiation is expected to exhibit a sharply peaked distribution, but with a long tail that extends to larger angles. This feature of ISR radiation is observed in the samples generated with PHOKHARA event generator. By comparing the parameters of the fitted additional photon to the true values, one can check the validity of the collinear approximation. The degradation of the χ^2 of the $\gamma_{\rm ISR}\gamma_{\rm SA}$ fit, which arises from the angular mismatch between the fitted and generated photons, is illustrated in Fig. 5.1. As expected, the effect is more pronounced for additional photons which are more energetic. Obviously, the most affected angular range, where the degradation of χ^2 distribution is more pronounced, corresponds to the detector acceptance range (0.3−2.45 rad). Within this range, the additional photon is detected and the $\gamma_{\rm ISR}\gamma_{\rm LA}$ fit takes over, and only the small fraction of events with an undetected large-angle photon relies on the $\gamma_{\rm ISR}\gamma_{\rm SA}$ fit.

Another consequence of the collinear assumption is introducing a bias in the fitted additional ISR photon energy. The fitted energy in the $\gamma_{\rm ISR}\gamma_{\rm SA}$ fit tends to be systematically lower than the true generated value. Additionally, in the $\gamma_{\rm ISR}\gamma_{\rm SA}$ fit, as the fitted energy is left completely free and thus a resolution tail is observed at negative values. The magnitude of the energy shift and the extent of the resolution tail depend on the true angle of emission of the additional photon. As the true angle deviates further from the beams and the energy of the additional photon increases, the shift becomes more pronounced. The energy shift should be well simulated since it has a purely kinematic origin, which can be directly checked by comparing the corresponding outputs of the $\gamma_{\rm ISR}\gamma_{\rm SA}$ and $\gamma_{\rm ISR}\gamma_{\rm LA}$ fits in the detector angular range with the detected photon treated as 'true' photon. To ensure a reliable reconstruction in the fit $\chi^2_{\gamma_{\rm ISR}\gamma_{\rm LA}} < \chi^2_{\gamma_{\rm ISR}\gamma_{\rm SA}}$ is required. The comparison for the $\mu\mu\gamma(\gamma)$ sample is presented in Fig. 5.2. Since the test involves only fitted quantities, it can be readily applied to data, using μ-ID for both good tracks to mitigate background at a negligible level in the selected 2D-χ^2 region. Figure 5.3 provides evidence of good agreement between data and MC simulation regarding the fitting bias, where the ratio of the fitted $E^*_{\gamma_{\rm SA}}$ over $E^*_{\gamma_{\rm LA}}$ distributions and the

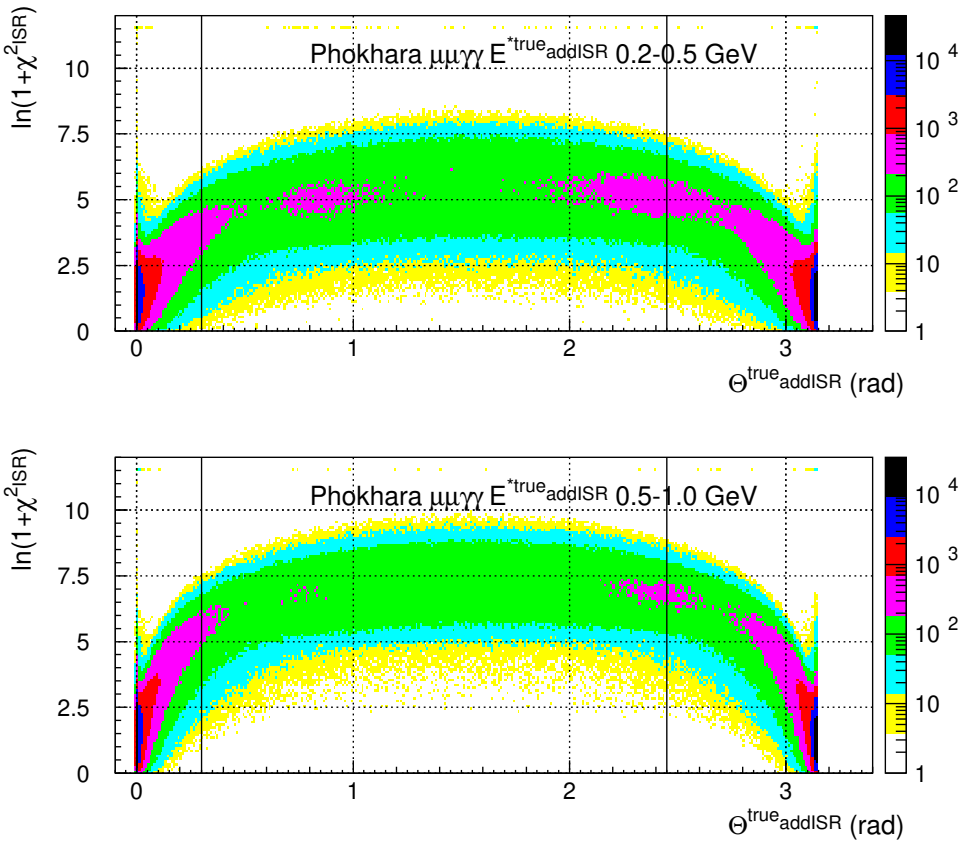

Figure 5.1: The χ^2 of the $\gamma_{\mathrm{ISR}}\gamma_{\mathrm{SA}}$ fit in the PHOKHARA $\mu\mu\gamma\gamma$ sample as a function of the true angle of the additional ISR (addISR) photon for two energy ranges, $0.2-0.5$ GeV (top) and $0.5-1.0$ GeV (bottom). The degradation of the χ^2 distribution arises as a consequence of the mismatch between the addISR photon angular distribution and the assumed collinearity with the beams in the fit hypothesis. The edges of the detector range are indicated at 0.3 and 2.45 rad.

double ratio of data/MC are demonstrated.

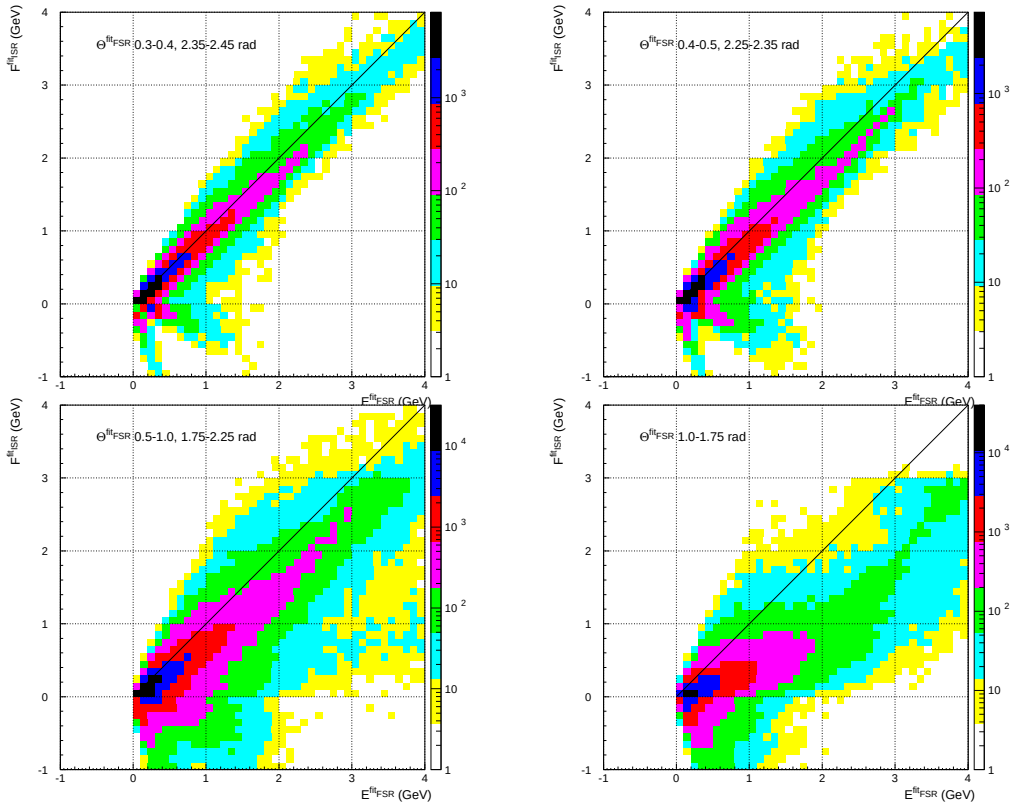

Figure 5.2: The fitted energies of the additional photons from the $\gamma_{\mathrm{ISR}}\gamma_{\mathrm{SA}}$ (y-axis) and $\gamma_{\mathrm{ISR}}\gamma_{\mathrm{LA}}$ (x-axis) fits using the $\mu\mu\gamma\gamma$ PHOKHARA sample with $\chi^2_{\gamma_{\mathrm{ISR}}\gamma_{\mathrm{LA}}} < \chi^2_{\gamma_{\mathrm{ISR}}\gamma_{\mathrm{SA}}}$ in four fitted θ_{FSR} ranges, showing the bias produced by the collinear hypothesis in the $\gamma_{\mathrm{ISR}}\gamma_{\mathrm{SA}}$ fit.

5.2 Separating additional FSR and large-angle ISR contributions

The $\gamma_{\mathrm{ISR}}\gamma_{\mathrm{LA}}$ fit selects events with an additional photon at large angle in the detector range. This photon is radiated either by the FSR or from the initial beams (LA ISR). While it is not feasible to identify the specific photon source for each event, it is still possible to statistically separate the two contributions by considering the minimum of the angles in the laboratory frame between the LA photon and the two tracks, notated as $\theta_{\mathrm{min(trk,LA)}}$. The distributions of $\theta_{\mathrm{min(trk,LA)}}$ are shown in Fig. 5.4, taking $\mu^+\mu^-\gamma(\gamma)$ below $1.4\,\mathrm{GeV}/c^2$ as an example. There are two fairly distinct components, the one component observed at low angles below 20° corresponds to the FSR contribution while the other component at larger angles arises primarily from the LA ISR contribution. The ability to achieve angular separation is facilitated by the high energies in the *BABAR* experiment. Due to the nature of the AFKQED generator,

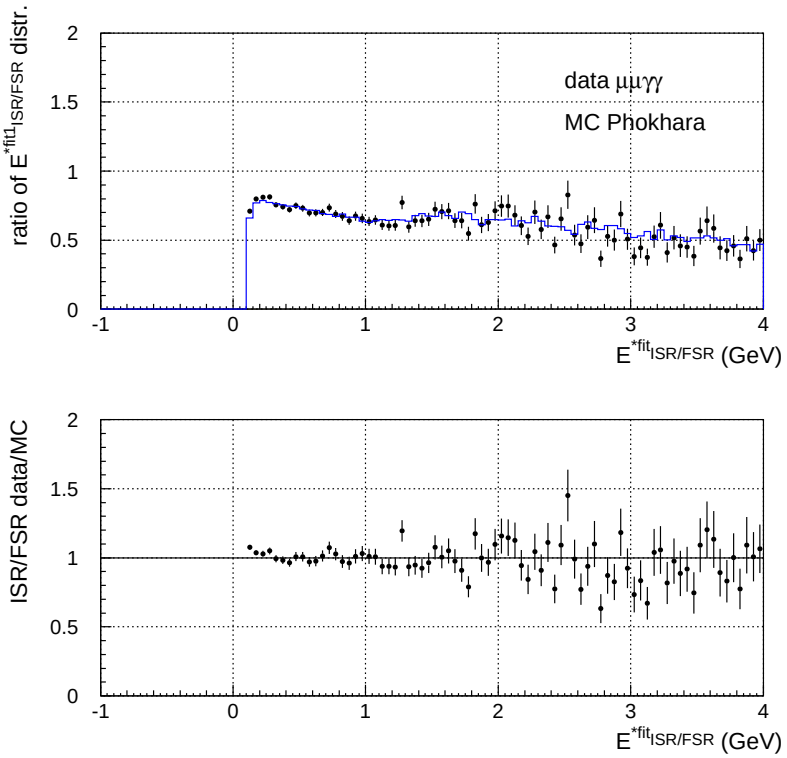

Figure 5.3: Top: the ratio of the distributions of fitted additional photon energy in the $\gamma_{ISR}\gamma_{SA}$ and $\gamma_{ISR}\gamma_{LA}$ fits for 'true' LA photon energy values larger than 0.2 GeV and $\chi^2_{\gamma_{ISR}\gamma_{LA}} < \chi^2_{\gamma_{ISR}\gamma_{SA}}$ in the 2D-χ^2 selected region, data (full dots) and MC (blue histogram). μ-ID is required for both tracks. Each distribution is normalized to the full sample without any energy cut. Bottom: the double ratio of data/MC showing good agreement between data and MC simulation for the collinear kinematic bias.

which generated additional ISR photons collinear to the beams, the LA ISR component is absent, resulting in only the FSR contribution remaining as shown in Fig. 5.4 (right).

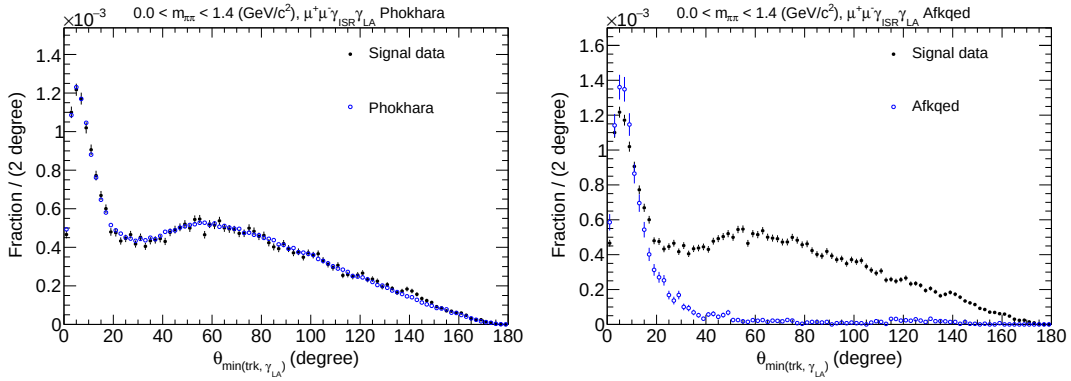

Figure 5.4: Comparison of the minimum angle $\theta_{\mathrm{min(trk,LA)}}$ between the additional LA photon and one of the two tracks for the data fraction (full dots) and PHOKHARA (left), and AFKQED (right) MC fractions (blue open dot) for the mass range between the threshold and 1.4 GeV/c^2 for the $\mu\mu\gamma_{\mathrm{ISR}}(\gamma_{\mathrm{LA}})$ process. The MC fraction is normalized to data fraction in the full range for PHOKHARA and only at small angle (below 20°) for AFKQED. The distributions show the FSR ($\theta_{\mathrm{min(trk,LA)}} < 20°$) and the large-angle ISR ($\theta_{\mathrm{min(trk,LA)}} > 20°$) contributions.

The two components of the $\gamma_{\mathrm{ISR}}\gamma_{\mathrm{LA}}$ sample, $\theta_{\mathrm{min(trk,LA)}} < 20°$ and $\theta_{\mathrm{min(trk,LA)}} > 20°$, are studied separately. A template fit is performed to correct the rate of events below 20° for the full FSR rate, and vice versa to correct the rate of events beyond 20° for the full LA ISR rate. The template fit can also be used to determine the fraction of FSR and LA ISR components in both data and MC. The FSR template distribution is taken from the AFKQED MC sample since it does not contain the LA ISR component and the LA ISR component is obtained from the difference between the PHOKHARA prediction and the FSR template when fixing the integrated number of events below 10° of the latter to be the same from the PHOKHARA distribution. The template fit of the full $\theta_{\mathrm{min(trk,LA)}}$ distribution then determines the overall normalization factor p_0 and the FSR, (LA ISR) component p_1, $(1 - p_1)$ using the following formula:

$$p_0 \times [p_1 \times (\mathrm{FSR\ template}) + (1 - p_1) \times (\mathrm{LA\ ISR\ template})]\,. \tag{5.1}$$

The background contribution which is small for $\mu\mu\gamma(\gamma)$ sample and larger for $\pi\pi\gamma(\gamma)$ sample has been subtracted in the data distribution. In both data and MC, a slight accumulation of events is observed around $120° - 140°$, due to the spatial fluctuations in the main ISR photon shower, generating fake photon clusters. To mitigate the impact of such events, the determination of the fits is finally performed within a restricted angular range of $\theta_{\mathrm{min(trk,LA)}} < 100°$ while using the the templates in the full angular range. The template fits performed for $\mu\mu\gamma(\gamma)$ in the full mass region and the intermediate mass region are shown in Fig. 5.5 and the $\pi\pi\gamma(\gamma)$ in the intermediate mass region are shown in Fig. 5.6. The results of the fits are summarized in Table 5.1.

The fractions of FSR and LA ISR below 20° can be derived from the corresponding templates and are presented in Table 5.2. When calculating the fraction of FSR, the FSR

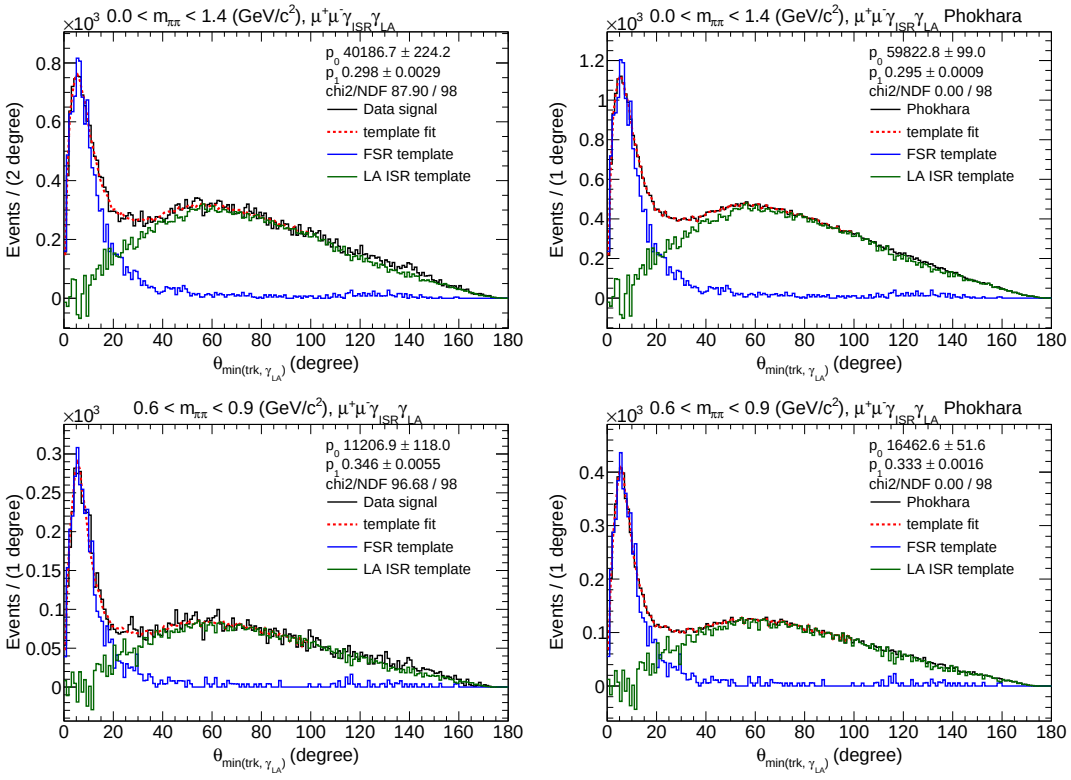

Figure 5.5: Template fit results to data (left) and PHOKHARA (right) distributions in the full mass region (top) and intermediate mass region (bottom) to determine the FSR and LA ISR components in the $\mu\mu\gamma(\gamma)$ sample.

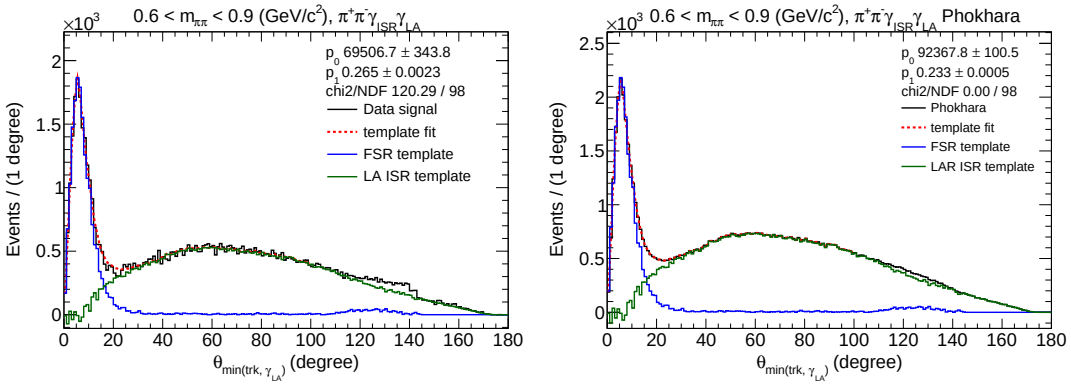

Figure 5.6: Template fit results to data (left) and PHOKHARA (right) distributions in the intermediate mass region to determine the FSR and LA ISR components in the $\pi\pi\gamma(\gamma)$ sample.

	$m_{\pi\pi} < 1.4$ GeV/c^2	$0.6 < m_{\pi\pi} < 0.9$ GeV/c^2	$0.6 < m_{\pi\pi} < 0.9$ GeV/c^2
samples	$\mu\mu\gamma(\gamma)$ samples		$\pi\pi\gamma(\gamma)$ samples
χ^2/ndf data	88.1/98	95.6/98	120.3/98
p_1 data	0.298 ± 0.003	0.346 ± 0.006	$0.265 \pm 0.002 \pm 0.0005$
p_1 MC	0.295 ± 0.001	0.333 ± 0.002	0.233 ± 0.0005

Table 5.1: Results of the template fits of the $\theta_{\mathrm{min(trk,LA)}}$ distributions for $\mu\mu\gamma(\gamma)$ and $\pi\pi\gamma(\gamma)$ samples in both data and MC, displaying the χ^2 over ndf (for data only as it is meaningless for MC by construction) and the fraction of FSR p_1. The first error is statistical which has been scaled by $\sqrt{\chi^2/\mathrm{ndf}}$ when it is larger than one and the second error if exists is from background subtraction for pion samples.

events beyond 80° in the template are not used to avoid the fake FSR contribution, particularly in the $\pi\pi\gamma(\gamma)$ sample. By utilizing the derived fractions, it becomes possible to convert the results of the $\gamma_{\mathrm{ISR}}\gamma_{\mathrm{LA}}$ $< 20^\circ$ and $> 20^\circ$ categories into those of FSR and LA ISR categories.

FSR or LA ISR	$m_{\pi\pi} < 1.4$ GeV/c^2	$0.6 < m_{\pi\pi} < 0.9$ GeV/c^2	$0.6 < m_{\pi\pi} < 0.9$ GeV/c^2
	$\mu\mu\gamma(\gamma)$ samples		$\pi\pi\gamma(\gamma)$ samples
FSR fraction ($< 20^\circ$)	0.814 (5)	0.854 (9)	0.957 (2)
LA ISR fraction ($< 20^\circ$)	0.0364 (0)	0.0233 (0)	0.0361 (0)

Table 5.2: The fractions of FSR and LA ISR below 20° derived from FSR and LA ISR templates. The uncertainties in parentheses are only statistical.

5.3 Background of fake photons in the FSR analysis of the pion sample

In the 2009 ans 2012 *BABAR* analysis [35, 38] an excess of $20 \pm 5\%$ was found in data compared to the AFKQED simulation based on the PHOTOS algorithm [42]. Indeed, it is crucial to validate the calculation of FSR from pions on a specific model. In PHOKHARA, scalar QED model is employed assuming point-like pions. It is therefore important to verify the model predictions using data sample. From the experimental side, a first possibility for a spurious signal is from underestimation of background contributions from uds and ISR hadronic processes in the pion sample. As discussed in Section 4.2.1 and Section 4.2.2, the background contributions were scrutinized by (a) normalizing the input cross sections used in the MC simulations of these background processes with direct measurements performed by *BABAR* experiment, and (b) detailed comparisons of specific distributions of characteristic variables between the selected data and MC samples. These efforts ensured the reliability of the background subtraction and the uncertainty associated with the absolute excess is estimated to be at 1% level.

Another issue for the observed excess could be the possibility of fake photons in the vicinity of the pion track. Indeed such a background may occur if the pion interacts within the EMC, generating a wide hadronic shower with possible secondary clusters mistakenly identified as photon candidates. In the 2009 analysis, this effect was not studied in detail which relied on the simulation. In this section, we delve deeper into this issue. Such a source of background involves fluctuations in the hadronic shower generating spurious photon candidates, possibly not simulated reliably, a specific study is performed here.

Three variables exhibit a high sensitivity to the presence of these fake photons. The first variable of interest is the energy deposit in the EMC associated with the pion track that is closest in angle to LA photon, since larger values of this variable are more likely to produce shower satellites. The second variable is the transverse shower shape of the photon candidate, as measured by the Z_{20} moment. Lastly, a mismatch is expected between the measured energy of the photon and its fitted value, thus associated with a $\chi^2_{\gamma_{\rm ISR}\gamma_{\rm LA}}$ greater than that for a true photon. To distinguish between true and fake photons, an efficient strategy can be developed by comparing two samples: one with small values of $\theta_{\rm min(trk,\gamma_{LA})}$ (typically smaller than 20°) that are characteristic of true and fake photons, and another sample with values larger than 20° with LA ISR photons and a negligible fake contribution. Figure 5.7 depicts the contribution of fake photons in the data sample through correlations between the three variables in the tails of their distributions.

The amount of fake photons present in the pion FSR sample can be checked by selection four different regions which contain an increasing fraction of pion interactions: (1) $E_{\rm cal} < 0.4$ GeV and $Z_{20} > 0.85$, (2) $E_{\rm cal} > 0.4$ GeV and $Z_{20} > 0.85$, (3) $E_{\rm cal} < 0.4$ GeV and $Z_{20} < 0.85$, (4) $E_{\rm cal} > 0.4$ GeV and $Z_{20} < 0.85$. In Fig. 5.8, the $\theta_{\rm min(trk,\gamma_{LA})}$ distributions for data with background subtraction and the PHOKHARA simulated sample in the four regions are shown. The PHOKHARA sample is normalized to data in the range between 40° and 100° dominated by LA ISR photons that are isolated from the pion track and not influenced by their interactions within the EMC. The first observation is that the FSR signal below 20° is significantly contaminated by fake photons as seen by the respective levels of the 'FSR' peak and the LA ISR continuum in the different four regions. The presence of such a contribution is absent in the muon sample. The effect is largely reproduced by the simulation. However, there is clear evidence for an excess in data, which increases with the level of pion interactions.

It is possible to disentangle the potential sources of discrepancy between data and MC simulations. These sources include a discrepancy at the physics level for the true pion FSR radiation or a deficiency of fake photons resulting from interactions in the simulation, with the latter case being dominant as presented in Fig. 5.8. To quantitatively distinguish between the contribution of true pion FSR radiation and fake photons, fitting the χ^2 distributions in data and MC for the four regions can be performed, as the events with a fake photon are expected to have worse $\gamma_{\rm ISR}\gamma_{\rm LA}$ fits due to the mismatch between the measured and fitted photon energies. Reference χ^2 distributions are obtained separately in data and MC by using clean samples. For events with a true FSR photon, the sample with $\theta_{\rm min(trk,\gamma_{LA})} > 20^\circ$ (well-isolated LA ISR photons) is used. On the other hand, for events with fake photons, the sample in region (4) ($E_{\rm cal} > 0.4$ GeV and $Z_{20} < 0.85$) which is dominated by interactions, is chosen.

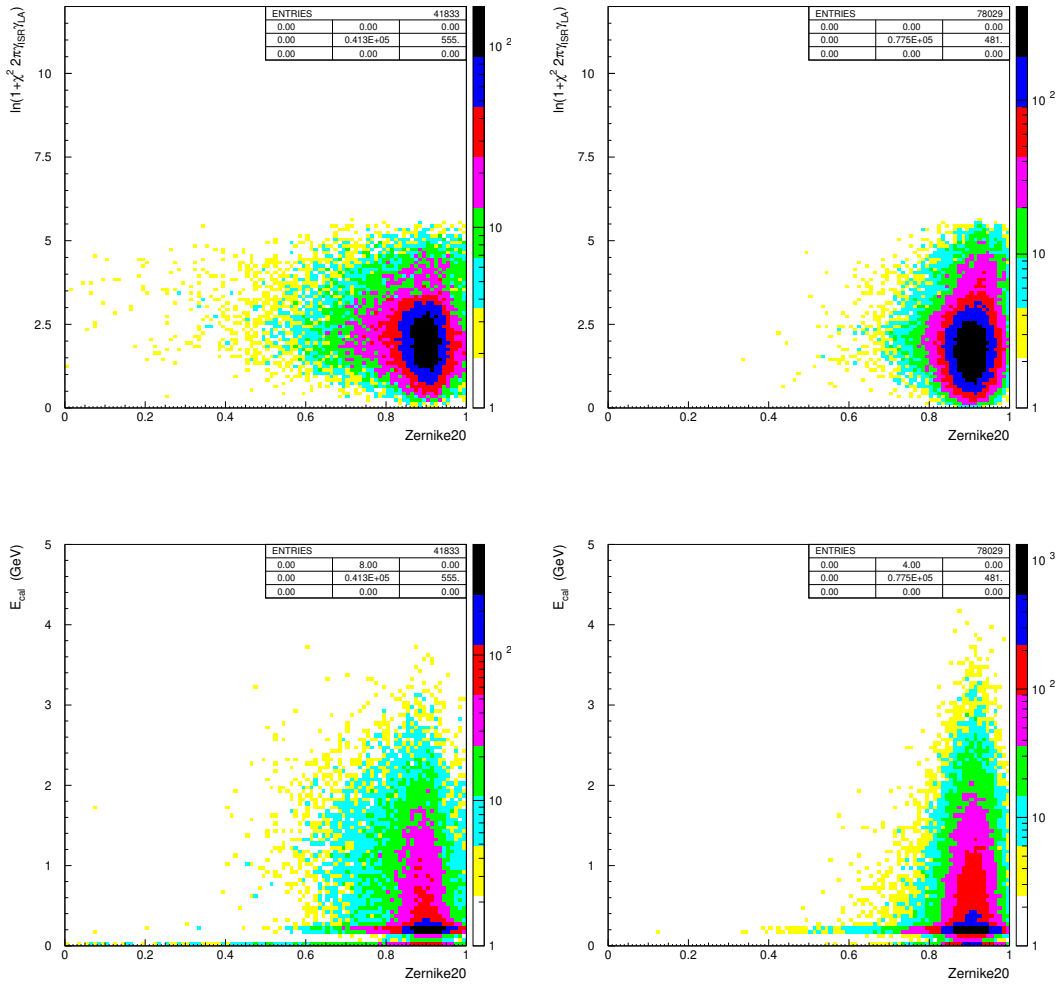

Figure 5.7: The correlation plots of $\chi^2_{\gamma_{\rm ISR}\gamma_{\rm LA}}$, the energy deposition $E_{\rm cal}$ in the EMC associated with the pion track closest in angle to the LA photon, and the transverse extent of the LA photon candidate Z_{20} in the data sample for $\theta_{\min({\rm trk},\gamma_{\rm LA})}$ below 20° (left) and above 20° (right). The contribution of fake photons is pronounced in the tails at larger $E_{\rm cal}$, larger $\chi^2_{\gamma_{\rm ISR}\gamma_{\rm LA}}$, and smaller Z_{20} values in the small $\theta_{\min({\rm trk},\gamma_{\rm LA})}$ region.

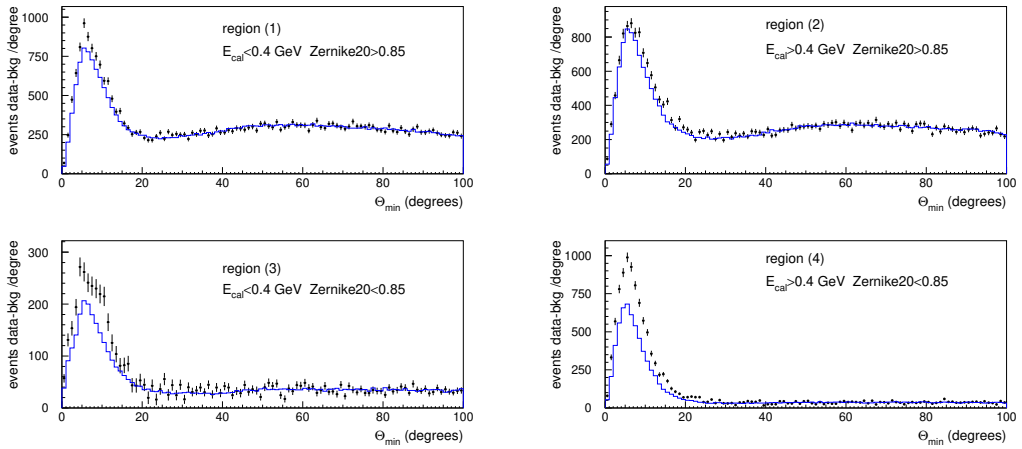

Figure 5.8: The $\theta_{\min(\mathrm{trk},\gamma_{\mathrm{LA}})}$ distributions of the $\gamma_{\mathrm{ISR}}\gamma_{\mathrm{LA}}$ pion sample in the four regions of increasing pion interactions in EMC. Data with background subtraction (full dotes) and the PHOKHARA prediction (blue histograms) normalized to data are shown in the region between 40° and 100° dominated by LA ISR photons well isolated from the pion track.

Fits are performed in Fig. 5.9 and Fig. 5.10 and the corresponding results provide a separation between the true and fake FSR components. From these fits, a systematic uncertainty from the reference χ^2 distributions is derived from the difference using a global fit or the sum from the separate fits in the four regions. The average values obtained reveal a significant fraction of fake photons in the pion FSR sample: $0.458 \pm 0.004_{\mathrm{stat}} \pm 0.010_{\mathrm{syst}}$ in data and $0.377 \pm 0.004_{\mathrm{stat}} \pm 0.007_{\mathrm{syst}}$ in the simulation. The higher fraction of fake photons in data compared to MC is taken into account to determine the true FSR signal in data.

5.4 Measurement of the large-angle additional photon efficiency

Unlike the main ISR photon efficiency, which cancels out in the ratio of $\pi\pi/\mu\mu$ cross sections, the efficiency of detected additional photons in the $\gamma_{\mathrm{ISR}}\gamma_{\mathrm{LA}}$ fits does not cancel out. Hence, it is crucial that their efficiency is under control and specifically the efficiency correction to be applied to the simulation in order to match the data has to be determined by direct measurements.

An approach based on photons originating from π^0 decays is implemented by using kinematically constrained events from the ISR process $e^+e^- \to \pi^+\pi^-\pi^0\gamma$. This process serves as one of the main backgrounds for the $\pi^+\pi^-\gamma(\gamma)$ cross section measurement and its main contribution is observed in the rejected region of the 2D-χ^2 plane. A specific kinematic fit $2\pi\gamma\pi^0[\gamma(\gamma)]$ is performed by using the two measured tracks, the ISR photon, one measured additional photon (γ_1) and a second measured photon (γ_2) to be computed by the fit assuming the mass of the two additional photons to be constrained by the π^0 mass (2C fit). In the case of γ_1, a loop is performed over the measured photons excluding the main ISR photon and the

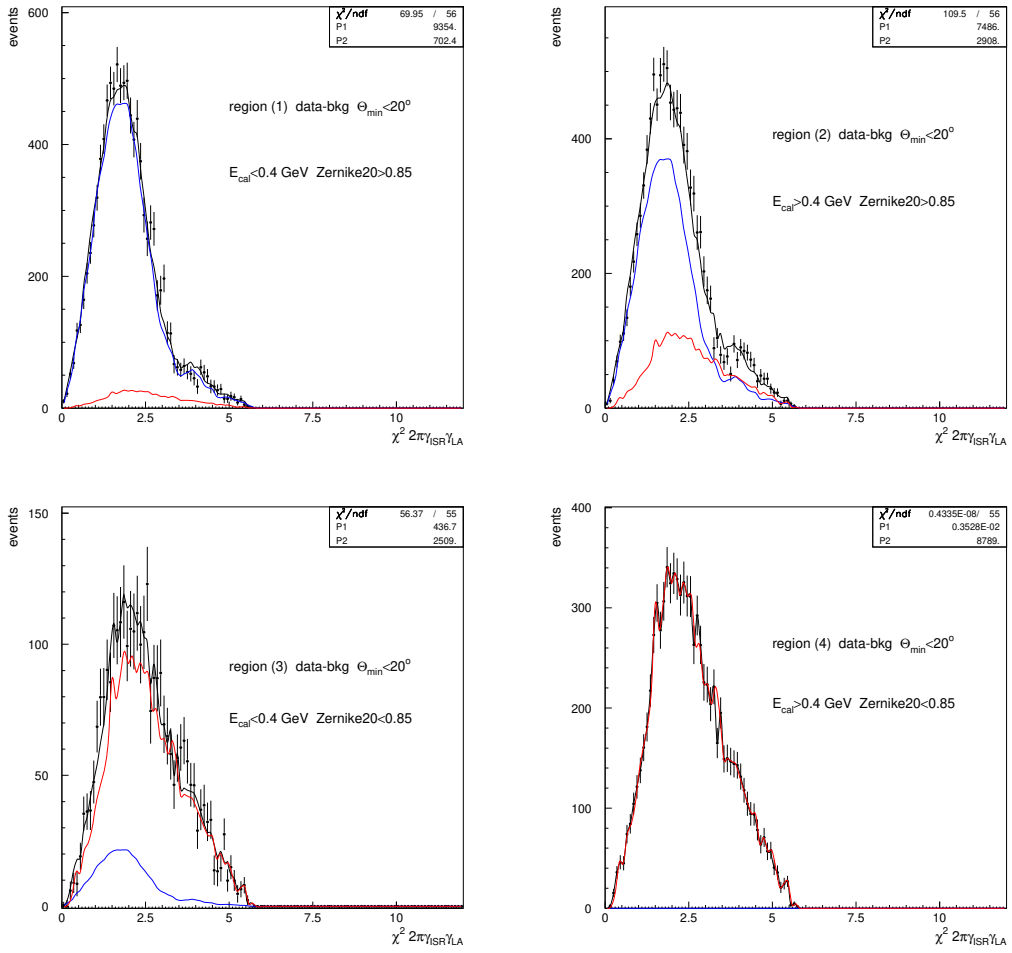

Figure 5.9: The fits of the $\gamma_{\rm ISR}\gamma_{\rm LA}$ χ^2 distributions in the pion sample for $\theta_{\min({\rm trk},\gamma_{\rm LA})} < 20^\circ$ in the four regions of increasing pion interactions in EMC with two components: true FSR photon signal (blue histograms) and fake photon contamination (red histograms). Full dots are data with background subtracted and the black line is the sum of the two components. The reference χ^2 components are taken from data and MC as described in the text.

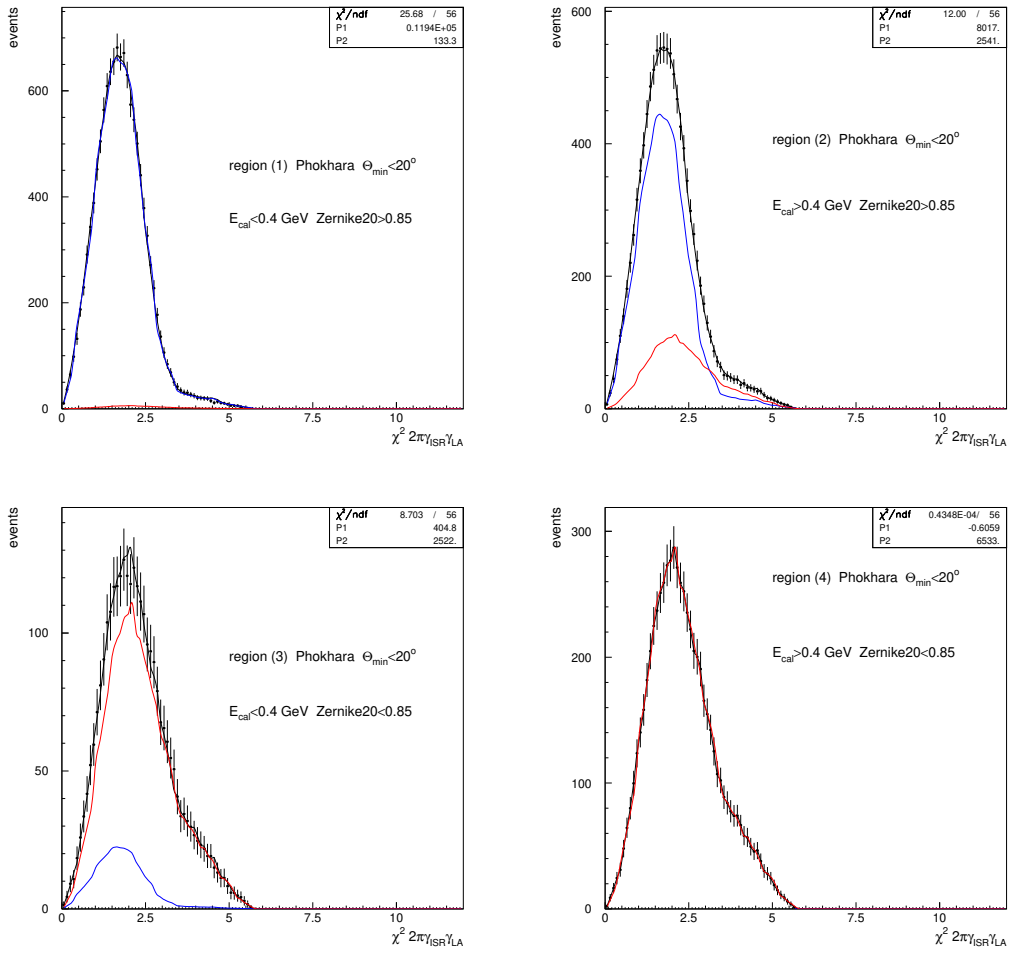

Figure 5.10: Similar fits of the $\gamma_{\rm ISR}\gamma_{\rm LA}$ χ^2 distributions in the pion sample for $\theta_{\min({\rm trk},\gamma_{\rm LA})} < 20^\circ$ in the four regions of increasing pion interaction for MC simulations. Full points are MC samples and the black line is the sum of the true FSR photon signal (blue histograms) and fake photon contamination (red histograms).

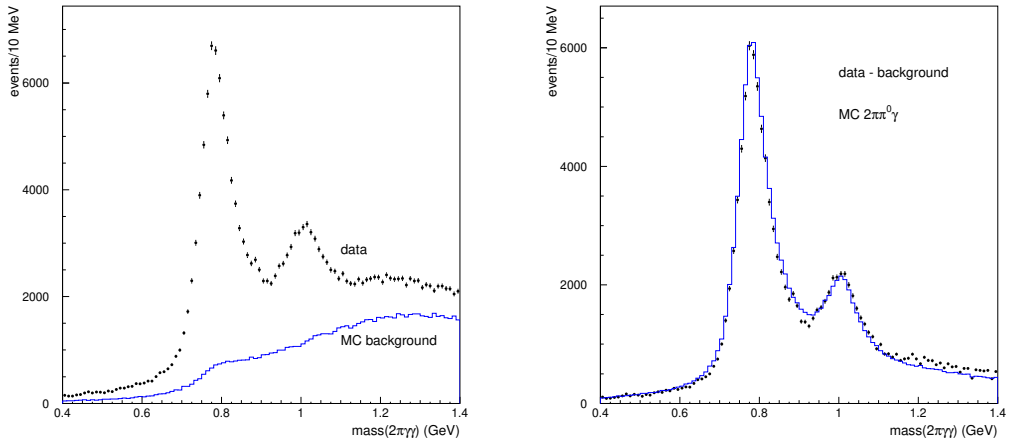

Figure 5.11: Left: The $2\pi\gamma\gamma$ mass distribution in data for the selected $2\pi\gamma\pi^0[\gamma(\gamma)]$ sample (black points) with the expected background level from MC (blue histogram). Right: The $2\pi\gamma\gamma$ mass distribution in data after background subtraction (black points) compared to the MC estimated for the process $\pi^+\pi^-\pi^0\gamma$ (blue histogram).

best fit is chosen. For the predicted (tag) γ_2, the phase space is adequate to cover the range of the additional FSR and part of LA ISR photons in this thesis which are strongly peaked at low energies.

The selected sample satisfies $\ln(\chi^2_{2\pi\gamma\pi^0[\gamma(\gamma)]}+1) < 6$ and no particle ID is applied to the tracks. Background from $\pi\pi\gamma(\gamma)$ and $\mu\mu\gamma(\gamma)$ processes is rejected by selections $\ln(\chi^2_{\pi\pi\gamma_{\rm ISR}\gamma_{\rm SA}}+1) > 5.0$ and $\ln(\chi^2_{\pi\pi\gamma_{\rm ISR}\gamma_{\rm LA}}+1) > 3.0$. In order to establish a solid constraint basis on the π^0 mass, the energy of γ_1 is required to be greater than 0.5 GeV. The remaining backgrounds are from multihadronic processes that are estimated using suitable MC samples. The dominant background contribution by far is from $2\pi2\pi^0\gamma$, with tiny contributions from $\eta2\pi\gamma$ and $q\bar{q}(uds)$ while $\tau\tau$, $\pi\pi\gamma(\gamma)$ and $\mu\mu\gamma(\gamma)$ are negligible. The comparison between data and MC is facilitated by the presence of dominant ω and ϕ resonances in the $2\pi\pi^0$ mass distributions. As shown in Fig. 5.11, the agreement between data and MC is satisfactory and the background level is reasonably well understood and under control.

The photon efficiency is determined both in data and MC by matching the directions of the tag candidate photons to the directions of the measured photons within ±0.5 rad in θ and ±1 rad in ϕ. To mitigate the impact of background contributions, separate determinations are performed in two mass regions: the ω region between 0.7 and 0.9 GeV/c^2 and the ϕ region between 0.9 and 1.1 GeV/c^2, allowing for a consistency check. Since both efficiencies are found to be in agreement within statistical uncertainties, the full mass region (0.7$-$1.1 GeV/c^2) is thus used to obtain the final results. Efficiencies are determined in three θ_γ intervals to study the edge effects within the detector range: forward edge (0.35$-$0.45 rad), central part (0.45$-$2.30 rad), and backward edge (2.30$-$2.40 rad). Determinations are made for each interval using two different scenarios: photons close to one of the two pion tracks ($\theta_{\gamma,\rm trk} < 20^\circ$) and isolated photons ($\theta_{\gamma,\rm trk} > 20^\circ$). Efficiency results for both data and MC are presented in Fig. 5.12, along with their ratios in the six cases defined. In all cases, the

efficiency decreases at low energy, exhibiting a consistent behavior between the data and MC. The ratio of data efficiency over MC efficiency is consistent with unity across all conditions. Therefore no data over MC correction is applied here while a systematic uncertainty of 2% is retained.

In this section, it is important to consider the possibility that the reconstructed photon associated with the predicted candidate is fake, produced by pion interactions in the EMC. This probability has been quantified in Section. 5.3 to be at the 1% level, which is comparable to the signal from FSR that has motivated the study. In the case of $2\pi\pi^0\gamma$ sample, one would expect a similar level which is further reduced by the constraint imposed by the π^0 mass. Therefore, for the determination of the LA photon efficiency, the contribution of fake photons from pion interactions is considered negligible and conservatively covered by the quoted systematic uncertainty of 2%. Moreover, the results obtained for the additional photon efficiency using pions can be safely applied to the muon sample for the same reasons.

Figure 5.13 provides insight into the behavior of the photon efficiency in the vicinity of the pion track showing its dependence on $\theta_{\min(\pi,\gamma)}$ for both data and MC, with a good agreement between data and MC. For the plot, the full detector angular range is utilized and photon energies are integrated from 0.2 to 1.0 GeV. The data over MC ratio is consistent with unity, showing a good agreement within the 2% systematic uncertainty. The observed apparent decrease in efficiency beyond 20° is attributed to a loss of resolution in the predicted photon efficiency. This effect occurs as it enters a region populated by the tail of the angular distribution allowed by the ω and ϕ resonances. This effect is well reproduced by the simulation, as demonstrated in Fig. 5.13.

5.5 Results of the NLO analyses

In this section, the focus is on studying the properties of events that satisfy either $\gamma_{\text{ISR}}\gamma_{\text{SA}}$ fit or $\gamma_{\text{ISR}}\gamma_{\text{LA}}$ fit (or both) in their respectively accepted region of the 2D-χ^2 cut, while ignoring the potential NNLO contributions for the moment. The additional small-angle ISR events are selected above the diagonal ($\chi^2_{\gamma_{\text{ISR}}\gamma_{\text{SA}}} < \chi^2_{\gamma_{\text{ISR}}\gamma_{\text{LA}}}$, denoted as SA sample), while for large-angle ISR or FSR sample (denoted as LA sample) reverse selection is applied. To define the NLO samples in both cases, an energy threshold is required for the additional photon, namely $E^*_\gamma > 0.2$ GeV for $\gamma_{\text{ISR}}\gamma_{\text{SA}}$ fit and $E_\gamma > 0.2$ GeV for $\gamma_{\text{ISR}}\gamma_{\text{LA}}$ fit, as described in Section 1.5. If events satisfy the fits but fail to meet the energy threshold requirements, they are considered as LO processes.

5.5.1 Analysis of the muon sample

The χ^2 distributions of the $\gamma_{\text{ISR}}\gamma_{\text{SA}}$ and $\gamma_{\text{ISR}}\gamma_{\text{LA}}$ fits for NLO events in data, PHOKHARA and AFKQED MC samples for $\mu\mu\gamma$ process are presented in Fig.5.14, with a small background contribution which amounts to be less than 0.4% for both fits subtracted from data distributions. The measured yields of NLO events are normalized to the total number of events of the data and MC distributions. However, it is important to note that this approximation of the NLO fraction does not include efficiency and feed-through corrections at this stage.

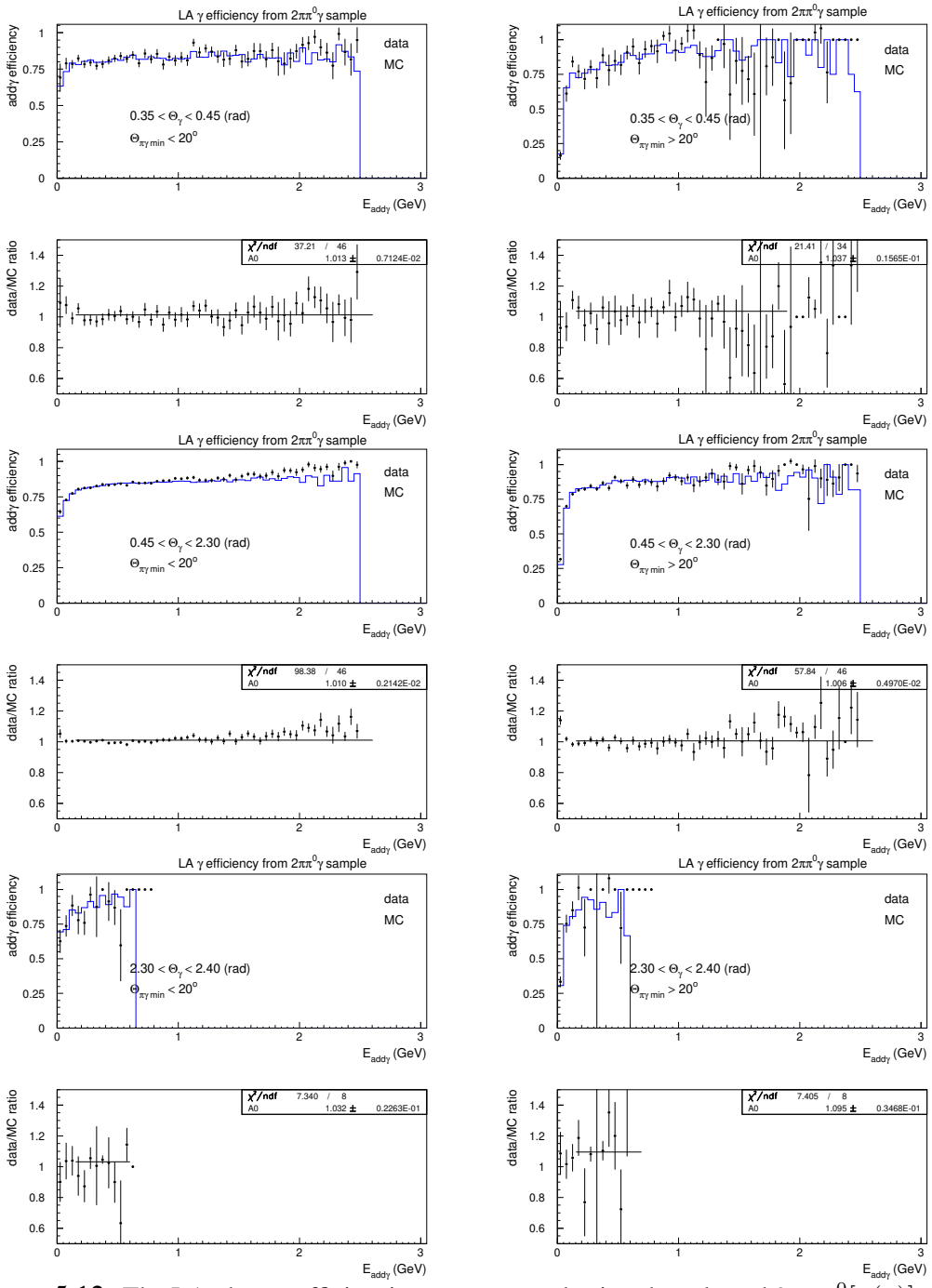

Figure 5.12: The LA photon efficiencies are measured using the selected $2\pi\gamma\pi^0[\gamma(\gamma)]$ sample, considering six different configurations as defined in the main text. For each configuration, the top plot shows the efficiency in data (black dots) and MC (blue histogram), with the bottom plot showing the ratio fitted to a constant value.

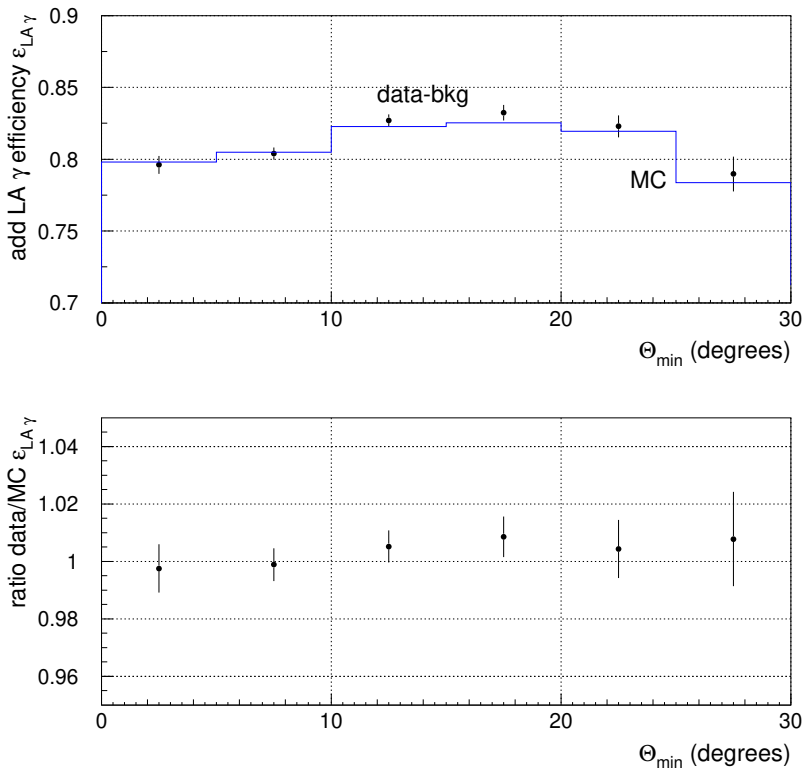

Figure 5.13: Top: the dependence of the LA photon efficiency $\theta_{\min(\pi,\gamma)}$ is shown. These measurements are obtained using the $2\pi\gamma\pi^0[\gamma(\gamma)]$ sample described in the text (data points and blue histogram for the MC simulation). The full angular range $0.35-2.40$ rad and energies $0.2-1.0\,\mathrm{GeV}$ are considered. Bottom: The corresponding ratio between data efficiency and MC efficiency is shown.

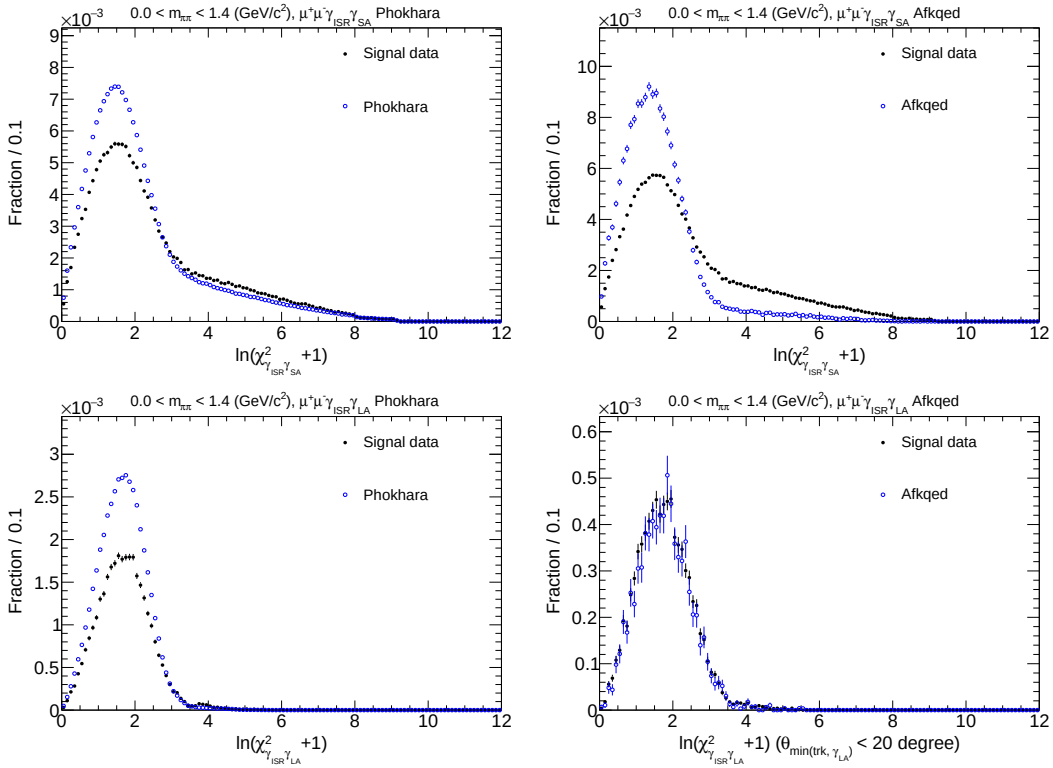

Figure 5.14: Comparison of NLO event fractions distributions as a function of the χ^2 of $2\pi\gamma_{\rm ISR}\gamma_{\rm SA}$ fit (top) and $2\pi\gamma_{\rm ISR}\gamma_{\rm LA}$ fit (bottom) between data and PHOKHARA (left) and AFKQED (right) MC $\mu\mu\gamma(\gamma)$ samples for the full mass region (<1.4 GeV/c^2). The bottom-right plot is restricted to events where the minimum angle between the LA photon and one of the tracks is less than 20 degree since no LA ISR component is generated in the AFKQED sample.

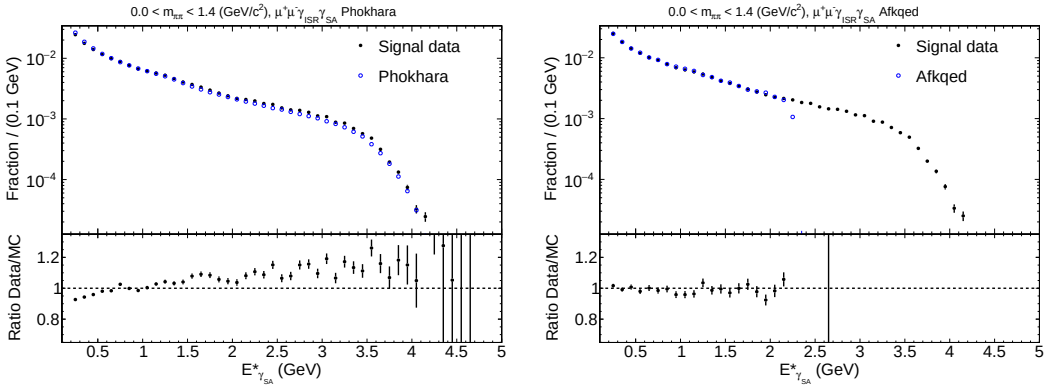

Figure 5.15: The fitted energy distributions of the additional SA photon in the CM frame are compared for data fraction (full points) and PHOKHARA (left) and AFKQED (right) MC fractions (blue open points) and ratios of data fraction over MC fraction (bottom panel) for the full mass region (<1.4 GeV/c^2). The MC fraction is normalized to that of data for the full energy range for the data/PHOKHARA and only below 2.3 GeV for the data/AFKQED comparison.

The comparison in Fig. 5.14 between data and PHOKHARA MC samples reveals a large difference in the normalization in the SA sample for the $\gamma_{\rm ISR}\gamma_{\rm SA}$ fit, while a similar difference is observed on the normalization of the LA sample for the $\gamma_{\rm ISR}\gamma_{\rm LA}$ fit. The comparison between data and AFKQED MC samples shows that the shape of the $\chi^2_{\gamma_{\rm ISR}\gamma_{\rm SA}}$ distribution in data has a wider tail than that of AFKQED MC samples. This difference is expected and can be attributed mainly to the collinear assumption hypothesis in the fit, as discussed in Section 5.1. For the $\gamma_{\rm ISR}\gamma_{\rm LA}$ fit, the shape comparison is considerably improved since the fit uses the measured parameters of the additional LA photon within the detector acceptance range.

The fitted energy spectrum in the CM frame $E^*_{\gamma_{\rm SA}}$ is compared between data and PHOKHARA and AFKQED simulations in Fig. 5.15. The NLO fractions in MC simulations are normalized to those in data so only the shape comparison is carried out. The comparison reveals that the energy spectrum in data is harder than the prediction from PHOKHARA. This hints that there are contributions in the data beyond the NLO part simulated in the PHOKHARA MC samples. The better agreement between data and AFKQED simulation further supports this observation, as the AFKQED MC samples incorporate higher-order contributions. However, it should be noted that the comparison is limited to energies below 2.3 GeV due to the absence of a higher energy tail in the AFKQED samples, as previously mentioned.

For the $\gamma_{\rm ISR}\gamma_{\rm LA}$ fit, the additional FSR and LA ISR fits are separated by using the minimum angle between the LA photon and one of the tracks, $\theta_{\rm min(trk,\gamma_{LA})}$ as discussed in Section 5.2. The $E_{\gamma_{\rm LA}}$ energy spectra in the laboratory frame are compared in Fig. 5.16 for data and PHOKHARA in both cases while for AFKQED the comparison is only performed for events with $\theta_{\rm min(trk,\gamma_{LA})} < 20^\circ$ (FSR contribution). The comparison of the measured polar angle of the LA photon $\theta_{\gamma_{\rm LA}}$ in the laboratory frame is presented in Fig. 5.17.

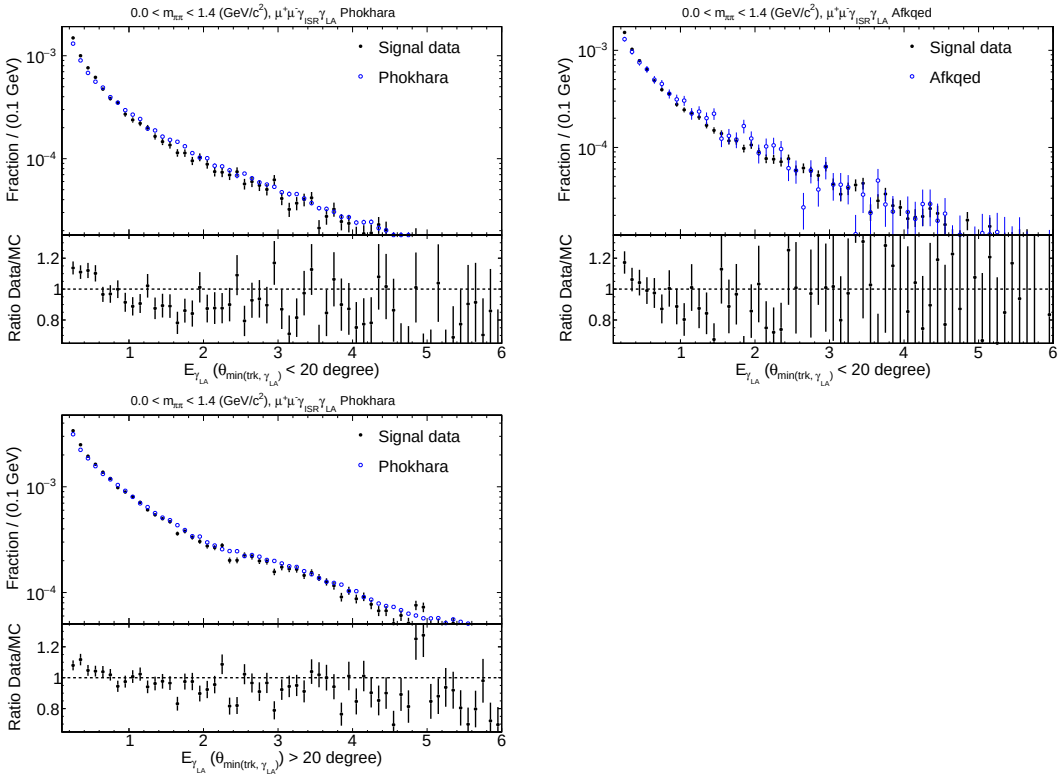

Figure 5.16: Comparison of energy distributions of the additional LA photon in the laboratory frame between data fractions (black points) and PHOKHARA fractions (blue open points) with $\theta_{\mathrm{min(trk,\gamma_{LA})}}$ below 20° (top left) and above 20° (bottom left), and AFKQED fractions (blue open points) with $\theta_{\mathrm{min(trk,\gamma_{LA})}}$ below 20° (top right), with ratios of data and MC fractions shown in the corresponding bottom panels for the full mass region (<1.4 GeV/c^2). The MC fraction is normalized to that of the data for all the plots above.

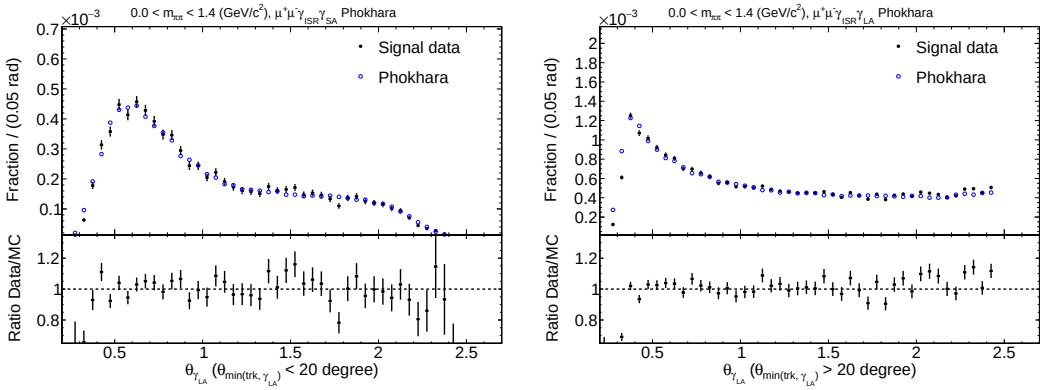

Figure 5.17: Comparison of the polar angle of the LA photon in the laboratory frame when the $\theta_{\mathrm{min(trk,\gamma_{LA})}}$ is below 20° (left) and above 20° (right) for data fraction (black points) and PHOKHARA MC fraction (blue open points) and ratios of data and MC fractions (bottom panel) for the mass range between the threshold and 1.4 GeV/c^2 for the $\mu\mu\gamma_{\mathrm{ISR}}\gamma_{\mathrm{LA}}$ process. The MC fraction is normalized to that of data.

5.5.2 Analysis for the pion sample and comparison with muons

For the samples with two identified pions, a similar analysis is performed. However, a major difference arises when compared to the analysis of muons. In this case, there is a much larger background originating from ISR hadronic and uds processes. This background is largely concentrated in the LA sample, as depicted in Fig. 5.18.

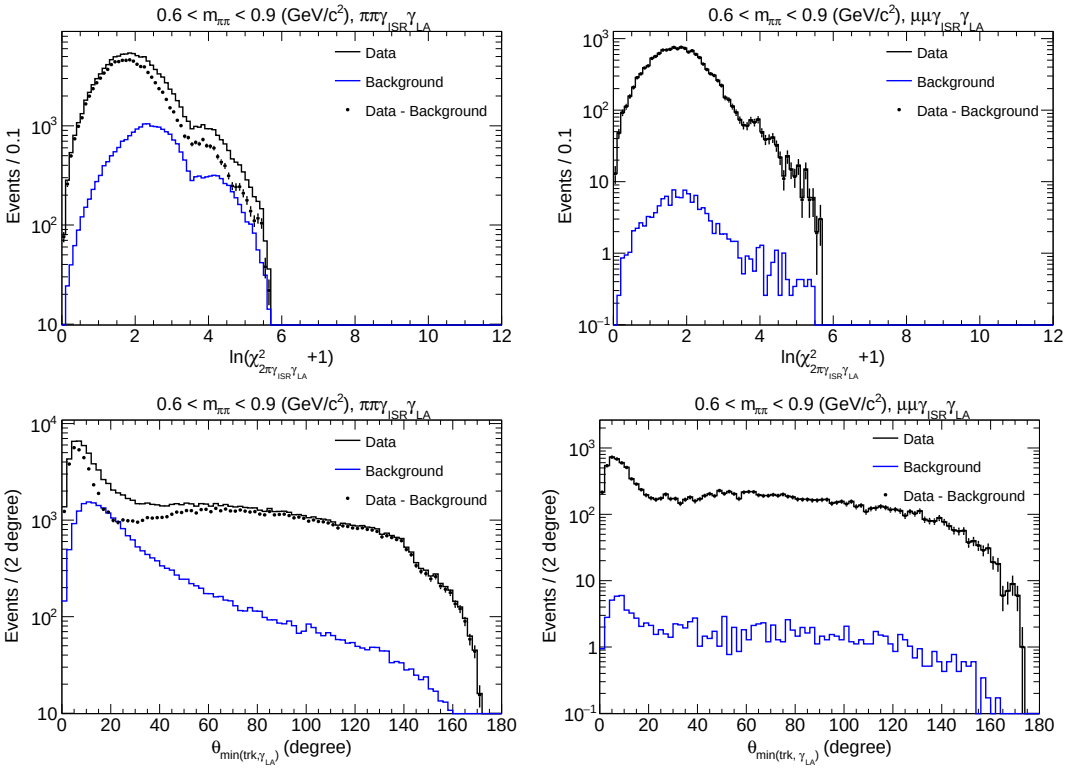

Figure 5.18: The distributions of two quantities are compared for the $\pi\pi\gamma_{\rm ISR}\gamma_{\rm LA}$ (left) and $\mu\mu\gamma_{\rm ISR}\gamma_{\rm LA}$ (right) processes. The top plots represent the distributions of χ^2 values and the bottom plots represent the minimum angle between the additional LA photon and one of the two tracks. A much larger background level in pions is observed compared to muons.

The study of the NLO radiation for pions is constrained to the ρ region, which refers to the mass region between 0.6 and 0.9 GeV/c^2. This limitation arises due to the fact that outside of this mass range, the fraction of background events becomes significantly larger compared to the signal events.

Similar comparisons between $\pi\pi$ and $\mu\mu$ NLO processes are then performed in the restricted ρ mass range in Fig. 5.19 for $\chi^2_{\gamma_{\rm ISR}\gamma_{\rm SA}}$, in Fig. 5.20 for $E^*_{\gamma_{\rm SA}}$, in Fig. 5.21 for $\chi^2_{\gamma_{\rm ISR}\gamma_{\rm LA}}$, in Fig. 5.22 for $\theta_{\rm min(trk,\gamma_{LA})}$, in Fig. 5.23 for $E_{\gamma_{\rm LA}}$ and in Fig. 5.24 for $\theta_{\gamma_{\rm LA}}$. The two processes show similar shapes and relative NLO rates, in particular for the $\gamma_{\rm ISR}\gamma_{\rm SA}$ fit. The $E^*_{\gamma_{\rm SA}}$ distribution in the $\pi\pi$ process data again shows a harder energy spectrum than the PHOKHARA simulation similar to the observation in the $\mu\mu$ process. In Fig. 5.22 the $\theta_{\rm min(trk,\gamma_{LA})}$ distribution is shown, with the MC fraction is normalized to data at $\theta_{\rm min(trk,\gamma_{LA})} > 20^\circ$ as the additional LA ISR component is expected to have good prediction by QED in the PHOKHARA simulation for both the $\mu\mu$ and $\pi\pi$ processes. At lower angles, the agreement between data

and MC simulation for the FSR contribution is good for the $\mu\mu$ process while the data show an excess over MC for $\pi\pi$ process mainly due to the fake photon contribution, as discussed in Section 5.3. For the $E_{\gamma_{\rm LA}}$ comparison, a noticeable difference is observed in the $\pi\pi$ process where the data show a harder energy spectrum than the AFKQED simulation considering events with $\theta_{\rm min(trk,\gamma_{LA})} < 20^\circ$. For events with $\theta_{\rm min(trk,\gamma_{LA})} > 20^\circ$ in the $\pi\pi$ process, a smaller difference is observed where the data spectrum is slightly softer compared with the PHOKHARA simulation.

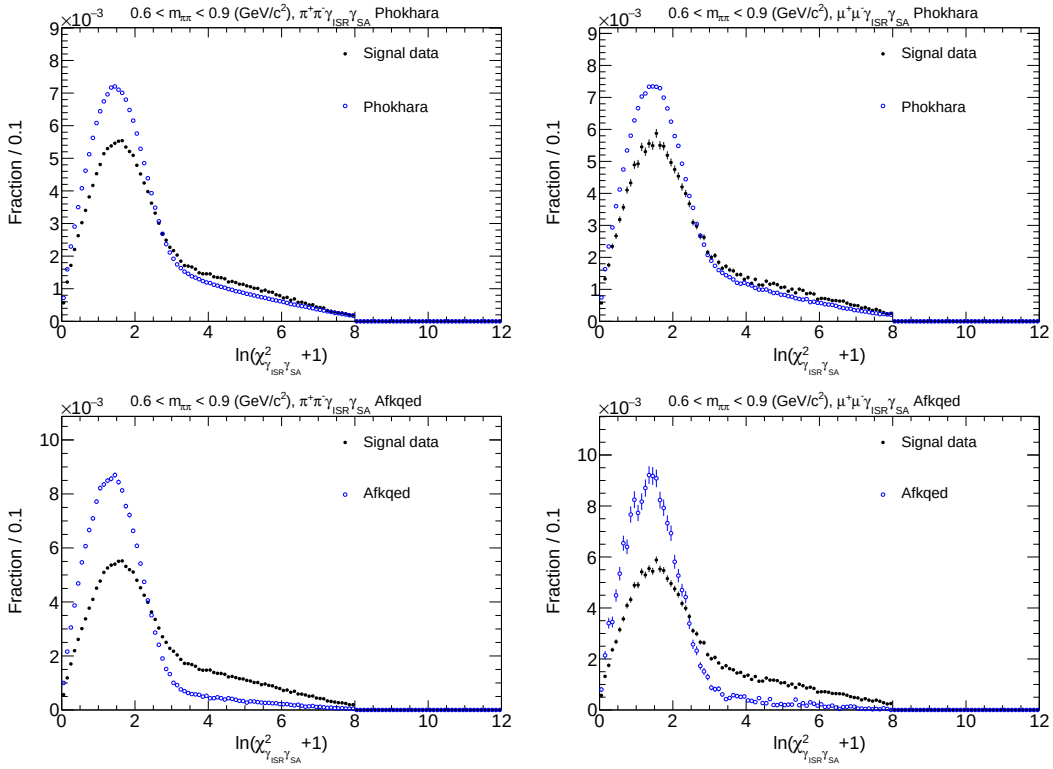

Figure 5.19: Distributions of NLO events fractions as a function of $\chi^2_{\gamma_{\rm ISR}\gamma_{\rm SA}}$ comparing data (black points) and PHOKHARA (blue open points) (top) and AFKQED (blue open points) (bottom) for $\pi\pi$ process (left) and $\mu\mu$ process (right) in the mass range between 0.6 and 0.9 GeV/c^2.

5.6 Summary of the NLO analysis

The NLO plots have been illustrated for $\mu\mu$ process in the full mass (<1.4 GeV/c^2), and $\pi\pi$ process as well as the comparison with the $\mu\mu$ process in the mass range between 0.6 and 0.9 GeV/c^2 in the last section. The rates of NLO $\gamma_{\rm ISR}\gamma_{\rm SA}$ and $\gamma_{\rm ISR}\gamma_{\rm LA}$ events satisfying the 2D-χ^2 and photon energy requirements are summarized in Table 5.3. The rates between data and PHOKHARA and AFKQED, as well as the two processes, are also compared. For a given event, if the fitted photon energy is below the threshold, the event is classified into the LO category. The LO rate is also compared in the table. The 2D-χ^2 selection efficiency is consid-

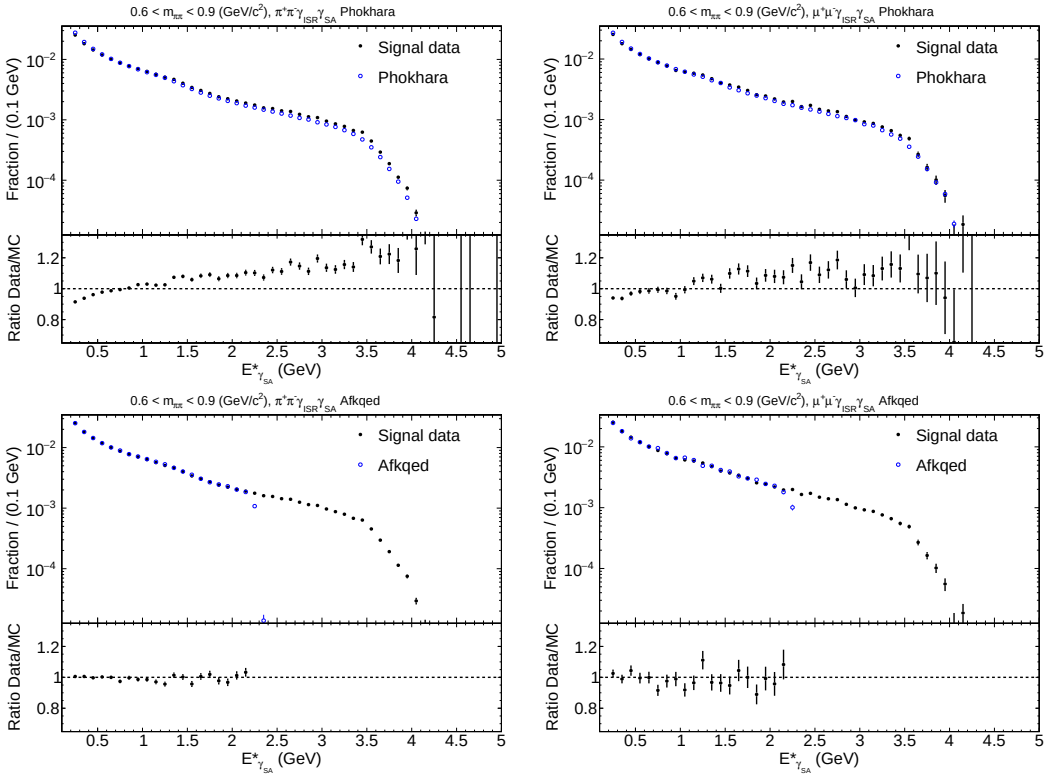

Figure 5.20: Distributions of NLO events fractions as a function of $E^*_{\gamma\mathrm{SA}}$ comparing data (black points) and PHOKHARA (blue open points) (top) and AFKQED (blue open points) (bottom) for the $\pi\pi$ process (left) and the $\mu\mu$ process (right) in the mass range between 0.6 and 0.9 GeV/c^2. The ratios between data fractions and MC fractions are shown in the corresponding bottom panels. The MC fraction is normalized to that of data for these plots. For the bottom AFKQED related plots, the normalization is done for the energy range below 2.3 GeV.

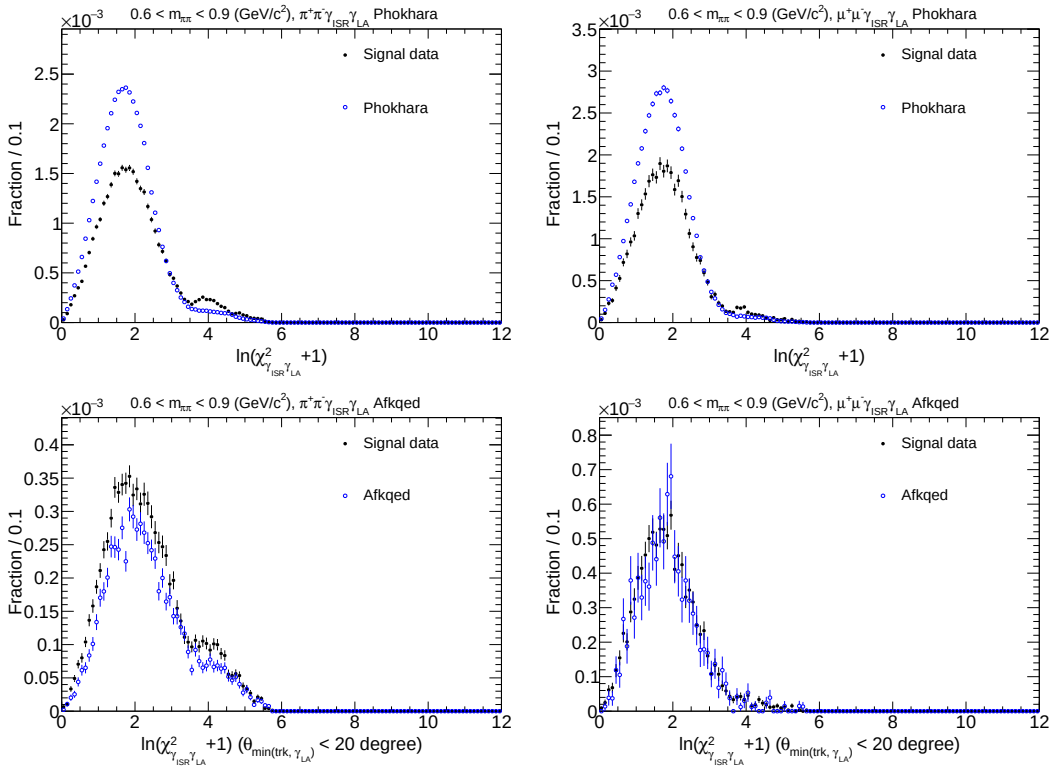

Figure 5.21: Distributions of NLO events fractions as a function of $\chi^2_{\gamma_{\rm ISR}\gamma_{\rm LA}}$ comparing data (black points) and PHOKHARA (blue open points) (top) and AFKQED (blue open points) (bottom) for the $\pi\pi$ process (left) and the $\mu\mu$ process (right) in the mass range between 0.6 and 0.9 GeV/c^2. For the bottom plots, the events are required to satisfy the minimum angle between the additional LA photon and one of the tracks be below 20 °.

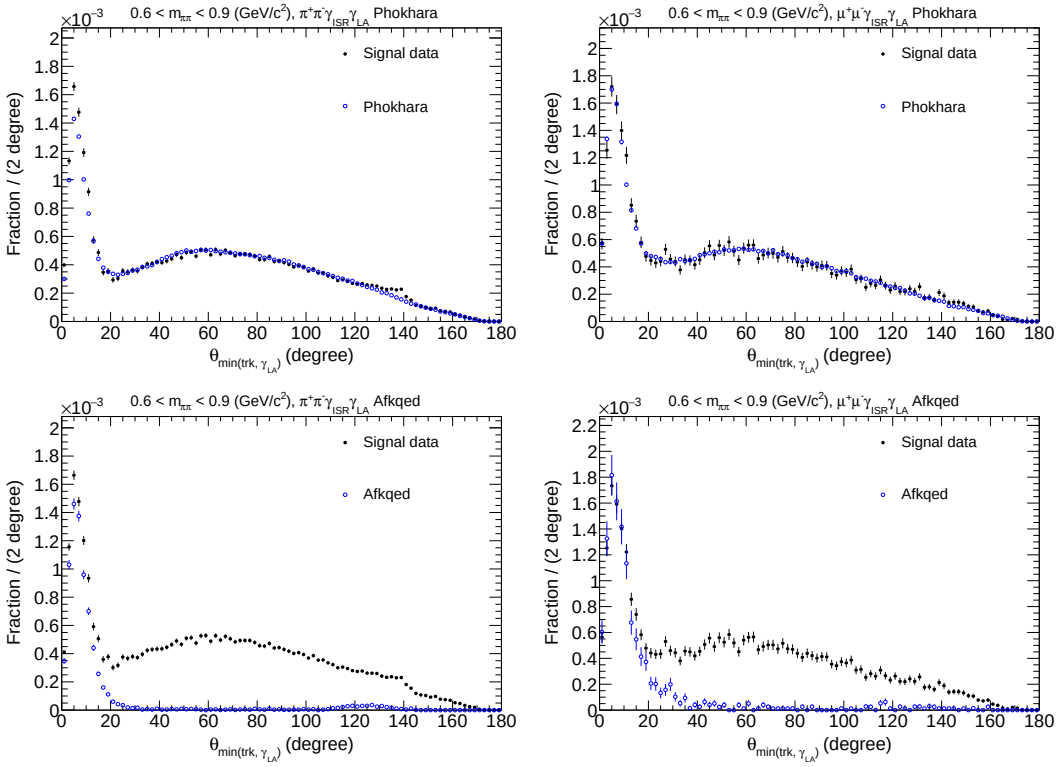

Figure 5.22: Distributions of NLO events fractions as a function of the minimum angle between the additional LA photon and one of the tracks comparing data (black points) and PHOKHARA (blue open points) (top) and AFKQED (blue open points) (bottom) for the $\pi\pi$ process (left) and the $\mu\mu$ process (right) in the mass range between 0.6 and 0.9 GeV/c^2. For the top plots, the MC fractions for events with the minimum angle above 20° have been normalized to those of data.

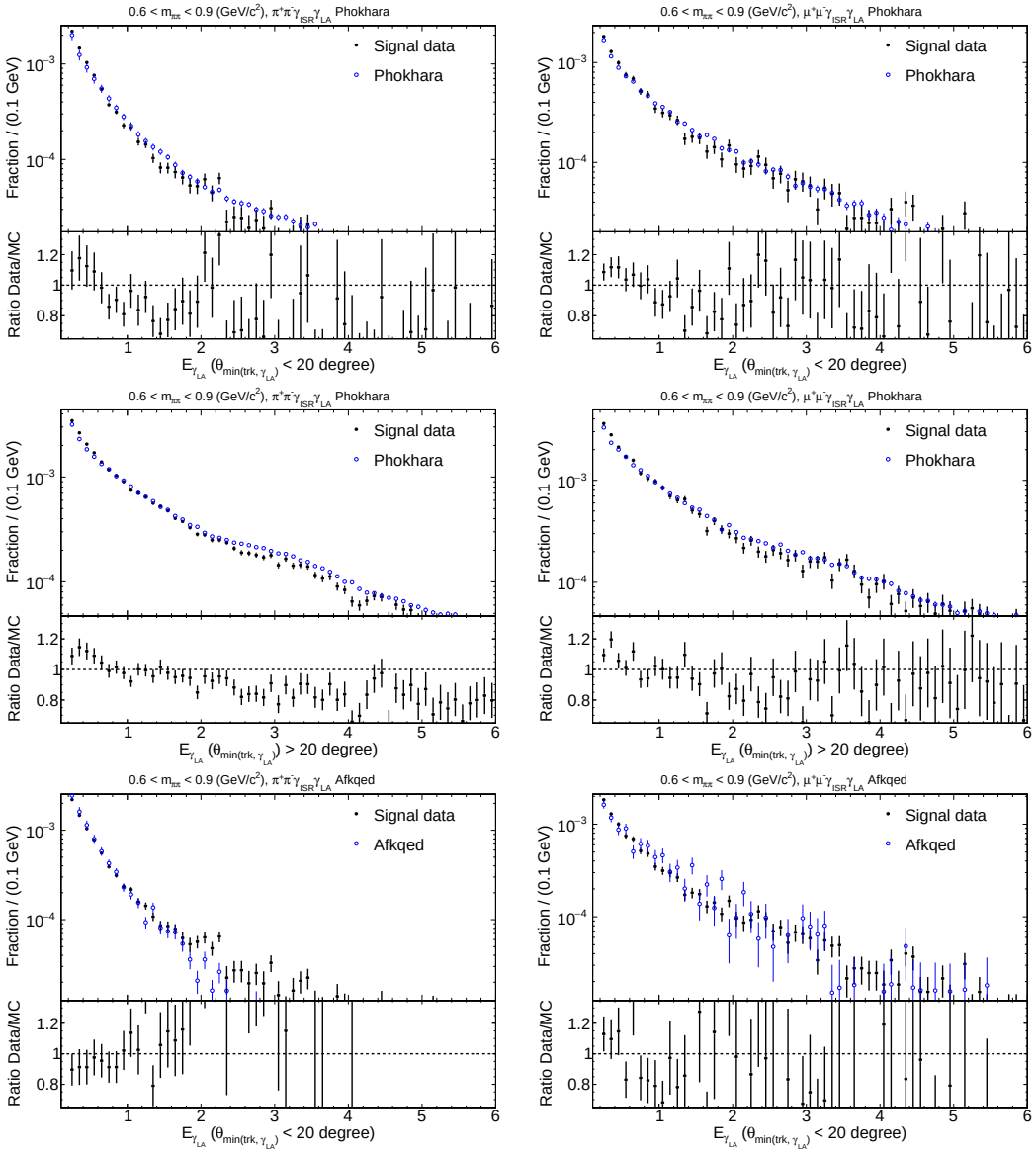

Figure 5.23: Distributions of NLO events fractions as a function of $E_{\gamma_{\rm LA}}$ comparing data (black points) and PHOKHARA (blue open points) (top and middle) and AFKQED (blue open points) (bottom) for the $\pi\pi$ process (left) and the $\mu\mu$ process (right) in the mass range between 0.6 and 0.9 GeV/c^2 when the minimum angle between the additional LA photon and one of the tracks is below 20° (top and bottom) and above 20° (middle). The MC fractions in all these plots have been normalized to those of data.

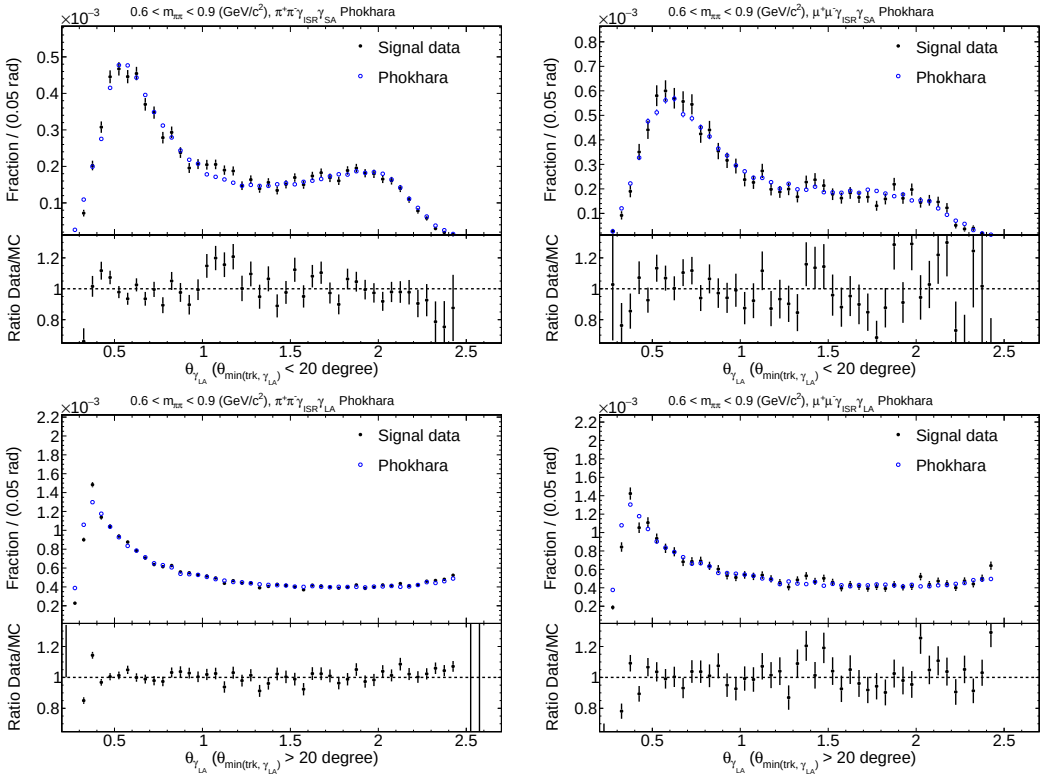

Figure 5.24: Distributions of NLO events fractions as a function of $\theta_{\gamma\mathrm{LA}}$ comparing data (black points) and PHOKHARA (blue open points) for the $\pi\pi$ process (left) and the $\mu\mu$ process (right) in the mass range between 0.6 and 0.9 GeV/c^2 when the minimum angle between the additional LA photon and one of the tracks is below 20° (top) and above 20° (bottom). The MC fractions in all these plots have been normalized to those of data.

ered in the calculation. For the $\pi\pi$ process, the 2D-χ^2 selection efficiency corrections in data are taken from the $\mu\mu$ process in the full mass range due to the large background contribution in the 2D-χ^2 rejected region in data. The efficiency correction affects more significantly the NLO $\gamma_{\text{ISR}}\gamma_{\text{LA}}$ sample in data, where the χ^2 tail is larger than that in the PHOKHARA simulation. For the $\gamma_{\text{ISR}}\gamma_{\text{LA}}$ category, the correction factors derived in Section 5.2 are also applied to obtain the corresponding FSR and LA ISR fractions. The FSR category is corrected for the fake photon contributions as discussed in Section 5.3. All these corrections are applied globally for each specified category.

LO or NLO fraction	$\mu\mu$ $m_{\pi\pi} < 1.4\,\text{GeV}/c^2$	$\mu\mu$ $0.6 < m_{\pi\pi} < 0.9\,\text{GeV}/c^2$	$\pi\pi$ $0.6 < m_{\pi\pi} < 0.9\,\text{GeV}/c^2$
LO			
Data	0.7792(4)(1)(0) [Eff: 0.9931(1)]	0.7812(7)(1)(1) [Eff: 0.9942(1)]	0.7867(5)(1)(2) [Eff: 0.9910(1)]
AFKQED	0.8046(7) [Eff: 0.9964(1)]	0.8053(14) [Eff: 0.9964(2)]	0.8118(4) [Eff: 0.9940(1)]
PHOKHARA	0.7560(1) [Eff: 0.9944(0)]	0.7576(3) [Eff: 0.9949(0)]	0.7656(1) [Eff: 0.9923(0)]
Ratio data/A	0.9684(10)(1)(0)	0.9701(20)(3)(1)	0.9691(8)(1)(2)
Ratio data/P	1.0307(5)(1)(0)	1.0312(10)(1)(1)	1.0276(7)(1)(2)
NLO $\gamma_{\text{ISR}}\gamma_{\text{SA}}$			
Data	0.1723(3)(1)(2) [Eff: 0.9310(4)]	0.1697(7)(2)(0) [Eff: 0.9319(9)]	0.1674(3)(1)(3) [Eff: 0.9275(4)]
PHOKHARA	0.1926(1) [Eff: 0.9428(2)]	0.1903(3) [Eff: 0.9414(3)]	0.1868(1) [Eff: 0.9392(1)]
Ratio data/P	0.895(2)(0)(0)	0.892(4)(1)(1)	0.896(2)(0)(2)
NLO $\gamma_{\text{ISR}}\gamma_{\text{LA}}$ FSR			
Data	0.01421(16)(33)(1) [Eff: 0.620(13)]	0.01681(31)(19)(2) [Eff: 0.653(7)]	0.01148(11)(28)(58) [Eff: 0.321(3)]
AFKQED	0.01270(27) [Eff: 0.748(8)]	0.01445(5) [Eff: 0.784(14)]	0.01008(25) [Eff: 0.384(6)]
PHOKHARA	0.01600(5) [Eff: 0.788(1)]	0.01849(15) [Eff: 0.817(2)]	0.01322(19) [Eff: 0.408(2)]
Ratio data/A	1.12(3)(3)(1)	1.16(5)(2)(0)	1.14(3)(3)(6)
Ratio data/P	0.888(10)(21)(1)	0.909(18)(10)(1)	0.868(15)(22)(44)
NLO $\gamma_{\text{ISR}}\gamma_{\text{LA}}$ LA-ISR			
Data	0.03386(21)(76)(2) [Eff: 0.623(13)]	0.03178(38)(73)(4) [Eff: 0.657(5)]	0.03357(17)(70)(28) [Eff: 0.643(2)]
PHOKHARA	0.03545(7) [Eff: 0.839(1)]	0.03363(19) [Eff: 0.876(1)]	0.03435(19) [Eff: 0.867(0)]
Ratio data/P	0.955(6)(21)(1)	0.945(13)(22)(1)	0.977(5)(20)(8)
NLO ISR ($E^*_{\gamma_{\text{SA}}} < 2.3\,\text{GeV}$)			
Data	0.1901(4)(7)(0)	0.1869(7)(7)(0)	0.1862(3)(7)(4)
AFKQED	0.1801(7)	0.1782(14)	0.1777(4)
Ratio data/A	1.055(5)(4)(1)	1.049(9)(4)(0)	1.048(3)(4)(2)

Table 5.3: Comparison of LO and NLO $\gamma_{\text{ISR}}\gamma_{\text{SA}}$ and $\gamma_{\text{ISR}}\gamma_{\text{LA}}$ event fractions between data and AFKQED and PHOKHARA and between $\mu\mu$ and $\pi\pi$ processes, where the numbers in brackets represent uncertainties with the first being the statistical, the second systematical due to the uncertainty of efficiency corrections and the third due to the background subtraction. For the comparison with AFKQED in the last block, a reduction to data has been applied due to the energy cut below 2.3 GeV in AFKQED.

In Table 5.3, the quoted AFKQED NNLO contributions are explicitly included to the NLO rates for a fair comparison with data, which may contain potential NNLO processes. The final results on the NLO fractions will be re-calculated after taking into account the NNLO contributions. However, even at this stage, it is evident that the data rates do not agree well with the PHOKHARA predictions. Specifically, both for muons and pions, the NLO small-angle ISR rates in data are significantly smaller than PHOKHARA predictions, while the NLO large-angle rates are much closer. The NLO FSR contributions are also found approximately 10% smaller than the PHOKHARA prediction. As PHOKHARA is limited to NLO and AFKQED includes NNLO contributions from the ISR structure function method, the final results of the NLO fractions and their comparison to MC generators are presented to Section 8.1 after the evaluation of the NNLO contributions.

Chapter 6

Further investigation of NLO additional radiation

In the previous chapter, the NLO radiation study is conducted using kinematic fits. In one of the fits, the collinear assumption is employed when the additional photon is not detected within the detector acceptance range. In order to assess whether the conclusions drawn in the previous chapter are influenced by the collinear assumption, a further and new kinematic reconstruction of the full event $e^+e^- \to \mu^+\mu^-\gamma(\gamma)$ sample is performed and investigated, so-called the 0C calculation which represents zero constraint. The energy and momentum conservation relations are utilized to calculate four unknown quantities: the energy and angles of the additional photon, denoted as γ_{0C}, as well as the energy of the main ISR photon, relying on the four-momenta of the beams, the two charged particles assumed to be pions, and the angles of the main ISR photon. Due to poorer resolution of the calculated quantities compared to the results from the $\gamma_{\mathrm{ISR}}\gamma_{\mathrm{SA}}$ and $\gamma_{\mathrm{ISR}}\gamma_{\mathrm{LA}}$ fits, the 0C calculation is used only for further studies. However, 0C calculation provides information on additional photons over the full energy range and over the full angular range and it is unlike the $\gamma_{\mathrm{ISR}}\gamma_{\mathrm{SA}}$ fit, which constrains the additional photon to be collinear with the e^+ or e^- beam, or unlike the $\gamma_{\mathrm{ISR}}\gamma_{\mathrm{LA}}$ fit, which requires a detected photon within the acceptance of the detector. This calculation is independent of whether the additional photon is detected or not, providing a means to investigate the observed discrepancy between the LO and NLO contributions of data and PHOKHARA.

As the constraint of the measured energy of the main ISR photon is not used in the 0C calculation, it is possible for some additional photon candidates to be aligned with the ISR photon. This alignment helps compensate for any energy loss in the EMC since the sum of energies of the ISR and additional photons is the only constraint in this calculation. The angle in space between the calculated direction of the additional photon and the measured direction of the main ISR photon, denoted as $\alpha(\gamma_{\mathrm{0C}}, \gamma_{\mathrm{ISR}})$, is shown in Fig. 6.1 as a function of either the calculated energy of the additional photon in the CM frame, $E^*_{\gamma_{\mathrm{0C}}}$, or the calculated energy difference in the CM frame using the reconstructed and true information, $E^*_{\gamma_{\mathrm{0C}}} - E^*_{\gamma_{\mathrm{true}}}$. Comparison between the two reveals that the calculated energy of the additional photon agrees well with that of the true photon beyond an energy threshold of approximately 200 MeV except when $\alpha(\gamma_{\mathrm{0C}}, \gamma_{\mathrm{ISR}})$ is below about 0.5 rad. The comparison between the PHOKHARA

MC and muon data of the $\alpha(\gamma_{0C}, \gamma_{ISR})$ distribution for events satisfying the polar angle in the laboratory $0.4 < \theta_{\gamma_{0C}} < 2.0$ and $E^*_{\gamma_{0C}} > 0.2$ GeV is shown in Fig. 6.2. Despite the slight difference from shapes, the contribution of fake photons at small $\alpha(\gamma_{0C}, \gamma_{ISR})$ angles are seen both in data and MC. A selection $\alpha(\gamma_{0C}, \gamma_{ISR}) > 0.5$ rad is applied in the following study related to 0C reconstruction to suppress the contribution of these fake photons.

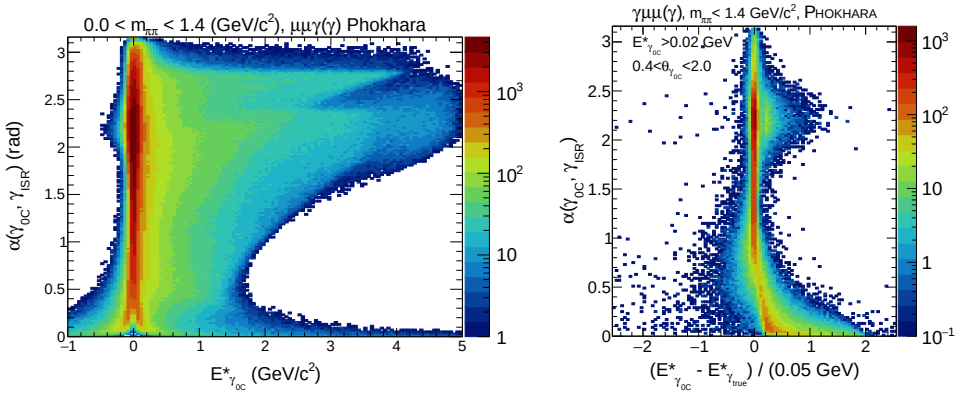

Figure 6.1: Angle in space between the calculated direction of the additional photon γ_{0C} and the measured direction of the main ISR photon, $\alpha(\gamma_{0C}, \gamma_{ISR})$, as a function of the calculated energy of the additional photon in the CM frame (left) and the energy difference between calculated energies in the CM frame using the reconstructed and true information (right).

The angular resolution of the additional photon direction is estimated by comparing the calculated polar angle $\theta_{\gamma_{0C}}$ with the fitted one obtained from the $\gamma_{ISR}\gamma_{LA}$ in muon data and MC, as presented in Fig. 6.3 for several angular ranges within the acceptance of the measured additional photons and for energies above 200 MeV in the CM frame. Good agreement is observed between data and simulation for the core of the resolution function, characterized by RMS values of 30 mrad with little dependence on $\theta_{\gamma_{0C}}$. However, there is a notable difference in the tail at values of $\theta_{\gamma_{0C}} - \theta_{\gamma_{LA}}$ above 0.5 rad up to 2 rad and the tail is more pronounced in data. As a consequence the reconstructed angular distribution of the additional photon at large angles will be contaminated by transfer of photons from the dominant sharp peaks along the incident beams. An excess of large-angle fake photons is expected in data compared to MC and is estimated a $\sim 10\%$ enhancement in the data/MC ratio in the 0C analysis.

The calculated polar angle θ_{0C} distribution is shown in Fig. 6.4 (left), requiring $E^*_{\gamma_{0C}}$ above 0.2 GeV. The polar angle distribution in data is compared with the corresponding one based on the PHOKHARA predictions, as well as the true polar angle of additional photons. A fair agreement between data and MC at large angles to the beams is observed. In fact data is roughly 10% larger than the true predictions in this region and this excess has been explained by the larger resolution tails in data as discussed in Fig. 6.3. Contrary to the fair agreement at large angles, PHOKHARA predicts a radiation rate that is too high at small angles. This observation remains consistent when using an event sample where the charged particles and the main ISR photon are restricted to the central region of the detector, reduced by 0.5 rad on both sides, with $0.85 < \theta_{\gamma_{ISR}} < 1.9$ rad and $0.9 < \theta_{\gamma_{trk}} < 1.95$ rad. Figure 6.4 (right) demonstrates that the discrepancy below 0.4 rad and above 2.4 rad is not induced by the detector range for muons and the ISR photon and more likely to be associated with the intrinsic shape

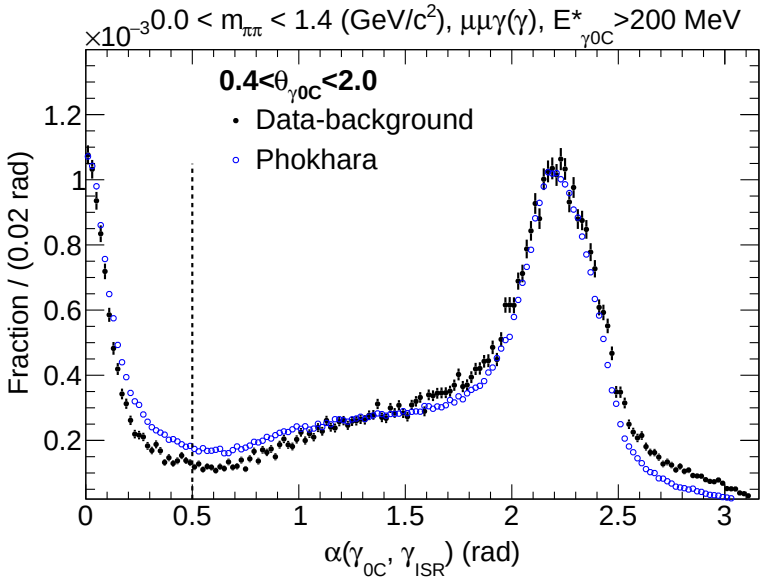

Figure 6.2: Distribution of the angle in space between the calculated direction of the additional photon γ_{0C} and the measured direction of the main ISR photon, $\alpha(\gamma_{0C}, \gamma_{ISR})$, is compared between muon data (black full dots) and PHOKHARA (blue open points) for $0.4 < \theta_{\gamma_{0C}} < 2.0$ and $E^*_{\gamma_{0C}} > 0.2$ GeV. The event yields in data and MC are normalized to the total number of events of the corresponding samples.

of the additional ISR. The larger difference between the calculated polar angles and the true ones from PHOKHARA is also observed and mostly due to the angular resolution effects of the 0C calculation. However, this cannot explain the discrepancy between data and PHOKHARA since the core part of the angular resolutions are well agreed for $E^*_{\gamma_{0C}} > 0.2$ GeV, as shown in Fig. 6.3. In addition, the discrepancy between the calculated and true distribution caused by the angular resolutions exhibits an opposite sign as the data to PHOKHARA difference at low angles to the beams. It has also been verified that the discrepancy between data and PHOKHARA predictions cannot be attributed to the tails of the angular resolution alone.

The calculated energy in the CM frame, $E^*_{\gamma_{0C}}$, is also compared between data and PHOKHARA in different $\theta_{\gamma_{0C}}$ bins in Fig. 6.5, together with the true MC spectrum. In all $\theta_{\gamma_{0C}}$ bins, a decent agreement is observed between the calculated energy spectrum and the true energy spectrum in PHOKHARA. However, a clear discrepancy is seen between data and PHOKHARA prediction particularly in the forward and backward radiation peaks. There is also a discrepancy on the shape of the energy spectrum in addition to the discrepancy on event rate mentioned before. To better visualize the shape difference, Fig. 6.6 (left) integrates all different polar bins and this confirms the slope observed on the data/PHOKHARA ratio of the energy distribution of the additional photon in the CM frame from the $\gamma_{ISR}\gamma_{SA}$ fit demonstrated in Fig. 5.15. To check the energy spectrum of AFKQED, a similar comparison between data and AFKQED prediction is illustrated in Fig. 6.6 (right), showing no such shape discrepancy. Unlike the separate SA and LA comparison with the $\gamma_{ISR}\gamma_{SA}$ and $\gamma_{ISR}\gamma_{LA}$ results presented in Fig. 5.15 and Fig. 5.16, in both PHOKHARA and AFKQED cases, the comparison of the true energy spectrum with the calculated $E^*_{\gamma_{0C}}$ spectrum is performed over the full

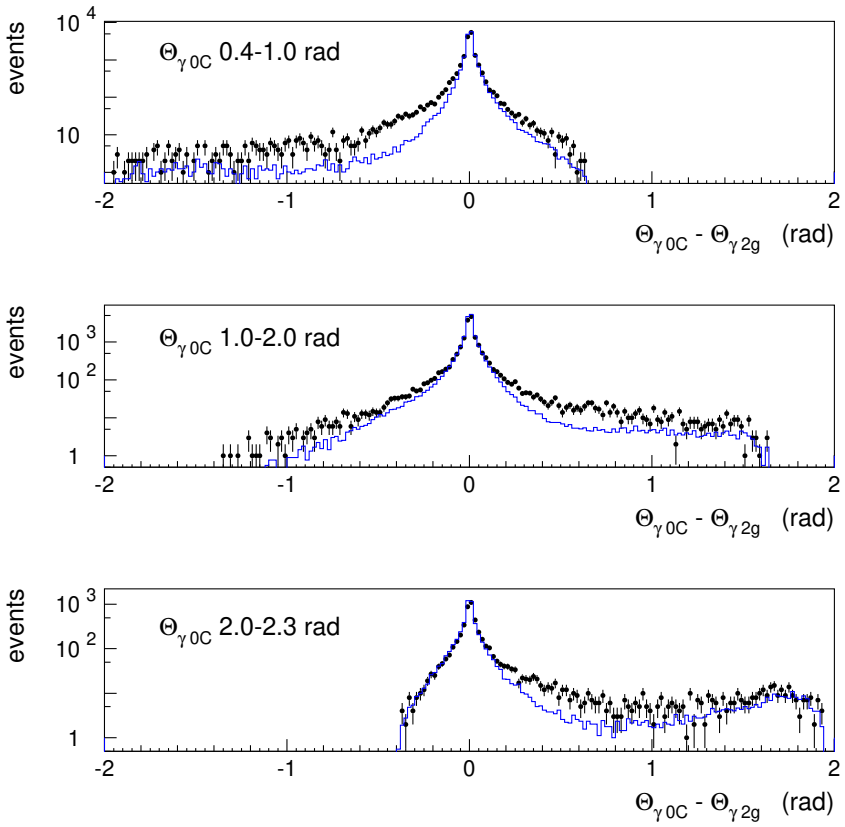

Figure 6.3: Distribution of angular differences between the calculated angles $\theta_{\gamma_{0C}}$ and the measured one $\theta_{\gamma_{LA}}$ from the $\gamma_{ISR}\gamma_{LA}$ fit, in three $\theta_{\gamma_{0C}}$ intervals where the additional photons is within the angular detector acceptance: data (black points) and PHOKHARA (blue histograms).

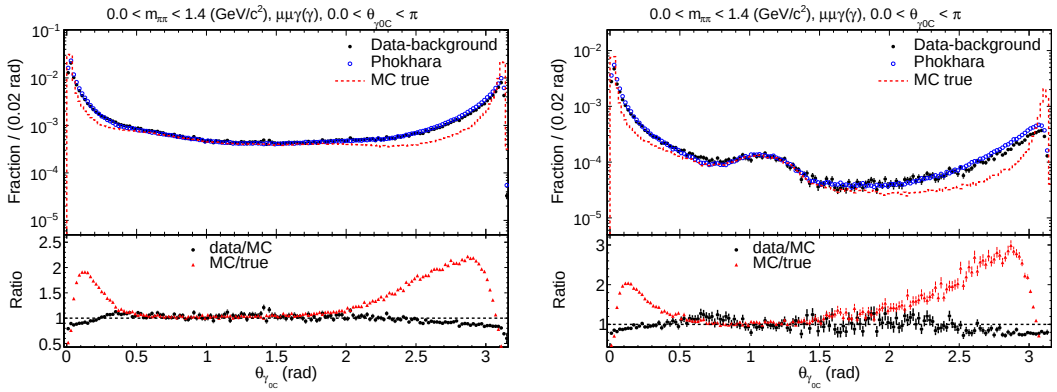

Figure 6.4: Distributions of the calculated polar angles $\theta_{\gamma 0C}$ of the additional photons requiring $E^*_{\gamma 0C} > 0.2$ GeV are compared between data and PHOKHARA simulation, as well as with the polar angles from the true additional photons. In the right side panel, the acceptance of the charged tracks and the main ISR photon is restricted by 0.5 rad on each side of the detector with respect to the left side panel, which is used in the calculation of $\theta_{\gamma 0C}$.

angular range. For the AFKQED sample beyond 2.3 GeV, the only contribution is from the FSR component and it is well reproduced by the 0C calculation.

The transition between the LO and NLO contributions is presented by a zoomed version at low energies in Fig. 6.7. In the left panel, the calculated spectra using both the reconstructed and true information are compared between the PHOKHARA and AFKQED MC samples. It reveals a significant discrepancy between the two MC predictions, with the radiation rate from PHOKHARA being too high compared to with AFKQED by up to 30% for energies down to 0.1 GeV. The conclusion remains the same independent of the true or reconstructed energy spectra. The reconstruction at very low energies below 0.1 GeV may be problematic due to the limited resolution of the 0C method and large variations are expected. At the right panel, a similar comparison is carried out between data and the two MC predictions. In order to avoid the potential issues such as the complications seen with the MC samples and the momentum calibration of muons, the LO events are merged into a large bin between -0.2 and 0.2 GeV centered around zero. The rate of data/PHOKHARA is not consistent between the LO and NLO contributions, with a clear change from LO to that of NLO above 0.2 GeV. However, the LO rate of data/AFKQED is consistent with that of the NLO above 0.2 GeV within the statistical uncertainty. The deviation of the AFKQED prediction from unity is considered as an artefact resulting from the absence of LA photon events in the MC sample for energies above 2.3 GeV as shown in Fig. 6.6.

Up to now, all the 0C studies are performed in the $\mu\mu\gamma$ process since the background contribution is tiny. However, for the $\pi\pi\gamma$ process, the background in data is much larger and the background estimation based on MC simulation may not be reliable, particularly in the 2D-χ^2 rejected region. Thus the 2D-χ^2 selection is applied to the $\pi\pi\gamma$ process and similar comparisons between the two MC predictions and between data and the MC samples can be made and are presented in the bottom of Fig. 6.7. The observations made above for the $\mu\mu\gamma$ process are found to hold true for the $\pi\pi\gamma$ process as well.

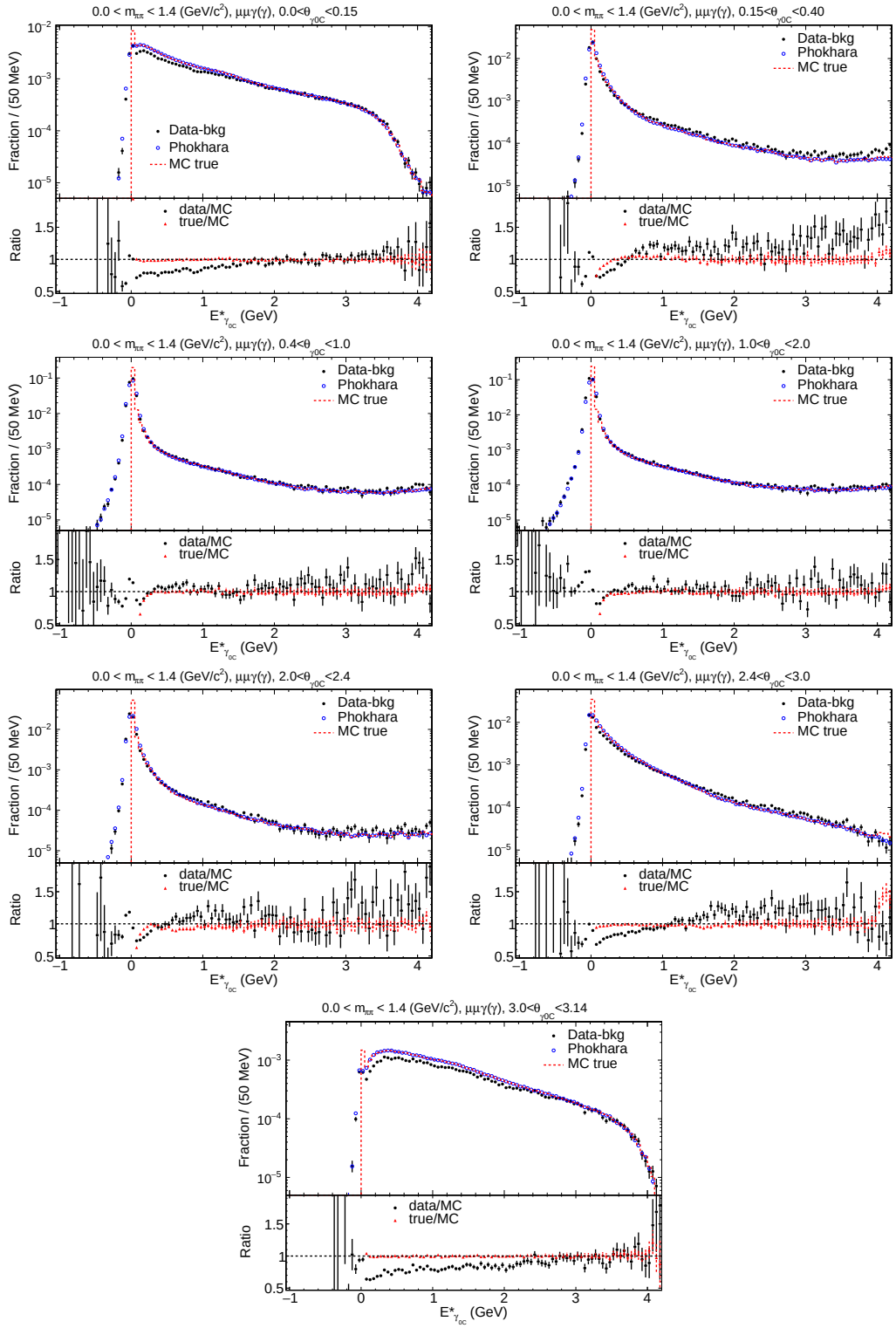

Figure 6.5: Distribution of the calculated energies in the CM frame $E^*_{\gamma 0C}$ is compared between data and PHOKHARA as well as the true energies of additional photons in different $\theta_{\gamma 0C}$ bins.

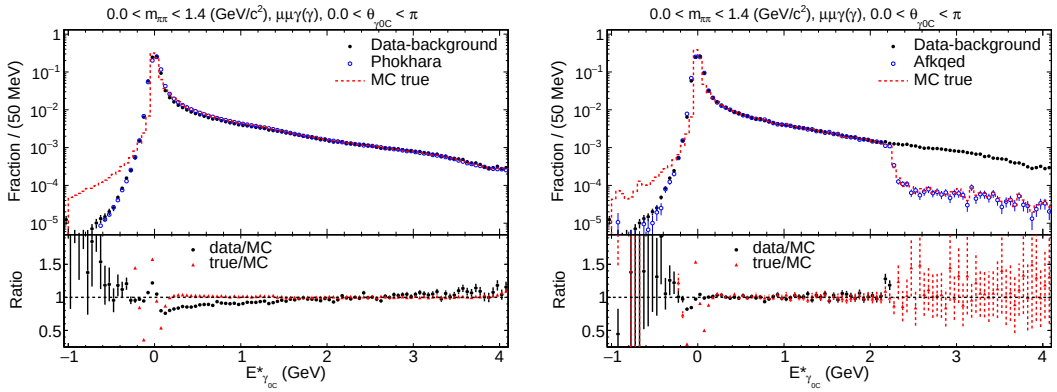

Figure 6.6: Distribution of the calculated energies in the CM frame $E^*_{\gamma 0C}$ is compared between data and PHOKHARA (left) and AFKQED (right) as well as the corresponding true energies of additional photons for events in full polar angle range. In the right panel, for the AFKQED sample beyond 2.3 GeV, the only contribution is from the FSR component and it is well reproduced by the 0C calculation.

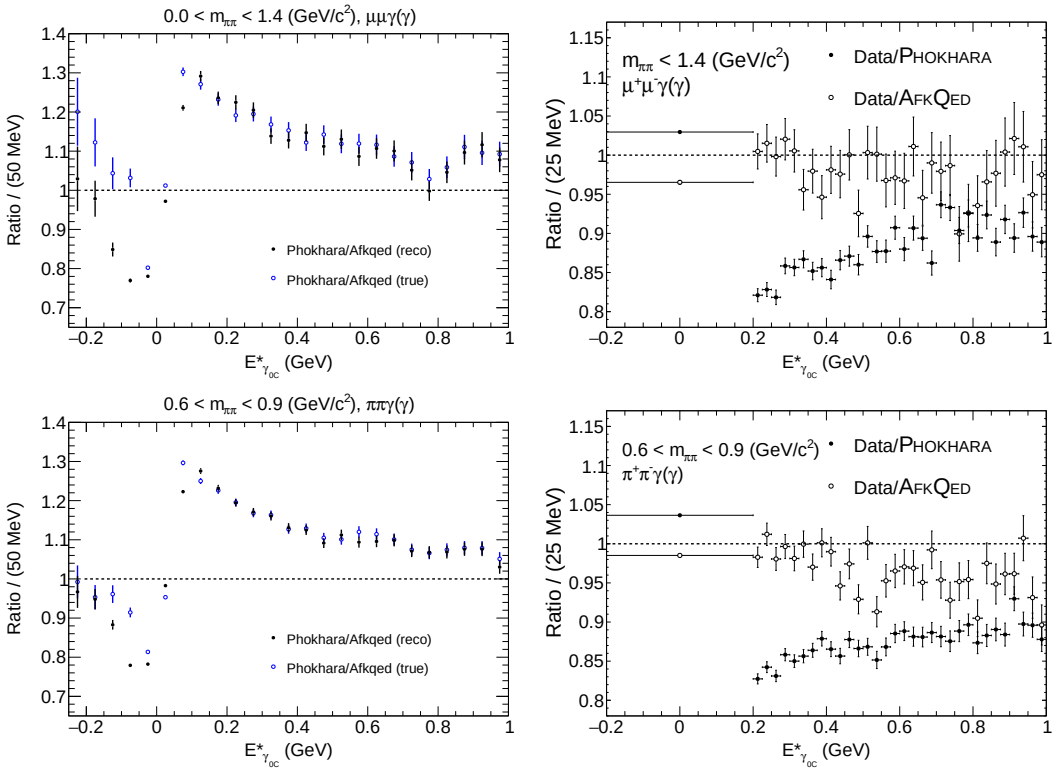

Figure 6.7: Distribution of the calculated energies in the CM frame $E^*_{\gamma 0C}$ is compared between PHOKHARA and AFKQED (left) using both the reconstructed (black full points) and true (blue open points) information, between data and the two MC predictions (right) for events in full polar angle range for the $\mu\mu\gamma$ (top) and $\pi\pi\gamma$ (bottom) processes.

Chapter 7

Analysis of NNLO radiation with results

In Chapter 5, there is already evidence to support the existence of NNLO events in data. In this chapter, a dedicated and detailed study of NNLO radiation is presented.

7.1 NNLO kinematic fitting description

In addition to the two NLO fits which have been described in Section 4.1, the events are submitted to three NNLO fits where two additional photons are allowed along with the main ISR photon and the two charged tracks:

- The $\gamma_{\mathrm{ISR}}2\gamma_{\mathrm{SA}}$ fit, where two additional SA photons are assumed to be emitted at small angles from the beams, one from the positron beam and the other from the electron beam. In this fit, the energies of the additional photons are unknown and their directions are assumed to be collinear with the beams, resulting in a 2C fit.
- The $\gamma_{\mathrm{ISR}}\gamma_{\mathrm{SA}}\gamma_{\mathrm{LA}}$ fit, where one additional photon is measured in the detector and the other is assumed to be collinear with either beam. In this fit, the best fit is chosen amongst the two possibilities of radiating beam. Since the energy of the additional SA photon is unknown, resulting in a 3C fit.
- The $\gamma_{\mathrm{ISR}}2\gamma_{\mathrm{LA}}$ fit, where two additional photons are both measured in the detector, resulting in a 4C fit.

All events are submitted to the $\gamma_{\mathrm{ISR}}2\gamma_{\mathrm{SA}}$ while only events with at least one or two detected photons are submitted to $\gamma_{\mathrm{ISR}}\gamma_{\mathrm{SA}}\gamma_{\mathrm{LA}}$ and $\gamma_{\mathrm{ISR}}2\gamma_{\mathrm{LA}}$ respectively. In the fits the reconstructed photons are required to have a minimum energy of 50 MeV. For all the fits, the measured energy of the detected photons is replaced by the symmetric Novosibirsk function Z [51]. For each photon, the initialization of the corresponding Z variable utilizes the measured energy of the photon. During each step of χ^2 minimization process, the four-momentum constraint is also applied using the photon energies calculated from the current Z values. The same fits are applied to MC events. As the PHOKHARA generator is up to NLO processes, the NNLO fits return degraded χ^2 values and the results represent NLO backgrounds under

the NNLO signals searched for in the data. On the contrary, the AFKQED generator is up to NNLO processes and the NNLO events are produced, hence $\gamma_{\rm ISR}2\gamma_{\rm SA}$ and $\gamma_{\rm ISR}\gamma_{\rm SA}\gamma_{\rm LA}$ fits return reliable fitting values of NNLO events. Since the collinear assumption of additional SA photons is made both at generation level and in the fits, the resulting χ^2 values from the fits are generally better for AFKQED simulated events compared to data where LA emission occurs. It is important to note that events falling into the $\gamma_{\rm ISR}2\gamma_{\rm LA}$ category are not simulated by either generator.

In this study where NNLO events are expected to have larger χ^2 values for the $\gamma_{\rm ISR}2\gamma_{\rm SA}$ and $\gamma_{\rm ISR}\gamma_{\rm SA}\gamma_{\rm LA}$ fits, no 2D-χ^2 selection is applied (see Fig. E. 1 in Appendix E for the 2D-χ^2 distributions of the AFKQED NNLO signal events). As described before, the background level in the pion channel with the known background subtraction remains large, even in the ρ mass range, shown in Fig. 7.1. To improve the selection efficiency and purity of the NNLO samples in data, BDT methods are adopted, which will be explained in the following sections related to pion. In the following sections of this chapter, detailed studies will be performed for the three NNLO fits in both muon and pion channels.

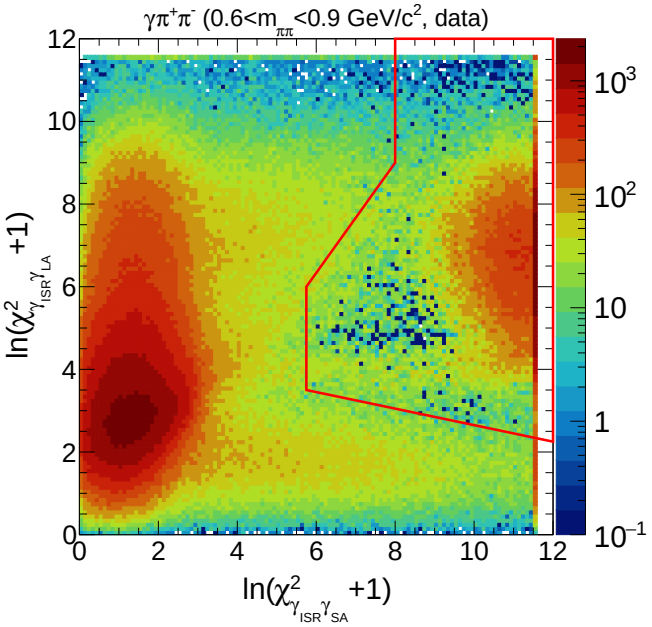

Figure 7.1: The 2D-χ^2 distribution for $\pi\pi\gamma_{\rm ISR}$ in the mass range between 0.6 and 0.9 GeV/c^2, after known background subtraction. The red lines correspond to the optimized 2D-χ^2 selection used in the NLO analysis.

7.2 Study of events with two additional SA photons

7.2.1 Analysis of the muon sample

For the muon sample in the mass range between threshold and 1.4 GeV/c^2, the $\gamma_{\rm ISR}2\gamma_{\rm SA}$ events are selected by requiring the χ^2 value of the $\gamma_{\rm ISR}2\gamma_{\rm SA}$ fit to be smaller than that of all

other NLO and NNLO fits. The reduction of the NLO background can be appreciated from Fig. 7.2, which shows the selected events from the PHOKHARA MC sample. To further reduce the NLO background contribution, the energy in the CM frame for one of the additional SA photons is required to be greater than 0.2 GeV and the other greater than 0.1 GeV. The resulting χ^2 distribution of $\gamma_{\rm ISR}2\gamma_{\rm SA}$ is shown in Fig. 7.3, where the NLO background from $\gamma_{\rm ISR}\gamma_{\rm SA}$ and $\gamma_{\rm ISR}\gamma_{\rm LA}$ events is estimated by using the PHOKHARA sample after correcting for the data and MC different rates discussed at LO and NLO levels (shown in Table 5.3). This NLO background from PHOKHARA (red line in the top-left panel) is observed to be largely dominant over the non-$\mu\mu$ background (in blue). The signal in data is derived by subtracting these backgrounds and is illustrated in the bottom of the left panel. To avoid potential bias between data and AFKQED, the fraction of the $\mu\mu\gamma_{\rm ISR}2\gamma_{\rm SA}$ signal, defined as these events divided by the total number of events in data including all LO, NLO and NNLO events considered in this analysis, is illustrated in the right panel. The signal fraction in data is further compared with the prediction from the AFKQED sample, where the AFKQED signal is restricted to the $\mu\mu\gamma_{\rm ISR}2\gamma_{\rm SA}$ events with two additional SA photons satisfying the energy thresholds. As expected, smaller χ^2 values in the AFKQED sample than that from signals in data are observed since the additional SA photons are generated along the beam directions and thus match the collinear assumption better in the fit.

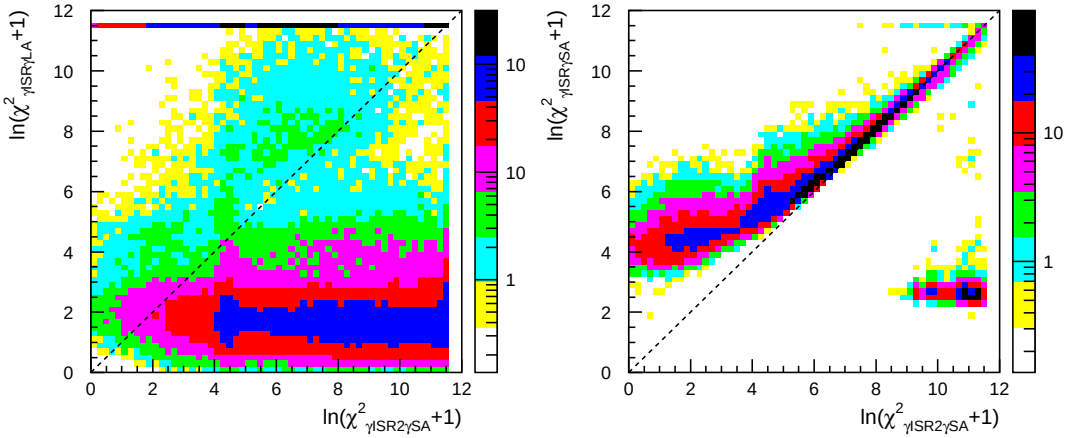

Figure 7.2: The correlation between $\chi^2_{\gamma_{\rm ISR}2\gamma_{\rm SA}}$ and $\chi^2_{\gamma_{\rm ISR}\gamma_{\rm LA}}$ (left) and $\chi^2_{\gamma_{\rm ISR}\gamma_{\rm SA}}$ (right). The dashed line indicates the selection $\chi^2_{\gamma_{\rm ISR}2\gamma_{\rm SA}} < \chi^2_{\gamma_{\rm ISR}\gamma_{\rm LA}}$ and $\chi^2_{\gamma_{\rm ISR}2\gamma_{\rm SA}} < \chi^2_{\gamma_{\rm ISR}\gamma_{\rm SA}}$.

Distributions for the energies of the two additional SA photons in the CM frame are shown in Fig. 7.5, signals in data with the non-$\mu\mu$ and NLO background subtracted are shown in the bottom panel respectively. The fraction of NNLO $\mu\mu\gamma_{\rm ISR}2\gamma_{\rm SA}$ signal in data is further compared in Fig. 7.5 with the prediction from AFKQED. The larger photon energy from AFKQED is limited to 2.3 GeV as stated earlier. A fair agreement is observed between the shapes of the energy distribution in data and AFKQED for both SA photons.

7.2.2 Analysis of the pion sample

For the $\pi\pi\gamma$ sample, the study is more challenging due to the presence of a much larger background from non-$\pi\pi$ background. The study is focused on the mass range between 0.6

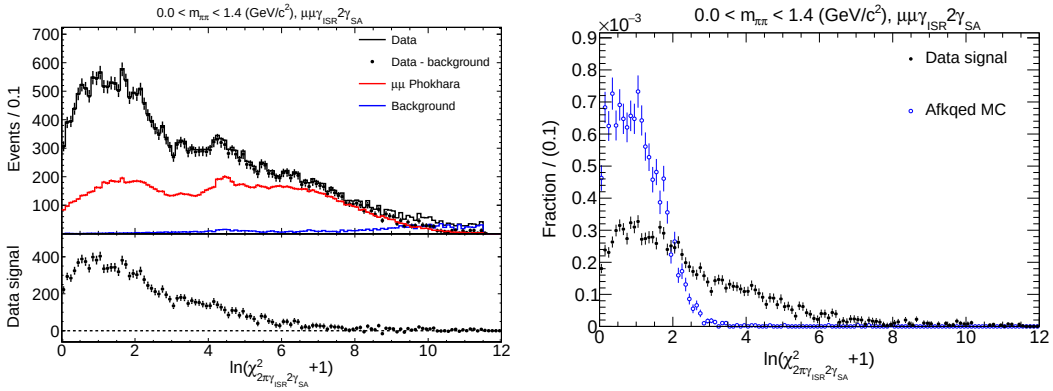

Figure 7.3: Distributions of χ^2 of the $\gamma_{\rm ISR}2\gamma_{\rm SA}$ fit with two additional SA photons ($E^*_{\rm max(2\gamma_{SA})} > 0.2\,{\rm GeV}$ and $E^*_{\rm min(2\gamma_{SA})} > 0.1\,{\rm GeV}$), one along each beam direction, for the mass range below 1.4 GeV/c^2 in the $\mu\mu\gamma_{\rm ISR}2\gamma_{\rm SA}$ process. The top-left panel shows data (black histogram), data with background subtraction (black points), non-$\mu\mu$ background (blue) and the NLO background from PHOKHARA (red). The left-bottom panel shows the $\gamma_{\rm ISR}2\gamma_{\rm SA}$ signals in data after subtracting related backgrounds. The right panel shows the comparison between signals in data and the predictions from AFKQED.

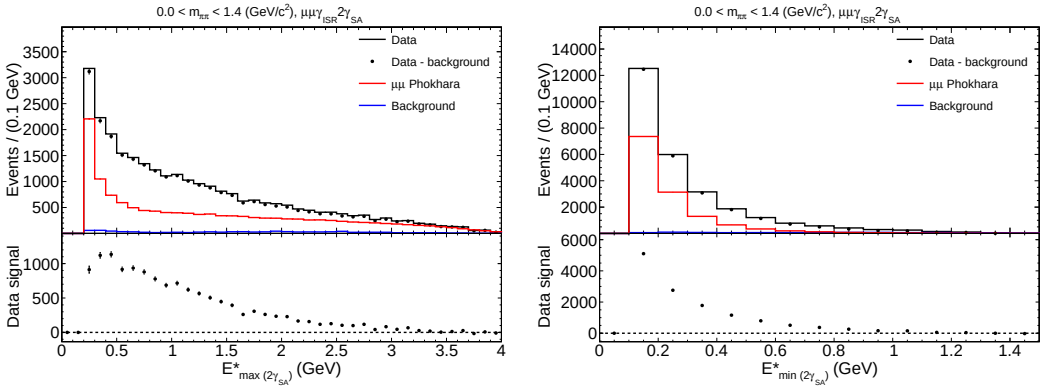

Figure 7.4: Distributions for energies of the additional SA photons in the CM frame with larger (left) and smaller (right) energies in the $\gamma_{\rm ISR}2\gamma_{\rm SA}$ fit for the mass range from threshold to 1.4 GeV/c^2 in the $\mu\mu\gamma_{\rm ISR}2\gamma_{\rm SA}$ process. The top panel shows data (black histogram), data with background subtraction (black points), non-$\mu\mu$ background (blue) and the NLO background from PHOKHARA (red). The bottom panel shows the $\gamma_{\rm ISR}2\gamma_{\rm SA}$ signals in data after subtracting these backgrounds.

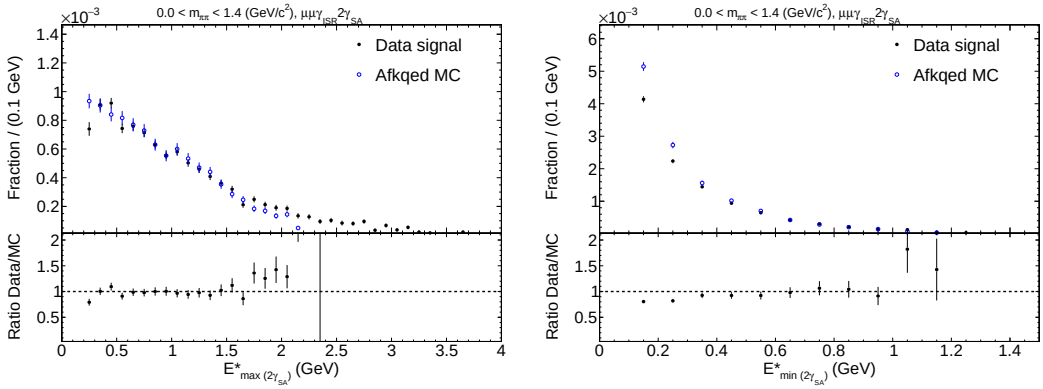

Figure 7.5: Fractions of NNLO $\gamma_{\rm ISR}2\gamma_{\rm SA}$ signals in data and AFKQED MC and their ratio as a function of the larger (left) and smaller (right) energies of the additional SA photons in the CM frame, for the mass range below 1.4 GeV/c^2 in the $\mu\mu\gamma_{\rm ISR}2\gamma_{\rm SA}$ process. For the left plot, the MC distributions have been scaled to that of data using integrated fraction below 2.3 GeV.

and 0.9 GeV/c^2 around the ρ resonance because the small cross section and relatively large background in the low mass range below 0.6 GeV/c^2 and high mass range between 0.9 and 1.4 GeV/c^2 make it difficult to perform an NNLO analysis in those regions. To suppress the non-$\pi\pi$ background and enhance the sensitivity to the expected NNLO signals, a BDT selection is applied by using the following set of discriminant variables based on their importance ranking:

Egcm The main ISR photon energy in the CM frame,

Einfit The total energy of the two tracks used in the fit,

Ephsum-Eph1 The difference between the total measured neutral energy in the calorimeter and the main ISR photon energy,

Nphgood The number of photons with a measured energy above 50 MeV,

Dpsing The angle in the laboratory frame between the ISR photon and the missing momentum of charged tracks and other photons,

Mgg2 The invariant mass of the second leading photon with another photon that has a value closest to π^0 mass,

Costhpi The pion angle with respect to the main ISR photon direction in the two-pion CM system,

Zernike20 and Zernike42 Transverse shower shape variables for the main ISR photon,

Mgg0 The invariant mass of the main ISR photon with another photon that has a value closest to π^0 mass.

The BDT method uses the events of $\pi\pi\gamma_{\rm ISR}2\gamma_{\rm SA}$ selected from AFKQED as signal and other non-$\pi\pi$ events as background. The BDT response outputs for the signal events and background events are shown in Fig. 7.6. The vertical dashed line in the figure corresponds to the nominal selection $\mathrm{BDT} > -0.07$ with the best SOB value. The BDT response distributions are further compared between data and backgrounds in Fig. 7.7 (left) and the good agreement observed in the background-dominant region on the left side of the distributions indicates that the estimation of the background is satisfactory. The BDT response distribution of the signal in data after background subtraction is compared with the prediction from AFKQED sample in Fig. 7.7 (right). The resulting BDT selection efficiencies are found to be $0.816(7)$ for signal in data and $0.926(2)$ for MC where the uncertainty is statistical.

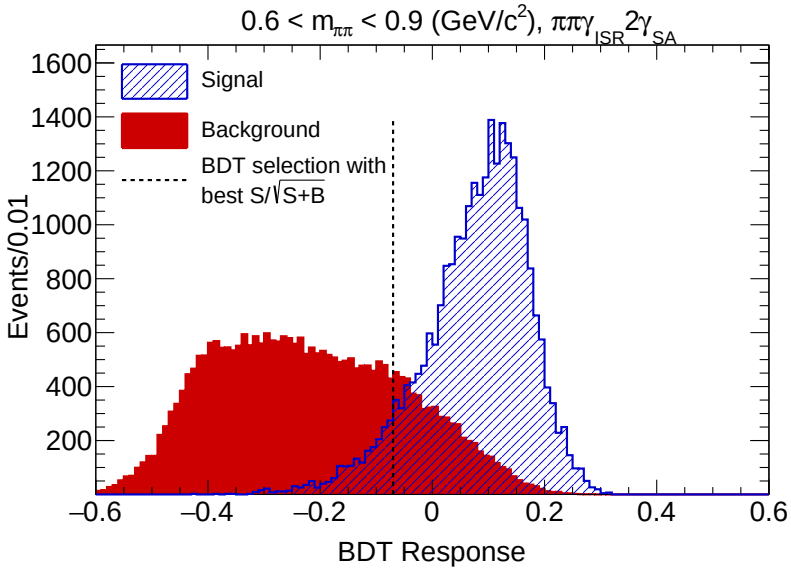

Figure 7.6: BDT response distribution for the $\gamma_{\rm ISR}2\gamma_{\rm SA}$ fit with two additional SA photons ($E^*_{\rm max(2\gamma_{SA})} > 0.2\,\mathrm{GeV}$ and $E^*_{\rm min(2\gamma_{SA})} > 0.1\,\mathrm{GeV}$), one along each beam direction, for the mass range between 0.6 and 0.9 GeV/c^2 in the $\pi\pi\gamma_{\rm ISR}2\gamma_{\rm SA}$ process.

After applying the BDT model to data, the $\pi\pi$ PHOKHARA and other non-$\pi\pi$ background MC samples, the resulting χ^2 distribution of $\gamma_{\rm ISR}2\gamma_{\rm SA}$ fit for the selected events are illustrated in Fig. 7.8 (left). With the BDT selection applied, it shows both the NLO background from PHOKHARA and non-$\pi\pi$ background is reduced to a level comparable to that of the $\mu\mu\gamma_{\rm ISR}2\gamma_{\rm SA}$ sample illustrated in Fig. 7.3. The χ^2 comparison of the $\gamma_{\rm ISR}2\gamma_{\rm SA}$ fit between the selected signals in data and the prediction from the AFKQED for the $\pi\pi\gamma_{\rm ISR}2\gamma_{\rm SA}$ sample is shown in Fig. 7.8 (right) and is also similar to that achieved in the $\mu\mu\gamma_{\rm ISR}2\gamma_{\rm SA}$ sample.

Distributions for the energies of the two additional SA photons in the CM frame with the nominal BDT selection are shown in Fig. 7.9 (left), the signal in data with the non-$\pi\pi$ and NLO background subtracted is shown in the bottom panel respectively. Similar $\mu\mu\gamma_{\rm ISR}2\gamma_{\rm SA}$ distributions in the mass range between 0.6 and 0.9 GeV/c^2 are shown on the right side of Fig. 7.9. The fraction of the NNLO $\gamma_{\rm ISR}2\gamma_{\rm SA}$ signal in data is compared with the prediction from AFKQED in Fig. 7.10 for the $\pi\pi\gamma_{\rm ISR}2\gamma_{\rm SA}$ sample with the nominal BDT selection, which is then further compared with similar fractions from the $\mu\mu\gamma_{\rm ISR}2\gamma_{\rm SA}$ sample in the

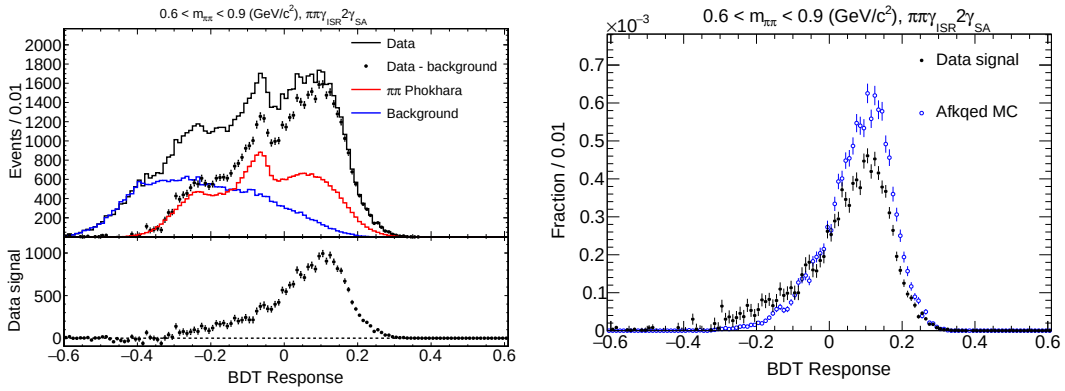

Figure 7.7: Left: BDT response distributions comparison between data and background. Right: BDT response distributions comparison between data with background subtraction and the prediction from the AFKQED MC sample.

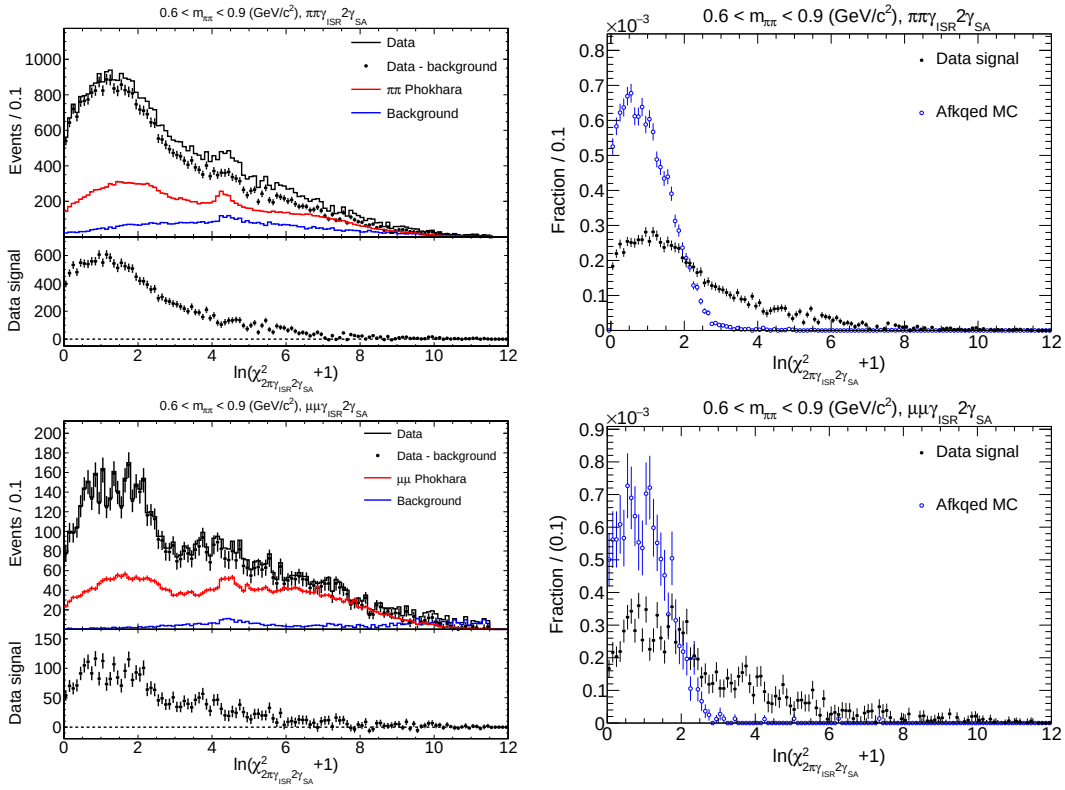

Figure 7.8: Distributions of χ^2 of the $\gamma_{\rm ISR}2\gamma_{\rm SA}$ fit with two additional SA photons ($E^*_{\rm max(2\gamma_{SA})} > 0.2\,{\rm GeV}$ and $E^*_{\rm min(2\gamma_{SA})} > 0.1\,{\rm GeV}$), one along each beam direction, after the nominal BDT selection for the mass range between 0.6 and 0.9 GeV/c^2 in the $\pi\pi\gamma_{\rm ISR}2\gamma_{\rm SA}$ process (top), compared to the $\mu\mu\gamma_{\rm ISR}2\gamma_{\rm SA}$ process (bottom) in the same mass range. Left: the top-left panel in each plot shows data (black histogram), data with background subtraction (black points), non-$\mu\mu$ background (blue) and the NLO background from PHOKHARA (red), while the left-bottom panel shows the $\gamma_{\rm ISR}2\gamma_{\rm SA}$ signals in data after subtracting these backgrounds. Right: each plot shows the comparison between signals in data and the predictions from AFKQED.

same mass range. The larger photon energy from AFKQED is again limited to 2.3 GeV. A fair agreement is observed between the shapes of the energy distribution in data and AFKQED for both SA photons for the $\pi\pi\gamma_{\mathrm{ISR}}2\gamma_{\mathrm{SA}}$ process.

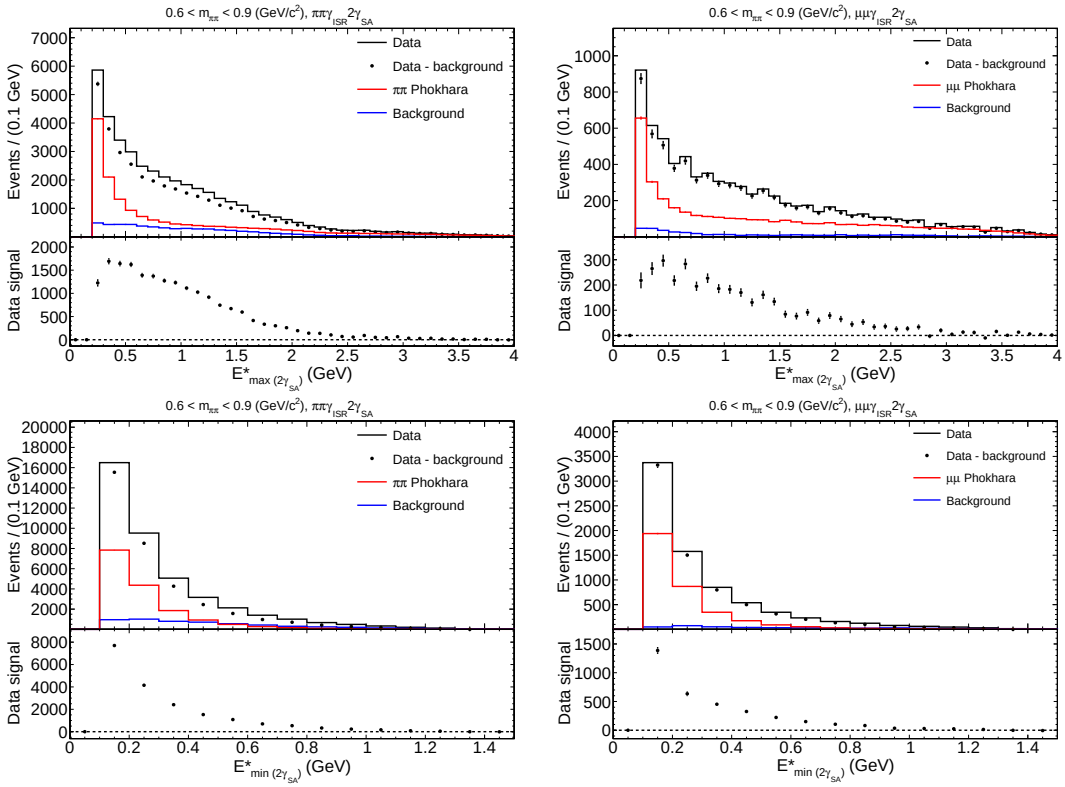

Figure 7.9: Distributions for energies of the additional SA photons in the CM frame with larger (top) and smaller (low) in the $\gamma_{\mathrm{ISR}}2\gamma_{\mathrm{SA}}$ fit for $\pi\pi\gamma_{\mathrm{ISR}}2\gamma_{\mathrm{SA}}$ process with the nominal BDT selection (left) and for $\mu\mu\gamma_{\mathrm{ISR}}2\gamma_{\mathrm{SA}}$ process (right) in the mass range between 0.6 and 0.9 GeV/c^2. For each single plot, the top panel shows data (black histogram), data with background subtraction (black points), non-$\pi\pi$ (or non-$\mu\mu$) background (blue) and the NLO background from PHOKHARA (red), while the bottom panel shows the $\gamma_{\mathrm{ISR}}2\gamma_{\mathrm{SA}}$ signals in data after subtracting these backgrounds.

7.2.3 Summary of the NNLO study with two additional SA photons

The fractions of the NNLO $\mu\mu\gamma_{\mathrm{ISR}}2\gamma_{\mathrm{SA}}$ (mass range below 1.4 GeV/c^2 and between 0.6 and 0.9 GeV/c^2) and $\pi\pi\gamma_{\mathrm{ISR}}2\gamma_{\mathrm{SA}}$ (mass range between 0.6 and 0.9 GeV/c^2) signals in data are summarized in Table 7.1. Each fraction is normalized to the total number of events in the respective muon and pion samples. The total number of events is dominated by the LO and NLO events. The background contribution as well as the feed-through contribution from LO and NLO events in data have been subtracted using predictions from the MC simulations. The fractions have also been corrected for selection efficiencies. For the $\pi\pi\gamma_{\mathrm{ISR}}2\gamma_{\mathrm{SA}}$ process, the selection efficiencies include the BDT selection efficiencies (Eff.). The larger uncertainty

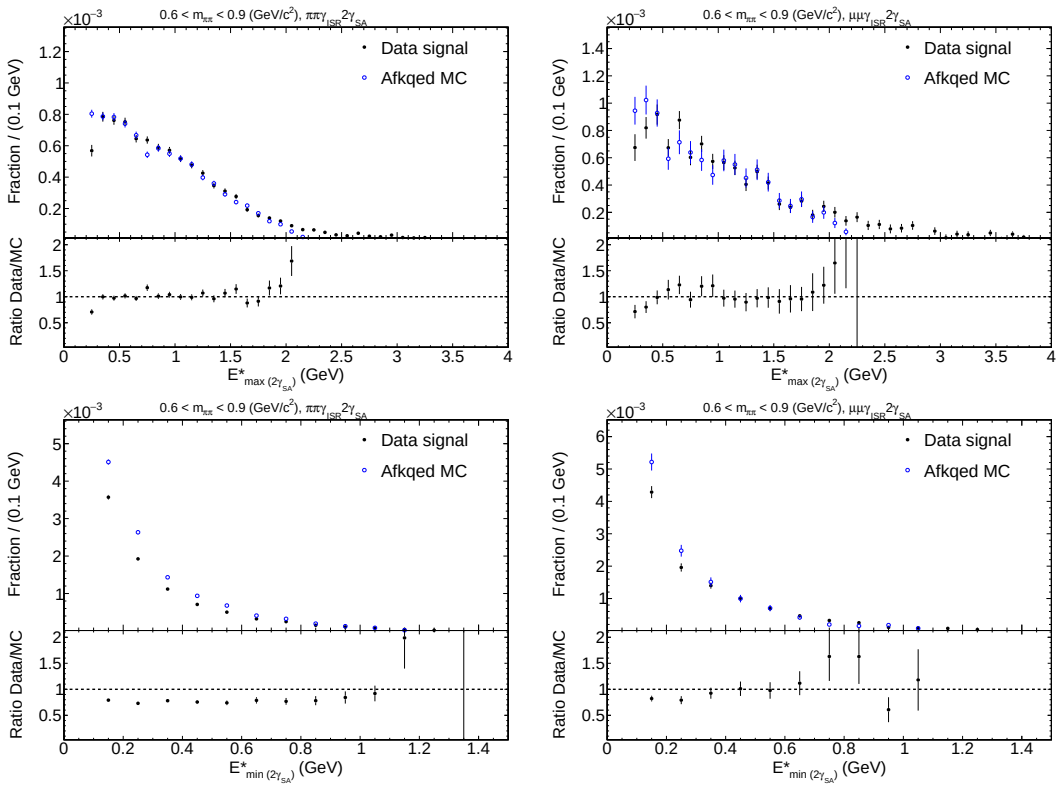

Figure 7.10: Fractions of NNLO $\gamma_{\rm ISR}2\gamma_{\rm SA}$ signals in data and AFKQED MC and their ratio as a function of the larger (top) and smaller (bottom) energies of the additional SA photons in the CM frame, for the mass range between 0.6 and 0.9 GeV/c^2 comparing the $\pi\pi\gamma_{\rm ISR}2\gamma_{\rm SA}$ process with the nominal BDT selection (left) and $\mu\mu\gamma_{\rm ISR}2\gamma_{\rm SA}$ process (right). In the top plots, the MC distributions have been scaled to that of data using integrated fractions for $E^*_{\rm max(2\gamma_{SA})}$ below 2.3 GeV.

shown in the table for data of the $\pi\pi\gamma_{\mathrm{ISR}}2\gamma_{\mathrm{SA}}$ process is mainly attributed to the difference in BDT efficiencies between data and MC, which exceeds the statistical uncertainties.

NNLO fraction	$\mu\mu\gamma_{\mathrm{ISR}}2\gamma_{\mathrm{SA}}$ $m_{\pi\pi} < 1.4\,\mathrm{GeV}/c^2$	$\mu\mu\gamma_{\mathrm{ISR}}2\gamma_{\mathrm{SA}}$ $0.6 < m_{\pi\pi} < 0.9\,\mathrm{GeV}/c^2$	$\pi\pi\gamma_{\mathrm{ISR}}2\gamma_{\mathrm{SA}}$ $0.6 < m_{\pi\pi} < 0.9\,\mathrm{GeV}/c^2$
Eff.	0.908(5)	0.899(10)	Da: 0.752(101), A: 0.853(3)
Data	0.01165(7)(6)(3)	0.01095(14)(12)(12)	0.01037(6)(140)(9)

Table 7.1: Resulting NNLO $\gamma_{\mathrm{ISR}}2\gamma_{\mathrm{SA}}$ signal fractions in data between $\mu\mu\gamma_{\mathrm{ISR}}2\gamma_{\mathrm{SA}}$ and $\pi\pi\gamma_{\mathrm{ISR}}2\gamma_{\mathrm{SA}}$ processes. The fractions have been corrected for the selection efficiency (Eff.). The numbers in brackets represent different uncertainties with the first one being statistical, the second being systematical due to the uncertainty of efficiency corrections and the third due to the background subtraction.

7.3 Study of events with one additional SA photon and one additional measured photon

The second NNLO process called $\gamma_{\rm ISR}\gamma_{\rm SA}\gamma_{\rm LA}$ involves one of the two additional photons corresponds to a measured photon at large angle within the detector acceptance with a fitted energy in the laboratory frame larger than 0.2 GeV. The other photon is assumed to be emitted along one of the beams with its fitted energy in the CM frame required to be above 0.1 GeV. In addition, the χ^2 value of the $\gamma_{\rm ISR}\gamma_{\rm SA}\gamma_{\rm LA}$ fit is required to be smaller than that from any other NLO or NNLO fits.

7.3.1 Study of the muon sample

For the $\mu\mu\gamma_{\rm ISR}\gamma_{\rm SA}\gamma_{\rm LA}$ sample in the mass range below 1.4 GeV/c^2, the distribution for χ^2 value of the $\gamma_{\rm ISR}\gamma_{\rm SA}\gamma_{\rm LA}$ fit is shown in Fig. 7.11, where the non-$\mu\mu$ background is tiny. The NLO background is estimated with the PHOKHARA sample, with corrections applied due to the different rates between data and MC observed at LO and NLO levels. The NLO background is much larger than the non-$\mu\mu$ background but remains still relatively smaller compared to the NNLO signal in $\mu\mu\gamma_{\rm ISR}\gamma_{\rm SA}\gamma_{\rm LA}$. In the right panel of Fig. 7.11, the χ^2 distribution of the NNLO signals in data is further compared with the prediction from the AFKQED sample for events with photons satisfying $\theta_{\rm min(trk,\gamma_{LA})} < 20^\circ$. This $\theta_{\rm min(trk,\gamma_{LA})} < 20^\circ$ cut is required since the LA ISR component is not produced in the AFKQED sample. The χ^2 shape comparison between data and AFKQED is better than that in the $\mu\mu\gamma_{\rm ISR}2\gamma_{\rm SA}$ case. This improvement can be attributed to the fact that the collinear assumption is applied only to one of the fitted photons in the $\mu\mu\gamma_{\rm ISR}\gamma_{\rm SA}\gamma_{\rm LA}$ fit.

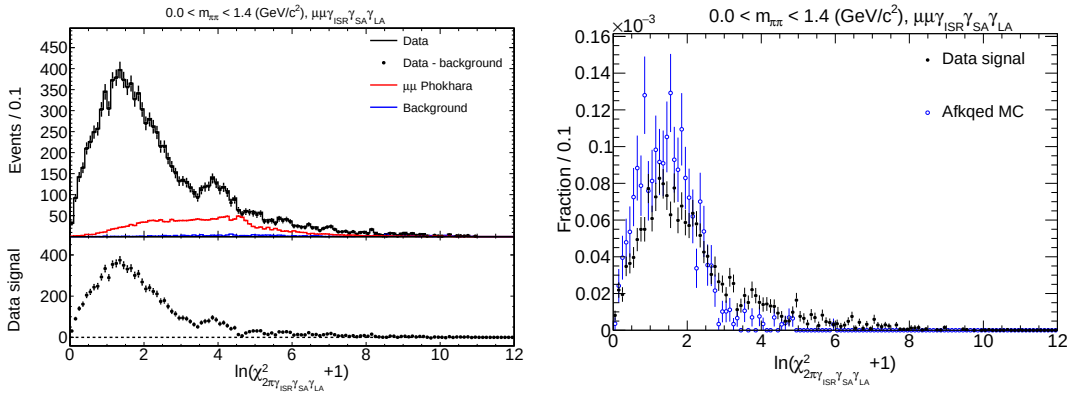

Figure 7.11: Distribution of χ^2 of the $\gamma_{\rm ISR}\gamma_{\rm SA}\gamma_{\rm LA}$ fit with one additional SA photon along one of the beam directions ($E^*_{\gamma_{\rm SA}} > 0.1$ GeV) and one additional measured LA photon ($E_{\gamma_{\rm LA}} > 0.2$ GeV) for the mass range below 1.4 GeV/c^2 for the $\mu\mu\gamma_{\rm ISR}\gamma_{\rm SA}\gamma_{\rm LA}$ process. The top-left panel shows data (black histogram), data with background subtraction (black points), non-$\mu\mu$ background (blue) which is tiny and the NLO background from PHOKHARA (red). The left-bottom panel shows the $\gamma_{\rm ISR}\gamma_{\rm SA}\gamma_{\rm LA}$ signals in data after subtracting related backgrounds. The right panel shows the comparison between signals in data and the predictions from AFKQED satisfying $\theta_{\rm min(trk,\gamma_{LA})} < 20^\circ$.

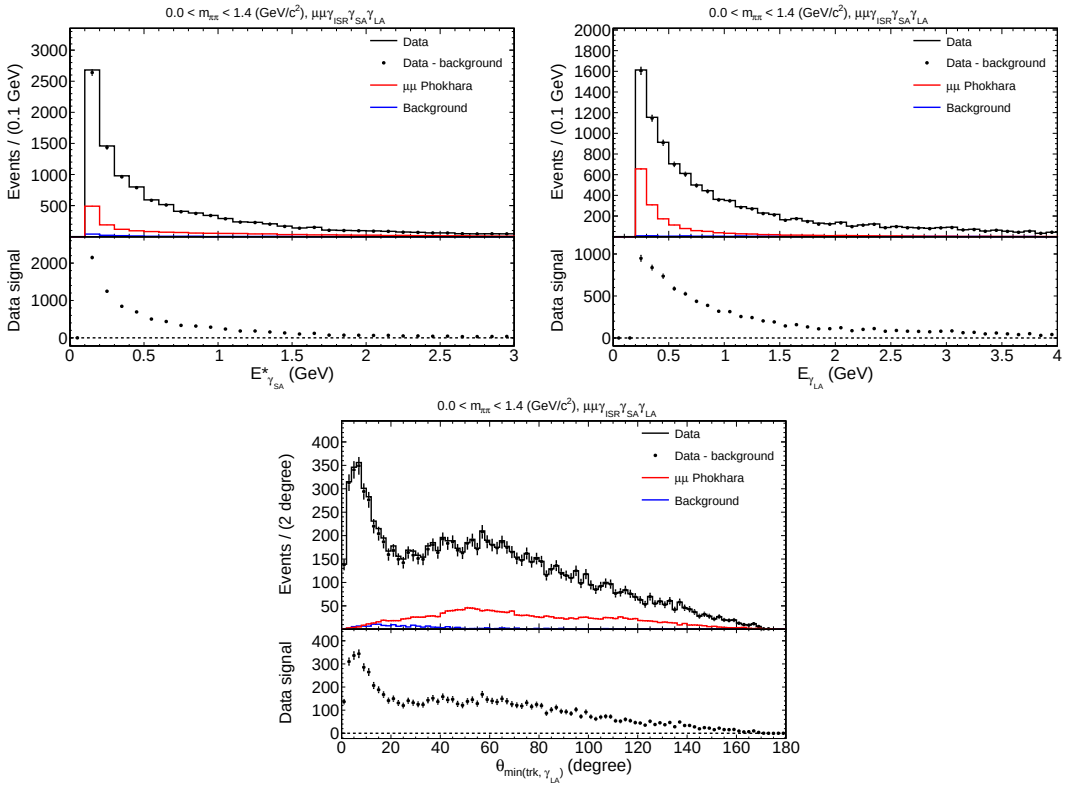

Figure 7.12: Top-left: Energy distribution of the additional SA photon in the CM frame. Top-right: Energy distribution of the additional LA photon in the laboratory frame. Bottom: The minimum angle between the additional LA photon and one of the two charged tracks in the $\gamma_{\rm ISR}\gamma_{\rm SA}\gamma_{\rm LA}$ fit. For each single plot, data (black histogram), PHOKHARA MC NLO background (red) and other non-$\mu\mu$ background (blue) and data with background subtraction (full points) are shown in the top panel, and the signal in data is shown in the respective bottom panel for the mass range below 1.4 GeV/c^2 for the $\mu\mu\gamma_{\rm ISR}\gamma_{\rm SA}\gamma_{\rm LA}$ samples.

Distribution of the fitted energy of the SA in the CM frame and the LA in the laboratory frame is shown in Fig. 7.12. The distribution of the minimum angle between the LA photon and one of the two charged tracks is shown in Fig. 7.12 as well. The $\theta_{\rm min(trk,\gamma_{LA})}$ distribution clearly shows two distinct components, one observed at small angles dominated by the FSR radiation while the other corresponds to the additional LA ISR radiation. The reason for larger energy threshold (0.2 GeV) used to select the LA photon is to suppress relatively larger NLO background contribution at the low energies in the energy spectra.

The fraction of the selected NNLO $\gamma_{\rm ISR}\gamma_{\rm SA}\gamma_{\rm LA}$ signals divided by the total number of events in data after background subtraction are further compared to the predictions from the AFKQED sample in Fig. 7.13. The fair comparison of the energy distribution is performed by requiring $\theta_{\rm min(trk,\gamma_{LA})}$ below 20° due to the missing LA ISR component for the AFKQED sample.

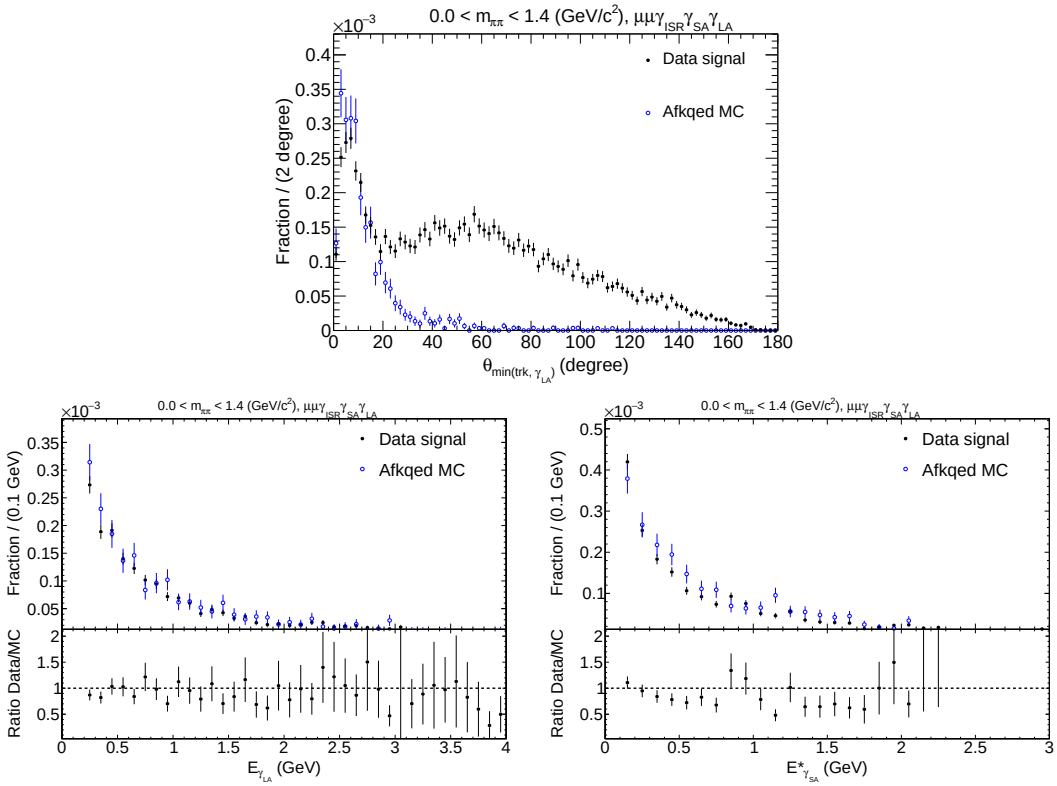

Figure 7.13: Top: Fraction of NNLO $\gamma_{\rm ISR}\gamma_{\rm SA}\gamma_{\rm LA}$ signals in data (black points) and AFKQED (blue open points) as a function of $\theta_{\rm min(trk,\gamma_{LA})}$ defined in the text for the mass range below 1.4 GeV/c^2 in the $\mu\mu\gamma_{\rm ISR}\gamma_{\rm SA}\gamma_{\rm LA}$ sample. The missing LA ISR component is clearly seen here. Bottom-left: Fraction of NNLO signals in data (black points) and AFKQED (blue open points) as a function of energy of the additional LA photon in the laboratory frame with $\theta_{\rm min(trk,\gamma_{LA})} < 20^\circ$ applied. Bottom-right: Fraction of NNLO signals in data (black points) and AFKQED (blue open points) as a function of energy of the additional SA photon in the CM frame with $\theta_{\rm min(trk,\gamma_{LA})} < 20^\circ$ applied.

7.3.2 Study of the pion sample

For the $\pi\pi\gamma_{\rm ISR}\gamma_{\rm SA}\gamma_{\rm LA}$ sample in the mass range between 0.6 and 0.9 GeV/c^2, the huge non-$\pi\pi$ background contribution prevents the reliable estimation of the NNLO signal fractions in both data and MC sample. To reduce the background, two different BDT models similar to that of $\gamma_{\rm ISR}2\gamma_{\rm SA}$ are constructed and then compared. For one of the BDTs (called BDT1), the training signal events are extracted from the AFKQED sample. The input discriminant variables used in BDT1 are:

- Einfit, Ephsum-Eph1, Nphgood, Mgg2, Costhpi, Zernike20, Zernike42 and Mgg0. All these variables are described in the $\pi\pi\gamma_{\rm ISR}2\gamma_{\rm SA}$ analysis part (Section 7.2.2).
- $E^*_{\gamma_{\rm SA}}$ is the new-added variable, namely the fitted energy of the SA photon in the CM frame.

However, given that the AFKQED MC sample does not include the complete signal sample due to the missing LA ISR component, another BDT model (named BDT2) is constructed where the training signal is extracted from the $\mu\mu\gamma_{\rm ISR}\gamma_{\rm SA}\gamma_{\rm LA}$ signal in data. To reduce the statistical fluctuations, signal events are selected from the full mass range below 1.4 GeV/c^2, then appropriate scale factors are applied taking into account the expected difference in the event rates between different mass ranges and between the $\mu\mu$ and $\pi\pi$ processes. For BDT2, the input variables are the same as those in BDT1 except the Costhpi variable has been excluded since its distribution is different between the $\pi\pi$ and $\mu\mu$ processes. The resulting BDT response distribution from BDT1 is shown in Fig. 7.14. The signal in this distribution has been scaled by a factor of around 3.78 to take into the difference due to the missing LA ISR component. The scale factor is calculated from the $\theta_{\rm min(trk,\gamma_{LA})}$ distribution of the $\gamma_{\rm ISR}\gamma_{\rm LA}$ signal from the PHOKHARA MC sample. For BDT2, it has been checked using the $\mu\mu\gamma_{\rm ISR}\gamma_{\rm SA}\gamma_{\rm LA}$ data sample that the shapes of the BDT input variables are fairly independent of $\theta_{\rm min(trk,\gamma_{LA})}$ by comparing the two samples above and below 20°.

The vertical dashed line in Fig. 7.14 (top-left) corresponds to the nominal BDT selection that maximizes the SOB value. The comparison of BDT response distributions between data and backgrounds is presented in Fig. 7.14 (top-right) to check their agreement. The good agreement observed in the background-dominant region on the left side of the corresponding distribution indicates that the background contribution is adequately modeled. The BDT response distribution of the signal in data after background subtraction is further compared to that from the AFKQED sample in Fig. 7.14 (bottom). The resulting BDT selection efficiencies for BDT1 are $0.748(49)$ for data and $0.853(11)$ for MC, with the quoted uncertainty being statistical. Similar procedures are performed for BDT2 and the corresponding efficiencies are $0.745(49)$ and $0.613(16)$ for data and MC, respectively. The following plots are based on BDT1 model while the BDT2 model will be used for systematic uncertainty estimation due to the missing LA ISR component for the AFKQED sample.

Applying the nominal BDT selection to the data, NLO background from the $\pi\pi$ PHOKHARA sample and other non-$\pi\pi$ background MC samples, the χ^2 distribution of the $\gamma_{\rm ISR}\gamma_{\rm SA}\gamma_{\rm LA}$ fit is presented in Fig. 7.15. The fraction of the signal distribution divided by the total number of events in data after the background subtraction is further compared with that from the AFKQED sample in the right panel for events satisfying $\theta_{\rm min(trk,\gamma_{LA})} < 20°$. Good agreement between data and the AFKQED MC prediction is observed.

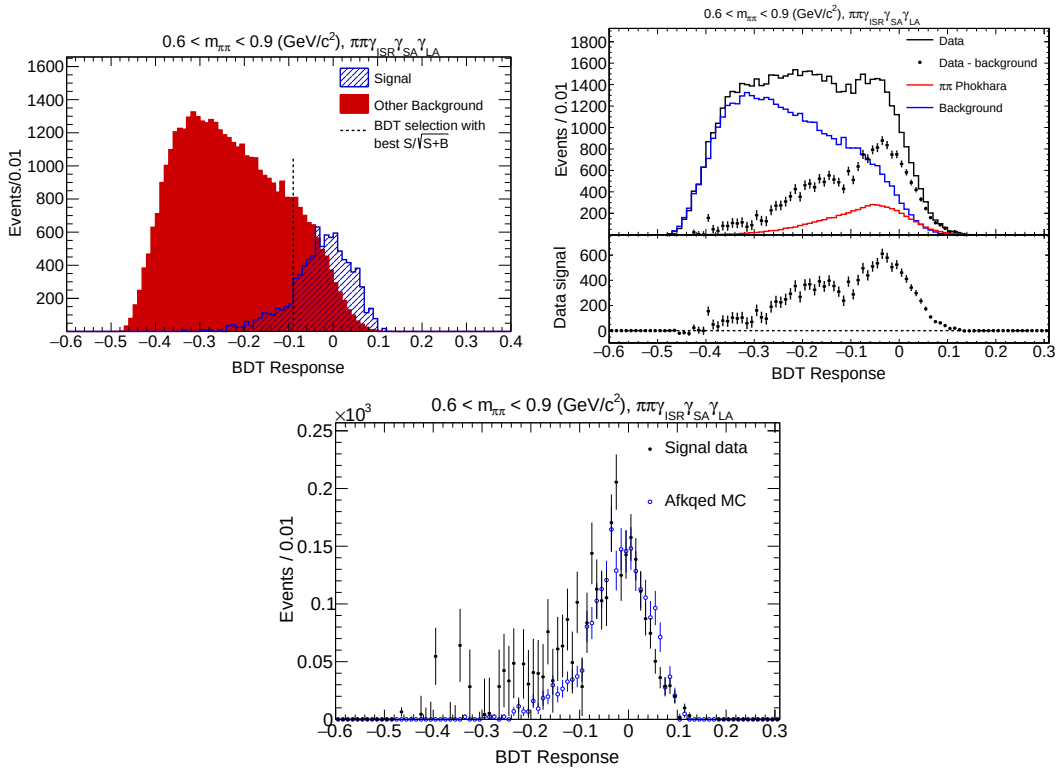

Figure 7.14: Top-left: BDT response distribution for events satisfying $\gamma_{\rm ISR}\gamma_{\rm SA}\gamma_{\rm LA}$ fit with one additional SA photon along one of the beam directions ($E^*_{\gamma_{\rm SA}} > 0.1$ GeV) and one additional LA photon ($E_{\gamma_{\rm LA}} > 0.2$ GeV) for the mass range between 0.6 and 0.9 GeV/c^2 for the $\pi\pi\gamma_{\rm ISR}\gamma_{\rm SA}\gamma_{\rm LA}$ process. Top-right: BDT response distributions comparing data and background. Bottom: BDT response distributions comparing data with background subtraction with the prediction from AFKQED requiring the additional LA photon to satisfy $\theta_{\rm min(trk,\gamma_{LA})}$ below 20°.

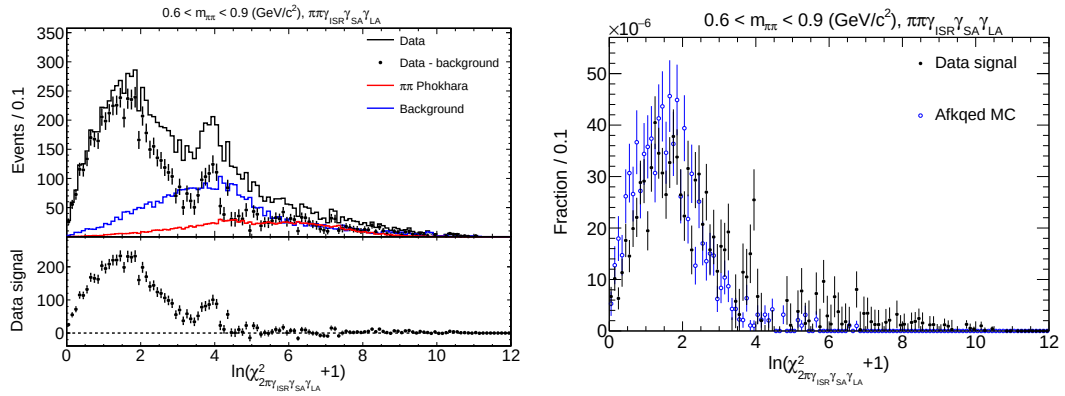

Figure 7.15: Distribution of χ^2 of the $\gamma_{\rm ISR}\gamma_{\rm SA}\gamma_{\rm LA}$ fit with one additional SA photon along one of the beam directions ($E^*_{\gamma_{\rm SA}} > 0.1$ GeV) and one additional measured LA photon ($E_{\gamma_{\rm LA}} > 0.2$ GeV) for the mass range between 0.6 and 0.9 GeV/c^2 for the $\pi\pi\gamma_{\rm ISR}\gamma_{\rm SA}\gamma_{\rm LA}$ process. The top-left panel shows data (black histogram), data with background subtraction (black points), non-$\pi\pi$ background (blue) and the NLO background from PHOKHARA (red). The left-bottom panel shows the $\gamma_{\rm ISR}\gamma_{\rm SA}\gamma_{\rm LA}$ signals in data after subtracting related backgrounds. The right panel shows the comparison between signals in data and the predictions from AFKQED satisfying $\theta_{\rm min(trk,\gamma_{LA})} < 20^\circ$

Distribution of the fitted energy of the SA in the CM frame and the LA in the laboratory frame is shown in Fig. 7.16. The distribution of the minimum angle between the LA photon and one of the two charged tracks is shown in Fig. 7.16 as well. The latter distribution shows the FSR and LA ISR components in the NNLO $\pi\pi\gamma_{\rm ISR}\gamma_{\rm SA}\gamma_{\rm LA}$ sample. The fractions of the signals in data and AFKQED MC are also compared in Fig. 7.17 as a function of $\theta_{\rm min(trk,\gamma_{LA})}$, $E^*_{\gamma_{\rm SA}}$ and $E_{\gamma_{\rm LA}}$ in the same mass range between 0.6 and 0.9 GeV/c^2 between the $\pi\pi\gamma_{\rm ISR}\gamma_{\rm SA}\gamma_{\rm LA}$ (left) and $\mu\mu\gamma_{\rm ISR}\gamma_{\rm SA}\gamma_{\rm LA}$ (right) samples. For the energy distributions of the SA and LA, the selection $\theta_{\rm min(trk,\gamma_{LA})} < 20^\circ$ is applied for a fair comparison. Similar distributions are observed between $\pi\pi\gamma_{\rm ISR}\gamma_{\rm SA}\gamma_{\rm LA}$ and $\mu\mu\gamma_{\rm ISR}\gamma_{\rm SA}\gamma_{\rm LA}$ processes, and fair agreement is observed between data and AFKQED sample.

7.3.3 Summary of the NNLO analysis of $\gamma_{\rm ISR}\gamma_{\rm SA}\gamma_{\rm LA}$ fit

The fractions of NNLO signals in $\mu\mu\gamma_{\rm ISR}\gamma_{\rm SA}\gamma_{\rm LA}$ and $\pi\pi\gamma_{\rm ISR}\gamma_{\rm SA}\gamma_{\rm LA}$ processes in data are summarized in Table 7.2 for additional photon satisfying $\theta_{\rm min(trk,\gamma_{LA})} < 20^\circ$. The fractions are normalized to the total number of events in the corresponding muon and pion samples. For the $\mu\mu\gamma_{\rm ISR}\gamma_{\rm SA}\gamma_{\rm LA}$ signals, the efficiency corrections for the χ^2 selection of $0.722(21)$ and $0.706(32)$ are also taken into account in the mass range below 1.4 GeV/c^2 and between 0.6 and 0.9 GeV/c^2, respectively. The numbers quoted in brackets are statistical errors. For $\pi\pi\gamma_{\rm ISR}\gamma_{\rm SA}\gamma_{\rm LA}$ signals, the efficiency corrections include the nominal BDT selection efficiencies described above. The fake photon correction has also been applied. The fractions of NNLO $\gamma_{\rm ISR}\gamma_{\rm SA}\gamma_{\rm LA}$ signals in data selected with $\theta_{\rm min(trk,\gamma_{LA})} > 20^\circ$ are summarized in Table 7.3. Since LA ISR component is not included in the AFKQED sample, the efficiency is taken from the AFKQED sample with $\theta_{\rm min(trk,\gamma_{LA})}$ below 20°, with an additional correction from the nominal BDT selection efficiencies for the $\pi\pi\gamma_{\rm ISR}\gamma_{\rm SA}\gamma_{\rm LA}$ signals. In additional,

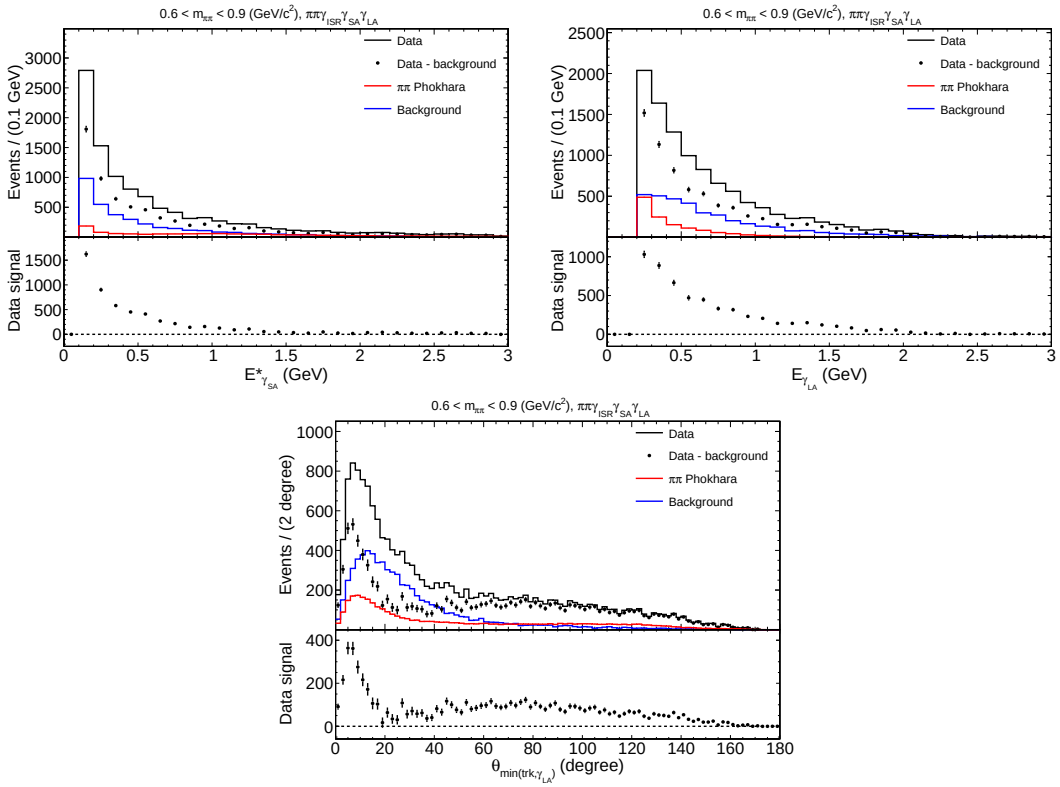

Figure 7.16: Top-left: Energy distribution of the additional SA photon in the CM frame. Top-right: Energy distribution of the additional LA photon in the laboratory frame. Bottom: The minimum angle between the additional LA photon and one of the two charged tracks in the $\gamma_{\rm ISR}\gamma_{\rm SA}\gamma_{\rm LA}$ fit. For each single plot, data (black histogram), PHOKHARA MC NLO background (red) and other non-$\pi\pi$ background (blue) and data with background subtraction (full points) are shown in the top panel, and the signal in data is shown in the respective bottom panel for the mass range between 0.6 and 0.9 GeV/c^2 in the $\pi\pi\gamma_{\rm ISR}\gamma_{\rm SA}\gamma_{\rm LA}$ sample.

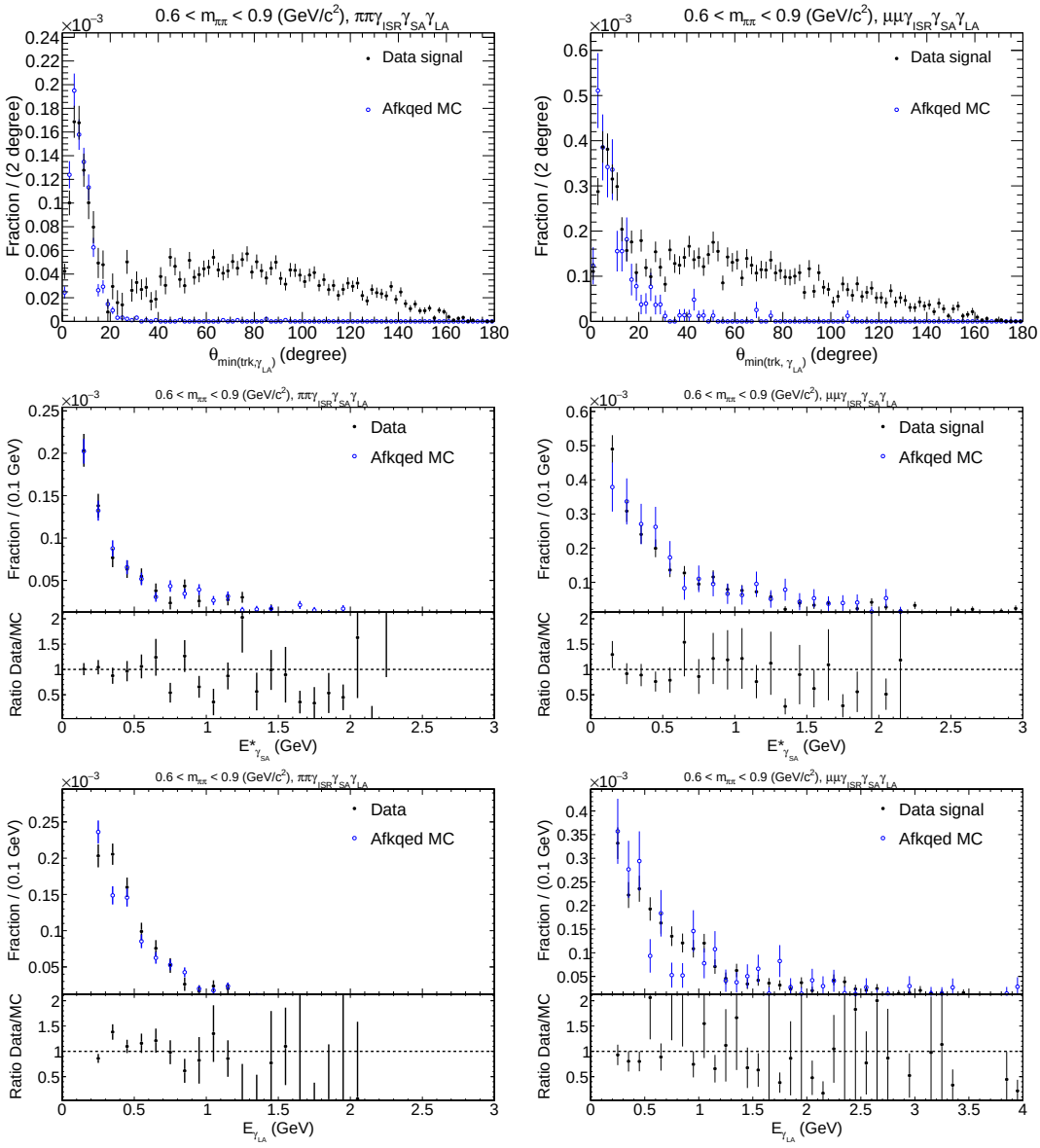

Figure 7.17: Fractions of NNLO signals of $\gamma_{\rm ISR}\gamma_{\rm SA}\gamma_{\rm LA}$ fit in data and AFKQED MC shown as a function of the minimum angle between the additional LA photon and one of the two charged tracks (top), of the additional SA photon in the CM frame (middle) and of the energy of the laboratory frame (bottom) for the mass range between 0.6 and 0.9 GeV/c^2 comparing $\pi\pi\gamma_{\rm ISR}\gamma_{\rm SA}\gamma_{\rm LA}$ (left) and $\mu\mu\gamma_{\rm ISR}\gamma_{\rm SA}\gamma_{\rm LA}$ (right) processes. For the fractions of the energies distributions, $\theta_{\rm min(trk,\gamma_{LA})} < 20^\circ$ has been applied.

for the $\pi\pi\gamma_{\mathrm{ISR}}\gamma_{\mathrm{SA}}\gamma_{\mathrm{LA}}$ process, the final mean value from BDT1 and BDT2 are presented with the quoted corresponding systematic uncertainty showing the difference between the two BDT selections.

NNLO fraction	$\mu\mu\gamma_{\mathrm{ISR}}\gamma_{\mathrm{SA}}\gamma_{\mathrm{LA}}(\theta_{\mathrm{min(trk,}\gamma_{\mathrm{LA}})} < 20^\circ)$ $m_{\pi\pi} < 1.4\,\mathrm{GeV}/c^2$	$\mu\mu\gamma_{\mathrm{ISR}}\gamma_{\mathrm{SA}}\gamma_{\mathrm{LA}}(\theta_{\mathrm{min(trk,}\gamma_{\mathrm{LA}})} < 20^\circ)$ $0.6 < m_{\pi\pi} < 0.9\,\mathrm{GeV}/c^2$	$\pi\pi\gamma_{\mathrm{ISR}}\gamma_{\mathrm{SA}}\gamma_{\mathrm{LA}}(\theta_{\mathrm{min(trk,}\gamma_{\mathrm{LA}})} < 20^\circ)$ $0.6 < m_{\pi\pi} < 0.9\,\mathrm{GeV}/c^2$
Eff.	0.722(21)	0.706(32)	BDT1: 0.198(26), BDT2: 0.199(34)
Data	0.00252(5)(7)(2)	0.00320(11)(15)(6)	BDT1: 0.00191(10)(25)(21) BDT2: 0.00197(10)(34)(26) Mean: 0.00194(10)(29)(24)(3)

Table 7.2: Resulting NNLO $\gamma_{\mathrm{ISR}}\gamma_{\mathrm{SA}}\gamma_{\mathrm{LA}}$ signal fractions for LA photons satisfying $\theta_{\mathrm{min(trk,}\gamma_{\mathrm{LA}})} < 20^\circ$ in data between $\mu\mu\gamma_{\mathrm{ISR}}\gamma_{\mathrm{SA}}\gamma_{\mathrm{LA}}$ and $\pi\pi\gamma_{\mathrm{ISR}}\gamma_{\mathrm{SA}}\gamma_{\mathrm{LA}}$ samples. The fractions have been corrected for the selection efficiency (Eff.). The numbers in brackets are uncertainties with the first one being the statistical uncertainty, the second one is due to the uncertainty of the efficiency corrections and the third one is due to background subtraction. The fourth one on the mean value corresponds to half of the difference between the two BDTs.

NNLO fraction	$\mu\mu\gamma_{\mathrm{ISR}}\gamma_{\mathrm{SA}}\gamma_{\mathrm{LA}}(\theta_{\mathrm{min(trk,}\gamma_{\mathrm{LA}})} > 20^\circ)$ $m_{\pi\pi} < 1.4\,\mathrm{GeV}/c^2$	$\mu\mu\gamma_{\mathrm{ISR}}\gamma_{\mathrm{SA}}\gamma_{\mathrm{LA}}(\theta_{\mathrm{min(trk,}\gamma_{\mathrm{LA}})} > 20^\circ)$ $0.6 < m_{\pi\pi} < 0.9\,\mathrm{GeV}/c^2$	$\pi\pi\gamma_{\mathrm{ISR}}\gamma_{\mathrm{SA}}\gamma_{\mathrm{LA}}(\theta_{\mathrm{min(trk,}\gamma_{\mathrm{LA}})} > 20^\circ)$ $0.6 < m_{\pi\pi} < 0.9\,\mathrm{GeV}/c^2$
Eff.	0.722(21)	0.706(32)	BDT1: 0.317(41), BDT2: 0.320(55)
Data	0.00685(8)(20)(2)	0.00660(15)(30)(4)	BDT1: 0.00680(11)(89)(23) BDT2: 0.00833(12)(143)(25) Mean: 0.00757(11)(116)(24)(76)

Table 7.3: Resulting NNLO $\gamma_{\mathrm{ISR}}\gamma_{\mathrm{SA}}\gamma_{\mathrm{LA}}$ signal fractions for LA photons satisfying $\theta_{\mathrm{min(trk,}\gamma_{\mathrm{LA}})} > 20^\circ$ in data between $\mu\mu\gamma_{\mathrm{ISR}}\gamma_{\mathrm{SA}}\gamma_{\mathrm{LA}}$ and $\pi\pi\gamma_{\mathrm{ISR}}\gamma_{\mathrm{SA}}\gamma_{\mathrm{LA}}$ samples. The fractions are corrected for the selection efficiency (Eff.). The numbers in brackets are uncertainties with the first one representing the statistical uncertainty, the second one is due to the uncertainty of the efficiency corrections and the third one is due to background subtraction. The fourth one on the mean value corresponds to half of the difference between the two BDTs.

7.4 Study of events with two additional measured LA photons

The third NNLO process called $\gamma_{\rm ISR}2\gamma_{\rm LA}$ focuses on events where two additional LA photons are detected and fitted within the detector acceptance range in addition to the main ISR photon. In this $\gamma_{\rm ISR}2\gamma_{\rm LA}$ analysis, the threshold of the fitted photon energies in the laboratory frame for both LA photons is set to 0.1 GeV. Similarly, the χ^2 value of the $\gamma_{\rm ISR}2\gamma_{\rm LA}$ fit is required to be smaller than that from any other NLO or NNLO fits. Distribution of χ^2 of the $\gamma_{\rm ISR}2\gamma_{\rm LA}$ fit for the $\mu\mu$ sample in the mass range below 1.4 GeV/c^2 is illustrated in Fig. 7.18, where both the NLO background and non-$\mu\mu$ background is relatively small. The χ^2 distribution of the $\gamma_{\rm ISR}2\gamma_{\rm LA}$ fit has a less pronounced tail compared to the other two NNLO fits.

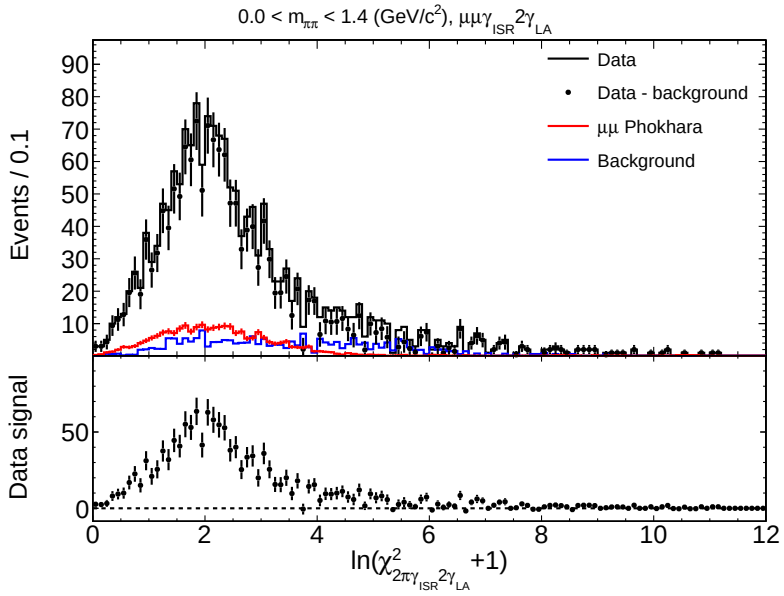

Figure 7.18: Distribution of χ^2 of the $\gamma_{\rm ISR}2\gamma_{\rm LA}$ fit with two measured additional LA photons (both $E_{\gamma_{\rm LA}} > 0.1$ GeV in the laboratory frame) for the mass range below 1.4 GeV/c^2 in the $\mu\mu\gamma_{\rm ISR}2\gamma_{\rm LA}$ sample.

The energy distributions of the two LA photons in the laboratory frame and the minimum angle between the photons and one of the two charged tracks are shown in Fig. 7.19. No further comparison is made with any prediction since this NNLO configuration with two LA photons is not generated in either MC simulation samples, since in PHOKHARA only NLO predictions are made and in AFKQED only one additional LA photon is allowed and all the other ISR photons are collinear to the beams.

For the $\gamma_{\rm ISR}2\gamma_{\rm LA}$ candidates in the $\pi\pi$ sample in the mass range between 0.6 and 0.9 GeV/c^2, all the processes with one or more π^0's in the final states are potential background. Thus the invariant mass distribution of the two fitted LA photons, denoted as $m_{\gamma_{\rm LA}\gamma_{\rm LA}}$, is checked at first. In the selected events from the $\gamma_{\rm ISR}2\gamma_{\rm LA}$ samples, a pronounced peak corresponding to π^0 peak is indeed observed in Fig. 7.20 (top-left). An additional peak around η is also observed. In order to reject the background within the π^0 and η peaks, mass

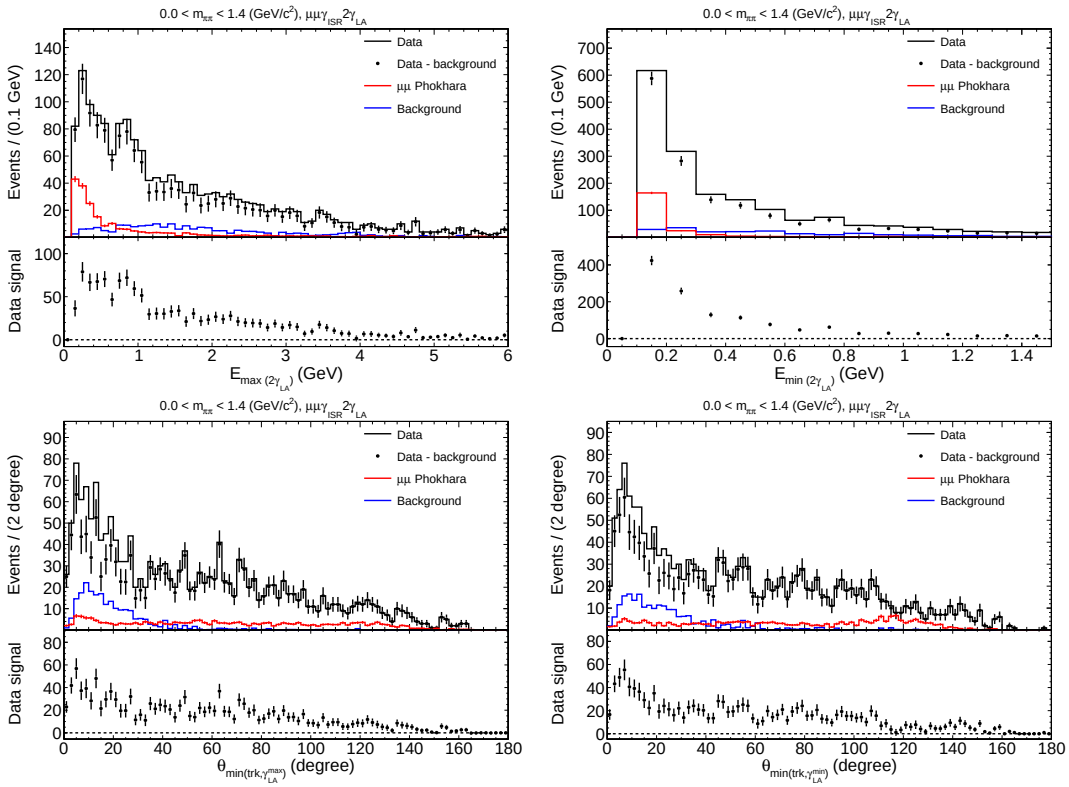

Figure 7.19: Top: Energy distribution of the two additional LA photons. Bottom: Minimum angle between the additional LA photon with one of the two charged tracks. For each single plot, data (black histogram), PHOKHARA MC NLO background (red) and other non-$\mu\mu$ background (blue) and data with background subtraction (full points) are shown in the top panel, and the signal in data is shown in the respective bottom panel.

window of $0.10-0.17$ GeV/c^2 and $0.50-0.58$ GeV/c^2 are defined. After applying the two mass window vetos, a new BDT trained using signal events in data from $\mu\mu$ sample (scaled in a similar way as described for the $\gamma_{\rm ISR}\gamma_{\rm SA}\gamma_{\rm LA}$ fit) is employed to discriminate the remaining events and background events from MC simulations. Six discriminant variables described below have been used:

- the sum of measured energies of extra photons that are not used in the fit,
- The number of photons with a measured energy above 50 MeV,
- The invariant mass of the second leading photon with another photon that has a value closest to π^0 mass,
- the fitted energies of the two additional LA photons,
- Zernike20 variable of the LA photon with larger energy.

The BDT response distribution is demonstrated in Fig. 7.20 (top-right). The comparison of BDT response between data and background is also performed in Fig. 7.20 (middle-left), which indicates that the background contribution is underestimated. To derive the data to background ratio, a background enriched region is defined with BDT < -0.3, where the data/background ratio is rather flat, shown in Fig. 7.20 (middle-right). The ratio is then determined as a scale factor of 1.276 ± 0.022 by integrating the event yields below -0.3, and this ratio has been used to increase the background contribution in the following $\gamma_{\rm ISR}2\gamma_{\rm LA}$ fit study. The $m_{\gamma_{\rm LA}\gamma_{\rm LA}}$ distribution of the selected events is presented in the bottom panel of Fig. 7.20 after applying the nominal BDT selection corresponding to the vertical dashed line in top-right plot of Fig. 7.20.

The χ^2 distribution of the final selected events is presented in Fig. 7.21 in comparison with the corresponding χ^2 distribution from the $\mu\mu\gamma_{\rm ISR}2\gamma_{\rm LA}$ sample in the same mass range. The $\chi^2 < 4.5$ cut is further applied to suppress the relative large background contribution in the high χ^2 tail. The energy distributions of the two additional LA photons and the minimum angles between the photons and one of the two charged tracks are shown in Fig. 7.22.

The fractions of the NNLO $\gamma_{\rm ISR}2\gamma_{\rm LA}$ signals in data from $\mu\mu\gamma_{\rm ISR}2\gamma_{\rm LA}$ (mass range below 1.4 GeV/c^2 and between 0.6 and 0.9 GeV/c^2) and $\pi\pi\gamma_{\rm ISR}2\gamma_{\rm LA}$ (mass range between 0.6 and 0.9 GeV/c^2) are summarized in Table 7.4. No efficiency correction for the $\mu\mu\gamma_{\rm ISR}2\gamma_{\rm LA}$ process is applied since there is no simulated signal from the MC simulations. For the $\pi\pi\gamma_{\rm ISR}2\gamma_{\rm LA}$ process, the fraction has been corrected for the π^0 and η veto selection loss based on the adjacent bins of the $m_{\gamma_{\rm LA}\gamma_{\rm LA}}$ distribution, the efficiency of the nominal BDT selection of 0.796 and the χ^2 of $\gamma_{\rm ISR}2\gamma_{\rm LA}$ below 4.5 which is estimated from the corresponding χ^2 distribution of the $\mu\mu\gamma_{\rm ISR}2\gamma_{\rm LA}$ sample.

Table 7.5 provides the decomposition of the NNLO $\gamma_{\rm ISR}2\gamma_{\rm LA}$ signals into three categories: double FSR, double LA ISR and mixed. This decomposition is performed using the variable $\theta_{\rm min(trk,\gamma_{LA})}$ to separate the events ($\theta_{\rm min(trk,\gamma_{LA})} < 20^\circ$ for FSR component and $\theta_{\rm min(trk,\gamma_{LA})} > 20^\circ$ for LA ISR component). The table indicates that the FSR category accounts for up to 7% of the total signal sample, while the majority of the signal is predominantly shared between the double LA ISR and mixed categories. It is important to note that the fake photon correction has been applied to the FSR components in the $\pi\pi\gamma_{\rm ISR}2\gamma_{\rm LA}$ signals for the results shown in both Table 7.4 and Table 7.5.

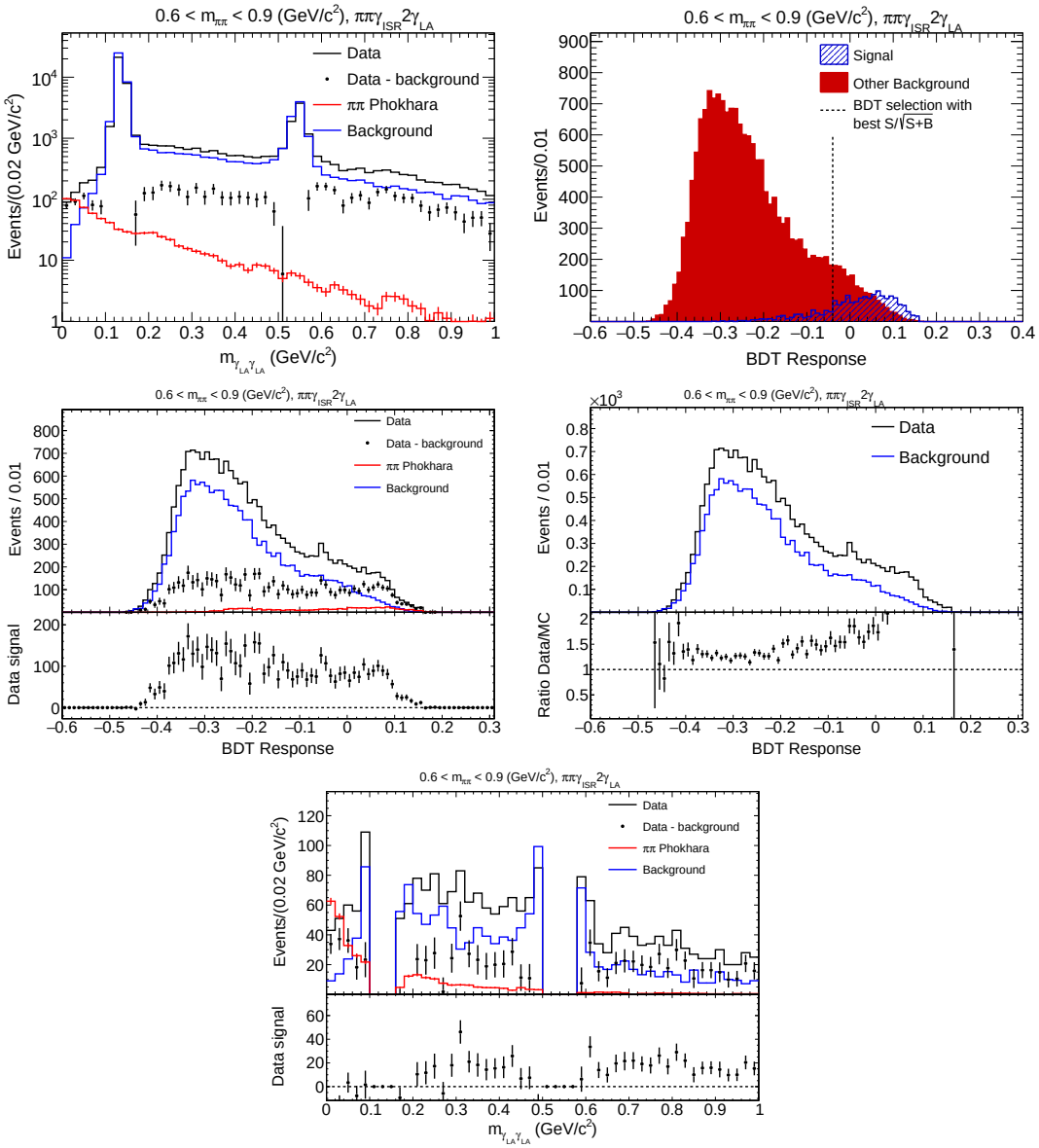

Figure 7.20: Top-left: Invariant mass distribution of two additional LA photons ($E_{\gamma_{\rm LA}} > 0.1$ GeV) in the $\gamma_{\rm ISR}2\gamma_{\rm LA}$ fit in the $\pi\pi\gamma_{\rm ISR}2\gamma_{\rm LA}$ sample before the π^0 and η veto selections described in the text. Top-right: BDT response with π^0 and η veto selections. Middle-left: Comparison of BDT response to data. Middle-right: Comparison of BDT response between signals in data and background and their ratio distribution. Bottom: Similar distribution as top-left one after the π^0 and η veto selections and nominal BDT selection (above -0.04). These plots are made in the mass range between 0.6 and 0.9 GeV/c^2.

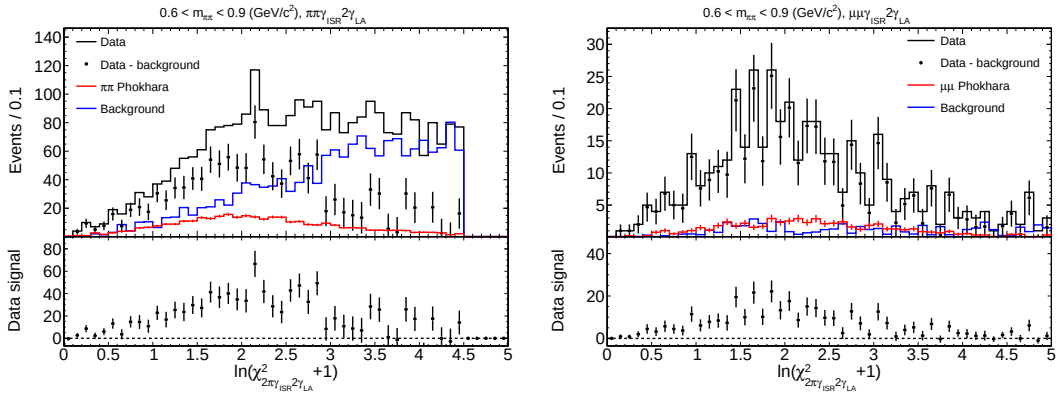

Figure 7.21: Distribution of χ^2 of the $\gamma_{\rm ISR}2\gamma_{\rm LA}$ fit with two additional LA photons ($E_{\gamma_{\rm LA}} > 0.1$ GeV) in the $\pi\pi\gamma_{\rm ISR}2\gamma_{\rm LA}$ sample (left) with the π^0 and η veto and nominal BDT selections compared to that from the $\mu\mu\gamma_{\rm ISR}2\gamma_{\rm LA}$ sample (right) in the mass range between 0.6 and 0.9 GeV/c^2.

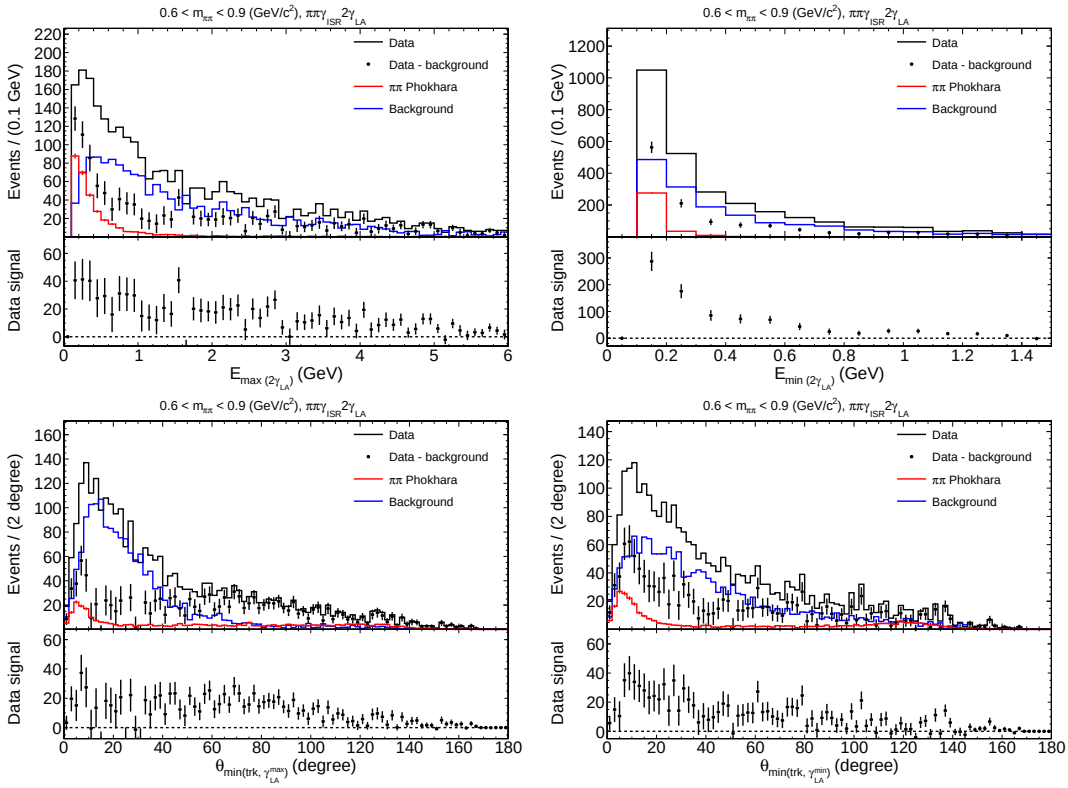

Figure 7.22: Top: Energy distributions of the two additional LA photons. Bottom: Minimum angle between the additional LA photon with one of the two charged tracks. For each single plot, data (black histogram), PHOKHARA MC NLO background (red) and other non-$\mu\mu$ background (blue) and data with background subtraction (full points) are shown in the top panel, and the signal in data is shown in the respective bottom panel for the mass range between 0.6 and 0.9 GeV/c^2 in the $\pi\pi\gamma_{\rm ISR}2\gamma_{\rm LA}$ samples.

NNLO fraction	$\mu\mu\gamma_{\text{ISR}}2\gamma_{\text{LA}}$ $m_{\pi\pi} < 1.4\,\text{GeV}/c^2$	$\mu\mu\gamma_{\text{ISR}}2\gamma_{\text{LA}}$ $0.6 < m_{\pi\pi} < 0.9\,\text{GeV}/c^2$	$\pi\pi\gamma_{\text{ISR}}2\gamma_{\text{LA}}$ $0.6 < m_{\pi\pi} < 0.9\,\text{GeV}/c^2$
Data	0.00103(3)(1)	0.00107(7)(1)	0.00066(4)(4)

Table 7.4: Comparison of NNLO $\gamma_{\text{ISR}}2\gamma_{\text{LA}}$ signal fractions in data between $\mu\mu\gamma_{\text{ISR}}2\gamma_{\text{LA}}$ and $\pi\pi\gamma_{\text{ISR}}2\gamma_{\text{LA}}$ processes, where the first number in brackets is the statistical uncertainty and the second one is related to background subtraction.

Decomposition	$\mu\mu\gamma_{\text{ISR}}2\gamma_{\text{LA}}$ $m_{\pi\pi} < 1.4\,\text{GeV}/c^2$	$\mu\mu\gamma_{\text{ISR}}2\gamma_{\text{LA}}$ $0.6 < m_{\pi\pi} < 0.9\,\text{GeV}/c^2$	$\pi\pi\gamma_{\text{ISR}}2\gamma_{\text{LA}}$ $0.6 < m_{\pi\pi} < 0.9\,\text{GeV}/c^2$
Double FSR	0.071(9)(1)	0.068(15)(2)	0.009(5)(8)
Double LA ISR	0.513(13)(1)	0.446(25)(3)	0.694(32)(13)
Mixed	0.416(15)(1)	0.486(31)(1)	0.297(25)(5)

Table 7.5: Decomposition of NNLO $\gamma_{\text{ISR}}2\gamma_{\text{LA}}$ signals in data for the $\mu\mu\gamma_{\text{ISR}}2\gamma_{\text{LA}}$ and $\pi\pi\gamma_{\text{ISR}}2\gamma_{\text{LA}}$ samples in double FSR, double LA ISR and mixed categories. The first number in brackets represents the statistical uncertainty while the other systematic uncertainty is related to background subtraction.

Chapter 8

Final results and discussion

8.1 Combining NLO and NNLO results

The correct classification of events with respect to the number of additional photons can indeed be affected by detector resolution effects and the chosen fit strategies. Detector resolution effects, such as the energy and angular resolutions, can cause fluctuations in the measured photon quantities. Additionally, the chosen fit strategy including assumptions of the emission angles and energies of additional photons, can introduce bias in the classification. Thus an event with 0, 1, or more additional photons may not always be correctly classified. By defining true event categories using the same energy thresholds as the fitted categories but using true photon energies, the mis-classification between fitted and true categories can be studied and provide valuable insights into the performance of the analysis technique. The results obtained using the two MC samples PHOKHARA and AFKQED are displayed in Table 8.1. The diagonal elements correspond to the overall efficiencies of the selection, whereas the off-diagonal elements stand for the mis-classification probabilities defined by dividing the number of events over the total number of events of a given MC sample. In the table, the upper part shows the results of the $\mu\mu$ process in the mass range below 1.4 GeV/c^2 and the lower part shows the results of the $\pi\pi$ process in the mass range between 0.6 and 0.9 GeV/c^2. The lower efficiencies for the NNLO fits in the $\pi\pi$ process than those in the $\mu\mu$ process are due to the application of BDT method to suppress the huge background contribution in data. The efficiencies for the $\gamma_{\mathrm{ISR}}\gamma_{\mathrm{LA}}$ $(> 20^{\circ})$ and $\gamma_{\mathrm{ISR}}\gamma_{\mathrm{SA}}\gamma_{\mathrm{LA}}$ $(> 20^{\circ})$ categories from AFKQED are tiny since they are not produced by AFKQED predictions.

After correcting the feed-through effects (refer to Appendix G for more details), correcting the full selection efficiency and the fake photon efficiency discussed in the earlier sections, the final fractions of different fit categories for data are shown in Table 8.2. Table 8.3 presents the complete comparison between data and predictions from the two MC samples for all fit categories. It should be mentioned that the $\gamma_{\mathrm{ISR}}\gamma_{\mathrm{LA}}$ rates separated by $\theta_{\mathrm{min(trk},\gamma_{\mathrm{LA}})} < 20^{\circ}$ and $\theta_{\mathrm{min(trk},\gamma_{\mathrm{LA}})} > 20^{\circ}$ have been corrected and then converted into NLO FSR and NLO LA ISR rates using template fits of the $\theta_{\mathrm{min(trk},\gamma_{\mathrm{LA}})}$ distributions described in Section 5.2. In a similar way, $\gamma_{\mathrm{ISR}}\gamma_{\mathrm{SA}}\gamma_{\mathrm{LA}}$ rates have been corrected and then converted into NNLO FSR and NNLO LA ISR rates using template fits of the $\theta_{\mathrm{min(trk},\gamma_{\mathrm{LA}})}$ distributions. The fit category with two additional LA photons has a tiny data fraction around 0.001 (no efficiency corrections

%	LO	$\gamma_{\rm ISR}\gamma_{\rm SA}$	$\gamma_{\rm ISR}\gamma_{\rm LA}$ $(< 20^\circ)$	$\gamma_{\rm ISR}\gamma_{\rm LA}$ $(> 20^\circ)$	$\gamma_{\rm ISR}2\gamma_{\rm SA}$	$\gamma_{\rm ISR}\gamma_{\rm SA}\gamma_{\rm LA}$ $(< 20^\circ)$	$\gamma_{\rm ISR}\gamma_{\rm SA}\gamma_{\rm LA}$ $(> 20^\circ)$
	$\mu\mu$ ($m_{\pi\pi} < 1.4$ GeV/c^2)						
LO	**99.64(1)**	*0.223(9)*	*0.008(2)*	*0.033(3)*	*0.139(7)*	*0.0004(4)*	*0.005(1)*
	99.439(3)	0.289(2)	0.0140(4)	0.0756(9)	0.136(1)	0.00011(3)	0.0073(3)
$\gamma_{\rm ISR}\gamma_{\rm SA}$	*0.327(1)*	**97.9(5)**	*0.006(1)*	*0.008(2)*	*0.254(9)*	*0.0021(9)*	*0.010(2)*
	0.325(2)	**94.28(2)**	0.0169(4)	0.212(1)	0.838(3)	0.0077(3)	0.127(1)
$\gamma_{\rm ISR}\gamma_{\rm LA}$ $(< 20^\circ)$	*0.096(6)*	*0.008(2)*	**74.8(8)**	*0.0017(7)*	*0.103(6)*	*0.005((1)*	*0.0014(7)*
	0.118(1)	0.0113(3)	**78.8(1)**	0.0057(2)	0.138(1)	0.0008(1)	0.0007(1)
$\gamma_{\rm ISR}\gamma_{\rm LA}$ $(> 20^\circ)$	*0.003(1)*	*0.0016(7)*	*0.0023(9)*	*0.181(8)*	*0.003(1)*	*0(0)*	*0.0010(6)*
	0.099(1)	0.0645(8)	0.0045(2)	**83.89(6)**	0.0517(7)	0.00021(5)	0.0135(4)
$\gamma_{\rm ISR}2\gamma_{\rm SA}$	0.19(2)	1.69(3)	0.014(2)	0.003(3)	**90.8(5)**	0.0010(5)	0.0015(5)
$\gamma_{\rm ISR}\gamma_{\rm SA}\gamma_{\rm LA}$ $(< 20^\circ)$	0.010(1)	0.074(4)	0.005(1)	0.0007(5)	0.035(4)	**72.2(1.6)**	0.0004(4)
$\gamma_{\rm ISR}\gamma_{\rm SA}\gamma_{\rm LA}$ $(> 20^\circ)$	0.0007(5)	0.010(2)	0(0)	0.0013(7)	0.004(1)	0.0007(5)	*0.042(4)*
Rest	0.0011(6)	0.003(1)	0.0011(6)	0(0)	0.011(2)	0.007(2)	0.003(1)
	$\pi\pi$ ($0.6 < m_{\pi\pi} < 0.9$ GeV/c^2)						
LO	**99.397(9)**	*0.318(6)*	*0.052(3)*	*0.044(2)*	*0.190(4)*	*0.0035(8)*	*0.0060(8)*
	99.228(2)	0.378(1)	0.0560(9)	0.0859(6)	0.1712(8)	0.0027(1)	0.0078(2)
$\gamma_{\rm ISR}\gamma_{\rm SA}$	*0.317(6)*	**98.0(3)**	*0.0019(6)*	*0.0055(8)*	*0.258(5)*	*0.0030(7)*	*0.0071(9)*
	0.333(1)	**94.01(1)**	0.0109(3)	0.254(1)	0.438(1)	0.0330(6)	0.0826(6)
$\gamma_{\rm ISR}\gamma_{\rm LA}$ $(< 20^\circ)$	*0.352(4)*	*0.068(2)*	**38.4(6)**	*0.0027(5)*	*0.128(4)*	*0.0037(8)*	*0.0020(5)*
	0.533(1)	0.0998(4)	**40.8(2)**	0.0065(2)	0.1703(8)	0.0043(2)	0.0029(1)
$\gamma_{\rm ISR}\gamma_{\rm LA}$ $(> 20^\circ)$	*0.0017(4)*	*0.0001(1)*	*0.0003(2)*	*0.0085(9)*	*0.0002(1)*	*0.0001(1)*	*0(0)*
	0.0948(6)	0.0471(4)	0.0026(1)	**86.65(4)**	0.0279(3)	0.0011(1)	0.0122(2)
$\gamma_{\rm ISR}2\gamma_{\rm SA}$	0.170(13)	1.98(2)	0.04(1)	0.01(1)	**85.3(3)**	0.0014(4)	0.0006(1)
$\gamma_{\rm ISR}\gamma_{\rm SA}\gamma_{\rm LA}$ $(< 20^\circ)$	0.010(1)	0.165(4)	0.009(1)	0.0021(5)	0.063(3)	**22.5(1.1)**	0.0007(3)
$\gamma_{\rm ISR}\gamma_{\rm SA}\gamma_{\rm LA}$ $(> 20^\circ)$	0(0)	0.0024(5)	0.0001(1)	0.0003(2)	0.0006(3)	0.0003(2)	*0.0019(4)*
Rest	0.0005(2)	0.0090(9)	0.0003(2)	0(0)	0(0)	0.0015(5)	0(0)

Table 8.1: Efficiencies (diagonal elements in bold) and mis-classification probabilities (non-diagonal elements) all shown in % calculated using MC samples AFKQED and PHOKHARA (1st and 2nd lines (if any) in each block, respectively) for fitted categories (column) versus true categories (row) for the $\mu\mu$ (upper) and $\pi\pi$ (lower) part of the table. The numbers in brackets are statistical errors. The last row 'Rest' corresponds to the phase space which is not covered by the other true categories. The numbers in italic shown for completeness are not used for efficiency or feed-through corrections.

applied) and is not included in these fraction tables since no predictions from the AFKQED MC can be used to either calculate the efficiency corrections or to further compare with the NNLO MC sample.

Data fraction	$\mu\mu$ $m_{\pi\pi} < 1.4\,\mathrm{GeV}/c^2$	$\mu\mu$ $0.6 < m_{\pi\pi} < 0.9\,\mathrm{GeV}/c^2$	$\pi\pi$ $0.6 < m_{\pi\pi} < 0.9\,\mathrm{GeV}/c^2$
		LO	
Eff	0.9931(1)	0.9942(1)	0.9910(1)
Fraction	0.7716(4)(1)(14)	0.7741(7)(1)(18)	0.7839(5)(1)(12)
		NLO SA-ISR	
Eff	0.9310(4)	0.9319(9)	0.9284(4)
Fraction	0.1469(3)(1)(36)	0.1437(6)(1)(32)	0.1401(2)(1)(16)
		NLO LA-ISR	
Eff	0.620(13)	0.657(5)	0.643(13)
Fraction	0.0340(2)(8)(4)	0.0320(4)(7)(7)	0.0338(2)(7)(5)
		NLO ISR	
Fraction	0.1809(4)(8)(34)	0.1757(7)(8)(28)	0.1739(3)(7)(19)
		NLO FSR	
Eff	0.623(13)	0.653(7)	0.321(7)
Fraction	0.0137(2)(3)(6)	0.0159(3)(4)(10)	0.0100(1)(2)(16)
		NNLO ISR	
Fraction	0.0309(2)(3)(38)	0.0307(3)(4)(34)	0.0310(2)(33)(19)(8)
		NNLO FSR	
Eff.	0.722(46)	0.706(32)	BDT1: 0.198(26), BDT2: 0.199(34)
Fraction	0.00275(6)(9)(3)	0.00357(13)(17)(79)	0.00194(12)(34)(36)(1)

Table 8.2: Final event fractions in data for the $\mu\mu$ and $\pi\pi$ processes in all fit categories, where the numbers in brackets represent uncertainties. The first is the statistical, the second and third uncertainties are systematical corresponding to efficiency corrections and the background subtraction including feed-through correction. The fourth uncertainty for the $\pi\pi$ process represents half of the difference between two BDT results.

To validate the NNLO signals in data and the missing NNLO signals in the PHOKHARA MC sample, the SA energy spectra after the corrections are presented in Fig. 8.1 for the $\gamma_{\mathrm{ISR}}\gamma_{\mathrm{SA}}$ fits. The dominant feed-through corrections for $\gamma_{\mathrm{ISR}}\gamma_{\mathrm{SA}}$ are from $\gamma_{\mathrm{ISR}}2\gamma_{\mathrm{SA}}$ events which have two distinct components: one corresponds to the case when the $\gamma_{\mathrm{ISR}}2\gamma_{\mathrm{SA}}$ event satisfies the $\gamma_{\mathrm{ISR}}\gamma_{\mathrm{SA}}$ fit with one additional SA photon as well; the other one corresponds to the case where two additional photons are emitted by the same beam and are then merged into one single photon which can not be distinguished from single photon radiation process (refer to Appendix G). The correction for $\gamma_{\mathrm{ISR}}2\gamma_{\mathrm{SA}}$ feed-through cannot be based on the AFKQED prediction due to the limitation of 2.3 GeV cut of the SA photons, consequently a data-driven method is performed to determine the corresponding rates. For the first component, the SA spectrum is derived by data with background subtraction and feed-through corrections from other fit categories satisfying both the $\gamma_{\mathrm{ISR}}2\gamma_{\mathrm{SA}}$ and $\gamma_{\mathrm{ISR}}\gamma_{\mathrm{SA}}$ fits. For the second component, as the $\gamma_{\mathrm{ISR}}2\gamma_{\mathrm{SA}}$ sample includes only events with additional SA photons from opposite beams, the spectrum with additional photons from the same beam is mimicked by summing

LO or NLO fraction	$\mu\mu$ $m_{\pi\pi} < 1.4\,\mathrm{GeV}/c^2$	$\mu\mu$ $0.6 < m_{\pi\pi} < 0.9\,\mathrm{GeV}/c^2$	$\pi\pi$ $0.6 < m_{\pi\pi} < 0.9\,\mathrm{GeV}/c^2$
LO			
Data	0.7716(4)(1)(14)	0.7741(7)(1)(18)	0.7839(5)(1)(12)
AFKQED	0.8024(7)	0.8029(14)	0.8099(4)
PHOKHARA	0.7560(1)	0.7576(3)	0.7656(1)
Ratio data/A	0.962(1)(0)(1)	0.964(2)(0)(1)	0.968(1)(0)(0)
Ratio data/P	1.021(1)(0)(2)	1.022(1)(0)(2)	1.024(1)(0)(2)
NLO SA-ISR			
Data	0.1469(3)(1)(36)	0.1437(6)(1)(32)	0.1401(2)(1)(16)
PHOKHARA	0.1926(1)	0.1903(3)	0.1868(1)
Ratio data/P	0.763(2)(0)(19)	0.755(3)(1)(17)	0.750(1)(0)(8)
NLO LA-ISR			
Data	0.0340(2)(8)(4)	0.0320(4)(8)(7)	0.0338(2)(7)(5)
PHOKHARA	0.0354(1)	0.0336(2)	0.0344(2)
Ratio data/P	0.96(1)(2)(1)	0.95(1)(2)(2)	0.98(1)(2)(1)
NLO ISR ($E^*_{\gamma_{\mathrm{SA}}} < 2.3\,\mathrm{GeV}$)			
Data	0.1664(3)(7)(32)	0.1626(6)(7)(27)	0.1608(3)(7)(18)
AFKQED	0.1569(3)	0.1551(6)	0.1542(4)
Ratio data/A	1.061(3)(5)(13)	1.048(6)(5)(13)	1.043(3)(4)(8)
NLO FSR			
Data	0.0137(2)(3)(6)	0.0159(3)(4)(10)	0.0100(1)(2)(16)
AFKQED	0.0126(3)	0.0141(5)	0.0092(3)
PHOKHARA	0.0160(1)	0.0185(2)	0.0132(2)
Ratio data/A	1.09(3)(3)(4)	1.13(5)(3)(5)	1.08(3)(3)(9)
Ratio data/P	0.86(1)(2)(4)	0.86(2)(2)(5)	0.76(1)(2)(12)
NNLO ISR ($E^*_{\gamma_{\mathrm{SA}}} < 2.3\,\mathrm{GeV}$)			
Data	0.0287(2)(2)(36)	0.0284(3)(4)(31)	0.0300(2)(32)(19)(8)
AFKQED	0.0247(4)	0.0241(6)	0.0244(2)
Ratio data/A	1.16(2)(1)(10)	1.18(4)(2)(9)	1.23(1)(13)(5)(3)
NNLO FSR			
Data	0.00275(6)(9)(3)	0.00357(13)(17)(79)	0.00194(12)(34)(36)(1)
AFKQED	0.00354(15)	0.00394(29)	0.00238(15)
Ratio data/A	0.78(4)(3)(1)	0.90(8)(6)(20)	0.81(7)(14)(15)(0)

Table 8.3: Final comparison of event fractions between data and AFKQED and PHOKHARA and between $\mu\mu$ and $\pi\pi$ processes for all fit categories, where the numbers in brackets represent uncertainties. The first is the statistical, the second and third uncertainties are systematical corresponding to efficiency corrections and the background subtraction including feed-through corrections. The fourth uncertainty for the $\pi\pi$ process represents half of the difference between two BDT results. When comparing to the predictions of AFKQED for NLO ISR and NNLO ISR, the data fractions have been reduced with respect to those given in Table 8.2 due to the missing energy spectrum beyond 2.3 GeV in AFKQED.

the energy of the two additional SA photons from the $\gamma_{\rm ISR}2\gamma_{\rm SA}$ fit. The feed-through corrections of the $\gamma_{\rm ISR}\gamma_{\rm SA}$ fit from the other topologies are based on the simulated PHOKHARA for NLO feed-through corrections and AFKQED for NNLO feed-through corrections.

When the NNLO contribution and the feed-through components are removed from the energy spectrum of the additional SA photon in the CM frame, the data over PHOKHARA MC ratios become much flatter in Fig. 8.1 than those seen in Figs. 5.15 and 5.20, where a significant slope has been observed. The fitted ratio also confirms that a significant discrepancy between the data and PHOKHARA rates of NLO SA ISR events.

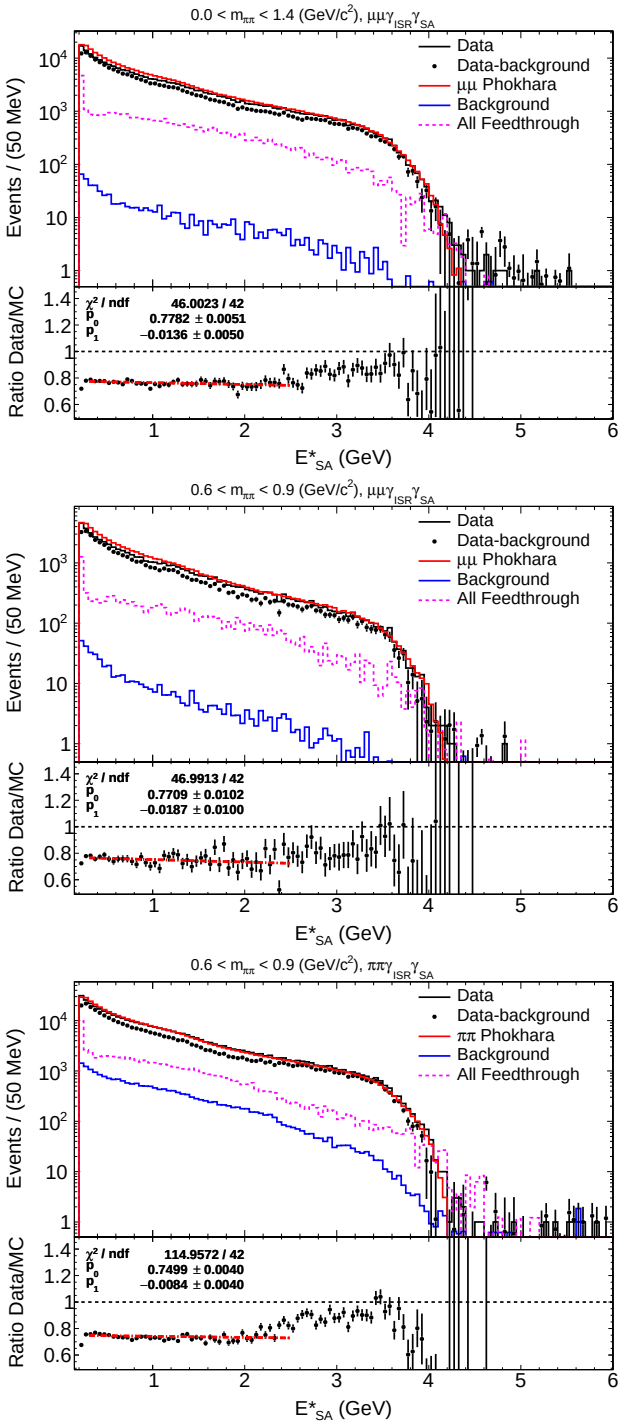

Figure 8.1: Energy distribution of the additional SA photon in the CM frame in the $\gamma_{\mathrm{ISR}}\gamma_{\mathrm{SA}}$ fits after the NNLO contribution and the feed-through corrections for the $\mu\mu$ samples in the mass range below 1.4 GeV/c^2 (top) and between 0.6 and 0.9 GeV/c^2 (middle) and for the $\pi\pi$ samples in the mass range between 0.6 and 0.9 GeV/c^2 (bottom).

8.2 Summary of the main findings

In this analysis of the *BABAR* ISR processes $e^+e^- \to \mu^+\mu^-\gamma$ and $e^+e^- \to \pi^+\pi^-\gamma$ data, all radiative topologies have been studied up to two additional photons. It provides for the first time an extensive experimental survey of radiative effects up to NNLO. All results are given for additional photons with fitted energy larger than $200\,\mathrm{MeV}$ (in the CM frame for fitted small-angle ISR photons and in the laboratory frame for large-angle ISR or FSR detected photons). For cases where two additional photons are considered, the less energetic one is required to be above $100\,\mathrm{MeV}$. For muons the full mass interval from threshold to $1.4\,\mathrm{GeV}/c^2$ is used, while for pions the range is restricted between 0.6 and $0.9\,\mathrm{GeV}/c^2$. Small-angle photons out of the acceptance are unmeasured but fitted. Otherwise they are called large-angle and measured. The main findings and results are summarized in the following:

- Direct searches for NNLO contributions have been performed using dedicated kinematical fits, which show clear evidence for their presence both at small and large angle to the $e^\pm$ beams. Taking also into account all topologies with two small-angle, one small-angle and one large-angle, and two large-angle photons, the total fraction of NNLO ISR contributions sums up to $(3.09 \pm 0.38)\%$ for muons and $(3.10 \pm 0.39)\%$ for pions, both consistent as expected from ISR. The NNLO FSR contributions, dominated by one FSR and one ISR photons, are found to be $(0.28 \pm 0.01)\%$ in muon and $(0.19 \pm 0.05)\%$ in pion. Thus the measured total NNLO fraction amounts to $(3.37 \pm 0.38)\%$ for muons and $(3.29 \pm 0.39)\%$ for pions. The NNLO contribution with two additional large-angle photons is measured with a rate around 1‰ (0.7‰) in muon (pion) data and is not included in the total rates above.

- Additional indirect evidence for NNLO ISR from the same beam is obtained from the shape of the energy distribution of the additional photons in the NLO $\gamma_{\mathrm{ISR}}\gamma_{\mathrm{SA}}$ fit which differs strongly from the NLO PHOKHARA prediction. The correction using the measured NNLO contribution with ISR for opposite beams re-establishes close agreement for the shape, thus providing good internal consistency of the results.

- The measurement of the NNLO contributions allows one to correct the initial NLO results by taking into account cross-feeds between the different radiative topologies. The fractions obtained for ISR NLO are $(18.08 \pm 0.35)\%$ for muons and $(17.39 \pm 0.20)\%$ for pions, thus consistent within uncertainties. The fractions for FSR NLO are $(1.38 \pm 0.07)\%$ for muons and $(1.00 \pm 0.16)\%$ for pions.

- NLO fractions can be compared to the predictions provided by the PHOKHARA generator used by all ISR experiments. The present measurements are not in agreement with the PHOKHARA rate for additional small-angle ISR, which yields significantly larger NLO fractions: the ratio between data and PHOKHARA is found to be 0.763 ± 0.019 for muons and 0.750 ± 0.008 for pions. At the moment, because of the blinding of the data/MC corrections for selection efficiencies prior to this radiation study, the absolute comparison between data and PHOKHARA cannot yet be performed. So what is observed here are different LO (LO and soft-virtual NLO) and NLO (hard) fractions in data and PHOKHARA. This discrepancy is independent of the transition energy of

5 MeV between soft and hard photons chosen for the MC production as it is much smaller than the threshold of 200 MeV used in the actual analysis for accepting a hard photon. Much better agreement is observed for the large-angle ISR NLO fractions, 0.96 ± 0.03 for muons and 0.98 ± 0.03 for pions, while again a discrepancy occurs for FSR NLO for muons with a ratio 0.86 ± 0.05. The situation observed for ISR NLO which is in principle controlled by QED indicates a problem in the angular distribution of the NLO photon generated by PHOKHARA. with a large excess at small angles to the beams.

- The situation of FSR NLO for pions should anyway be considered separately as its theoretical prediction goes beyond QED. In PHOKHARA generation, pions are assumed point-like from scalar QED. Experimentally the detection of photons nearby a pion track necessitates a careful evaluation of the contribution of fake photon candidates from hadronic shower fluctuations in the EMC. The study reveals a significant contribution which is furthermore underestimated by the detector simulation. After correction the ratio between data and the PHOKHARA prediction is found to be 0.76 ± 0.12, a low value consistent with the muon result. Thus apart from the deficit occurring for both pions and muons compared to PHOKHARA the agreement with the FSR pion model appears to be approximately valid within 15%.

- NLO and NNLO results have also been compared with the expectations of the AFKQED generator, which incorporates both ISR NLO and NNLO contributions through collinear emission using the structure function method. As a consequence NLO data fractions for small-angle and large-angle ISR are added to compare with the AFKQED prediction. The additional ISR photon energy cut-off at 2.3 GeV imposed in the generation is also accounted for. The total ISR NLO fraction in data up to 2.3 GeV photon energy is measured to be $(16.6 \pm 0.3)\%$ for muons and $(16.1 \pm 0.2)\%$ for pions. The ratios to their respective AFKQED predictions, 1.060 ± 0.015 and 1.043 ± 0.010, differ from one, however much less than for PHOKHARA.

- The FSR NLO fractions can also be compared with the prediction from AFKQED based on the PHOTOS algorithm. For muons the ratio between data and AFKQED turns out to be 1.10 ± 0.06, while for pions, after correction for the fake photon contribution, the similar ratio is 1.08 ± 0.10. Both ratios are consistent with unity with limited precision because of the NNLO feedthrough uncertainties. The ratio pion/muon is consistent with one and as such supports, albeit with a large uncertainty the pion point-like behavior for additional FSR. As mentioned previously in Chapter 5 for the analysis limited to NLO, this conclusion disagrees with the result in the published *BABAR* analysis [35,38], where a $(21 \pm 5)\%$ excess was quoted. However the difference is explained by the data/MC correction for the fake photon subtraction, which was then not applied. Therefore the new result presented here and based on a detailed study of the fake photon contribution and taking into account NNLO feed-throughs supersedes the previous result.

8.2.1 Consequences for the *BABAR* $\mu\mu/\pi\pi$ cross section analysis

The study presented in this thesis has only minor consequences for the *BABAR* final cross section analysis. In fact only the initial selection efficiency from acceptance cuts outlined in Section 3.3, determined using the PHOKHARA generator interfaced with detector simulation, is affected. For the *BABAR* cross section measurement, the event samples obtained after acceptance cuts are further selected according to the χ^2 of the NLO kinematic fits allowing one additional photon, whether measured in the detector or inferred from kinematics. It should be pointed out that, since the χ^2-cut efficiency is measured with data [35,38], directly for muons and after some small corrections for pions, all effects of NLO and higher-order radiation are included and no dependence on a particular Monte Carlo generator is introduced when handling additional radiation. Thus the *BABAR* analyses are fully inclusive of additional radiation at all orders. This property holds for the ongoing new analysis and the previously published *BABAR* results as well. This is an important difference with respect to all the other analyses characterized by a more strict event definition, which requires the full validity of the generator in order to estimate the rejected radiative events fraction. For *BABAR* it is only when calculating the event acceptance prior to the kinematic fits that generator dependence occurs.

To quantify the effect of the overestimated hard NLO contribution in PHOKHARA, the *BABAR* acceptance efficiency is calculated as a function of mass using different options for the generation. In Fig. 8.2 the efficiencies for LO ISR and LO+NLO ISR with/without hard NLO, defined by $E^*_{\mathrm{add}\ \gamma} > 50\,\mathrm{MeV}$ are compared. Figure 8.2 (right) shows that final states at LO (only the ISR photon + 2 charged particles) have the same acceptance at better than 1 per mil in *BABAR* as NLO events when excluding hard radiation with E^*_γ larger than 50 MeV, despite small differences in their angular distributions. This property indicates an important consequence: from an experimental point of view, final states are identical for LO and NLO soft+virtual contributions and they are measured together indistinguishably [1]. On the other hand, hard radiation in full NLO does affect the acceptance as shown in Fig. 8.2 (left) indicating a small variation in mass within 1%. It is the only instance in the *BABAR* analysis where a correction affecting the cross section needs to be computed from PHOKHARA. However it is strongly correlated between the $\pi\pi\gamma(\gamma)$ and $\mu\mu\gamma(\gamma)$ processes, and therefore the effect largely vanishes when taking their ratio, as shown in Fig. 8.2 bottom. The double ratio is constant with mass from threshold up to 1.4 GeV with a fitted value (0.9981 ± 0.0004) ($\chi^2/\mathrm{NDF} = 1.2$). The systematic bias induced on the $\pi\pi(\gamma)$ cross section by the hard NLO excess observed in PHOKHARA and the missing hard NNLO component is estimated from this result to be $(0.3 \pm 0.1) \times 10^{-3}$, thus negligible at the level of precision of 0.5% achieved in the published analysis [35,38].

The re-evaluation of the pion FSR contribution taking into account the fake photons from interacting pions also introduces a small change in the published *BABAR* $\pi\pi$ cross section [35, 38]. The correction then applied on the pion χ^2-cut efficiency induced by the spurious excess was less than 1 per mil.

Therefore we reiterate that the limitations in using PHOKHARA as the reference generator has a negligible incidence on the published and ongoing *BABAR* cross section mea-

[1] Actually the loop contributions induce a small forward-backward asymmetry, but the latter disappears when averaging over the particles in a charge-symmetric detector.

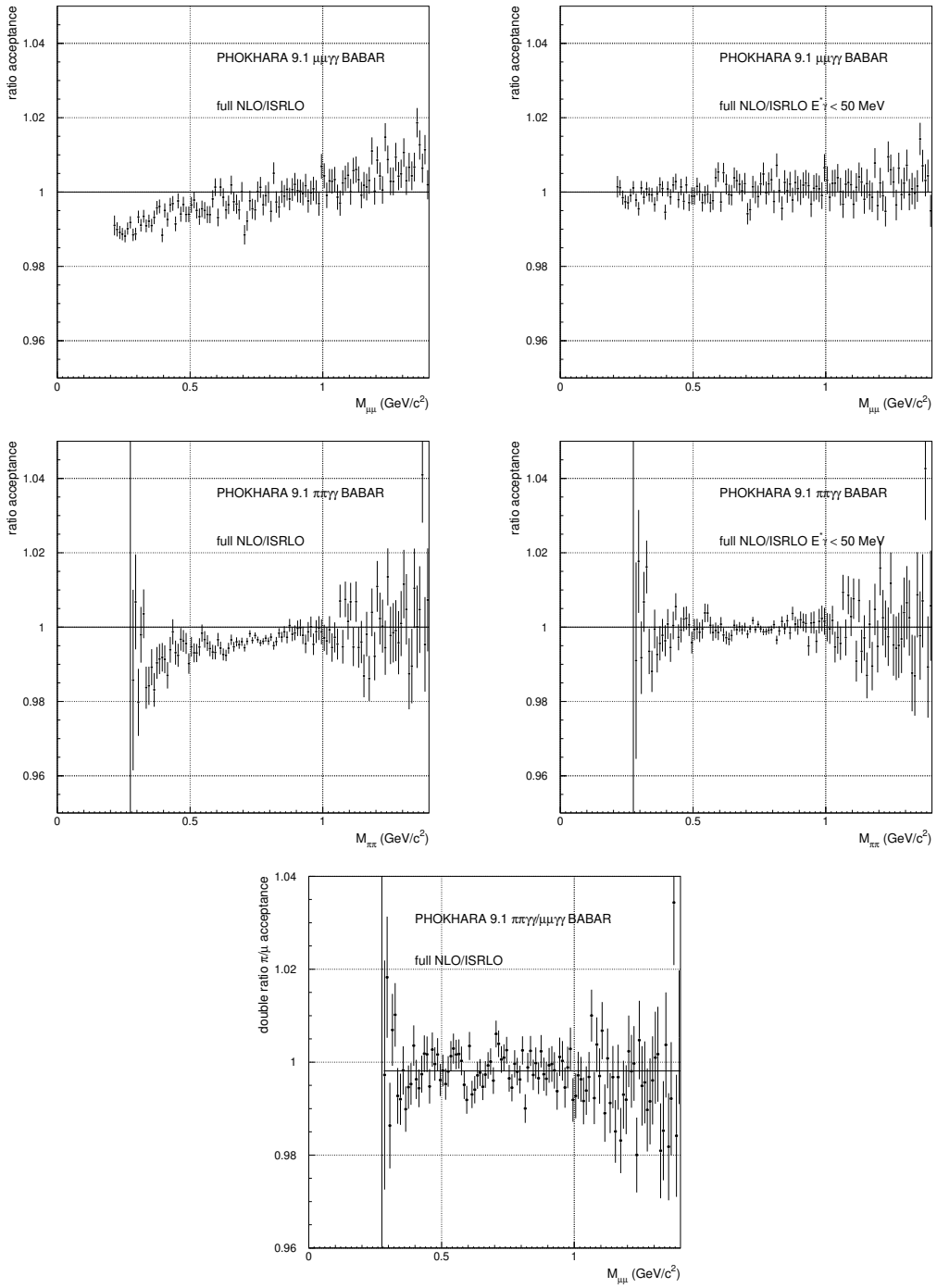

Figure 8.2: The ratio of the *BABAR* acceptance for full NLO PHOKHARA to LO acceptance for $\mu\mu\gamma(\gamma)$ (top) and $\pi\pi\gamma(\gamma)$ (middle). Full NLO without energy cut on the additional photon (left) and with E^*_γ <50 MeV (right). Double ratio of acceptances π/μ (bottom).

surements [35, 38], whether considering the incorrect NLO rates or the lack of higher-order radiation.

8.2.2 Consequences for other ISR experiments

An important consideration follows from the studies performed in Section 1.5. The complete ISR cross section at NLO level involves three contributions with large cancellations: the positive LO and hard NLO parts and the negative part originating from virtual/soft radiation. Both LO and virtual/soft NLO contributions lead to an experimental 'LO' topology without measurable additional radiation, while the hard NLO contribution produces a distinct 'NLO' topology affecting the selection procedure. As a consequence, measuring a cross section with tight 'LO'-topology cuts selects true LO and to a very good approximation virtual/soft NLO to all orders. This is the case with the experimental approach adopted by KLOE [54–56], BESIII [57,58] and CLEO-c [59]. In their case it is necessary to add to the measured cross section the missing part of the hard-NLO contribution, assumed to be provided by the PHOKHARA generator. The results of the present analysis question the validity of this procedure on two grounds: first the discrepancy on the hard NLO yield in PHOKHARA which is significantly larger than our measurement, and second, the absence of NNLO contributions in PHOKHARA, the latter at a level larger than the quoted systematic uncertainties in these experiments. Any quantitative evaluation of these effects requires a careful analysis of the specific experimental conditions of these experiments, which is beyond the scope of this thesis.

As explained above, the *BABAR* $\mu^+\mu^-(\gamma)$ and $\pi^+\pi^-(\gamma)$ cross section measurements do not follow this approach, as they are performed with a very loose selection incorporating all radiative processes. The disagreement within their quoted systematic uncertainties between the cross sections measured by *BABAR* and KLOE, both in shape and in normalization, could be understood, at least partly, by the shortcomings of PHOKHARA at both NLO and NNLO levels discussed above.

8.2.3 Related comments for the scan experiments

The experiments performed in Novosibirsk (CMD-2, CMD-3, SND) use the scan method and measure directly the cross section at LO as a function of the e^+e^- CM energy. Thus radiative corrections are very different from those using the ISR approach where the cross section is determined as a function of the measured hadronic mass. For ISR approach the radiative corrections involve the knowledge of additional FSR and most importantly of the ISR luminosity including higher orders. For the scan experiments ISR radiative corrections are important and highly dependent on the LO cross section line shape. They also have to be determined including higher orders, provided approximately by specific programs. The additional FSR should also be taken into account.

The recent release of new results from CMD-3 [28] on the $\pi\pi$ cross section leads to a rather confusing situation since they disagree with all previous measurements, including KLOE, *BABAR* and CMD-2, and also with the most recent results from SND [60]. The reason for the discrepancy is not yet understood, although it looks unlikely to originate from the radiative corrections as they are treated similarly in all scan experiments. Nevertheless the

issue of higher-order corrections, as identified in this analysis, is relevant to their analyses using incomplete generators.

Chapter 9

Conclusion

Based on the total integrated luminosity of 424.2 fb^{-1} at the $\Upsilon(4S)$ resonance and 43.9 fb^{-1} below the resonance of data collected at the *BABAR* detector, the analysis is a comprehensive study with the full *BABAR* data of radiative processes affecting the measurements of the ISR cross sections for $e^+e^- \to \mu^+\mu^-\gamma$ and $e^+e^- \to \pi^+\pi^-\gamma$. Two NLO kinematic fits and three NNLO kinematic fits are well defined and studied extensively. This thesis has achieved the following progress and conclusions for the *BABAR* ISR process analysis, which are crucial and will be used for the ongoing final $\pi^+\pi^-$ cross section measurement:

- The 2D-χ^2 cut has been optimized in the low mass range (below 0.6 GeV/c^2), intermediate mass range (between 0.6 and 0.9 GeV/c^2) and high mass range (between 0.9 and 1.4 GeV/c^2) respectively, taking the $\mu\mu$, $\pi\pi$ and KK processes as the signal and all other processes as the background. The optimization is done by first using the BDT method with the χ^2 values of $\gamma_{\mathrm{ISR}}\gamma_{\mathrm{SA}}$ fit and $\gamma_{\mathrm{ISR}}\gamma_{\mathrm{LA}}$ fit as discriminant variables, and then simple cut-based 2D contours are chosen to approximate the BDT results to facilitate the analysis in practice.

- Background studies for the multihadrons from the $q\overline{q}$ (uds) process, multihadronic ISR process and $\tau\tau$ process are investigated. For the first two background processes, detailed BDT selections have been used to achieve better estimation and the corresponding data/MC ratios in different mass ranges, while for the third $\tau\tau$ background process, a corner region in the rejected 2D-χ^2 region is defined to determine the respective data/MC ratio.

- Detailed studies of the χ^2 cut efficiency are performed, including the study of bias introduced by the μ-ID requirement, the additional FSR radiation in pions and the effect of pion secondary interactions. For the FSR radiation study in dimuon and dipion, template fits are performed by using two components, $\theta_{\mathrm{min(trk},\gamma_{\mathrm{LA}})} < 20^\circ$ and $\theta_{\mathrm{min(trk},\gamma_{\mathrm{LA}})} > 20^\circ$ templates from the corresponding $\gamma_{\mathrm{ISR}}\gamma_{\mathrm{LA}}$ samples with proper normalization.

- Detailed studies of the $\gamma_{\mathrm{ISR}}\gamma_{\mathrm{SA}}$ and $\gamma_{\mathrm{ISR}}\gamma_{\mathrm{LA}}$ NLO fits are presented between $\mu\mu$ and $\pi\pi$ processes. The hypothesis of collinear additional ISR photons has been checked by comparing the energies and polar angles from their fitted values to the true ones,

with good agreement observed between data and simulation for the fitting bias. Fake photon corrections for FSR NLO in pion samples have been studied and then applied in the final fractions computation stage, which supersedes the result from the previous analysis [35, 38]. The measurement of the LA additional photon efficiency has been performed and the data/MC ratio is found to be consistent with unity within 2% systematic uncertainty. The 0C kinematic reconstruction has been further investigated to confirm the NLO results obtained from PHOKHARA MC predictions.

- This thesis extends from NLO fits to NNLO fits through the selection of events with two additional photons whether from ISR and/or FSR. The fraction of NNLO contributions to the inclusive ISR cross section is found to be at the 3.3% level for both muons and pions with a precision of 12% dominated by systematic uncertainties. This is the first experimental observation for these higher-order contributions.

- The new experimental information obtained at the NNLO level is utilized to improve and refine the NLO analysis by taking into account the cross-feeds between the different fit categories as identified in the analysis. The final NLO results are compared to the predictions from the NLO PHOKHARA generator: whereas the energy dependence of the additional photon is in fair agreement with data, it is found that its angular distribution is not, with a strong disagreement for photons emitted close to the $e^{\pm}$ beams. As the small-angle radiation is the dominant part of the NLO contribution, it results in a quite significant excess in the NLO rate predicted by PHOKHARA of $(25.4 \pm 2.5)\%$ for muons and of $(27.5 \pm 1.7)\%$ for pions. Despite the fact that the collinear ISR approximation used in the AFKQED generator does not agree with data, the predicted rates for both NLO and NNLO levels are much closer to our measurements with a deficit of $(5.9 \pm 1.1)\%$ and $(10 \pm 11)\%$, respectively for muons, and $(4.3 \pm 0.7)\%$ and $(16 \pm 9)\%$, respectively for pions.

- Due to the inclusive nature of the *BABAR* cross section measurements, the shortcomings of PHOKHARA found in this thesis have a negligible effect on the published results and the ongoing ones. On the contrary, the fact that PHOKHARA does not include NNLO contributions and its SA ISR NLO predictions are significantly larger than data, has implications for other ISR experiments such as KLOE and BES, relying on this generator to take into account unmeasured radiative events.

Appendix

A χ^2 distributions of LO events

In the ISR process, most events are LO events peaked at low χ^2 values without any additional photons satisfying the defined energy threshold. The 2D χ^2 distribution for the LO events are presented in Fig. A. 1.

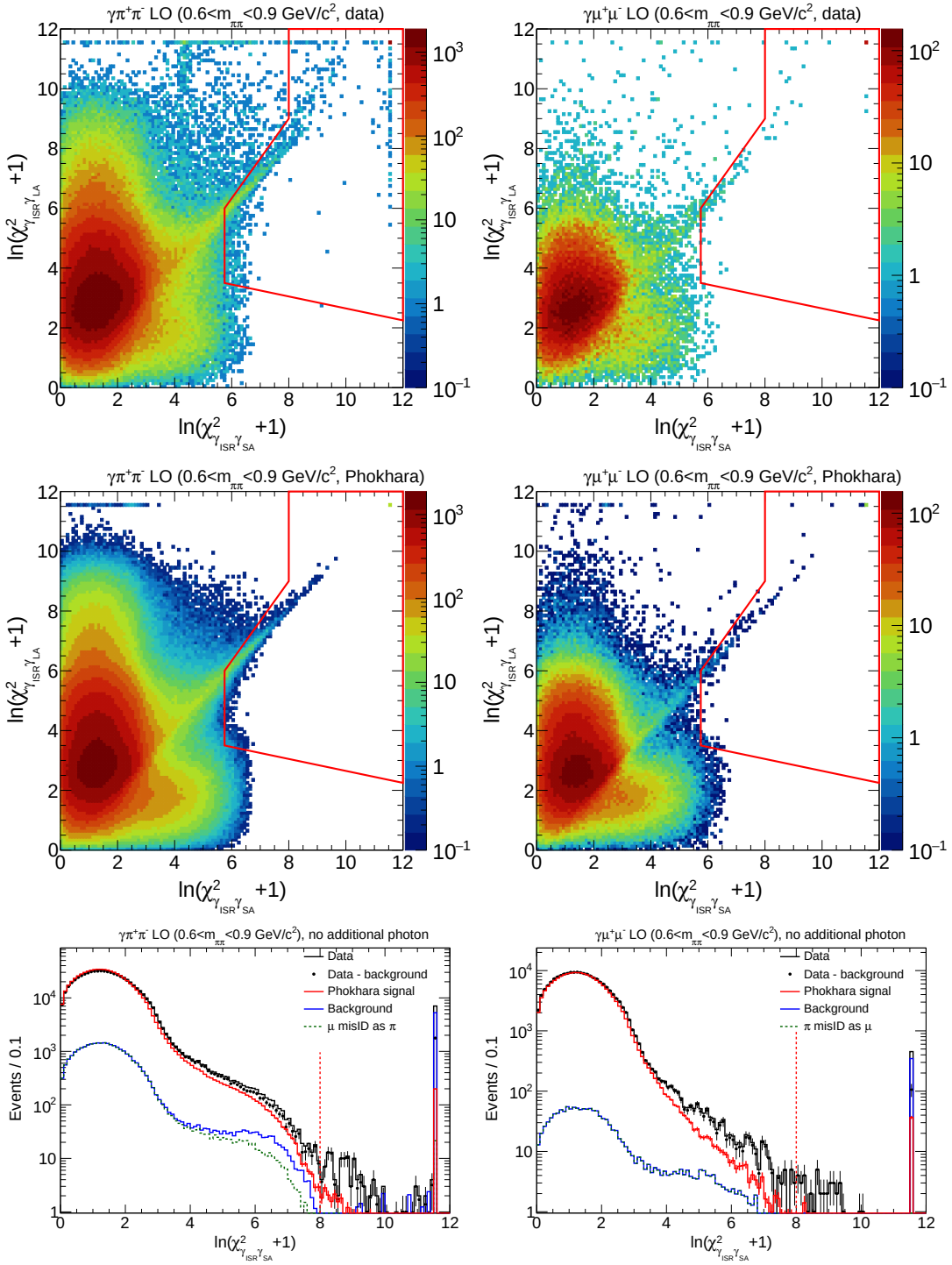

Figure A. 1: The 2D-χ^2 distribution for LO events of $\pi\pi$ (left) and $\mu\mu$ (right) in data (top), PHOKHARA MC (middle) and comparison of χ^2 of the $\gamma_{\rm ISR}\gamma_{\rm SA}$ fit between data and MC for the events without any additional measured photon (bottom) in the mass range between 0.6 and 0.9 GeV/c^2. The zone defined by red solid lines in the 2D plots and the dashed vertical red lines in the 1D plot indicate the optimized selection.

B Additional plots for the uds process

The $\gamma\gamma$ mass distributions obtained with BDT selections corresponding to the solid and dashed vertical lines in the bottom-left panel in Fig. 4.3 are shown in Fig. B. 1 for $m_{\gamma\gamma} < 0.3$ GeV/c^2 in the high mass range. The distributions here show explicit non-uds contributions from the $\tau\tau$ process (shown in red) and other processes (shown in blue) before subtraction, which differ from the distributions in Fig. 4.8. The small bump observed close to the expected π^0 peak in the non-uds distribution is an artefact of the $\gamma\gamma$ mass reconstruction, namely by selecting the photon pair that has the closet mass value to the π^0 mass.

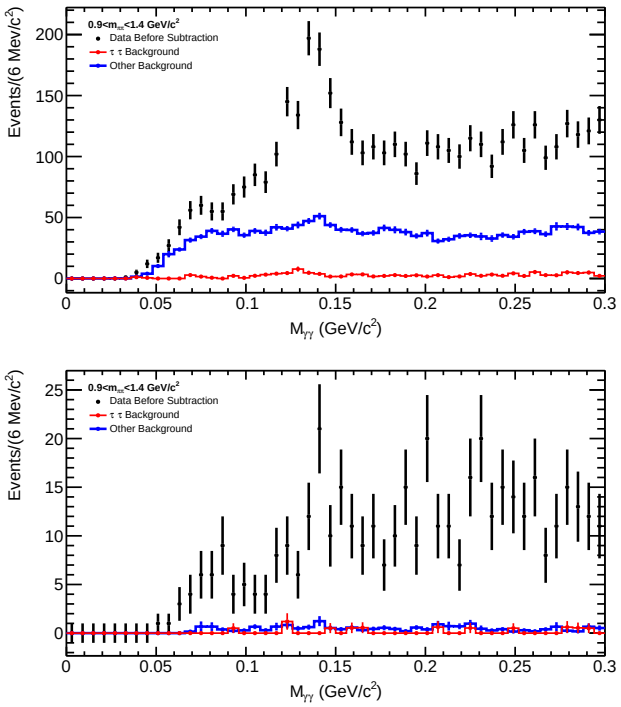

Figure B. 1: Distributions of the $\gamma\gamma$ mass obtained with BDT selections corresponding to the solid (top) and dashed (bottom) vertical lines in the bottom-left panel in Figure 4.3 before subtracting the $\tau\tau$ (red) and other non-uds (blue) contributions from data (black). For those bins with empty data entry, the statistical uncertainty of the data is set to one.

C Details on the study of the 3π process

The selected discriminating variables are listed in Table C. 1. [1] The shapes of these variables between the 3π and non-3π samples are compared in Fig. C. 1. The corresponding comparison between the data sample and the MC simulation for these variables is shown in Fig. C. 2.

Variable	Description
$\ln(\chi^2_{2\pi\gamma_{\rm ISR}\gamma_{\rm SA}}+1)$	χ^2 value of $e^+e^-\to\pi^+\pi^-\gamma_{\rm ISR}\gamma_{\rm SA}$
$E_{\gamma 2}$	Energy of the second photon in addition to the ISR photon
$\mathrm{M}_{\gamma_2\gamma_3}$	Invariant mass of the second and third photon in addition to the ISR photon
$\ln(\chi^2_{2\pi\gamma_{\rm ISR}2\gamma_{\rm LA}}+1)$	χ^2 of the $e^+e^-\to\pi^+\pi^-\gamma_{\rm ISR}2\gamma_{\rm LA}$ fit
$E_{\gamma_2}+E_{\gamma_3}$	Energy sum of the second photon and third photon in additional to the ISR photon
$\mathrm{PTOT0}_1$	Momentum of the second good track
Ephsum	Energy sum of all measured photons
$\mathrm{PTOT0}_0$	Momentum of the first good track
$\ln(\chi^2_{2\pi\gamma_{\rm ISR}\gamma_{\rm LA}}+1)$	χ^2 value of $e^+e^-\to\pi^+\pi^-\gamma_{\rm ISR}\gamma_{LA}$ fit
M2PI_2pi2g or M2PI_2pi1g1bm	Fitted $\pi^+\pi^-$ mass depending on the fit χ^2 value
COSTHPI	$\cos\theta^*$ with the π hypothesis
DPSING	Angle between ISR photon and missing momentum in laboratory

Table C. 1: Selected discriminating variables used in the BDT selection of the 3π process. They are sorted according to their relative importance for the low $\pi\pi$ mass range with $n_\gamma > 2$.

The correlation between the BDT discriminating variables for 3π and non-3π MC samples is shown in Fig. C. 3. Highly correlated and less discriminating variables have been removed.

The χ^2 distribution of the BDT selected candidates in data without subtracting non-3π contributions is shown in Fig. C. 4 in the accepted 2D χ^2 region. The BDT selection corresponds to the solid vertical line in the top-left panel in Fig. 4.13. In Fig. C. 4, the 3π MC events are also shown with (top right) and without (bottom) the BDT selection for comparison. Similar distributions between data and MC in the accepted χ^2 region are observed.

Figure C. 5 provides an alternative evaluation of the BDT selection, which presents the $m_{\gamma\gamma}$ distribution of two non-ISR photons for the case of $n_\gamma > 2$ in the low mass range. The plots demonstrate that the BDT selection effectively suppress non-3π contributions to the percent level within the dominant π^0 peak region, while maintaining an efficiency of approximately 60% in that region.

[1] Unless stated otherwise, the discussion is concentrated on the low $\pi\pi$ mass window where the 3π background dominates the background contribution.

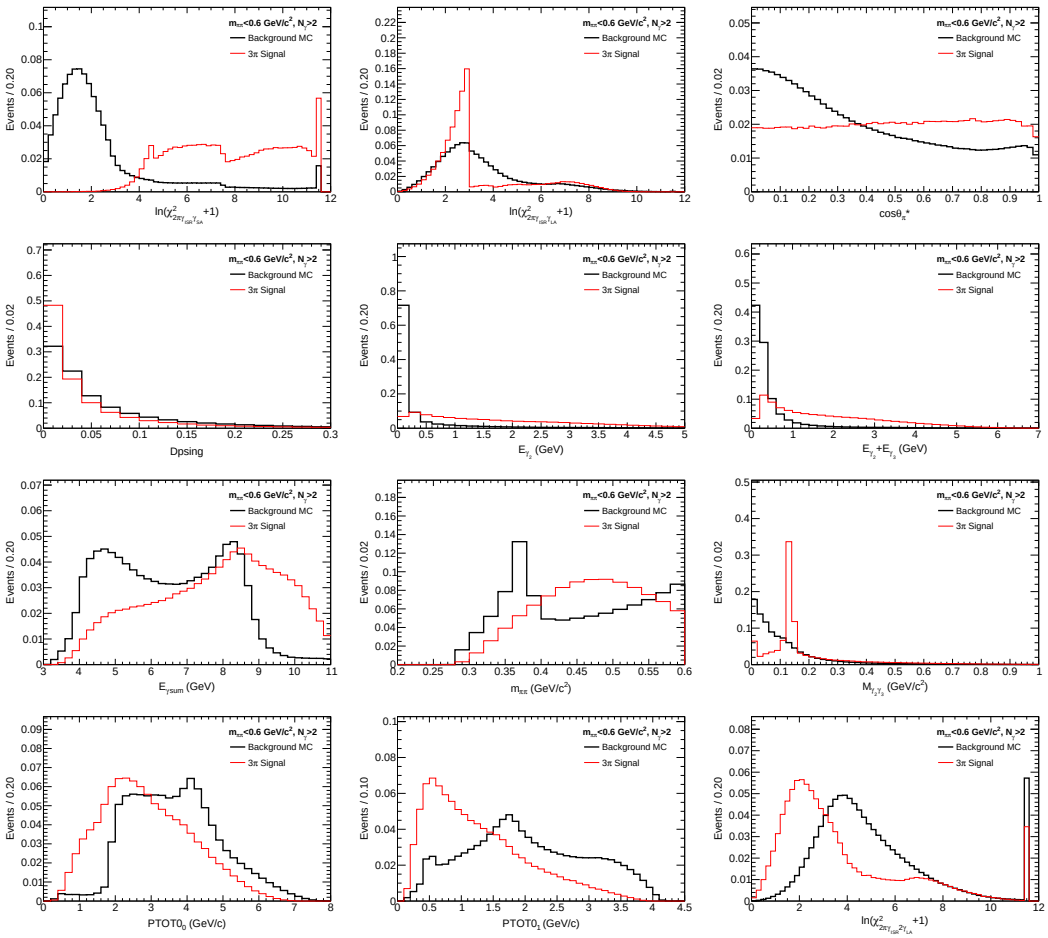

Figure C. 1: Comparison of shapes between the 3π (red solid line) and non-3π (black solid line) MC samples for the selected BDT input variables.

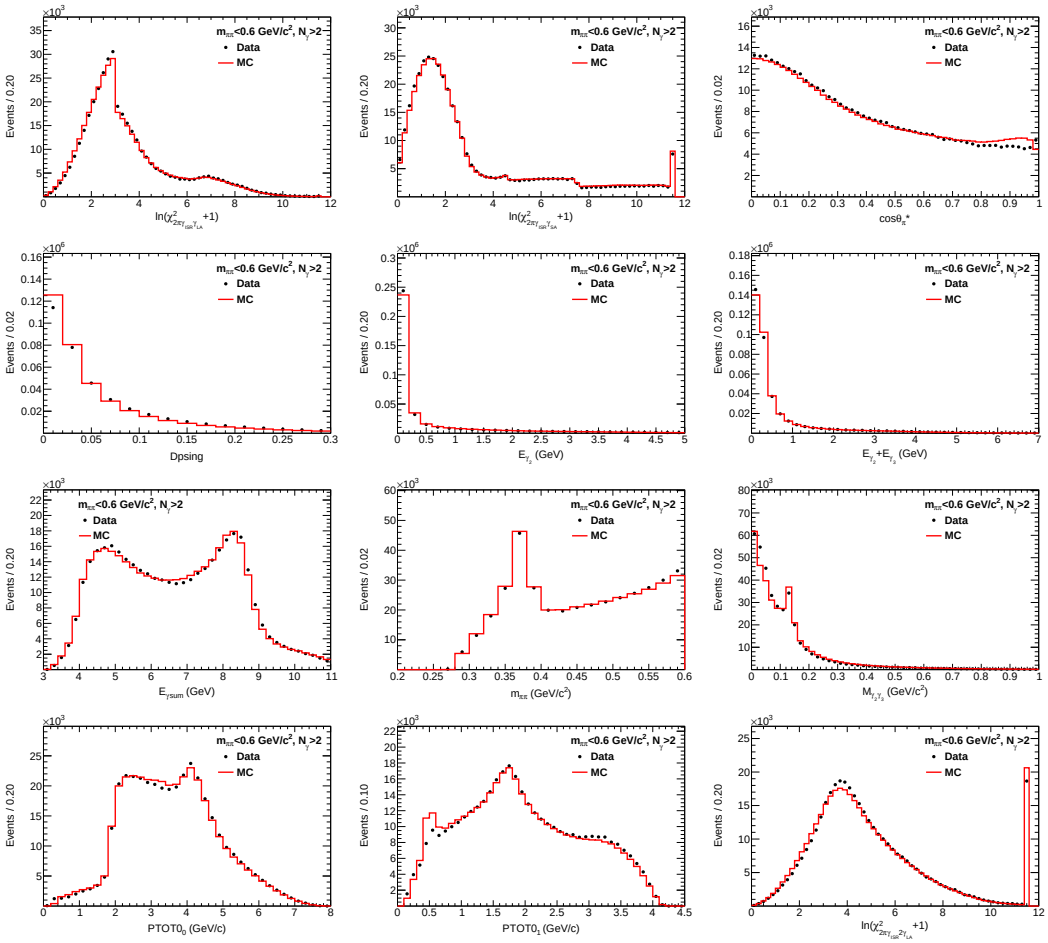

Figure C. 2: Distributions of the data (shown with full points) compared to MC distributions (shown with the histograms) which are normalized for the selected BDT input variables.

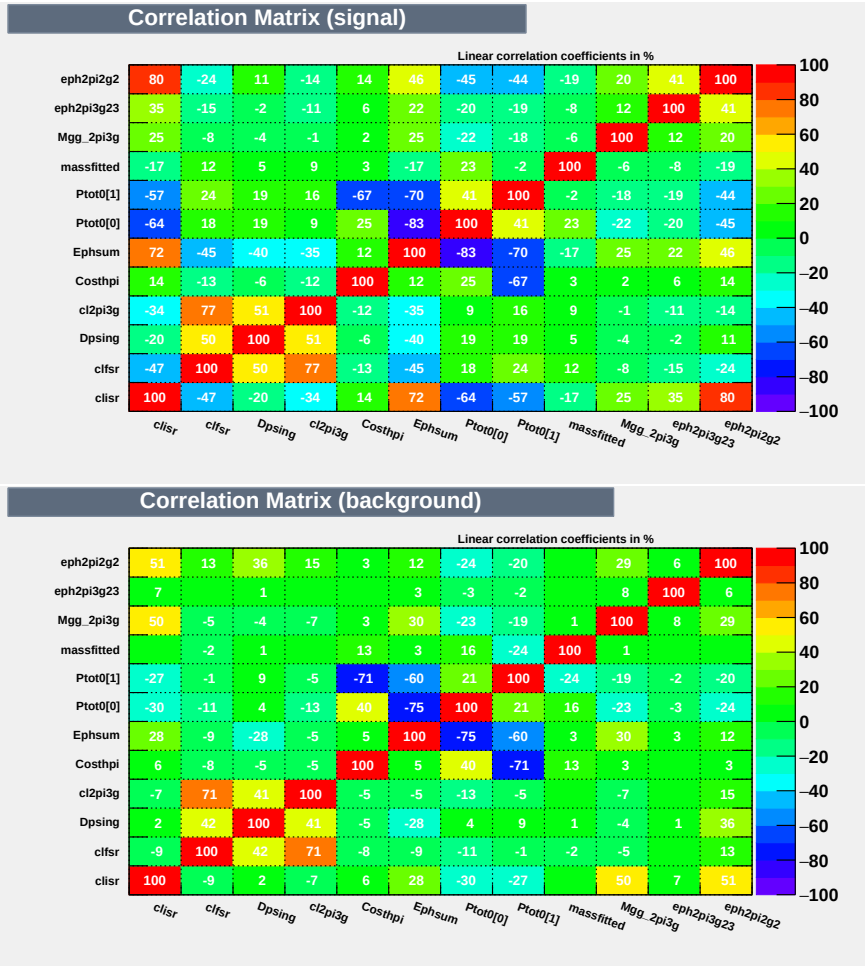

Figure C. 3: Correlations between the BDT input variables for 3π (top) and non-3π (bottom) MC samples.

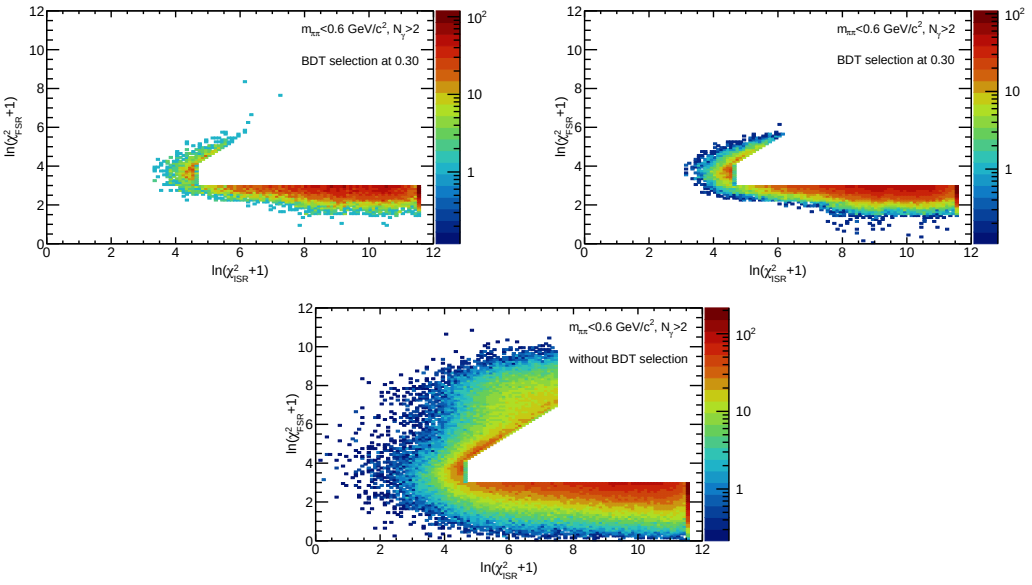

Figure C. 4: Candidates in data (top left) with the BDT selection corresponding to the solid vertical line in the top-left panel in Fig. 4.13. The 3π MC events with (top right) and without (bottom) the BDT selection are also shown for comparison.

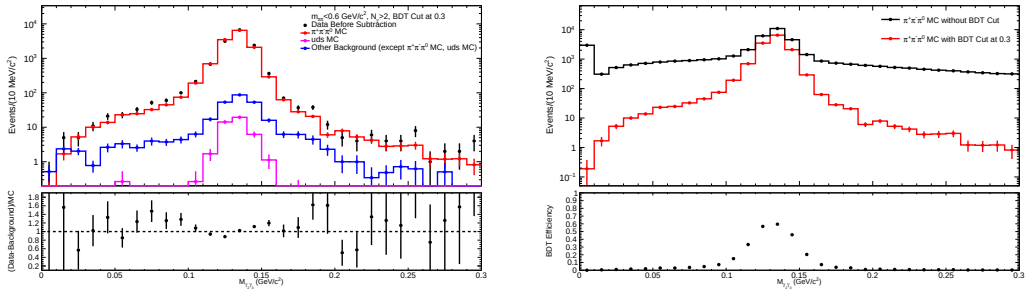

Figure C. 5: Left: distribution of $m_{\gamma\gamma}$ of 3π candidates in data and the selected MC events from 3π and non-3π processes corresponding to the nominal BDT selection shown in Fig. 4.13, with the ratio of data with background subtraction over the 3π MC prediction. Right: Similar distribution from 3π MC events with (red histogram) and without (black histogram) BDT selection, with the corresponding BDT selection efficiency.

D Additional plots for the 2D-χ^2 optimization

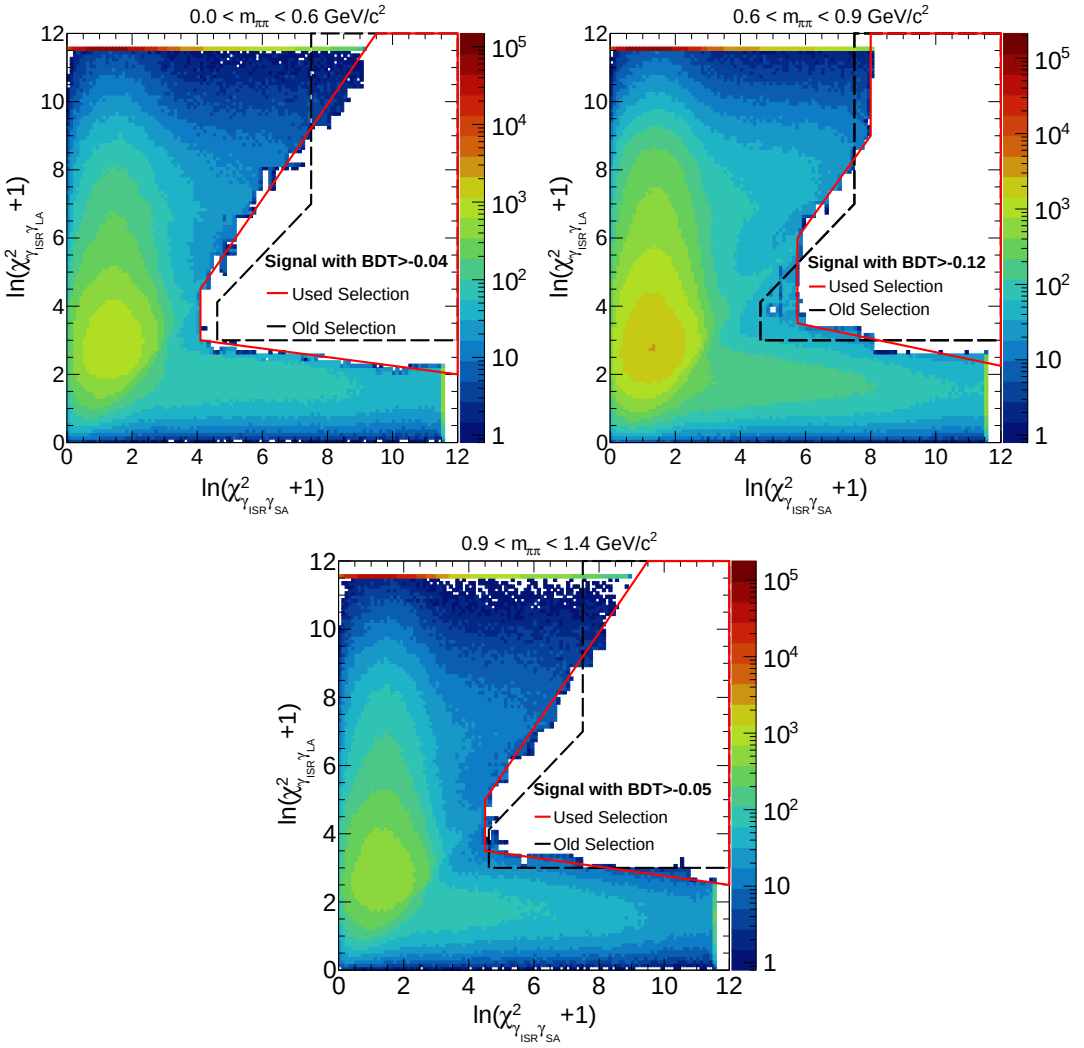

Figure D. 1: Comparison showing the 2D contours of the signal MC events selected with the best SOB BDT optimization, the optimized cut-based selection (red solid lines) and an old selection (black dashed lines) for the low (top-left), intermediate (top-right) and high (bottom) mass windows.

Figure D. 1 compares the contours of the signal selected MC events with the best SOB BDT optimization, the cut-based selections in use (shown in red solid lines) and an old selection (shown in black dashed lines) in three different $m_{\pi\pi}$ ranges. The old selection, which was mass-independent, was used in the uds and 3π background study.

E χ^2 distributions for NNLO events

The 2D-χ^2 distributions for NNLO events based on the AFKQED samples are illustrated in Fig. E. 1.

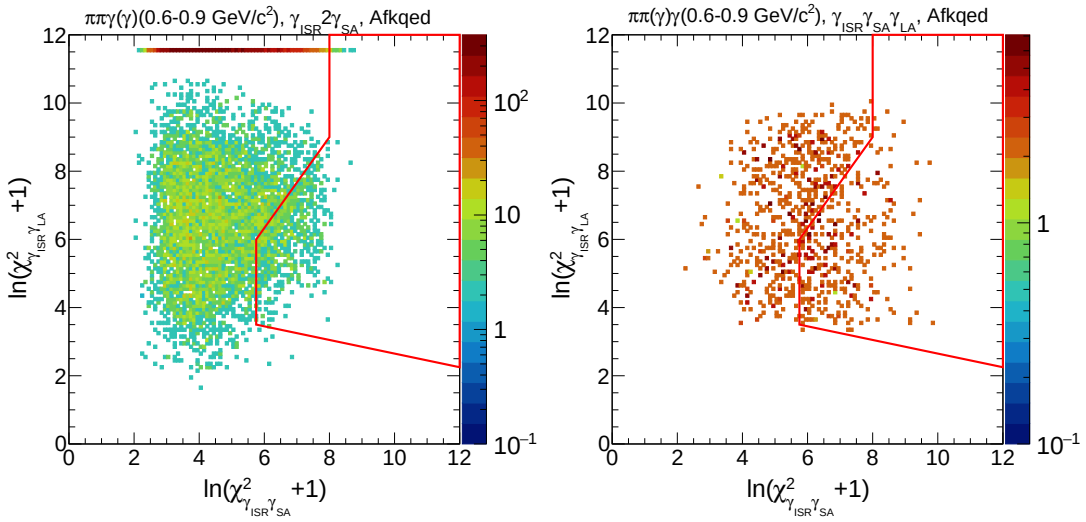

Figure E. 1: The 2D-χ^2 distributions for NNLO $\gamma_{\mathrm{ISR}}2\gamma_{\mathrm{SA}}$ (left) and $\gamma_{\mathrm{ISR}}\gamma_{\mathrm{SA}}\gamma_{\mathrm{LA}}$ (right) events in the mass range between 0.6 and 0.9 GeV/c^2 based on AFKQED predictions for the $\pi\pi\gamma$ process.

F Effect of pion secondary interactions

The effects of secondary interactions are mostly observed in the tracking efficiency due to the tight cuts imposed on the tracks pointing to the interaction region. Some small residual effect is also expected in the 2D-χ^2 selection efficiency. Detailed investigations show that the requirement used in the event selection, for the two-track $\mathrm{V_{xy}}$ in the transverse plane close to the interaction point within 0.5 cm, is also effective against secondary interactions. In view of the correlation between the 2D-χ^2 and $\mathrm{V_{xy}}$ efficiencies, the study of the bias induced by secondary interactions in data/MC is performed jointly for the two selection cuts. Therefore, the $\mathrm{V_{xy}}$ requirement has been removed for the study of secondary interactions. In the previous analysis [35], it has been demonstrated that two variables are particularly useful for this study. One of them is $\mathrm{R_{xy}}$, which means the radial distance from the initial interaction point to the secondary vertex formed between one of the two well-reconstructed tracks with another non-well-constructed track in the $x-y$ transverse plane. The other variable called $\mathrm{docaxy^{max}}$ (the unit is cm) which is the largest distance of minimum approach to the beam axis also in the $x-y$ plane, with a larger deviation indicating a kink suffered by the interacting track. In terms of statistical precision, the $\mathrm{docaxy^{max}}$ variable is much more effective and thus it is used in the current study. The low mass region which has a more restrictive 2D-χ^2 selection than the intermediate mass region is taken as an example. Figure F. 1 shows the $\mathrm{docaxy^{max}}$ distributions of the $\mu\mu\gamma(\gamma)$ and $\pi\pi\gamma(\gamma)$ PHOKHARA MC samples along with those after 2D-χ^2 selection, and their corresponding 2D-χ^2 efficiency. At low $\mathrm{docaxy^{max}}$ values, the efficiency is high and comparable for the two samples. However, as the $\mathrm{docaxy^{max}}$ values increase, the efficiency decreases for both samples. Notably, the decrease in efficiency is more pronounced for the $\pi\pi\gamma(\gamma)$ sample than the $\mu\mu\gamma(\gamma)$ sample, reflecting the effects of pion interactions.

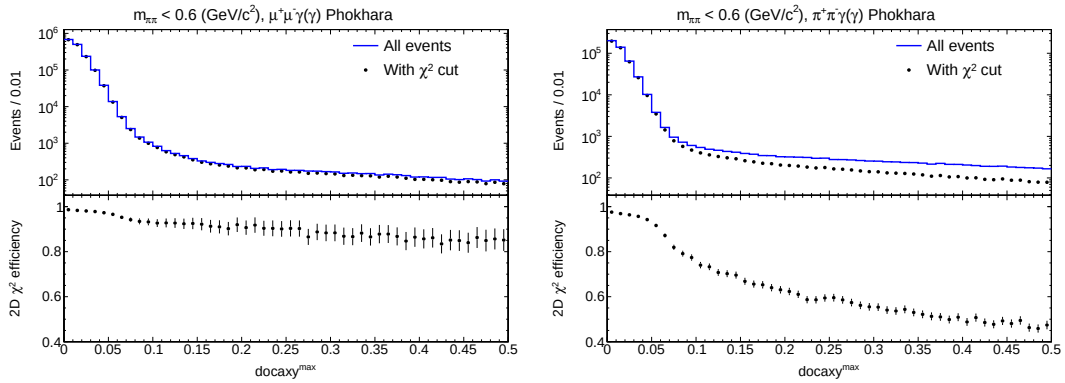

Figure F. 1: Distributions of $\mathrm{docaxy^{max}}$ of the $\mu\mu\gamma(\gamma)$ (left) and $\pi\pi\gamma(\gamma)$ (right) PHOKHARA MC samples in comparison with those with the 2D-χ^2 selection in the low mass region, with the corresponding 2D-χ^2 selection efficiency as a function of $\mathrm{docaxy^{max}}$.

The lower efficiency in the $\pi\pi\gamma(\gamma)$ sample also implies that the effects of pion interactions are relatively more important in the rejected 2D-χ^2 region. The $\mathrm{docaxy^{max}}$

distributions in the rejected region are compared for the $\pi\pi\gamma(\gamma)$ and $\mu\mu\gamma(\gamma)$ samples in Fig. F. 2, with the latter being normalized to the former in the range of $\mathrm{docaxy}^{\mathrm{max}} < 0.05$ where the effect of secondary interactions is expected to be negligible. The difference observed between the two samples in the high $\mathrm{docaxy}^{\mathrm{max}}$ range defines the effects of pion interactions in the rejected 2D-χ^2 region. In addition, the rejected 2D-χ^2 region may include a contribution from pion decays-in-flight, resulting in the production of a final muon. To remove this contribution, which is comparatively easier to simulate than secondary interactions, pion ID is applied to the good track with a larger docaxy in the event. By applying this criterion, the effects of pion secondary interactions on the 2D-χ^2 selection inefficiency, shown in Table F. 1 in three mass regions and in Fig. F. 3 as a function of $\mathrm{m}_{\pi\pi}$. The effect of the pion decays-in-flight is quantified in Table F. 1: 2 per mil in the low mass region and 1.5 per mil in the high mass region, and only 0.5 per mil in the intermediate region because of the looser 2D-χ^2 selection.

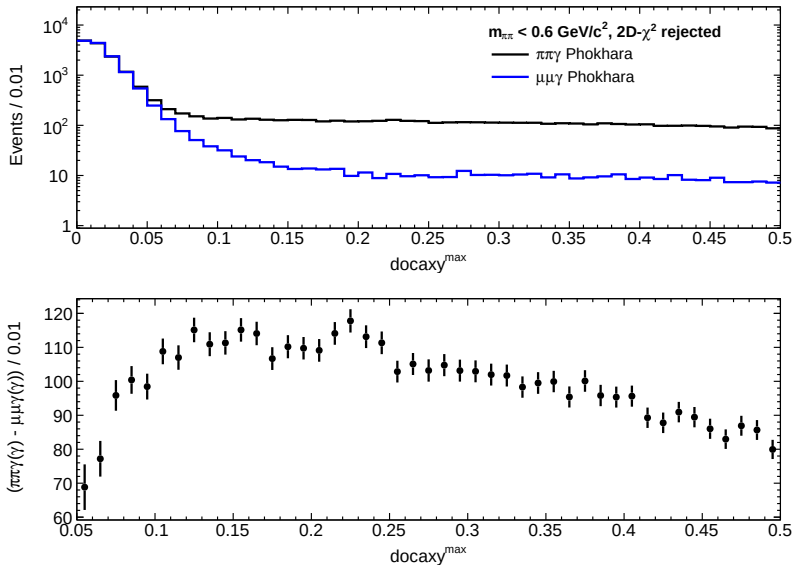

Figure F. 2: Top: Distributions of $\mathrm{docaxy}^{\mathrm{max}}$ of the $\pi\pi\gamma(\gamma)$ PHOKHARA MC sample (black) in comparison with that of the $\mu\mu\gamma(\gamma)$ sample (blue) in the rejected 2D-χ^2 region for the low mass region. $\mu\mu\gamma(\gamma)$ sample is normalized to $\pi\pi\gamma(\gamma)$ in the range of $\mathrm{docaxy}^{\mathrm{max}} < 0.05$. Bottom: The difference of the two samples above is shown in linear scale (Note here the x-axis starts from 0.05).

.

Until now, the results have been obtained using MC simulations. In the following, the rate of pion interactions is compared with the corresponding rate in the data. Given the fact that the background in the rejected 2D-χ^2 region for the $\pi\pi\gamma(\gamma)$ process in data is significant and the background estimation based on the MC may not be reliable, an enriched region of pion interactions in the 2D-χ^2 plane which overlaps the accepted region and rejected region around the 2D-χ^2 cut boundary is defined using an event sample selected from $\pi\pi\gamma(\gamma)$ PHOKHARA MC sample with

	< 0.6 GeV/c^2	$0.6 - 0.9$ GeV/c^2	$0.9 - 1.4$ GeV/c^2
PHOKHARA with pion ID	0.675%	0.053%	0.550%
PHOKHARA w/o pion ID	0.879%	0.110%	0.657%

Table F. 1: The efficiency loss of the 2D-χ^2 selection induced by pion secondary interactions and decays-in-flight in the three mass regions, are separated applying pion ID (only secondary interactions included) or not (both secondary interactions and decays included) based on PHOKHARA MC samples.

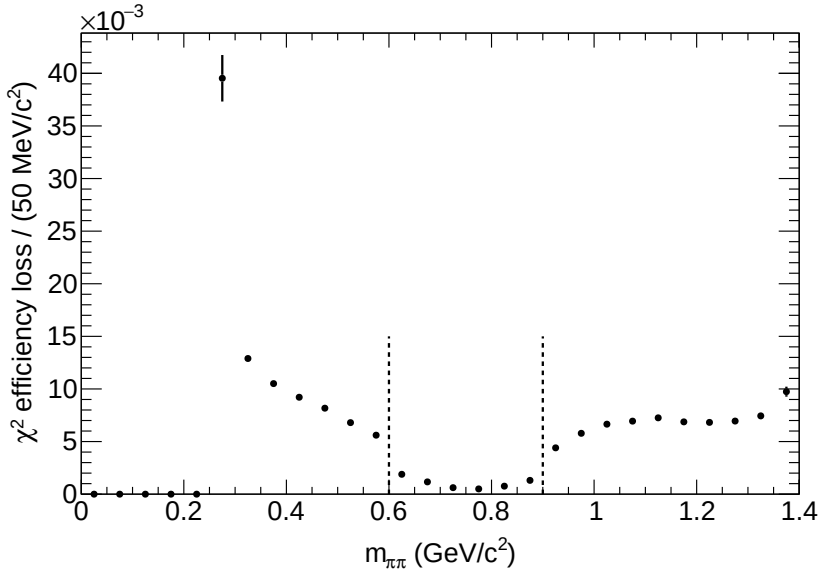

Figure F. 3: The loss of 2D-χ^2 efficiency from pion secondary interactions as a function of $m_{\pi\pi}$ derived from PHOKHARA MC samples.

.

$\mathrm{docaxy}^{\mathrm{max}} > 0.1$ in the low mass region, as illustrated in Fig. F. 4. The red dotted lines along the diagonal boundaries represent the corresponding defined enriched region and the full red lines define the 2D-χ^2 selection contour.

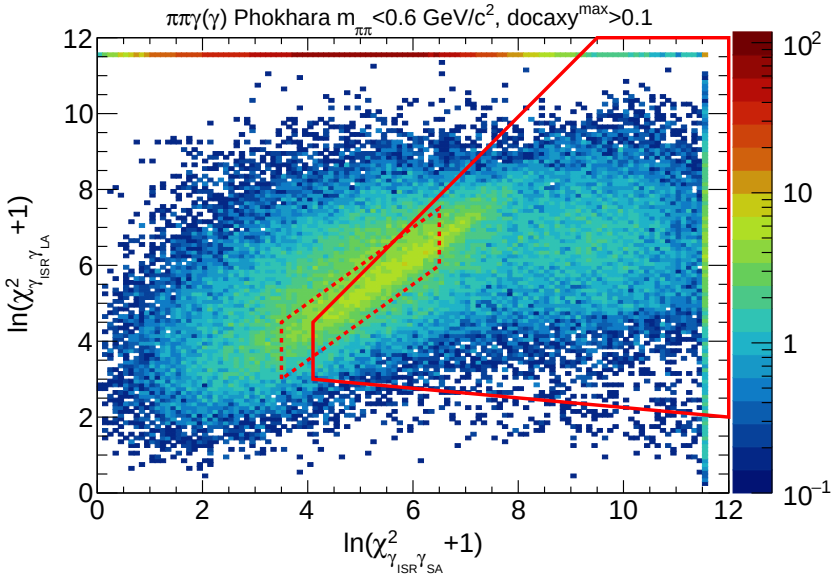

Figure F. 4: Sample selected with $\mathrm{docaxy}^{\mathrm{max}} > 0.1$ from $\pi\pi\gamma(\gamma)$ PHOKHARA MC sample in the low mass region. The red dotted lines represent the defined enriched region for comparing data and MC on the effects of pion interactions, while the full red lines define the 2D-χ^2 selection contour.

.

Figure F. 5 shows a comparison of $\mathrm{docaxy}^{\mathrm{max}}$ distributions of events satisfying pion ID in the enriched region in data and MC sample in the three mass regions. Using the integrated event yields with $\mathrm{docaxy}^{\mathrm{max}} > 0.1$, one can calculate the data/MC ratios for pion interactions in the three mass regions which are summarized in Table F. 2. Additionally, the systematic uncertainty is quoted by extending the integration from 0.1 to 0.05.

	< 0.6 GeV/c^2	$0.6 - 0.9$ GeV/c^2	$0.9 - 1.4$ GeV/c^2
Data/MC ratio	$1.62(0.05)(0.00)$	$1.58(0.06)(0.04)$	$1.03(0.04)(0.01)$

Table F. 2: Ratios of data and MC event yields after the $\mathrm{docaxy}^{\mathrm{max}} > 0.1$ selection in the enriched region for the pion interactions study in the three mass ranges. The first uncertainty is statistical and the second systematic corresponding to the variation when the selection of $\mathrm{docaxy}^{\mathrm{max}}$ is varied from 0.1 to 0.05.

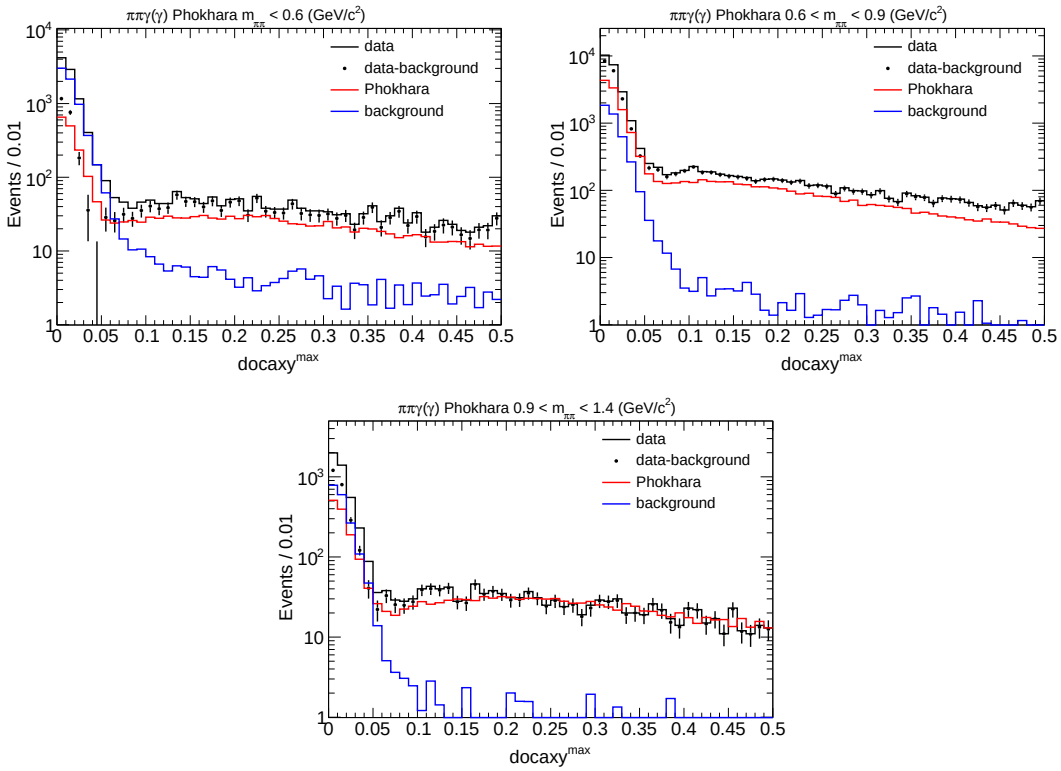

Figure F. 5: Distributions of $\mathrm{docaxy}^{\mathrm{max}}$ of the sample satisfying the pion ID in the enriched region in the 2D-χ^2 plane comparing data (black histograms), data with background subtraction (full dots), $\pi^+\pi^-\gamma(\gamma)$ MC (red) and background (blue), in the low (top-left), intermediate (top-right) and high (bottom) mass ranges.

G Feed-through study

Each fitted sample of a given category contains events that may have been misclassified. As shown in Table 8.1, the main components come from NLO (NNLO) feed-through into NNLO (NLO) categories, in particular, there is a cross-feed between the $\gamma_{\text{ISR}}\gamma_{\text{SA}}$ and $\gamma_{\text{ISR}}2\gamma_{\text{SA}}$ topologies.

For NLO feed-throughs, the PHOKHARA is directly used, which simulates the data better with an angular emission of additional ISR photons. Each true NLO category is distributed over different fitted categories, with full selection efficiency and misclassification probabilities shown in Table 8.1.

For NNLO feed-throughs, only AFKQED can be used. However, additional corrections are needed to simulate feed-throughs in the data since the collinear assumptions of all additional photons. The only configuration identified as NNLO $\gamma_{\text{ISR}}2\gamma_{\text{SA}}$ is when the two additional photons are emitted from opposite beams ('open NNLO'). When the two additional photons are emitted from the same beam, they are merged into one single photon ('hidden NNLO'). In the former case, events are classified as $\gamma_{\text{ISR}}2\gamma_{\text{SA}}$ category, while in the latter case, events are indistinguishable from the NLO events and they are classified as $\gamma_{\text{ISR}}\gamma_{\text{SA}}$ category.

In the data, different NNLO ISR topologies are identified depending on the angles of the additional ISR photons. Assuming p the probability for an additional photon to be out of angular range of the detector acceptance, the different topologies between AFKQED and data are illustrated in Fig. G. 1, with their respective probabilities shown. To simulate the complete feed-throughs in the data sample, the 'open NNLO' and the 'hidden NNLO' events in the AFKQED are assumed to be produced at the same rate. They are recast over the categories in the data with proper probabilities and then distributed over the fitted categories accordingly.

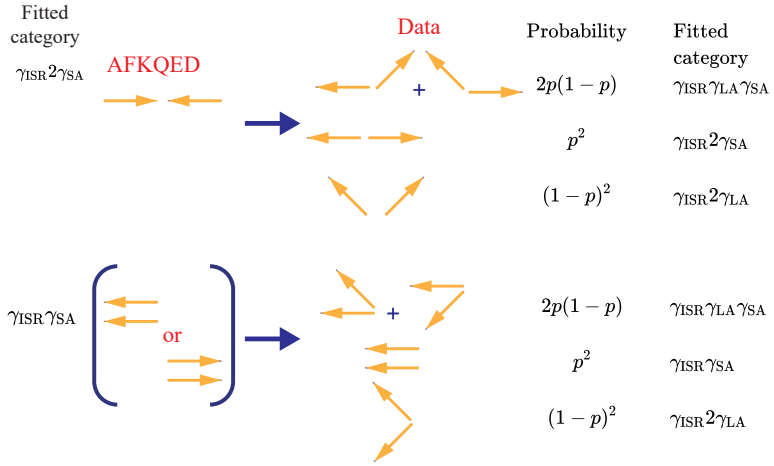

Figure G. 1: Sketch of additional ISR photons emission in AFKQED (collinear to the beam) and in data (emitted at some angle), with p defined as the probability of the additional ISR photon out of the detector acceptance range.

To account for the normalization of feed-through components and potential differ-

ences in rates between data and MC, an iterative approach has been used. Data/MC ratios for each feed-through component are obtained from the feed-through-subtracted samples of a given topology in data. The final rates are obtained through data over PHOKHARA ratios (for NLO) and data over AFKQED ratios (for NNLO) updated at each step. The process is iterated a few times until convergence is achieved. Additionally, a correction is applied to the NNLO feed-throughs to account for the missing tail of the spectra of the additional ISR photons beyond 2.3 GeV in AFKQED.

The final resulting rates, obtained through the iterative procedure and corrected for the efficiencies, determine the composition of the full data sample in terms of true topologies to be compared to the corresponding true topologies in the MC samples.

Bibliography

[1] G. Arnison *et al*. (UA1 Collaboration). Experimental observation of isolated large transverse energy electrons with associated missing energy at s = 540 GeV. *Physics Letters B*, 122(1):103–116, 1983.

[2] M. Banner *et al*. (The UA2 Collaboration). Observation of single isolated electrons of high transverse momentum in events with missing transverse energy at the CERN pp collider. *Physics Letters B*, 122(5-6):476–485, 1983.

[3] G. Arnison *et al*. (UA1 Collaboration). Experimental observation of lepton pairs of invariant mass around 95 GeV/c^2 at the CERN SPS collider. *Physics letters B*, 126(5):398–410, 1983.

[4] F. Abe *et al*. (CDF Collaboration). Observation of Top Quark Production in $\overline{p}p$ Collisions with the Collider Detector at Fermilab. *Physical review letters*, 74(14):2626, 1995.

[5] G. Aad *et al*. (ATLAS Collaboration). Observation of a new particle in the search for the Standard Model Higgs boson with the ATLAS detector at the LHC. *Physics Letters B*, 716(1):1–29, 2012.

[6] S. Chatrchyan *et al*. (CMS Collaboration). Observation of a new boson at a mass of 125 GeV with the CMS experiment at the LHC. *Physics Letters B*, 716(1):30–61, 2012.

[7] CDF Collaboration. High-precision measurement of the W boson mass with the CDF II detector. *Science*, 376(6589):170–176, 2022.

[8] J. Schwinger. On quantum-electrodynamics and the magnetic moment of the electron. *Physical Review*, 73(4):416, 1948.

[9] P. Kusch and H.M. Foley. The magnetic moment of the electron. *Physical Review*, 74(3):250, 1948.

[10] B. Abi *et al.* (Muon $g-2$ Collaboration). Measurement of the Positive Muon Anomalous Magnetic Moment to 0.46 ppm. *Physical Review Letters*, 126(14):141801, 2021.

[11] G.W. Bennett *et al.* (Muon $g-2$ Collaboration). Final report of the E821 muon anomalous magnetic moment measurement at BNL. *Physical Review D*, 73(7):072003, 2006.

[12] D. P. Aguillard *et al.* (Muon $g-2$ Collaboration). Measurement of the Positive Muon Anomalous Magnetic Moment to 0.20 ppm. *arXiv preprint arXiv:2308.06230*, 2023.

[13] T. Blum *et al.* Calculation of the hadronic vacuum polarization contribution to the muon anomalous magnetic moment. *Physical Review Letters*, 121(2):022003, 2018.

[14] S. Borsanyi *et al.* Leading hadronic contribution to the muon magnetic moment from lattice QCD. *Nature*, 593(7857):51–55, 2021.

[15] C. Alexandrou *et al.* Lattice calculation of the short and intermediate time-distance hadronic vacuum polarization contributions to the muon magnetic moment using twisted-mass fermions. *Physical Review D*, 107(7):074506, 2023.

[16] HPQCD MILC A. Bazavov *et al.* (Fermilab Lattice and Collaborations). Light-quark connected intermediate-window contributions to the muon $g-2$ hadronic vacuum polarization from lattice QCD. *Physical Review D*, 107(11):114514, 2023.

[17] W. Greiner and J. Reinhardt. *Field quantization*, chapter 8. Springer Science & Business Media, 1996.

[18] T. Aoyama, M. Hayakawa, T. Kinoshita, and M. Nio. Complete Tenth-Order QED Contribution to the Muon g-2. *Physical Review Letters*, (11):109, 2012.

[19] T. Aoyama, M. Hayakawa, T. Kinoshita, and M. Nio. Tenth-Order QED Contribution to the Electron $g-2$ and an Improved Value of the Fine Structure Constant. *Physical Review Letters*, 109:111807, 2012.

[20] T. Aoyama *et al.* The anomalous magnetic moment of the muon in the Standard Model. *Physics reports*, 887:1–166, 2020.

[21] A. Pivovarov. Spectrality, coupling constant analyticity and the renormalization group. *arXiv preprint hep-ph/0104213*, 2001.

[22] A. Keshavarzi, D. Nomura, and T. Teubner. $g-2$ of charged leptons, $\alpha(M_Z^2)$, and the hyperfine splitting of muonium. *Physical Review D*, 101(1):014029, 2020.

[23] A. Kurz, T. Liu, P. Marquard, and M. Steinhauser. Hadronic contribution to the muon anomalous magnetic moment to next-to-next-to-leading order. *Physics Letters B*, 734:144–147, 2014.

[24] M. Davier, A. Hoecker, B. Malaescu, and Z. Zhang. A new evaluation of the hadronic vacuum polarisation contributions to the muon anomalous magnetic moment and to $\alpha(M_Z^2)$. *The European Physical Journal C*, 80(3):241, 2020.

[25] M. Benayoun, L. Delbuono, and F. Jegerlehner. BHLS 2, a New Breaking of the HLS Model and its Phenomenology. *The European Physical Journal C*, 80(2):81, 2020.

[26] F. Jegerlehner. The Anomalous Magnetic Moment of the Muon. *Springer Tracts in Modern Physics*, 274, 2017.

[27] A. Anastasi *et al.* (KLOE-2 Collaboration). Combination of KLOE σ ($e^+e^- \to \pi^+\pi^-\gamma(\gamma)$) measurements and determination of $a_\mu^{\pi^+\pi^-}$ in the energy range 0.10< s< 0.95 GeV^2. *Journal of High Energy Physics*, 2018(3):1–25, 2018.

[28] F. V. Ignatov *et al.* (CMD-3 collaboration). Measurement of the $e^+e^- \to \pi^+\pi^-$ cross section from threshold to 1.2 GeV with the CMD-3 detector. *arXiv preprint arXiv:2302.08834*, 2023.

[29] R. R. Akhmetshin *et al.* Measurement of $e^+e^- \to \pi^+\pi^-$ cross-section with CMD-2 around ρ-meson. *Physics Letters B*, 527(3-4):161–172, 2002.

[30] R. R. Akhmetshin *et al.* High-statistics measurement of the pion form factor in the ρ-meson energy range with the CMD-2 detector. *Physics Letters B*, 648(1):28–38, 2007.

[31] V.N. Baier and V.S. Fadin. RADIATIVE CORRECTIONS TO THE RESONANT PARTICLE PRODUCTION. Technical report, Inst. of Nuclear Physics, Novosibirsk, USSR, 1968.

[32] A.B. Arbuzov, E.A. Kuraev, N.P. Merenkov, and L. Trentadue. Hadronic cross sections in electron-positron annihilation with tagged photon. *Journal of High Energy Physics*, 1998(12):009, 1999.

[33] S. Binner, J.H. Kühn, and K. Melnikov. Measuring σ ($e^+e^- \to$ hadrons) using tagged photons. *Physics Letters B*, 459(1-3):279–287, 1999.

[34] M. Benayoun, S.I. Eidelman, V.N. Ivanchenko, and Z.K. Silagadze. Spectroscopy at B-factories using hard photon emission. *Modern Physics Letters A*, 14(37):2605–2614, 1999.

[35] J. P. Lees *et al.* (BABAR Collaboration). Precise measurement of the $e^+e^- \to \pi\pi\gamma(\gamma)$ cross section with the initial-state radiation method at BABAR. *Physical Review D*, 86(3):032013, 2012.

[36] J. P. Lees *et al.* (BABAR Collaboration). Measurement of initial-state–final-state radiation interference in the processes $e^+e^- \to \mu^+\mu^-\gamma$ and $e^+e^- \to \pi^+\pi^-\gamma$. *Physical Review D*, 92(7):072015, 2015.

[37] F. Campanario, H. Czyż, J. Gluza, M. Gunia, T. Riemann, G. Rodrigo, and V. Yundin. Complete QED NLO contributions to the reaction $e^+e^- \to \mu^+ \mu^- \gamma$ and their implementation in the event generator PHOKHARA. *Journal of High Energy Physics*, 2014(2):1–27, 2014.

[38] B. Aubert *et al.* (BABAR Collaboration). Precise Measurement of the $e^+e^- \to \pi^+\pi^-(\gamma)$ Cross Section with the Initial State Radiation Method at BABAR. *Physical Review Letters*, 103:231801, 2009.

[39] T. Kinoshita. Phys.(NY) 3, 650 (1962); TD Lee and M. Nauenberg. *Phys. Rev*, 133:B1549, 1964.

[40] H. Czyż and J.H. Kühn. Four pion final states with tagged photons at electron positron colliders. *The European Physical Journal C-Particles and Fields*, 18(3):497–509, 2001.

[41] M. Caffo, H. Czyż, and E. Remiddi. BHAGEN95: a Monte Carlo program for Bhabha scattering at LEP1/SLC and LEP2 energies. *Il Nuovo Cimento A (1971-1996)*, 110:515–536, 1997.

[42] E. Barberio, B. van Eijk, and Z. Was. PHOTOS — a universal Monte Carlo for QED radiative corrections in decays. *Computer Physics Communications*, 66(1):115–128, 1991.

[43] PEP-II Collaboration *et al.* PEP-II Conceptual Design Report. *SLAC Report SLAC-418*, 1993.

[44] BaBar Collaboration. The BaBar detector. *arXiv preprint hep-ex/0105044*, 2001.

[45] B. Aubert *et al.* (BABAR collaboration). The BABAR detector. *Nuclear Instruments and Methods in Physics Research Section A: Accelerators, Spectrometers, Detectors and Associated Equipment*, 479(1):1–116, 2002.

[46] B. Aubert *et al.* (BABAR collaboration). The BaBar detector: upgrades, operation and performance. *Nuclear Instruments and Methods in Physics Research Section A: Accelerators, Spectrometers, Detectors and Associated Equipment*, 729:615–701, 2013.

[47] J.P. Lees *et al.* Time-integrated luminosity recorded by the BABAR detector at the PEP-II e^+ e^- collider. *Nuclear Instruments and Methods in Physics Research Section A: Accelerators, Spectrometers, Detectors and Associated Equipment*, 726:203–213, 2013.

[48] T. Sjöstrand. High-energy-physics event generation with PYTHIA 5.7 and JETSET 7.4. *Computer Physics Communications*, 82(1):74–89, 1994.

[49] Z. Was. TAUOLA the library for τ lepton decay, and KKMC/KORALB/KORALZ/... status report. *Nuclear Physics B-Proceedings Supplements*, 98(1-3):96–102, 2001.

[50] Agostinelli S. *et al.* (Geant4 Collaboration). GEANT4—a simulation toolkit. *Nuclear instruments and methods in physics research section A: Accelerators, Spectrometers, Detectors and Associated Equipment*, 506(3):250–303, 2003.

[51] J. P. Lees *et al.* (BABAR Collaboration). Exclusive measurements of $b \to s\gamma$ transition rate and photon energy spectrum. *Physical Review D*, 86(5):052012, 2012.

[52] A. Hocker *et al.* TMVA-toolkit for multivariate data analysis with ROOT: users guide. Technical report, CERN, 2007.

[53] M. Davier, A. Hoecker, B. Malaescu, C.Z. Yuan, and Z. Zhang. Reevaluation of the hadronic contribution to the muon magnetic anomaly using new $e^+e^- \to \pi^+\pi^-$ cross section data from BABAR. *The European Physical Journal C*, 66:1–9, 2010.

[54] F. Ambrosino *et al.* (KLOE Collaboration). Measurement of $\sigma(e^+e^- \to \pi^+\pi^-\gamma(\gamma))$ and the dipion contribution to the muon anomaly with the KLOE detector. *Physics Letters B*, 670(4-5):285–291, 2009.

[55] F. Ambrosino *et al.* (KLOE Collaboration). Measurement of $\sigma(e^+e^- \to \pi^+\pi^-)$ from threshold to 0.85 GeV^2 using initial state radiation with the KLOE detector. *Physics Letters B*, 700(2):102–110, 2011.

[56] D. Babusci *et al.* (KLOE and KLOE-2 Collaboration). Precision measurement of $\sigma(e^+e^- \to \pi^+\pi^-\gamma)/\sigma(e^+e^- \to \mu^+\mu^-\gamma)$ and determination of the $\pi^+\pi^-$ contribution to the muon anomaly with the KLOE detector. *Physics Letters B*, 720(4-5):336–343, 2013.

[57] M. Ablikim *et al.* (BESIII Collaboration). Measurement of the $e^+e^- \to \pi^+\pi^-$ cross section between 600 and 900 MeV using initial state radiation. *Physics Letters B*, 753:629–638, 2016.

[58] M. Ablikim *et al.* (BESIII Collaboration). Erratum to "Measurement of the $e^+e^- \to \pi^+\pi^-$ cross section between 600 and 900 MeV using initial state radiation". *arXiv preprint arXiv:2009.05011*, 2020.

[59] T. Xiao, S. Dobbs, A. Tomaradze, Kamal K. Seth, and G. Bonvicini. Precision measurement of the hadronic contribution to the muon anomalous magnetic moment. *Physical Review D*, 97(3):032012, 2018.

[60] N.N. Achasov *et al.* (SND collaboration). Measurement of the $e^+e^- \to \pi^+\pi^-$ process cross section with the SND detector at the VEPP-2000 collider in the energy region $0.525 < \sqrt{s} < 0.883$ GeV. *Journal of High Energy Physics*, 2021(1):1–24, 2021.

Acknowledgements

The four years of my PhD study will end soon. The globe has just experienced a serious COVID-19 epidemic. Fortunately, everything is getting better and gradually getting back on track.

During these four years of study, I would like to express my sincere gratitude for the valuable opportunity to receive China-France joint PhD training and the financial support by the "ADI 2020" project funded by the IDEX Paris-Saclay, ANR-11-IDEX-0003-02. I would like to show my deep and sincere gratitude to my thesis advisors Zhiqing ZhANG from IJCLab and Liang LI from Shanghai Jiao Tong University for their valuable guidance. I am grateful and lucky to have the opportunity to carry out research in the *BABAR* collaboration group, although I have been working on a very complex project. I also want to thank Michel DAVIER and Anne-Marie LUTZ for their helpful discussion which have greatly benefited me.

What also has a great impact on me is the passion, enjoyment and dedication of the researchers in France towards science and research. I have great respect for their obsession with true science. Very often, fundamental scientific research requires time and patience, and many challenging projects cannot be done in a short time in particular for high-energy physics filed, which is quite different from engineering research. All of these have enlightened me with new ideas and insights about how to conduct scientific research since I worked on engineering projects during my master degree. I am very lucky to have this opportunity to purely carry out *BABAR* analysis and slowly began to enjoy it.

I would express my sincere thanks to my parents and friends for their understanding, trust, encouragement and support. I am also grateful to meet new people in romantic and historical Paris.

Maybe I will not continue doing scientific research as my career in the future, the methodology I learned during my PhD phase will benefit me for the rest of my life. Instead of choosing short and quick research, now I prefer to choose difficult one and be rigorous and patient to do it right.

List of publications

1. *BABAR* collaboration. Study of additional radiation in the initial-state-radiation processes $e^+e^- \to \mu^+\mu^-\gamma$ and $e^+e^- \to \pi^+\pi^-\gamma$ in the *BABAR* experiment, arXiv preprint arXiv:2308.05233.

Synthèse

Introduction

Développé au cours du XXe siècle, le modèle physique décrivant le monde au niveau subatomique est appelé modèle standard (SM). Le SM est une théorie quantique des champs qui décrit trois des quatre forces fondamentales connues : interactions électromagnétiques, faibles et fortes, sauf l'interaction gravitationnelle. Le SM est un modèle efficace et cohérent des constituants fondamentaux et peut expliquer la plupart des résultats expérimentaux jusqu'à présent. Cependant, le SM laisse subsister quelques phénomènes physiques inexpliqués qui indiquent une nouvelle physique au-delà du modèle standard (BSM). Une méthode pour rechercher la physique BSM consiste à améliorer la précision des mesures afin d'observer de réelles carences du SM.

Le moment magnétique anormal du muon, défini par $a_\mu = (g_\mu - 2)/2$, avec g_μ le rapport gyromagnétique du muon, joue un rôle important dans le développement du SM et continue de servir de test du SM à ce jour. L'écart de longue date entre les mesures expérimentales $a_\mu^{\rm exp}$ et la prédiction théorique du SM $a_\mu^{\rm SM}$ a suscité un intérêt considérable car il pourrait être un premier indice pour une nouvelle physique encore méconnue. Le dernier résultat de mesure du laboratoire national des accélérateurs Fermi (FNAL) atteint $a_\mu^{\rm exp} = 116.592.061(41) \times 10^{-11}$ (0,35 ppm), tandis que la valeur de la prédiction SM de l'initiative théorique du groupe muon g-2 est $a_\mu^{\rm SM} = 116.591.810(43) \times 10^{-11}$ (0,37 ppm). La différence entre les deux s'élève désormais à 4,2σ [1], ce qui motivera davantage le développement des extensions du SM. Il convient de mentionner que la tension est réduite à 2,1σ par le récent résultat théorique prédit par la QCD sur réseau de la collaboration BMW.

Du côté de la prédiction théorique SM, $a_\mu^{\rm SM}$ est limité en précision par la contribution hadronique de la polarisation du vide (HVP), dont les termes hadroniques dominants peuvent être évalués en utilisant des relations de dispersion avec les sections efficaces des processus $e^+e^- \to \text{hadrons}$ à basse énergie. Le canal $\pi^+\pi^-$ devrait avoir la plus haute précision car il contribue de plus de 70% à a_μ hadronique à l'ordre le plus bas (LO) et 58% de son incertitude. Toutefois, la situation actuelle n'est pas idéale car les deux mesures les plus précises, effectuées par *BABAR* et KLOE, ne sont pas en bon accord avec leurs incertitudes, cette dernière étant de 2,9σ en dessous de

[1] La différence est augmentée à 5,1σ en incluant la nouvelle mesure du Fermilab rapportée en août 2023.

la première dans la région de la résonance ρ. Une nouvelle tension dans ce canal est aussi observée avec l'expérience CMD-3 fonctionnant en mode scan, ce qui nécessite des études complémentaires pour clarifier la situation.

La méthode du rayonnement dans l'état initial (ISR) a été proposée comme une méthode nouvelle et efficace pour étudier les processus d'annihilation e^+e^- au lieu de la méthode traditionnelle en mode scan. L'approche ISR peut fournir une mesure de section efficace à partir du seuil sur un large intervalle d'énergie avec un meilleur contrôle des erreurs systématiques, tandis que la réduction de la section efficace peut être compensée par la disponibilité d'un anneau de stockage e^+e^- à haute luminosité. Dans l'approche ISR, la section efficace pour $e^+e^- \to X$ (où X peut représenter n'importe quel état final) à une énergie réduite $\sqrt{s'} = m_X$ est déduite d'une mesure du processus radiatif $e^+e^- \to X\gamma$ où le photon est émis par une particule chargée initiale. L'énergie réduite est calculée comme $s' = s(1 - 2E^*_\gamma/\sqrt{s})$, où E^*_γ est l'énergie du photon ISR dans le repère du centre de masse (CM) e^+e^- et s est le carré de l'énergie CM e^+e^-. Dans cette thèse, $s \sim (10,58\,\mathrm{GeV})^2$ et $\sqrt{s'}$ va du seuil à 3 GeV, nous effectuons une première étude expérimentale du rayonnement additionnel au premier ordre (NLO) et au deuxième ordre (NNLO) dans les événements $e^+e^- \to \mu^+\mu^-\gamma$ et $e^+e^- \to \pi^+\pi^-\gamma$ avec un rayonnement dur dans l'état initial.

Expérience *BABAR*

L'objectif principal de l'expérience *BABAR* était d'étudier la disparité entre la matière et l'antimatière de l'univers via la mesure de la violation Charge-Parité (CP). Le détecteur *BABAR* a été con*c*cu pour l'étude des millions de mésons B produits par l'anneau de stockage PEP-II. Le système PEP-II comprenait quatre principaux sous-systèmes : injecteur, anneau à haute énergie (HER), anneau à basse énergie (LER) et région d'interaction (IR). Le HER était destiné au faisceau d'électrons de 9 GeV et le LER monté au-dessus du HER était responsable du faisceau de positons de 3,1 GeV. Les collisions du deux faisceaux asymétriques d'électrons et de positons ont permis au collisionneur de fonctionner à $\sqrt{s} = 10,58$ GeV, la valeur de masse de la résonance $\Upsilon(4S)$.

Le système du détection *BABAR* a été optimisé pour avoir une acceptance large et uniforme dans le système CM pour atteindre les objectifs de physique requis. Son efficacité de reconstruction permet de descendre jusqu'à l'impulsion de 40 MeV/c. Les photons sont reconstruits efficacement jusqu'à l'énergie de 20 MeV. De bonnes résolutions en énergie et en angle de 20 MeV à 4 GeV sont obtenues pour les photons des désintégrations π^0 et η ainsi que des désintégrations radiatives. De plus il faut noter une excellente résolution des vertex primaires, une reconstruction efficace des vertex secondaires, une bonne identification des électrons et des muons, une discrimination précise et efficace entre les hadrons et un étiquetage de saveur des mésons B. Pour obtenir l'acceptance géométrique maximale pour les désintégrations de l'$\Upsilon(4S)$ boosté, l'ensemble du détecteur est décalé de 0,37 m dans la direction du faisceau de l'électron par rapport au point d'interaction. L'angle polaire θ est mesuré par rapport à l'axe z, avec une couverture de 350 mrad dans le sens des électrons et

de 400 mrad dans le sens des positons, et l'angle d'azimut ϕ est mesuré à partir de l'axe x dans le plan $x - y$. De l'intérieur vers l'extérieur, le détecteur est composé de six sous-systèmes principaux : détecteur de vertex à silicium (SVT), chambre de dérive (DCH), détecteur de rayonnement Cerenkov à réflection interne (DIRC), calorimètre électromagnétique (EMC) à l'iodure de césium (CsI), solénoïde supraconducteur avec un champ magnétique de 1,5 T et retour de flux instrumenté (IFR). L'objectif principal du SVT est de mesurer la position des traces chargées à proximité de la région d'interaction avec une grande précision afin de reconstruire les trajectoires et les vertex de désintégration des particules chargées. Le SVT est également con$c$ cu pour détecter les particules chargées à faible impulsion qui n'atteignent pas la DCH. La DCH multifilaire est le principal dispositif de suivi du détecteur *BABAR* et il est con$c$ cu pour mesurer l'impulsion et les angles des particules chargées avec une grande précision. Elle fournit aussi une mesure dE/dx pour les particules chargées. Le DIRC présente une excellente séparation entre pions et muons, d'environ 4,2σ à 3 GeV/c et toujours d'environ 2,5σ à 4,1 GeV/c, ce qui aide à l'identification des particules chargées. L'EMC de *BABAR* est un calorimètre à absorption qui présente une excellente résolution angulaire et en énergie, sur l'intervalle d'énergie comprise entre 20 MeV et 9 GeV. Cette capacité permet une efficacité élevée de détection des photons issus des désintégrations de π^0 et de η, ainsi que des processus radiatifs et électromagnétiques. L'IFR est le détecteur le plus externe de *BABAR* et il a été con$c$ cu pour détecter les muons avec un grand angle solide et une efficacité élevée, et les hadrons neutres à longue durée de vie sur une large gamme d'impulsions et avec une bonne résolution angulaire. Le système de déclenchement dans *BABAR* est implémenté hiérarchiquement à deux niveaux, le niveau 1 (L1) en matériel suivi du niveau 3 (L3) en logiciel. L'expérience *BABAR* a collecté des données entre 1999 et 2008. Sur cette période, la luminosité instantanée de PEP-II a été améliorée d'un facteur quatre, $12 \times 10^{33}\mathrm{cm}^{-2}\mathrm{sec}^{-1}$, avec un record de luminosité maximale en août 2006.

Données et échantillons de Monte Carlo

Cette thèse s'appuie sur les données collectées avec le détecteur *BABAR* à la résonance $\Upsilon(4S)$, du run 1 au run 6. Les données utilisées correspondent à une luminosité intégrée de $\mathcal{L} = 424,2\,\mathrm{fb}^{-1}$ avec en plus des données de 43,9 fb^{-1} collectées juste en dessous de la résonance. Les événements sont simulés à l'aide de méthodes Monte Carlo (MC) et les processus de signal ISR $e^+e^- \to X\gamma_{\mathrm{ISR}}$ avec $X = \mu\mu$ ou $\pi\pi$ sont simulés avec le générateur PHOKHARA à NLO. Le photon ISR, γ_{ISR} est généré avec une large plage angulaire, $20^\circ - 160^\circ$ dans le système CM encadrant le plage de détection des photons avec une marge pour tenir compte de la résolution finie. Les échantillons générés correspondent à 10 fois le nombre d'événements de données pour le signal. De plus, des échantillons relativement petits de processus de signal ISR sont simulés avec le générateur AFKQED. Une masse minimale $m_{X_{\mathrm{ISR}}} > 8\,\mathrm{GeV/c}^2$ est imposée à l'étape de génération avec ce dernier MC, ce qui fixe une limite supérieure de 2,3 GeV sur les énergies des photons additionnels. Les photons ISR additionnels produits par le générateur AFKQED sont émis le long de la

direction du faisceau e^+ ou e^-. Dans la limite intrinsèque du générateur AFKQED, des échantillons d'événements sont simulés jusqu'à NNLO. Les processus ISR de bruit de fond $e^+e^- \to K^+K^-\gamma(\gamma)$ et $e^+e^- \to X\gamma$ ($X = \pi^+\pi^-\pi^0, \pi^+\pi^-2\pi^0, \cdots$) sont simulés avec PHOKHARA et AFKQED, respectivement. Les processus de bruit de fond $e^+e^- \to qq$ ($q = u, d, s, c$) sont générés avec JETSET et $e^+e^- \to \tau^+\tau^-$ avec KORALB. La réponse du détecteur *BABAR* est simulée avec GEANT4, en tenant compte des variations du faisceau et conditions du détecteur au fil du temps.

Les événements radiatifs sont sélectionnés en exigeant la détection d'un photon dans la plage des angles polaires du laboratoire 0,35 $< \theta <$ 2,4 rad, et avec une énergie mesurée $E^*_\gamma > 4$ GeV dans CM. Exactement deux particules de charges opposées sont nécessaires pour extrapoler à la région de collision, chacune avec : une impulsion transversale $> 0,1$ GeV/c ; θ dans la plage de 0,4 à 2,45 rad ; au moins 15 coups dans la DCH. Les événements peuvent contenir n'importe quel nombre de photons additionnels et de particules chargées qui ne satisfont pas aux exigences. Seulement les photons avec $E_\gamma > 50$ MeV sont pris en compte dans les ajustements cinématiques décrits ci-dessous. Le photon avec la plus haute énergie mesurée dans CM est noté $\gamma_{\rm ISR}$.

L'objectif de cette thèse est l'étude du rayonnement pour les processus $e^+e^- \to \mu^+\mu^-\gamma(\gamma)$ et $e^+e^- \to \pi^+\pi^-\gamma(\gamma)$. L'étude présente du rayonnement additionnel est réalisée en distinguant les canaux de muons et de pions événement par événement, en utilisant l'identification (PID) pour les particules chargées. Ceci est justifié par la commodité de gérer séparément des échantillons d'événements radiatifs afin d'étudier leur comportement spécifique. On s'attend donc à des performances PID limitées pour les particules chargées à faible impulsion. Cependant, ce défi est tempéré par le fait que l'étude du rayonnement additionnel n'exige pas les mêmes niveaux de précision correspondant à ceux nécessaires pour la détermination de la section efficace. La méthode d'étiquette et sonde a été utilisée pour déterminer les efficacités PID séparément pour les données et les échantillons MC PHOKHARA dans des intervalles en 2D $(p_{\rm T}, \theta)$. Pour les données, la contribution des bruits de fond est soustraite en utilisant la prédiction des échantillons MC. Pour chaque événement MC, le produit des rapports données/MC des efficacités PID pour les deux particules chargées est appliqué à titre de correction.

Ajustements cinématiques

Pour $\mu\mu\gamma$ et $\pi\pi\gamma$, la définition de l'événement est élargie pour inclure le rayonnement d'un photon en plus du photon ISR déjà requis. Deux types d'ajustements, notés $\gamma_{\rm ISR}\gamma_{\rm LA}$ et $\gamma_{\rm ISR}\gamma_{\rm SA}$, sont pris en compte, où pour le premier cas, un photon détecté à grand angle (LA) dans EMC est ajusté, et pour le deuxième cas, un photon est estimé être un photon ISR additionnel à petit angle (SA), en fait colinéaire à l'un des faisceaux.

Chaque événement est caractérisé par deux valeurs de χ^2, $\chi^2_{\gamma_{\rm ISR}\gamma_{\rm LA}}$ et $\chi^2_{\gamma_{\rm ISR}\gamma_{\rm SA}}$ des deux ajustements cinématiques correspondants, qui peuvent être examinés sur un plan bidimensionnel (2D). Les quantités $\ln(\chi^2 + 1)$ sont utilisées pour que les

longues queues puissent être correctement visualisées. Les événements sans photons additionnels mesurés n'ont que la value $\chi^2_{\gamma_{\rm ISR}\gamma_{\rm SA}}$ et elles sont tracées séparément. Dans le cas où plusieurs photons additionnels sont détectés, les ajustements $\gamma_{\rm ISR}\gamma_{\rm LA}$ sont effectués en utilisant chaque photon tour à tour et l'ajustement avec le meilleur χ^2 est conservé. Pour être cohérent avec l'analyse de section efficace finale sans utiliser PID, la masse du pion est supposée pour les deux particules chargées, et les distributions de la masse $\pi\pi$ sont obtenues à partir des paramètres des deux particules chargées de l'ajustement $\gamma_{\rm ISR}\gamma_{\rm SA}$ si $\chi^2_{\gamma_{\rm ISR}\gamma_{\rm SA}} < \chi^2_{\gamma_{\rm ISR}\gamma_{\rm LA}}$ ou à partir de ceux de l'ajustement $\gamma_{\rm ISR}\gamma_{\rm LA}$ dans le cas inverse.

Etudes du bruit de fond

Multihadrons du processus $q\bar{q}$

Le processus hadronique, également appelé processus uds, introduit un bruit de fond dans l'échantillon du signal qui est considérablement réduit par la sélection en χ^2 des ajustements cinématiques. La contribution uds est estimée à l'aide d'échantillons simulés pour le processus $e^+e^- \to q\bar{q}$. Cependant, la prédiction JETSET pour la fragmentation $q\bar{q}$ en états finaux à faible multiplicité n'est pas nécessairement fiable, le taux MC est donc normalisé à l'aide de données.

Le processus uds est le bruit de fond dominant pour une plage de masse supérieure à 0,9 GeV/c^2 et sous-dominant entre 0,6 et 0,9 GeV/c^2. Dans ces événements, le candidat photon ISR est en fait produit à partir de la désintégration d'un π^0 énergique. La recherche d'une telle signature est réalisée à la fois dans les données et les échantillons MC en appariant le photon ISR avec tous les photons additionnels détectés ayant une énergie supérieure à 50 MeV. La paire de masse $\gamma\gamma$ (appelée $m_{\gamma\gamma}$) proche de la masse nominale π^0 est conservée. Le processus uds comporte deux populations principales correspondant aux cas avec un π^0 résolu et non résolu. La normalisation MC est obtenue à partir des taux π^0 observés d'une part et des taux π^0 non résolus d'autre part.

L'optimisation d'un arbre de décision boosté (BDT) basé sur une technique multivariable est utilisée pour sélectionner les processus hadroniques dans la région χ^2 acceptée dans trois fenêtres distinctes de masse $\pi\pi$: la fenêtre de faible masse entre le seuil et 0,6 GeV/c^2, la fenêtre de masse intermédiaire comprise entre 0,6 et 0,9 GeV/c^2 près du pic de masse ρ, et la fenêtre de masse élevée entre 0,9 et 1,4 GeV/c^2. Pour chaque fenêtre de masse $\pi\pi$, deux BDTs séparés sont effectués respectivement pour $m_{\gamma\gamma} < 0,3$ GeV/c^2 et $m_{\gamma\gamma} > 0,3$ GeV/c^2. Pour l'apprentissage du BDT, dix-sept variables discriminantes sont choisies. Les formes de ces variables entre les échantillons MC uds et non-uds sont également comparées. Un écart non négligeable dans la résolution de l'énergie des photons ISR dans le système CM (E^*_γ) est observé entre données et simulation. La correction de repondération de E^*_γ améliore également d'autres variables liées à l'énergie alors qu'elle a peu d'impact sur les autres variables. La sélection nominale de BDT correspondent à la valeur qui maximise le signal sur le bruit de fond à partir des distributions de réponses du BDT dans différents cas.

Les ajustements aux distributions de masse $\gamma\gamma$ sont effectués à la fois dans les données et dans le MC en supposant une forme gaussienne de la distribution de masse des π^0 résolus et prenant en compte la partie non résolue identifiée par la forme transverse de la gerbe dans l'EMC. Pour l'ajustement du pic π^0, une sélection BDT plus lâche est utilisée pour obtenir plus de statistiques. Pour la contribution non résolue, une sélection BDT plus stricte est choisie pour minimiser les contributions non-uds pour lesquelles la distribution de masse $\gamma\gamma$ issue de la simulation peut ne pas être vraiment fiable. La partie non résolue est paramétrisée par une fonction d'erreur ERF dans les distributions MC uds puis la forme ajustée est utilisée dans l'ajustement aux données. Les trois paramètres (amplitude, masse et largeur) du pic gaussien sont ajustés dans toutes les distributions MC uds mais dans les données uniquement avec la sélection lâche BDT où le pic gaussien est prononcé. Pour la sélection BDT stricte, les paramètres de masse et de largeur dans l'ajustement aux données sont extraits de l'ajustement correspondant avec la sélection BDT lâche. Les résultats des facteurs de normalisation ajustés dans les trois fenêtres de masse différentes pour $m_{\gamma\gamma} < 0,3\,\text{GeV/c}^2$ sont obtenus et leur variation avec les fenêtres de masse $\pi\pi$ est faible et reste dans les incertitudes statistiques. Les sélections du BDT sont variées afin de vérifier l'impact de la soustraction non-uds et la dépendance des facteurs de normalisation sur la sélection BDT. Des BDT similaires sont utilisés pour sélectionner les événements uds dans chacune des trois fenêtres de masse $\pi\pi$ pour $m_{\gamma\gamma} > 0,3\,\text{GeV/c}^2$. Dans tous les cas, les facteurs de normalisation sont cohérents avec ceux de la contribution non résolue à $m_{\gamma\gamma} < 0,3\,\text{GeV/c}^2$. Dans le cas des faibles $m_{\gamma\gamma}$, les variations dans la sélection du BDT ont été explorés, mais aucun effet systématique significatif n'est observé.

Processus ISR multihadroniques

Le bruit de fond pour les processus ISR multihadroniques est estimé en utilisant des échantillons simulés $e^+e^- \to X\gamma_{\text{ISR}}$ où X représente les états finaux : $\pi^+\pi^-\pi^0$, $2\pi^+2\pi^-$, $\pi^+\pi^-2\pi^0$, $\eta\pi^+\pi^-$ et K_SK_L, etc. Le spectre de masse de ces processus a été adapté à la section efficace mesurée basé sur la méthode de combinaison implémentée dans HVPTools. Ils totalisent environ 10% au bord inférieur du pic du ρ mais sont fortement supprimés par la sélection 2D χ^2. La contribution dominante pour $m_{\pi\pi}$ jusqu'à 0,9 GeV/c^2 provient du premier processus (appelé 3π pour plus de simplicité).

Une approche BDT similaire à celle appliquée au bruit de fond uds est utilisée pour déterminer les facteurs de normalisation de l'échantillon MC 3π dans deux régions $m_{\pi\pi}$: faible masse (inférieure à 0,6 GeV/c^2) et masse intermédiaire (entre 0,6 et 0,9 GeV/c^2). Le processus MC 3π est dominé par la production des résonances ω et ϕ. Chacune des deux fenêtres de masse $m_{\pi\pi}$ mentionnées ci-dessus est divisée en deux cas, un avec au moins deux photons non ISR reconstruits ($n_\gamma > 2$) et l'autre avec un seul photon non ISR reconstruit ($n_\gamma = 2$). Ils représentent respectivement environ 72% et 25% des échantillons 3π. Les 3% restants n'ont aucun photon du π^0 reconstruit avec une énergie supérieure à 50 MeV dans l'acceptance du détecteur.

Pour le cas où $n_\gamma > 2$, douze variables d'entrée sont utilisées dans le BDT pour séparer les événements 3π d'autres processus. Pour le cas de $n_\gamma = 2$, neuf variables

d'entrée sont utilisées dans le BDT. Pour une sélection BDT donnée, la distribution de la masse 3π, $m_{3\pi}$, est utilisée pour déterminer le facteur de normalisation du processus 3π dans la région de masse de 0,7−1,1 GeV/c^2 couvrant les résonances ω et ϕ. Le facteur de normalisation correspondant est obtenu comme le rapport du taux total des événements de données après la soustraction de bruit de fond au taux des événements des échantillons MC 3π, dans la région de masse ci-dessus avec une sélection BDT nominale. Le facteur de normalisation nominal est également comparé à la sélection BDT avec la deuxième meilleure valeur de χ^2 proche de la valeur nominale et toute incohérence entre les deux facteurs de normalisation après avoir pris en compte la corrélation entre les échantillons sélectionnés est traité comme une incertitude systématique. Tous les facteurs de normalisation sont cohérents dans les incertitudes indiquées. Pour le cas le plus important de $m_{\pi\pi} < 0,6\,\text{GeV/c}^2$ et $n_\gamma > 2$, nous obtenons une précision de 1,5%. Les résultats pour $n_\gamma = 2$ sont appliqués à la petite fraction d'événements avec $n_\gamma = 1$ et les résultats pour $0,6 < m_{\pi\pi} < 0,9\,\text{GeV/c}^2$ sont appliqués au MC 3π à une masse plus élevée, où la contribution devient également petite.

Bruit de fond du processus $\tau\tau$

Le processus $\tau\tau$ s'avère faible dans la région 2D-χ^2 acceptée. Cependant, il domine de loin dans la région rejetée 2D-χ^2 dans la sélection dimuons. La région spécifique où les deux valeurs de χ^2 dépassent la valeur maximale (10^5) est utilisée pour vérifier le facteur de normalisation de l'échantillon $\tau\tau\gamma$. Pour obtenir un échantillon d'événement $\tau\tau\gamma$ très pur, on requiert $E_{\text{tot}} < 9,0\,\text{GeV}$, où E_{tot} est l'énergie totale mesurée Les taux intégrés des données et des événements MC donnent un rapport données/MC de 1,12 ± 0,04. Etant donné que le processus MC $\tau\tau\gamma$ est bien modélisé, il est proposé de conserver la normalisation du processus inchangée mais de citer une incertitude systématique de 12% pour la soustraction du bruit de fond $\tau\tau\gamma$.

Optimisation de la sélection 2D-χ^2

Le bruit de fond multicorps peuple la région où les deux valeurs χ^2 sont grandes et par conséquent une région de bruit de fond est définie dans le plan 2D-χ^2, ce qui assure l'efficacité pour le signal et le rejet du bruit de fond. La méthode BDT est appliquée dans trois fenêtres de masse distinctes, faible ($m_{\pi\pi} < 0,6\,\text{GeV/c}^2$), intermédiaire (0,6−0,9 GeV/c^2) et élevée (0,9−1,4 GeV/c^2). Elle utilise les deux variables $\chi^2_{\gamma_{\text{ISR}}\gamma_{\text{LA}}}$ et $\chi^2_{\gamma_{\text{ISR}}\gamma_{\text{SA}}}$, traitant les processus $\pi\pi(\gamma)$, $\mu\mu(\gamma)$ et $KK(\gamma)$ comme signal et tous les autres processus comme bruit de fond. La comparaison de forme de ces deux variables dans différentes fenêtres de masse est faite à l'aide des échantillons MC PHOKHARA pour le signal et des échantillons MC des bruits de fond utilisant AFKQED pour les processus ISR, KORALZ pour $\tau\tau\gamma$ et JETSET pour $q\bar{q}(u,d,s)$. Le rapport de signification statistique du signal sur le bruit de fond (SOB) est défini comme $S/\sqrt{S+B}$, S et B étant le signal intégré et le bruit de fond se trouvant à droite d'une sélection SOB donnée dans la distribution de réponse BDT. La sélection

BDT nominale correspond au choix qui maximise la valeur SOB. En pratique, des sélections simples basées sur des coupures, choisies pour être proches des contours de la meilleure valeur SOB de la sélection BDT, sont utilisés dans les trois fenêtres de masse. L'efficacité de la sélection du signal, la contamination du bruit de fond et les valeurs SOB sont comparées entre l'optimisation BDT et la sélection basée sur les coupures, et dans tous les cas, les valeurs basées sur les coupures correspondent bien aux valeurs optimisées de la sélection BDT, avec une valeur d'efficacité élevée, supérieure à 98,5%, et une faible contamination de bruit de fond, inférieure à 2,0%.

La sélection 2D-χ^2 optimisée est appliquée aux échantillons $\pi\pi\gamma_{\rm ISR}$ et $\mu\mu\gamma_{\rm ISR}$ après la sélection PID. Les bruits de fond connus sont soustraits des données, et les bruits de fond restant, dominés par l'erreur d'identification $\mu \to \pi$ et $\pi \to \mu$, représentent 3,9% et 0,25% des échantillons $\pi\pi\gamma(\gamma)$ et $\mu\mu\gamma(\gamma)$ sélectionnés respectivement. En général, l'efficacité de la sélection 2D-χ^2 est élevée, autour de 99% ou plus. L'impact le plus important concerne l'échantillon $\gamma_{\rm ISR}\gamma_{\rm LA}$. Pour l'ajustement $\gamma_{\rm ISR}\gamma_{\rm LA}$, la différence d'efficacité entre les deux échantillons MC AFKQED et PHOKHARA peut être due au fait que le composant photonique LA-ISR est absent dans l'échantillon AFKQED. Pour l'ajustement $\gamma_{\rm ISR}\gamma_{\rm SA}$, la différence est due à l'approximation de l'émission colinéaire du photon SA-ISR dans l'ajustement ainsi que dans la génération AFKQED. Des différences entre les données et les MC sont observées dans le processus $\mu\mu$, en particulier pour la catégorie $\gamma_{\rm ISR}\gamma_{\rm LA}$, et sont prises en compte dans cette thèse. Pour le processus $\pi\pi$, l'efficacité dans les données ne peut pas être déterminée de manière fiable en raison du très fort bruit de fond dans la région 2D-χ^2 rejetée, et les corrections données/MC sont supposées être les mêmes que celles du processus $\mu\mu$.

Analyse du rayonnement NLO

Dans cette section, après avoir testé l'approximation colinéaire pour les photons ISR additionnels, utilisé la méthode de séparation du FSR et de l'ISR additionnel à grand angle, étudié les photons parasites dans l'analyse FSR de l'échantillon de pion et mesuré l'efficacité de détection des photons additionnels à grand angle, les résultats des analyses NLO sont présentés dans ce qui suit. L'accent est mis sur l'étude des propriétés des événements qui satisfont soit $\gamma_{\rm ISR}\gamma_{\rm SA}$ soit $\gamma_{\rm ISR}\gamma_{\rm LA}$ (ou les deux) dans leurs régions respectivement acceptées de la sélection 2D-χ^2, tout en ignorant pour le moment les contributions potentielles du NNLO. Les événements avec les ISR additionnels aux petits angles sont sélectionnés au-dessus de la ligne diagonale dans le plan 2D-χ^2 avec $\chi^2_{\gamma_{\rm ISR}\gamma_{\rm SA}} < \chi^2_{\gamma_{\rm ISR}\gamma_{\rm LA}}$ (noté échantillon SA), tandis que pour un échantillon FSR ou ISR à grand angle (noté échantillon LA), la sélection inverse est appliquée. Pour définir les échantillons NLO dans les deux cas, un seuil d'énergie est requis pour le photon additionnel, à savoir $E^*_\gamma > 0,2\,\text{GeV}$ pour l'ajustement $\gamma_{\rm ISR}\gamma_{\rm SA}$ et $E_\gamma > 0,2\,\text{GeV}$ pour l'ajustement $\gamma_{\rm ISR}\gamma_{\rm LA}$. Si les événements satisfont les sélections en χ^2 mais ne parviennent pas à atteindre le seuil d'énergie, ils sont considérés comme des processus LO.

Pour le processus $\mu\mu\gamma$, les distributions χ^2 de $\gamma_{\rm ISR}\gamma_{\rm SA}$ et $\gamma_{\rm ISR}\gamma_{\rm LA}$ dans les don-

nées sont comparées avec les prédictions basées sur les échantillons MC PHOKHARA et AFKQED. La contribution du bruit de fond s'élève à moins de 0,4% pour les deux cas et est soustraite des distributions de données. La comparaison entre les données et l'échantillon MC AFKQED montre que la forme de la distribution χ^2 pour l'ajustement $\gamma_{\rm ISR}\gamma_{\rm SA}$ dans les données a une queue plus grande que celle de l'échantillon MC AFKQED. Cette différence est attendue et peut être attribuée principalement à l'approximation colinéaire dans l'ajustement. Pour l'ajustement $\gamma_{\rm ISR}\gamma_{\rm LA}$, la comparaison des formes est considérablement améliorée puisque l'ajustement utilise les paramètres mesurés du photon LA additionnel dans l'acceptance du détecteur. Le spectre d'énergie ajusté dans CM $E^*_{\gamma_{\rm ISR}\gamma_{\rm SA}}$ est également comparé entre les données et les simulations PHOKHARA et AFKQED. La comparaison révèle que le spectre d'énergie des données est plus dur que la prédiction de PHOKHARA. Cela implique qu'il y a des contributions dans les données au-delà de la partie NLO qui est simulée dans l'échantillon MC PHOKHARA. Le meilleur accord entre les données et la simulation AFKQED conforte en outre cette observation, car l'échantillon MC AFKQED intègre des contributions d'ordre supérieur. Cependant, la comparaison est limitée aux énergies inférieures à 2,3 GeV en raison de l'absence de photons additionnels d'énergie plus élevée dans l'échantillon AFKQED, comme mentionné précédemment. Pour l'ajustement $\gamma_{\rm ISR}\gamma_{\rm LA}$, les composants FSR et ISR additionnels à grand angle sont séparés en utilisant l'angle minimum entre le photon LA et une des particules chargées $\theta_{\rm min(trk,\gamma_{LA})}$. Les spectres d'énergie $E_{\gamma_{\rm LA}}$ dans le référentiel du laboratoire sont comparés pour les données et PHOKHARA dans les deux cas tandis que pour AFKQED, la comparaison n'est effectuée que pour les événements avec $\theta_{\rm min(trk,\gamma_{LA})} < 20^\circ$ (contribution FSR).

Pour les échantillons comportant deux pions identifiés, une analyse similaire est effectuée. Cependant, une différence majeure apparaît par rapport à l'analyse des muons. Dans le cas des pions, il existe un bruit de fond beaucoup plus important provenant des processus hadroniques ISR et uds, et ce bruit de fond est largement concentré dans l'échantillon de $\gamma_{\rm ISR}\gamma_{\rm LA}$. L'étude du rayonnement NLO des pions est limité à la région du ρ, qui correspond à la région de masse entre 0,6 et 0,9 GeV/c^2. Des comparaisons similaires entre les processus $\pi\pi$ et $\mu\mu$ NLO sont ensuite effectués dans cet intervalle de masse restreint $E^*_{\gamma_{\rm SA}}$, $\chi^2_{\gamma_{\rm ISR}\gamma_{\rm LA}}$, $\theta_{\rm min(trk,\gamma_{LA})}$, $E_{\gamma_{\rm LA}}$, et $\theta_{\gamma_{\rm LA}}$. Les deux processus présentent des formes et taux similaires, en particulier pour l'ajustement $\gamma_{\rm ISR}\gamma_{\rm SA}$. La distribution $E^*_{\gamma_{\rm SA}}$ dans les données du processus $\pi\pi$ montre encore une fois un spectre d'énergie plus dur que la simulation PHOKHARA, similaire à l'observation dans le processus $\mu\mu$.

Autre étude sur le rayonnement NLO

Dans cette section, une nouvelle reconstruction cinématique de l'événement $e^+e^- \to \mu^+\mu^-\gamma(\gamma)$ est réalisée et étudiée, appelée calcul 0C qui signifie zéro contrainte. Les relations de conservation de l'énergie et l'impulsion sont utilisées pour calculer quatre inconnues : l'énergie et les angles du photon additionnel, noté γ_{0C}, ainsi que

l'énergie du photon ISR principal, en utilisant les quadrivecteurs des faisceaux et des deux particules chargées supposées être des pions, et les angles du photon ISR principal. En raison d'une résolution plus faible des quantités calculées par rapport aux résultats des ajustements $\gamma_{\mathrm{ISR}}\gamma_{\mathrm{SA}}$ et $\gamma_{\mathrm{ISR}}\gamma_{\mathrm{LA}}$, le calcul 0C est utilisé uniquement pour des études complémentaires. Cependant, le calcul 0C fournit des informations sur les photons additionnels sur tout l'intervalle d'énergie et sur toute la plage angulaire, contrairement à l'ajustement $\gamma_{\mathrm{ISR}}\gamma_{\mathrm{SA}}$, qui contraint le photon additionnel à être colinéaire avec le faisceau e^+ ou e^-, et contrairement à l'ajustement $\gamma_{\mathrm{ISR}}\gamma_{\mathrm{LA}}$, qui nécessite un photon détecté dans l'acceptance du détecteur. Ce calcul, indépendant du fait que le photon additionnel soit détecté ou non, permet d'étudier l'écart observé entre les contributions LO et NLO des données et de PHOKHARA.

Pour le processus $\mu\mu\gamma$, le bruit de fond étant infime, les études 0C sont réalisées dans toute líntervalle de masse sans la sélection 2D-χ^2. L'angle dans l'espace entre la direction calculée du photon additionnel et celle mesurée du photon ISR principal, noté $\alpha(\gamma_{0C}, \gamma_{\mathrm{ISR}})$, est étudié en fonction soit de l'énergie calculée du photon additionnel dans le repère CM, $E^*_{\gamma_{0C}}$, soit de la différence d'énergie calculée dans le repère CM en utilisant les informations reconstruites et vraies, $E^*_{\gamma_{0C}} - E^*_{\gamma_{\mathrm{true}}}$. La comparaison entre les deux révèle que l'énergie calculée du photon additionnel s'accorde bien avec celui du vrai photon au-delà d'un seuil d'énergie d'environ 200 MeV sauf lorsque $\alpha(\gamma_{0C}, \gamma_{\mathrm{ISR}})$ est inférieur à environ 0,5 rad. Une sélection $\alpha(\gamma_{0C}, \gamma_{\mathrm{ISR}}) > 0,5$ rad est donc appliquée dans l'étude suivante relative à la reconstruction 0C, afin de supprimer la contribution des photons parasites. La résolution angulaire de la direction du photon additionnel est estimée en comparant l'angle polaire calculé avec celui obtenu par l'ajustement $\gamma_{\mathrm{ISR}}\gamma_{\mathrm{LA}}$ dans les données muons et MC. Un bon accord est observé entre les données et la simulation pour le cœur de la fonction de résolution, cependant, une différence notable dans la queue de distribution aux valeurs de $\theta_{\gamma_{0C}} - \theta_{\gamma_{\mathrm{LA}}}$ supérieures à 0,5 rad jusqu'à 2 rad, plus prononcée dans les données. Un excès de photons parasites aux grands angles est attendu dans les données par rapport au MC et est responsable d'une augmentation d'environ 10% du rapport données/MC dans l'analyse 0C.

La distribution θ_{0C} de l'angle polaire calculé dans les données est comparé à celle prédite par PHOKHARA, ainsi que celle calculée avec l'information vraie. Un bon accord entre les données et MC aux grands angles par rapport aux faisceaux est observé. En fait, les données sont environ 10% plus grandes que les prévisions MC dans cette région et cet excès s'explique par les plus grandes queues de la résolution dans les données. Contrairement à l'assez bon accord aux grands angles, PHOKHARA prédit un taux de rayonnement trop élevé aux petits angles. Ce constat reste cohérent lors de l'utilisation d'un échantillon d'événements où les particules chargées et le photon principal ISR sont limités à la région centrale du détecteur, réduits de 0,5 rad sur les deux côtés, avec $0,85 < \theta_{\gamma_{\mathrm{ISR}}} < 1,9$ rad et $0,9 < \theta_{\gamma_{\mathrm{trk}}} < 1,95$ rad. Il a également été vérifié que l'écart entre les données et les prévisions de PHOKHARA ne peut pas être attribué aux queues de la résolution angulaire seule. L'énergie calculée dans le CM, $E^*_{\gamma_{0C}}$, est également comparée entre les données et PHOKHARA dans différents intervalles $\theta_{\gamma_{0C}}$, et avec le spectre MC calculé avec l'information vraie. Dans toutes

les intervalles $\theta_{\gamma 0C}$, un accord décent est observé entre le spectre d'énergie calculé et le spectre réel d'énergie de PHOKHARA. Cependant, un écart évident est observé entre les données et les prévisions de PHOKHARA, en particulier dans les pics de rayonnement vers l'avant et vers l'arrière. Il y a aussi un écart sur la forme du spectre d'énergie en plus de l'écart sur le taux d'événement. Dans les deux cas PHOKHARA et AFKQED, la comparaison du spectre d'énergie calculé avec l'information vraie avec le spectre calculé avec l'information simulée est réalisée sur toute la plage angulaire. Pour l'échantillon AFKQED au-delà de 2,3 GeV, la seule contribution vient de la composante FSR et est bien reproduite par le calcul 0C. La transition entre les contributions LO et NLO est démontrée par une version agrandie aux basses énergies. Le taux des données/PHOKHARA n'est pas cohérent entre les contributions LO et NLO, avec un changement net de LO à celui de NLO au-dessus de 0,2 GeV. Cependant, le taux LO des données/AFKQED est cohérent avec celui du NLO au-dessus de 0,2 GeV dans l'incertitude statistique. Le faible écart de la prédiction AFKQED par rapport à l'unité résulte de l'absence d'événements avec les photons aux grands angles dans l'échantillon MC pour les énergies au-dessus de 2,3 GeV.

Pour le processus $\pi\pi\gamma$ entre 0,6 et 0,9 GeV/c^2, le bruit de fond dans les données est bien plus grand et l'estimation du bruit de fond basée sur la simulation MC peut ne pas être fiable, en particulier dans la région 2D-χ^2 rejetée. Ainsi, la sélection 2D-χ^2 est appliquée au processus $\pi\pi\gamma$ et les comparaisons similaires entre les deux prédictions MC et entre les données et les échantillons MC peuvent être effectués. Les observations faites ci-dessus pour le processus $\mu\mu\gamma$ s'avère également vrai pour le processus $\pi\pi\gamma$.

Analyse du rayonnement NNLO

En plus des deux ajustements NLO, les événements sont soumis à trois ajustements NNLO où deux photons additionnels sont autorisés avec le photon ISR principal et les deux particules chargées :

- Ajustement $\gamma_{\rm ISR}2\gamma_{\rm SA}$: les énergies de deux photons SA sont ajustées, chacun étant supposé être colinéaire avec l'un des faisceaux.
- Ajustement $\gamma_{\rm ISR}\gamma_{\rm SA}\gamma_{\rm LA}$: un photon LA additionnel est mesuré dans le détecteur et un photon SA est supposé être colinéaire avec l'un des faisceaux, celui qui fournit le meilleur ajustement.
- Ajustement $\gamma_{\rm ISR}2\gamma_{\rm LA}$: deux photons LA additionnels sont mesurés dans le détecteur. L'ajustement avec la valeur de χ^2 la plus petite parmi toutes les combinaisons de deux photons est conservé.

Tous les événements sont soumis à l'ajustement $\gamma_{\rm ISR}2\gamma_{\rm SA}$ tandis que seuls les événements avec au moins un ou deux photons détectés sont soumis respectivement aux ajustements $\gamma_{\rm ISR}\gamma_{\rm SA}\gamma_{\rm LA}$ et $\gamma_{\rm ISR}2\gamma_{\rm LA}$. Dans tous les ajustements, les photons reconstruits doivent avoir une énergie minimale de 50 MeV. Comme le générateur

PHOKHARA est à limité à NLO, les ajustements NNLO donnent en retour des valeurs χ^2 dégradées et les résultats représentent le bruit de fond NLO sous les signaux NNLO recherchés dans les données. Au contraire, le générateur AFKQED produit des événements NNLO, donc les ajustements $\gamma_{\rm ISR}2\gamma_{\rm SA}$ et $\gamma_{\rm ISR}\gamma_{\rm SA}\gamma_{\rm LA}$ donnent en retour des valeurs χ^2 fiables pour les événements NNLO. Il est important de noter que les événements de la catégorie $\gamma_{\rm ISR}2\gamma_{\rm LA}$ ne sont simulés par aucun des deux générateurs. Dans cette étude, aucune sélection 2D-χ^2 n'est appliquée puisque les événements NNLO devraient avoir de grandes valeurs de χ^2 pour les ajustements $\gamma_{\rm ISR}\gamma_{\rm SA}$ et $\gamma_{\rm ISR}\gamma_{\rm LA}$. Il convient de mentionner que le niveau du bruit de fond dans le canal pion avec la soustraction du bruit de fond connue reste importante, même dans l'intervalle de masse du ρ. Pour améliorer l'efficacité de la sélection et la pureté des échantillons NNLO dans les données, les méthodes BDT sont adoptées.

Pour l'étude NNLO avec deux photons SA additionnels, les fractions des signaux NNLO $\mu\mu\gamma_{\rm ISR}2\gamma_{\rm SA}$ et $\pi\pi\gamma_{\rm ISR}2\gamma_{\rm SA}$ dans les données sont mesurées. Chaque fraction est normalisée par rapport au nombre total d'événements dans les échantillons de muons et de pions, dominé par les événements LO et NLO. La contribution du bruit de fond ainsi que la contamination par des événements LO et NLO dans les données ont été soustraits à l'aide des prédictions des simulations MC. Les fractions ont également été corrigées pour l'efficacité de la sélection. Pour le processus $\pi\pi\gamma_{\rm ISR}2\gamma_{\rm SA}$, les efficacités de sélection incluent les efficacités de sélection BDT. La plus grande incertitude pour les données du processus $\pi\pi\gamma_{\rm ISR}2\gamma_{\rm SA}$ est principalement attribuée à la différence d'efficacité du BDT entre les données et MC, qui dépasse les incertitudes statistiques.

Pour l'étude NNLO de l'ajustement $\gamma_{\rm ISR}\gamma_{\rm SA}\gamma_{\rm LA}$, les fractions des signaux NNLO dans les processus $\mu\mu\gamma_{\rm ISR}\gamma_{\rm SA}\gamma_{\rm LA}$ et $\pi\pi\gamma_{\rm ISR}\gamma_{\rm SA}\gamma_{\rm LA}$ dans les données sont obtenus pour des photons additionnels satisfaisant $\theta_{\min({\rm trk},\theta_{\rm LA})} < 20^\circ$ et $\theta_{\min({\rm trk},\theta_{\rm LA})} > 20^\circ$ séparément. Les fractions sont normalisées au nombre total d'événements dans les échantillons muons et pions correspondants. Lorsque $\theta_{\min({\rm trk},\theta_{\rm LA})} < 20^\circ$, pour les signaux $\mu\mu\gamma_{\rm ISR}\gamma_{\rm SA}\gamma_{\rm LA}$, les corrections d'efficacité pour la sélection χ^2 de 0,722(21) et 0,706(32) sont également prises en compte dans l'intervalle de masse inférieure à 1,4 GeV/c^2 et comprise entre 0,6 et 0,9 GeV/c^2, respectivement. Les chiffres cités entre parenthèses sont des erreurs statistiques. Pour les signaux $\pi\pi\gamma_{\rm ISR}\gamma_{\rm SA}\gamma_{\rm LA}$, les corrections d'efficacité incluent les efficacités nominales de sélection du BDT décrites ci-dessus. La correction des photons parasites a également été appliquée. Lorsque $\theta_{\min({\rm trk},\theta_{\rm LA})} > 20^\circ$, puisque la composante ISR à grand angle n'est pas incluse dans l'échantillon AFKQED, l'efficacité est extraite de l'échantillon AFKQED avec $\theta_{\min({\rm trk},\theta_{\rm LA})}$ inférieur à 20°, avec une correction supplémentaire des efficacités nominales de sélection BDT pour les signaux $\pi\pi\gamma_{\rm ISR}\gamma_{\rm SA}\gamma_{\rm LA}$. De plus, pour le processus $\pi\pi\gamma_{\rm ISR}\gamma_{\rm SA}\gamma_{\rm LA}$, la valeur moyenne finale de BDT1 et BDT2 est présentée avec l'incertitude systématique incluant la différence entre les deux sélections du BDT.

Pour l'étude NNLO de l'ajustement $\gamma_{\rm ISR}2\gamma_{\rm LA}$ avec deux photons additionnels détectés à grand angle et ajustés dans la plage d'acceptance du détecteur en plus du photon principal ISR, les fractions des signaux $\gamma_{\rm ISR}2\gamma_{\rm LA}$ dans les données de $\mu\mu\gamma_{\rm ISR}2\gamma_{\rm LA}$ et $\pi\pi\gamma_{\rm ISR}2\gamma_{\rm LA}$ sont obtenues. Aucune correction d'efficacité pour le

processus $\mu\mu\gamma_{\rm ISR}2\gamma_{\rm LA}$ n'est appliquée car il n'y a pas de signal simulé provenant des simulations MC. Pour le processus $\pi\pi\gamma_{\rm ISR}2\gamma_{\rm LA}$, la fraction a été corrigée pour i) la perte due au veto des π^0 et η, estimée à partir des lintervalles adjacents de la distribution $m_{\gamma_{\rm LA}\gamma_{\rm LA}}$, ii) l'efficacité de la sélection nominale BDT de 0,796 et iii) l'efficacité de la sélection $\chi^2_{\gamma_{\rm ISR}2\gamma_{\rm LA}} < 4,5$, estimée à partir de la distribution χ^2 correspondante de l'échantillon $\mu\mu\gamma_{\rm ISR}2\gamma_{\rm LA}$. Les signaux NNLO $\gamma_{\rm ISR}2\gamma_{\rm LA}$ sont également décomposés en trois catégories : double FSR, double LA ISR et mixte. Cette décomposition est effectuée en utilisant la variable $\theta_{\min({\rm trk},\theta_{\rm LA})}$ pour séparer les événements ($\theta_{\min({\rm trk},\theta_{\rm LA})} < 20^\circ$ pour la composante FSR et $\theta_{\min({\rm trk},\theta_{\rm LA})} > 20^\circ$ pour la composante LA ISR). La catégorie double FSR représente jusqu'à 7% de l'échantillon total de signaux, tandis que la plupart du signal est majoritairement partagée entre les doubles LA ISR et catégories mixtes. Il est important de noter que la correction des photons parasites a été appliquée.

Résultats finaux et conclusion

Après avoir corrigé les effets de contamination entre les catégories, corrigé l'efficacité complète de la sélection et l'efficacité des photons parasites discutée dans les sections précédentes, les fractions finales des différentes catégories pour les données sont obtenues. Les résultats sont également comparés aux prédictions des deux échantillons MC pour toutes les catégories. Il convient de mentionner que les taux $\gamma_{\rm ISR}\gamma_{\rm LA}$ séparés par $\theta_{\min({\rm trk},\theta_{\rm LA})} < 20^\circ$ et $\theta_{\min({\rm trk},\theta_{\rm LA})} > 20^\circ$ ont été corrigés, puis convertis en taux NLO FSR et NLO LA ISR à l'aide d'ajustements de modèles des distributions $\theta_{\min({\rm trk},\theta_{\rm LA})}$. D'une manière similaire, les taux $\gamma_{\rm ISR}\gamma_{\rm SA}\gamma_{\rm LA}$ ont été corrigés, puis convertis en taux NNLO FSR et NNLO LA ISR à l'aide d'ajustements de modèles des distributions $\gamma_{\rm ISR}\gamma_{\rm SA}\gamma_{\rm LA}$. Lorsque les contributions de NNLO sont soustraites du spectre d'énergie du photon SA dans le CM, la distribution du rapport des données sur le MC PHOKHARA devient beaucoup plus plate que celle avant corrections qui présente une pente significative. Le rapport ajusté confirme également qu'il existe un écart significatif entre les données et les taux des événements NLO SA ISR de PHOKHARA.

Les principaux résultats sont résumés ci-dessous :

- Les contributions NNLO sont clairement observées avec une fraction totale de (3,47 ± 0,38)% pour les muons et (3,36 ± 0,39)% pour les pions. Cela permet de corriger les taux NLO des effets de contamination des catégories NNLO. La forme de la distribution d'énergie pour les photons à petit angle fournit des preuves additionnelles et une bonne cohérence interne.

- Les fractions NLO SA-ISR dans le générateur PHOKHARA sont supérieures aux données, avec des rapports données/PHOKHARA de 0,763 ± 0,019 pour les dimuons et de 0,750 ± 0,008 pour dipions, tandis que les rapports LA-ISR, 0,96 ± 0,03 et 0,98 ± 0,03, sont compatibles avec l'unité. Cela indique un problème dans la distribution angulaire du photon NLO généré par PHOKHARA, avec un large excès aux petits angles par rapport aux faisceaux.

- Le générateur AFKQED fournit une description raisonnable des taux et des distributions d'énergie des données NLO et NNLO. Les taux pour la somme de SA-ISR et LA-ISR dans les données pour l'énergie du photon jusqu'à 2,3 GeV conduisent à des valeurs des rapports données/AFKQED légèrement élevées de 1,061 $\pm$ 0,015 pour les muons et de 1,043 $\pm$ 0,010 pour les pions.

- Le rapport entre les données et la prédiction PHOKHARA pour NLO FSR s'élève à 0,86 $\pm$ 0,05 pour les muons et à 0,76 $\pm$ 0,12 pour les pions. Les rapports correspondants de données/AFKQED sont de 1,09 $\pm$ 0,06 pour les muons et de 1,08 $\pm$ 0,10 pour les pions. Dans les deux cas, le rapport pion/muon est compatible avec l'unité et soutient l'hypothèse du comportement ponctuel du pion pour un FSR additionnel. Ce résultat, obtenu après une soustraction des photons parasites qui inclut à la fois une correction data/MC et prend en compte la contamination NNLO, remplace le résultat précédent où un excès de $(21 \pm 5)\%$ était observé dans l'analyse *BABAR* publiée.

Les conséquences de ces résultats sur les mesures de sections efficaces $\mu\mu(\gamma)$ et $\pi\pi(\gamma)$ dépendent fortement de l'approche expérimentale. Les mesures *BABAR* sont effectuées avec une sélection très lâche qui intègre tous les processus radiatifs NLO et ordres supérieurs. Par conséquent, aucune dépendance à l'égard d'un générateur d'événements particulier n'est introduite par des rayonnements additionnels. Seule l'acceptance, déterminée à l'aide de PHOKHARA interfacé avec la simulation du détecteur, est affectée par les défauts du générateur. Cependant, la correction d'acceptance de $(0{,}3 \pm 0{,}1) \times 10^{-3}$ est négligeable par rapport à l'incertitude systématique estimée de 0,5% pour la section efficace mesurée $\pi\pi(\gamma)$. En revanche, d'autres expériences utilisant l'approche ISR ne mesurent pas le rayonnement additionnel. Dans ces expériences les événements sont sélectionnés principalement dans la topologie LO, qui inclut les émissions virtuelles et de photons mous, et s'appuie sur le générateur PHOKHARA pour tenir compte de la contribution manquante de NLO. De plus ce générateur n'inclut aucune contribution NNLO ce qui représente un biais compte-tenu de nos mesures. En résumé les résultats de cette thèse remettent en question la validité de la procédure des expériences ISR autres que *BABAR* s'appuyant sur PHOKHARA pour deux raisons : d'une part, la contribution de NLO dur prédite par PHOKHARA est significativement plus grande que notre mesure, et d'autre part, les contributions du NNLO, absentes dans PHOKHARA, se situent à un niveau plus grand que les incertitudes systématiques citées par ces expériences.